Doctoral theses at NTNU, 2022:332

Sergey Bublik

# Slag-metal Separation in Mn Ferroalloy Production

Doctoral thesis

**NTNU**
Norwegian University of Science and Technology
Thesis for the Degree of
Philosophiae Doctor
Faculty of Natural Sciences
Department of Materials Science and Engineering

NTNU
Norwegian University of
Science and Technology

Sergey Bublik

# Slag-metal Separation in Mn Ferroalloy Production

Thesis for the Degree of Philosophiae Doctor

Trondheim, October 2022

Norwegian University of Science and Technology
Faculty of Natural Sciences
Department of Materials Science and Engineering

NTNU
Norwegian University of
Science and Technology

**NTNU**
Norwegian University of Science and Technology

Thesis for the Degree of Philosophiae Doctor

Faculty of Natural Sciences
Department of Materials Science and Engineering

© Sergey Bublik

ISBN 978-82-326-5233-4 (printed ver.)
ISBN 978-82-326-6006-3 (electronic ver.)
ISSN 1503-8181 (printed ver.)
ISSN 2703-8084 (online ver.)

Doctoral theses at NTNU, 2022:332

Printed by NTNU Grafisk senter

# Preface

This thesis is submitted to the Norwegian University of Science and Technology (NTNU) for partial fulfilment of the requirements for the degree of philosophiae doctor. The doctoral work has been carried out at the Department of Materials Science and Engineering, NTNU, Trondheim, Norway, between July 2018 and March 2022. The work has been supervised by Professor Kristian Etienne Einarsrud as the main supervisor and by Professor Merete Tangstad as a co-supervisor.

The research was funded by the Research Council of Norway (KPN Project, 267621). The author gratefully acknowledges the financial support from the Research Council of Norway and the Norwegian Ferroalloy Producers Research Association (FFF).

The computational resources employed in this research was provided by the NTNU IDUN/EPIC computing cluster and the Resources, Energy & Environment group at the Department of Materials Science and Engineering, NTNU.

Sergey Bublik
Trondheim, October 2022

# Abstract

The separation of slag and metal in the ferroalloy production process is an important issue that has an impact on both the ecological and environmental considerations of the entire production process. The extensive mixing of metal and slag during the tapping into ladles leads to the formation of a considerable amount of metal droplets in slag due to interfacial interaction and turbulence of the molten flow from the tap-hole. The entrainment of metal droplets into the slag phase causes ferroalloy losses with the slag, creating additional difficulties in the removal of metal from the slag. It is known that the separation of metal and slag is strongly influenced by interfacial phenomena and for this reason they were studied in this thesis, and the influence of interfacial tension and surface tension were also discussed for ferroalloy-slag systems.

The main goal of this research work was to understand interfacial phenomena between ferroalloy and slag. This has been achieved by developing a methodology for investigating the interfacial interaction in ferroalloy-slag systems, modelling the separation of molten slag and metal in OpenFOAM, and assessing operational parameters and physical properties affecting the formation of metal-slag emulsion and metal droplets in slag. The microstructure of slag and metal phases under different conditions has also been extensively addressed.

This thesis demonstrates a novel methodology for estimating the interfacial tension between metal and slag which combines experiments in the sessile drop furnace and multiphase modelling in OpenFOAM. It was concluded that the interfacial interaction can be significantly altered by surface-active elements such

as sulfur in ferroalloy-slag systems, as well as by changing the composition of the slag, which causes to the transfer of species or elements across the interface, creating interfacial instability and reducing the interfacial tension. As a consequence, the significant instability of the interface leads to higher losses of metal with the slag.

# Acknowledgement

First and foremost, I would like to thank my supervisors, Professor Kristian Etienne Einarsrud and Professor Merete Tangstad. I am extremely grateful for their guidance and involvement in every step of my PhD project. It has always been a pleasure for me to take on new challenges from them, which have helped me in both personal and professional development.

I am grateful to the Controlled Tapping project participants for many meetings where I had the opportunity to present my research to industrial partners and receive extensive feedback to enhance the relevance of my research. Especially, I owe many thanks to Mehdi Kadkhodabeigi and Benjamin Ravary from Eramet Norway for actively participating in many parts of my project and providing incredibly important ideas and comments. In addition, I am thankful to Eirik Fatnes and Anne Grethe Lindseth from Eramet Norway Sauda for a productive month of industrial traineeship in the beginning of my PhD, which gave me an incredible boost in understanding ferroalloy production.

I appreciate the opportunity to work on several research projects with Sarina Bao, Sylvain Gouttebroze, Terence Coudert, Jan Erik Olsen, Quinn Gareth Reynolds, which was a wonderful chance to gain valuable research experience and problem-solving skills from different perspectives. I would also like to express my high appreciation to the engineering staff at the Department of Materials Science and Engineering at NTNU for training me in working on various equipment and giving practical advices in conducting experiments and analysis. In particular, thanks to Morten Peder Raanes for assistance in carrying out EPMA, Arman

Hoseinpur-Kermani, Ivar Andre Ødegård and Jonas Einan Gjøvik for training on using many furnaces, discussing and solving problems associated with my experiments.

My deepest gratitude to Dmitry Slizovskiy for his tremendous help and support throughout the PhD project. It is an honor for me to know a great person like you and I very much hope that our family friendship will continue for very many years in the future. A big thanks to Trygve Storm Aarnæs, for being not only a colleague and office mate, but also a great friend with whom it is always a pleasure to communicate and have a good time. Many thanks to Varun Loomba, Trygve Lindahl Schanche, Sindre Engzelius Gylver, Kurian Jomy Vachaparambil, Vincent Canaguier, Hamideh Kaffash, Daniel Perez Clos, Dmitry Sukhomlinov, Didier Ngoy and many others for a lot of fun and interesting discussions. I am also grateful to everyone from the SiManTiAl-group for an excellent opportunity to refine my presentation skills and for providing feedback on different parts of my research work, which certainly made it many times better.

Finally, my sincere appreciation goes to my wife, Julia, for her constant support and unwavering faith in me not only during my thesis, but throughout every aspect of my life. For every successful man, there is a beautiful woman behind him; you are the moonlight as well as the sunshine of my life, thank you for everything you have been to me and for taking this journey with me. I would also like to thank my son, Adrian, for such a great privilege of being your father. It is a tremendous motivation for me to see how happy you are and how you grow every day.

# Contents

# List of Figures

# List of Tables

# Nomenclature

## Abbreviations

| | |
|---|---|
| CFD | Computational fluid dynamics |
| EPMA | Electron Probe Micro Analyzer |
| FVM | Finite volume method |
| LBADSA | Low-bond axisymmetric drop shape analysis |
| MPLIC | Multicut piecewise-linear interface calculation |
| SAF | Submerged arc furnace |
| VOF | Volume of fluid |
| XRF | X-ray fluorescence |

## Greek Symbols

| | |
|---|---|
| $\alpha$ | Phase fraction |
| $\gamma$ | Surface or interfacial tension |
| $\theta$ | Contact angle |
| $\mu$ | Dynamic viscosity |
| $\nu$ | Kinematic viscosity |
| $\rho$ | Density |

## Latin Symbols

| | |
|---|---|
| $A$ | Surface area |

| | |
|---|---|
| $A_s$ | Surface area of a sphere |
| $C_m$ | Molar heat capacity |
| $C_p$ | Specific heat capacity |
| $g$ | Gravitational acceleration |
| $h$ | Height |
| $\overline{h}$ | Average height |
| $\Delta H$ | Enthalpy |
| $k$ | Surface curvature |
| $k_R$ | Surface roughness correction coefficient |
| $m$ | Weight |
| $M$ | Molar mass |
| $t$ | Time |
| $U$ | Fluid velocity |
| $U_c$ | Critical velocity |
| $U_r$ | Compression velocity |
| $V$ | Partial molar volume |
| $W_t$ | Total work of adhesion |
| $x$ | Molar fraction |

**Subscripts & Superscripts**

| | |
|---|---|
| $T,liq$ | Used for properties at a given temperature for the liquid state |
| $T,sol$ | Used for properties at a given temperature for the solid state |
| $liq$ | Liquid state |
| $sol$ | Solid state |
| $bulk$ | Bulk components |
| $surf$ | Surfactants |

| | |
|---|---|
| $i$ | i-component in slag |
| $vis$ | Visible |
| $non-vis$ | Non-visible |
| $exp$ | Corresponding to experiments |
| $sim$ | Corresponding to simulations |
| $slag$ | Corresponding to slag |
| $metal$ | Corresponding to metal/ferroalloy |
| 1773 | at 1773 K |

**Other Notation**

| | |
|---|---|
| $[A_i]$ | Species or elements in the metal phase |
| $(A_i)$ | Species or elements in the slag phase |
| $\approx$ | Approximately |

# Part I

# Introduction

# Chapter 1

# Importance of metal-slag separation

Pyrometallurgical processes for the production of many metals are inextricably linked to the high-temperature interaction between molten metal and slag generated during smelting. Specifically, in ferroalloy production, a large quantity of metal and slag is produced during carbothermic reduction of oxides to their metallic form. Slags primarily consist of oxides of Mn, Si, Al, Ca and Mg, introduced to the furnace by raw materials (ores, coke, fluxes), while the metal phase is a mixture of Fe, saturated C and other metals such as Mn, Si and Cr. Ferroalloys are typically produced in a submerged arc furnace (SAF) as sketched in Figure 1.1. Both molten metal and slag are tapped from the furnace through tap-holes into several ladles, where metal and slag separate based on their density difference. The ladles are usually arranged in a cascade with slightly different heights, allowing molten slag to flow out of the first ladle, leaving most of the molten metal phase in the first (metal) ladle. Due to extensive mixing of metal and slag during filling the metal ladle, slag overflowing to the second (slag) ladle involves small metal droplets entrained in the slag phase, which form as a result of interfacial interaction and turbulence of the molten flow from the tap-hole. A thin layer of slag, which is left in the metal ladle after tapping, is then removed either by tilting the ladle and pouring slag or/and by dragging off the slag with a mechanical rake [1]. A schematic showing the tapping of molten material into the cascade of ladles is shown 1.2.

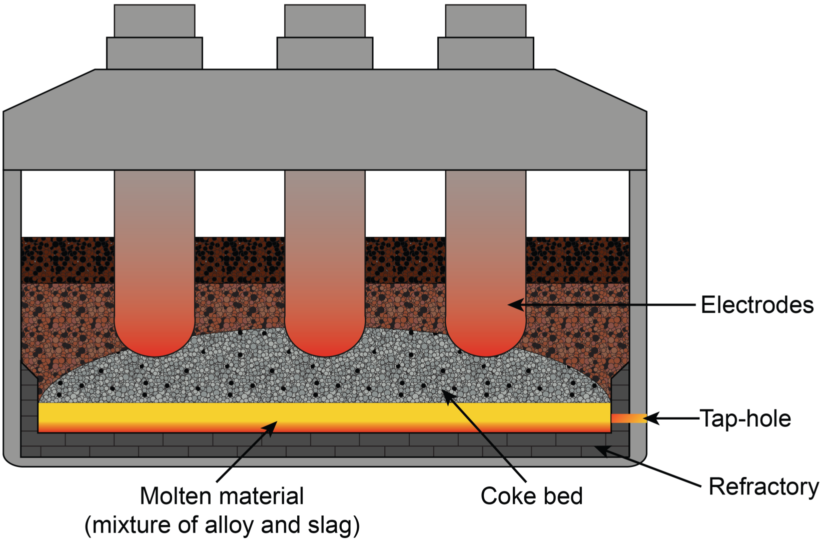

**Figure 1.1:** Schematic of SAF for production of ferroalloys. Reprinted from Bublik et al. [2] under the terms of the Creative Commons CC BY license.

Both entrainment of metal droplets in the slag phase and mechanical removal of slag layer from the metal ladle lead to losses of ferroalloy with slag, creating additional operational difficulties for the removal of metal from slag. Due to the rising importance of sustainable production and environmental considerations [4], it is crucial to ensure high metal and slag separation to reduce the economical and environmental consequences.

Previously, several studies have shown that the metal-slag separation can be improved by modifying properties of metal and slag such as interfacial tension and viscosity [5–7], or the geometry of the tapping equipment, e.g. changing the position or rotation of ladles in the cascade [8]. The separation of molten materials can be studied by a wide range of methodologies, as for example:

- sessile drop technique [9], where the interaction between metal and slag in

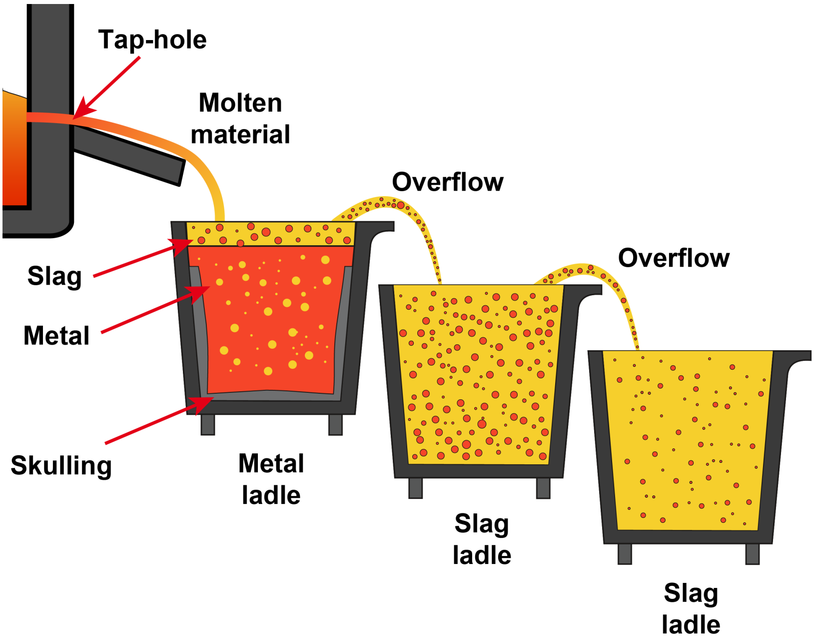

**Figure 1.2:** Tapping of SAF into ladles. Reprinted from Bublik and Einarsrud [3].

inert, reducing or oxidizing atmosphere is recorded at high temperatures.

- X-ray technique [10], where a metal droplet settles down in the slag layer and X-ray source penetrates the slag layer, allowing to capture images of different intensity, which characterize the metal-slag interaction.
- computational approach [11], where the interfacial interaction between molten metal and slag can be simulated/modelled at a laboratory or industrial scale using physical properties found experimentally.

The problem with poor separation of metal droplets from slag and formation of metal-slag emulsion is also important for pyrometallurgical production of other metals, e.g. steel [12] or Cu [13]. Therefore, understanding the phenomena governing the separation of metal and slag will provide knowledge which can be applied in production to reduce metal losses and hence production costs.

The interfacial tension and capillary forces acting on a droplet are of great importance for separation of metal and slag as described by Zhang et al. [14]. The interfacial tension affects the droplet velocity as well as the displacement at the steel-slag interface, increasing both values as the interfacial tension increases, which promotes metal-slag separation. Therefore, interfacial tension and wettability govern the separation behaviour of metal droplets in slag, including the formation of a metal-slag emulsion and the entrainment of metal droplets by the slag.

Assuming laminar flow, the terminal velocity of a liquid droplet can be expressed from Stokes' Law [15]:

$$U = \frac{d^2 g \Delta\rho}{18\mu} \tag{1.1}$$

Grace et al. [16] suggested that liquid droplets settling in another phase or rising gas bubbles have a maximum stable diameter after which they tend to break-up into smaller droplets. The maximum stable droplet diameter is found as:

$$d_{max} = 4\sqrt{\frac{\gamma_{s-m}}{g(\rho_{metal} - \rho_{slag})}} \tag{1.2}$$

For a slag or metal droplet with the maximum diameter $\mathrm{d}_{max}$, Eq. 1.1 is rewritten as:

$$U = \frac{d_{max}^2 g(\rho_{metal} - \rho_{slag})}{18\mu} \tag{1.3}$$

It is evident from Eq. 1.2 and 1.3 that the interfacial tension affects the terminal velocity of droplets and is therefore an important parameter characterizing the separation of molten slag and metal. Figure 1.3 shows the change in the maximum droplet diameter of FeMn as a function of the interfacial tension from 1.0 to 1.5 N/m, calculated from Eq. 1.2 using density of FeMn and slag. Figure 1.4 illustrates the change in the terminal velocity of the FeMn droplet depending upon the maximum droplet diameter as found from Eq. 1.3. Based on the described equations and figures, it can be concluded that a higher value of the interfacial tension between metal and slag contributes to their better separation.

Metal entrainment in slag is an important problem for ferroalloy industry [17,

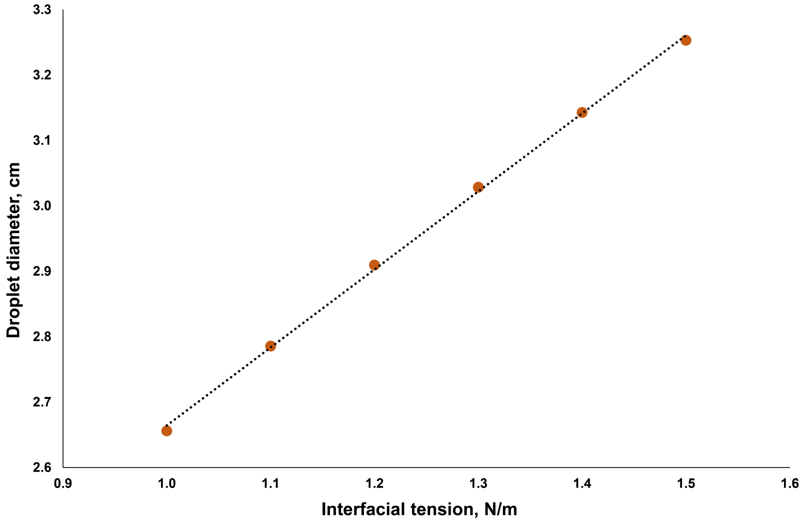

**Figure 1.3:** The influence of interfacial tension on the maximum stable droplet diameter.

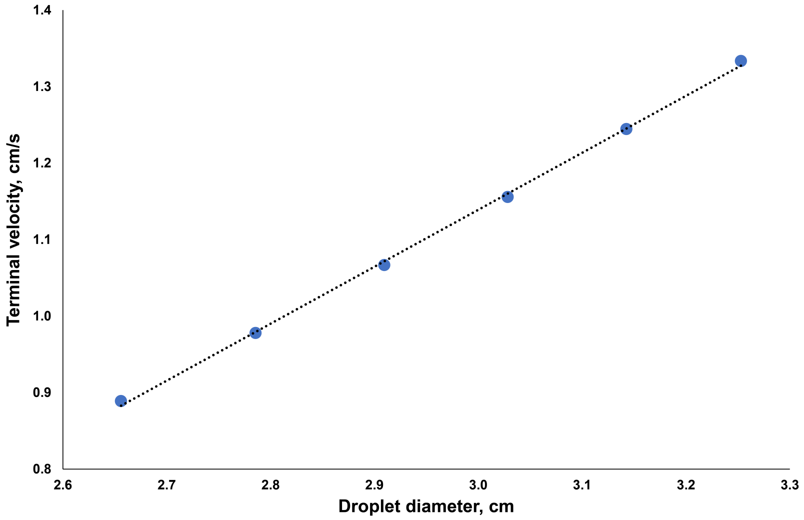

**Figure 1.4:** The influence of the maximum stable droplet diameter on the terminal velocity of a droplet.

18]. However, the mechanisms of metal and slag separation for the ferroalloy-slag system have not been studied in detail to suggest effective ways of their separation at the industrial scale. In addition, the study of the mechanisms of interaction between two molten materials is a significant challenge, since it requires involvement of complex techniques, such as X-ray analysis [7, 19], and also does not allow investigating separation mechanisms in dynamics with high accuracy. This work aims to study mechanisms of slag-metal separation and to provide new knowledge for the ferroalloy industry that can be used to improve existing operations as well as for developing new procedures to improve slag and metal separation.

In this thesis, the scope is limited to Mn ferroalloys production, but many phenomena discussed here are also valid for other pyrometallurgical processes involving separation of metal and slag phases.

# Chapter 2

# Goals, outline and contributions

## 2.1 Goals and research questions

The main goal of this doctoral thesis is to provide new knowledge of separation mechanisms of molten FeMn/SiMn and slag. As the methodology for investigating interfacial interaction between molten materials is not extensively studied, one of the sub-goals is to develop a methodology allowing to characterize interfacial phenomena and assess interfacial tension between molten slag and metal at high temperatures, as an alternative to the sessile drop [9, 20] and X-ray [19, 21, 22] methods. As indicated in previous studies [6, 10, 23–26], slag-metal separation is influenced by absorption of surface active elements such as sulfur at the interface, or by mass transfer due to the composition change after reaction between slag and metal.

The following research questions will be considered:

- How can the interfacial interaction between two molten phases be studied at the laboratory scale?
- How can Computational Fluid Dynamics (CFD) facilitate the determination of interfacial tension?
- How does the interfacial interaction change depending on the sulfur concentration, slag composition and experimental conditions?

- How does the interfacial tension affect metal losses with slag?
- What are the main properties of the slag affecting the interfacial interaction and how can they be estimated?

In addition to the research goals and question mentioned above, the thesis also addresses a review of methods for modelling of ferroalloy tapping, which also includes a review of literature related to interfacial interaction and separation of slag and metal.

The following objectives were defined to achieve the established research goals and answer the research questions:

- Study literature and discuss modelling approaches of ferroalloy tapping, including separation of FeMn/SiMn and slag.
- Review equipment that can be used to study the interfacial interaction between FeMn/SiMn and slag and propose a relevant methodology for this purpose.
- Simulate and investigate the interfacial interaction using CFD tools (e.g. OpenFOAM).
- Investigate the influence of sulfur addition and slag composition, as well as experimental parameters, such as temperature and holding time, on metal droplet formation and metal entrainment in slag.
- Study microstructure of FeMn/SiMn and slag phases after the interfacial interaction at different experimental conditions.

## 2.2 Outline of the thesis

An outline of the thesis parts is provided below:

- **Part I: Introduction** - describes the importance of metal-slag separation, and aims and scope of the thesis.
- **Part II: Background** - provides theoretical background on physical properties related to the metal-slag separation, explains mechanisms of metal-slag emulsification and metal droplet formation, and shows the most relevant

experimental data on surface and interfacial tension of metal and slags.

- **Part III: Methodology** - introduces the developed methodology for studying the interfacial interaction between metal and slag.
- **Part IV: Scientific dissemination** - presents summary of manuscripts published during the PhD research period.
- **Part V: Final conclusions and further work** - summarizes the research work and suggests topics for future research.

## 2.3 List of publications

The thesis is written based on a collection of articles which has been submitted or published during the doctoral period. In addition to the journal publications and conference proceedings, conferences attended during the PhD have also been mentioned. The following publications are included in the thesis:

- **Paper I** (conference paper): "Slag-metal Interactions in the FeMn Tapping Process: Interfacial Properties and Wetting". Sergey Bublik, Sarina Bao, Merete Tangstad, Kristian Etienne Einarsrud, *Proceedings of the Liquid Metal Processing & Casting Conference 2019*, Birmingham, UK, 2019.
- **Paper II** (conference paper): "Inverse Modelling of Interfacial Tension Between Ferroalloy and Slag Using OpenFOAM". Sergey Bublik, Kristian Etienne Einarsrud, *Proceedings from the 14th International Conference on CFD in Oil & Gas, Metallurgical and Process Industries*, Trondheim, Norway, 2020.
- **Paper III** (journal article): "A Review of Ferroalloy Tapping Models". Sergey Bublik, Jan Erik Olsen, Varun Loomba, Quinn Gareth Reynolds, Kristian Etienne Einarsrud, *Metallurgical and Materials Transactions B*, 52, pp. 2038-2047, 2021.
- **Paper IV** (journal article): "Interfacial Behaviour in Ferroalloys: The Influence of Sulfur in FeMn and SiMn Systems". Sergey Bublik, Sarina Bao, Merete Tangstad, Kristian Etienne Einarsrud, *Metallurgical and Materials Transactions B*, 52, pp. 3624-3645, 2021.

- **Paper V** (journal article): "Interfacial Behaviour in Ferroalloys: The Influence of FeMn Slag Composition". Sergey Bublik, Merete Tangstad, Kristian Etienne Einarsrud, *Metallurgical and Materials Transactions B*, 2022.
- **Paper VI** (journal article): "Slag Properties in the Primary Production Process of Mn-Ferroalloys". Merete Tangstad, Sergey Bublik, Shokouh Haghdani, Kristian Etienne Einarsrud, Kai Tang, *Metallurgical and Materials Transactions B*, 52, pp. 3688-3707, 2021.
- **Paper VII** (conference paper): "SlagCalculator: A Framework for Slag and Metallurgical Properties". Sergey Bublik, Sylvain Gouttebroze, Terrence Coudert, Merete Tangstad, Kristian Etienne Einarsrud, *Proceedings of the 16th International Ferro-Alloys Congress (INFACON XVI) 2021*, Trondheim, Norway, 2021.

In addition to the manuscripts included in the thesis, the developed methodology has been utilized in:

- **Paper VIII** (extended abstract): "Influence of sulphur on the interfacial behaviour between FeMn alloy-slag and SiMn alloy-slag". Sergey Bublik, Sarina Bao, Merete Tangstad, Kristian Etienne Einarsrud, *The 11th International Conference on Molten Slags, Fluxes and Salts (MOLTEN 2021)*, Seoul, Korea, 2021.
- **Paper IX** (journal article): "Investigation of Two Immiscible Liquids Wetting at Elevated Temperature: Interaction Between Liquid FeMn Alloy and Liquid Slag". Sarina Bao, Merete Tangstad, Kai Tang, Kristian Etienne Einarsrud, Martin Syvertsen, Morten Onsøien, Artur Kudyba, Sergey Bublik, *Metallurgical and Materials Transactions B*, 52, pp. 2847–2858, 2021.

A schematic overview of the thesis structure is presented in Figure 2.1.

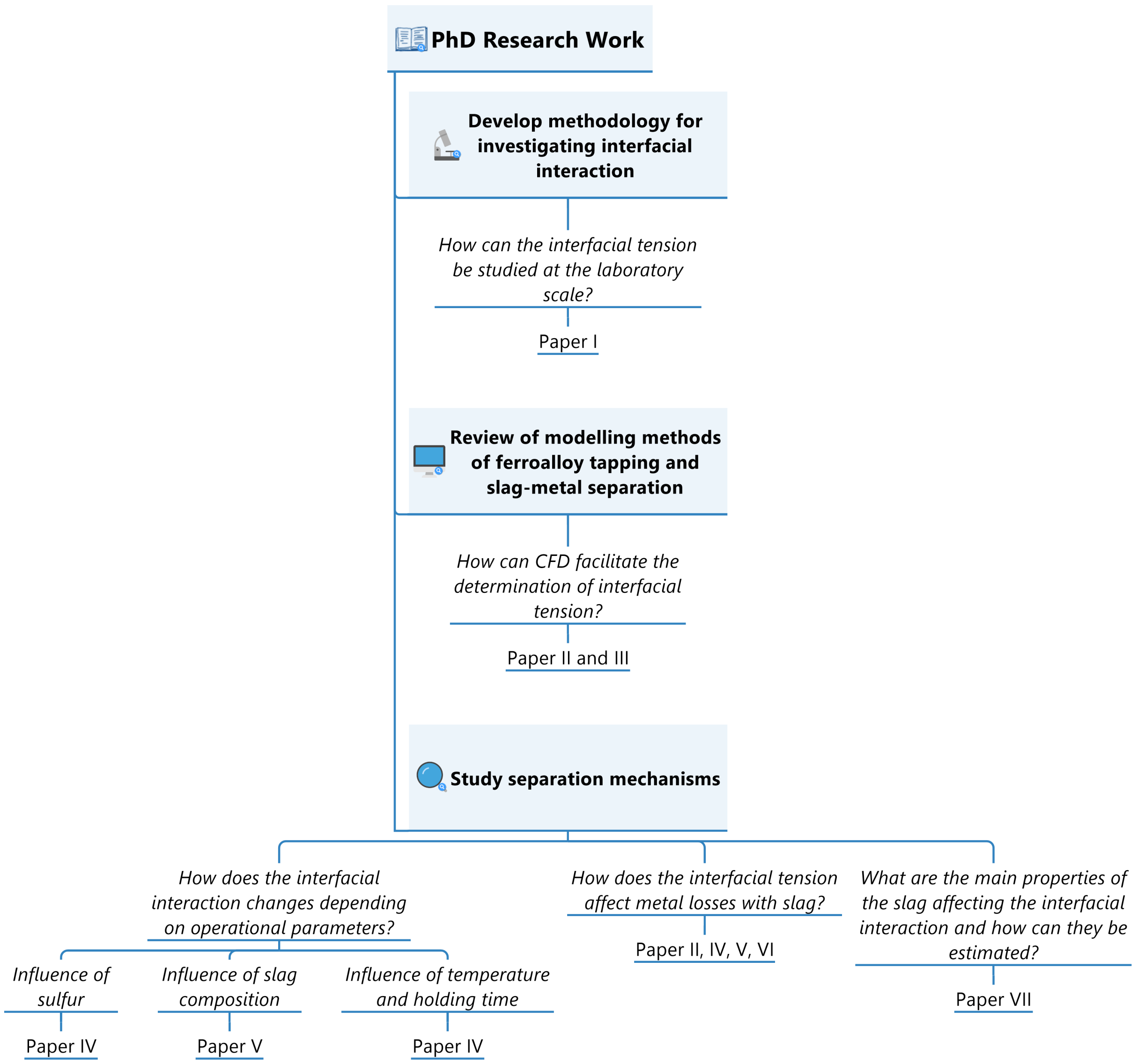

**Figure 2.1:** Schematic outline of the thesis.

# Part II

# Background

# Chapter 3

# Contact angle, surface and interfacial tension

Surface or interfacial tension is the thermodynamic quantity characterizing the reversible work at a surface or an interface, which is needed to create unit area of the surface or the interface at constant temperature, volume and chemical potentials [27]. Both surface and interfacial tension are expressed in terms of $\gamma$.

As shown in Figure 3.1, a liquid drop (phase 1) comes in contact and adheres with a solid or liquid (phase 2), forming a finite contact area, only if the total energy of the system reduces; hence, the total energy of the system is reduced by the amount of the work of adhesion of the phase 1 to phase 2. Therefore, the work of adhesion per unit area is the amount of energy per unit area required to separate phase 1 and phase 2. The work of adhesion per unit area is expressed as [28]:

$$W_A = \gamma_1 + \gamma_2 - \gamma_{12}, \tag{3.1}$$

where $W_A$ is the work of adhesion at the solid-liquid or liquid-liquid interface, $\gamma_1$ and $\gamma_2$ are surface tension of phase 1 and phase 2, and $\gamma_{12}$ is the interfacial tension between these phases. When $W_A$ is positive then there is an attraction between phase 1 and 2 leading to wetting and when it is negative then there is a repulsion between them resulting in non-wetting behaviour.

When the liquid drop is surrounded by gas (Figure 3.1A), its total interfacial free energy is defined as:

$$W_t = \gamma_1 A_s \rightarrow \gamma_1 = \frac{W_t}{A_s}. \tag{3.2}$$

When the liquid is in contact with a solid or liquid, the total area of the liquid drop is equal to $A_{12} + A_{13}$ (Figure 3.1B, 3.1C). The total free energy after deformation is expressed as:

$$W_t = \gamma_1(A_{12} + A_{13}) - W_A A_{12}. \tag{3.3}$$

At equilibrium, the surface or interfacial energy of the liquid is minimized by minimizing the contact areas:

$$\gamma_1(dA_{12} + dA_{13}) - W_A dA_{12} = 0. \tag{3.4}$$

Knowing that $dA_{13}/dA_{12} = \cos\theta_Y$ in Figure 3.1D, the Young equation can be expressed in terms of the surface and interfacial tension and the contact angle [29]:

$$\cos\theta_Y = \frac{\gamma_{23} - \gamma_{12}}{\gamma_{13}} \quad or \quad \gamma_{12} = \gamma_{23} - \gamma_{13}\cos\theta_Y. \tag{3.5}$$

Rewriting this equation for metal and slag in gas, it becomes:

$$\cos\theta = \frac{\gamma_m - \gamma_{s-m}}{\gamma_s} \quad or \quad \gamma_{s-m} = \gamma_m - \gamma_s\cos\theta. \tag{3.6}$$

According to Eq. 3.6, the interfacial tension $\gamma_{s-m}$ is lower than the surface tension $\gamma_m$ when $\theta < 90°$, which corresponds to partial wetting ($\theta < 90°$) and complete wetting when $\theta$ is close to 0°). When the contact angle is higher than 90°, $\gamma_{s-m}$ becomes higher than $\gamma_m$ and to minimize the total surface/interfacial energy of the liquid, the contact area ($A_{12}$) will be reduced and in this case the liquid has a low degree of wetting and forms a spherical liquid droplet.

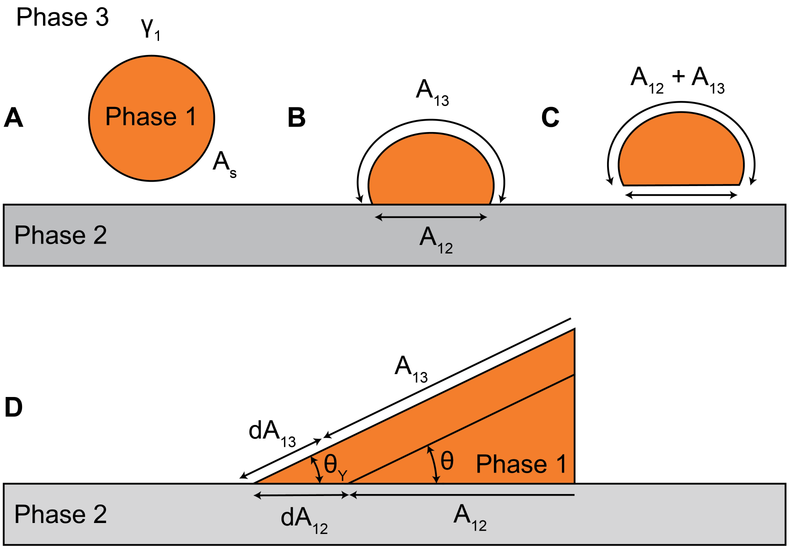

**Figure 3.1:** A - a liquid drop (phase 1) in gas phase (phase 3) without contact with a solid or liquid (phase 2), where the surface area of the liquid drop is $A_s$, B - the curved area of the liquid drop at liquid-gas interface ($A_{13}$ and the flat area of the liquid drop in contact with ($A_{12}$), C - the total interfacial area of the deformed liquid drop ($A_{LG}+A_{SL}$), D - the surface area change after the interfacial interaction.

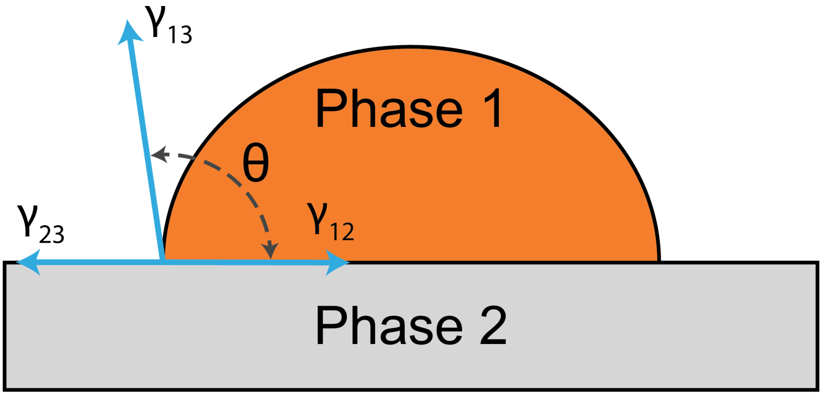

**Figure 3.2:** Schematic representation of the contact angle formed by the sessile liquid drop on the smooth and flat substrate.

In addition, the Young equation (3.5) can be obtained by balancing the forces at the three-phase contact line as shown schematically in Figure 3.2.

The contact angle, the surface and interfacial tension are closely related to the Helmholtz free energy (Eq. 3.7) [30], which is a function of temperature and chemical composition of the system. The chemical composition of the liquid droplet varies with the dissolution of elements or compounds into the droplet, as a result the contact angle and surface/interfacial tension will change after chemical reactions in the system. The Helmholtz free energy in this case is defined as:

$$dF = \gamma dA + \mu dN, \tag{3.7}$$

where $dF$ is the change of surface excess Helmholtz energy, $\mu$ is the surface chemical potential, $N$ is the number of mobile particles.

## Chapter 4

# Mechanisms of metal-slag emulsification and metal droplet formation

### 4.1 Mass transfer of elements and species across the interface

Jakobsson et al. [31, 32] suggested that low interfacial tension is associated with the rapid mass transfer of chemical elements at the interface between metal and slag, and that interfacial tension tends to increase if the mass transfer rate decreases. Hence, the force balance and contact angles at at the three-phase contact line can be described by Figure 4.1, where the force balance is expressed as:

$$\frac{\gamma_s}{\sin\theta_1} = \frac{\gamma_m}{\sin\theta_2} = \frac{\gamma_{s-m}}{\sin\theta_3}. \tag{4.1}$$

The horizontal interface between metal and gas confirms that the equilibrium between metal and gas is reached rapidly, while interfacial tension slowly decreases over time if there are reactions in the system and chemical elements distribute between metal and slag. The ratio $\gamma_{s-m}/\sin\theta_3$ has to be constant, and

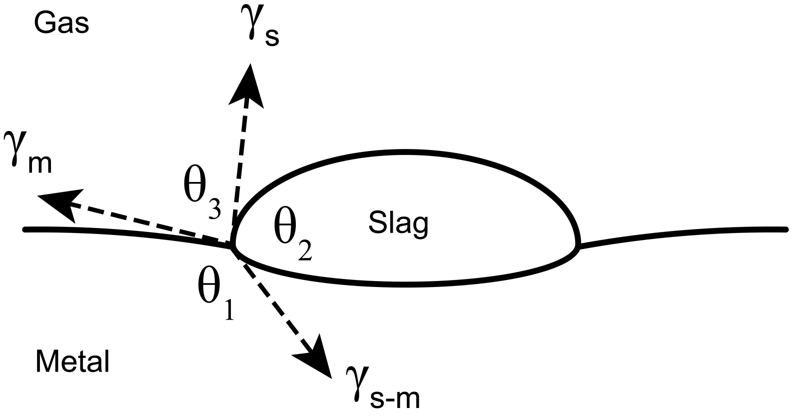

**Figure 4.1:** Force balance at the three-phase contact line for metal, slag and gas. Reprinted from Bublik et al. [33] under the terms of the Creative Commons CC BY license.

therefore $\sin\theta_3$ decreases with time as well. The total force, which acts in the vertical direction pulls the slag droplet upwards when $\gamma_{s-m}$ is decreasing.

Already in 1955, Kozakevitch et al. [34] described interfacial phenomena between molten iron alloy and slag by carrying out experiments with Fe-C-S droplets and CaO-$SiO_2$-$Al_2O_3$ slag in a furnace equipped with an X-ray source. It was found that the droplet shape changes and the dynamic interfacial tension decreases considerably during the desulfurization reaction. This phenomenon was confirmed by Ooi et al. [35], where the sessile drop by applying the X-ray radiograph technique was used to study the interfacial interaction between molten iron and CaO-$SiO_2$-$Al_2O_3$ slag. It was observed that addition of Al to the metal-slag system causes sharp decrease in the interfacial tension due to reduction of $SiO_2$ in slag by Al and transfer of Si from slag to metal:

$$4[Al] + 3(SiO_2) = 2(Al_2O_3) + 3[Si]. \tag{4.2}$$

Kim and Park [36] performed experimental and thermodynamic study of reaction mechanisms between molten slag and Mn/Al-containing steel. It was shown that Mn content in steel with 1 wt. % Al rapidly decreases due to reduction of $SiO_2$ in slag by Mn:

$$2[Mn] + (SiO_2) = 2(MnO) + [Si]. \tag{4.3}$$

However, for 3 and 6 wt. % Al in steel, Mn is not oxidized by the slag, and thus only Reaction 4.2 governs the mass transfer through the interface for such a system. Besides that, it was emphasized that metal droplets are dispersed in the slag if the Si content of the metal droplets is high.

Ni et al. [26, 37] showed that the drop in the interfacial tension during reactions between slag and steel is observed for both low- and high-viscosity slags. The interfacial tension decreases until the slag and metal are in equilibrium, therefore the dynamic interfacial tension behaviour depends on the oxygen adsorption rate at the metal-slag interface, the oxygen consumption rate by reactions with Al and the oxygen desorption from the interface to the metal bulk.

Rhamdhani and Brooks [24] studied the interfacial interaction between a metal droplet (Fe-Al) and slag, where it was reported that the droplet flattens during reactions with the slag. At the moment of intense reactions between slag and metal, spontaneous emulsification occurs, drastically increasing the interfacial area from ≈400 $mm^2$ to 1200 $mm^2$. In a following study, Rhamdhani et al. [38] described the mechanism of droplet formation during interfacial reactions. Observations at the interface demonstrated that microscopic emulsification and the formation of small metal droplets occurs 5 minutes after the metal droplet is immersed in the slag, meaning that the interfacial area between slag and metal increases while the interfacial tension decreases. As the reaction proceeded and the equilibrium between metal and slag is reached, the metal droplets coalesce to form one whole droplet and the interfacial area decreases. However, the droplet after reactions has a larger volume due to the slag entrainment in metal [39]. Riboud and Lucas [25] investigated the mass transfer and the interfacial phenomena more extensively, where they determined that a drop in the interfacial tension also occurs in other metal-slag systems with alloying elements and impurities, such as Al, S, Ti, P, B, Cr and Si. It was found that the dynamic interfacial tension decreases nearly to 0 N/m during the mass transfer of elements across the interface. The microscopic analysis highlighted that intense reactions between metal and slag result in spontaneous emulsification which increases the interfacial area and leads to the formation of metal droplets of different diameter, which are then entrained in slag.

During the tapping of ferroalloys into ladles, emulsification occurs mainly due the intensive mixing of metal and slag as a result of turbulent flow from the tap-hole. The slag-metal emulsion stabilizes after the tapping is finished and the droplets begin to settle down under the influence of gravity as well as coagulate with each other. The most important parameters affecting the slag-metal emulsion stability are interfacial tension between metal and slag, slag viscosity, solid particles in a metal-slag system and surface-active elements [40].

## 4.2 Kelvin-Helmholtz interfacial instability and critical flow velocity

Chung and Cramb [39] pointed out that the emulsification of two distinct phases are closely related to the interaction of fluids at the interface, and that the driving force across the interface depends upon the concentration gradient at the interface. In case of the concentration gradient and the fluid flow driven by the interfacial reaction, the interface eventually becomes unstable and the metal-slag interfacial area increases (relating to the Kelvin-Helmholtz interfacial instability). Based on the Kelvin-Helmholtz model, Gopal [41] discussed the mechanism of small droplet formation and emulsification of slag and metal during reactions between them. If the mass transfer rate of elements or compounds across the interface is low, it results in a slight destabilization of the interface (Figure 4.2a).

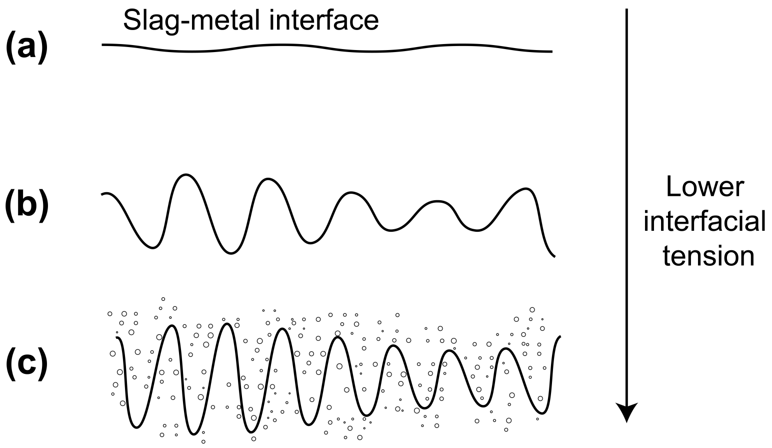

**Figure 4.2:** Emulsification of slag and metal and formation of small droplets due to the Kelvin-Helmholtz instability. Reprinted from Bublik et al. [33] under the terms of the Creative Commons CC BY license.

At higher mass transfer rates, the destabilization of the interface is more severe, resulting in the formation of the metal-slag emulsion (Figure 4.2b) and droplets of one phase into another (Figure 4.2c).

Krishnapisharody and Irons [42] described three different stages in evolution of the fluctuations induced by the Kelvin-Helmholtz interfacial instability at the interface between two liquids and, as a consequence, the formation of small droplets:

1. Initial disturbance of the interface and the lip formation at the interface.
2. Growth of the lip into a ligament.
3. Break-up of the ligament and the formation of small droplets.

The Kelvin-Helmholtz instability criterion for two incompressible liquids is expressed via the critical velocity between the fluids [43]:

$$\Delta U_c^2 = \frac{\rho_1 + \rho_2}{\rho_1 \rho_2}(\rho_1 - \rho_2)\frac{g}{k} + \gamma k. \tag{4.4}$$

The critical flow velocity, as defined in Eq. 4.4, plays a significant role in droplet entrainment as it is a limiting value above which the flow becomes turbulent [44, 45]. As such, the amount of entrainment increases sharply when the critical velocity reaches a certain value and the metal-slag interface becomes unstable. Experiments by Zhang et al. [44] demonstrated that the critical velocity of water-oil systems slowly increases with the increase of the interfacial tension. However, it can be argued that the effect of the interfacial tension can be more pronounced in metal-slag systems, when the interfacial tension changes considerably due to chemical reactions and the mass transfer across the interface. It was also concluded that the effect of viscosity becomes more important when the interfacial tension between metal and slag is low, which can reduce the entrainment of slag/metal droplets. Irons et al. [46] modelled the entrainment rate in a ladle by applying Large Eddy Simulation approach, where it was found that at constant slag viscosity, higher values of interfacial tension contribute to low entrainment rates and therefore better separation of slag and metal. The effect of viscosity change at constant interfacial tension was found to be less significant and the entrainment rate slightly decreases when slag viscosity increases.

Fatehi et al. [45] indicated that interfacial and gravity forces affect the formation of secondary Kelvin-Helmholtz instabilities (shorter wave-length disturbances), resulting in the formation of a large amount of small droplets. Here, the Eötvös number or the Bond number is a dimensionless number that characterizes the importance of gravity compared to interfacial forces and the interface stability, and is defined as:

$$Eo = Bo = \frac{\Delta \rho g L^2}{\gamma} \quad (\frac{\text{gravitational force}}{\text{surface tension force}}), \tag{4.5}$$

where $Eo$ is the Eötvös number, $Bo$ is the Bond number, $L$ is the characteristic length (typically the droplet diameter).

For a metal-slag system and a metal droplet settling in slag, this equation is rewritten as:

$$Eo = Bo = \frac{(\rho_{metal} - \rho_{slag}) g d_{metal}^2}{\gamma_{s-m}}. \tag{4.6}$$

The formation of secondary instabilities can be reduced or completely prevented by high interfacial tension (low Bond number), while the higher Bond number causes a significant decrease in interfacial stability and a sharp increase in secondary instabilities [45].

## 4.3 Marangoni flow

Marangoni convection or Marangoni flow is another important mechanism for slag and metal emulsification, appearing due to the surface/interfacial tension gradient along the surface or the interface. In turn, the surface or interfacial tension gradient can be caused by temperature difference, surface-active elements or electrical potential gradients. Marangoni convection can enhance the mass transfer at the interface, and therefore the reaction rate becomes higher as well. In metallurgical processes, Marangoni flow can be induced if surface-active elements transfer across the interface in a metal-slag system. Here, Marangoni convection may also be one of the reasons for interface turbulence due to the high velocity of the flow along the interface [10, 47]. As a result of the interface disturbance, droplets of molten metal will be entrained in slag, resulting in metal losses.

The instability of the interface causes interfacial fluctuations propagating in the normal direction, leading to the formation of a droplet at the interface as indicated in Figure 4.3. Bainbridge and Sawistowski [48] suggested that the necking stage of the drop formation appears before the detachment of a droplet, and that this stage is governed by the Marangoni effect. As the result of the concentration difference inside the droplet and the region between the droplet and the interface, interfacial tension generates Marangoni flow around the droplet and the neck, which accelerates the droplet detachment. However, if the interfacial tension between the droplet and another phase is lower than between the neck and another phase, Marangoni convection will hamper the emulsification and the droplet detachment [39]. Muhmood et al. [22] discussed that Marangoni flow causes the droplet flattening due do the interfacial tension gradient along the metal-slag in-

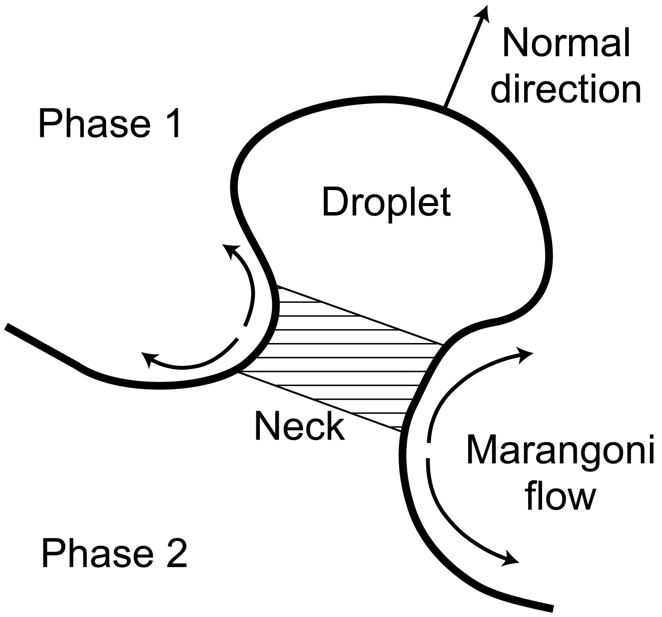

**Figure 4.3:** Emulsification caused by Marangoni flow.

terface. Sulfur transfer across the metal-slag interface can be mentioned as one of the most common examples of Marangoni flow in metal-slag system. Several studies [22, 32] confirmed that sulfur addition to a metal-slag system leads to the fluctuations at the metal-slag interface, resulting in change of the surface area of the interface. Sulfur, which is present in a metal-slag system, distributes between metal and slag, as well as along the metal-slag interface.

## Chapter 5

# Experimental data on surface and interfacial tension

The surface and interfacial tension of manganese ferroalloy systems have not been extensively reported. It is however reasonable to analyze the data for systems corresponding to steel production in addition, since they have similar components to manganese ferroalloys.

## 5.1 Surface tension of metal

Lee et al. [49] pointed out that the surface tension of a pure Fe-system is relatively high ($\approx$1.90 N/m), however, it can be significantly reduced by other elements such as Mn, which reduces the surface tension to 1.00 N/m when the Mn content increases to 100 wt. %. Si reduces the surface tension in a similar way when added to Fe, reaching a value of 0.70 N/m for a pure Si-system [50]. The surface tension of Fe gradually decrease with sulfur addition, which is caused by a high concentration of sulfur at the surface [51, 52]. Lee and Morita [51] demonstrated that the addition of carbon to low sulfur Fe ($S < 0.001$ wt. %) on alumina or aluminium nitride substrates increases the surface tension. In contrast, Moronoshi et al. [53] emphasized that carbon does not have a direct influence on the surface tension of Fe-C-O melts, but reduces the activity of oxygen in the metal, which in turn contributes to a higher surface tension.

The surface tension of Fe-Mn alloys slightly decreases when the temperature rises from 1800 to 1860 K, decreasing by ≈2 % in this temperature range, i.e. when temperature is increased by 1 K, the surface tension drops by 0.67 mN/m [49]. For a temperature range from 1660 to 2140 K, the surface tension of Fe-C-O melts decreases by ≈11 %, corresponding to a decrease of 0.45 mN/m when temperature increases by 1 K [53]. Keene [54] analyzed a wide range of studies on surface tension of Fe, where it was summarized that the surface tension of pure Fe and its alloys tend to decrease as temperature increases with the temperature coefficient varying from -0.20 to -1.00 mN/(m·K).

## 5.2 Surface tension of slag

Similarly to metals, the surface tension of slag depends on its composition and temperature, therefore any changes in these values will affect the surface tension as well. Depending on the composition, multicomponent slags typically have surface tension in the range from 0.30 to 0.70 N/m [22, 55–62].

Xin et al. [56] modelled the surface tension of $CaO-MgO-SiO_2-Al_2O_3$ slags based on a statistical modelling and found that the surface tension decreases with higher content of $SiO_2$ in slag, while MgO increases the slag surface tension. Hanao et al. [57] and Zhang et al. [55] indicated that the surface tension is considerably dependent upon the slag composition and showed that the surface tension increases with the slag basicity ($CaO/SiO_2$ ratio) and $Al_2O_3$ content. Nakamoto et al. [58] demonstrated that the surface tension of $MnO-SiO_2-Al_2O_3$ and $MnO-CaO-SiO_2$ slags also increases with increasing the content of MnO. In addition, previous studies concluded that the temperature linearly decreases the surface tension of multicomponent slags [22, 55, 56, 59, 60, 62].

## 5.3 Interfacial tension between metal and slag

Gaye et al. [63] studied the interfacial interaction in Fe-Si-C-O/slag systems by applying X-ray measurements and the sessile drop method with a slag droplet resting on a liquid metal. It was found that a higher $SiO_2$ content in slag results in a higher contact angle between metal and slag, and therefore in lower values of interfacial tension, while the change in the $CaO/Al_2O_3$ ratio had almost no effect on the interfacial tension. It was also shown that increasing the activity of sulfur in a metal-slag system sharply decreases the interfacial tension.

The apparent interfacial tension between steel and slag can be affected by the slag basicity ($CaO/SiO_2$) as it was reported by Hagemann et al. [23]. As the slag basicity increases, the apparent interfacial tension increases as well, reducing the possibility of droplet entrainment [19, 64].

The addition of $Al_2O_3$ slightly decreases the apparent interfacial tension, which may be associated with reactions at the metal-slag interface [23]. On the contrary, Park et al. [19] and Sun et al. [64] reported that the interfacial tension is decreased by $Al_2O_3$ only after reaching a significant content in slag (10-20 wt. %) at constant slag basicity.

Sun et al. [64] specified that interfacial tension is nearly constant for the MgO content in slag less than 18 wt. %, while the interfacial tension sharply drops with further addition of MgO due to the precipitation of solid $CaMgSiO_4$ particles at the interface [19].

In general, the MnO addition to slags decreases the interfacial tension [20, 61], however, for $CaO-SiO_2-Al_2O_3$ slags the drop in the interfacial tension has a minimum value, which is achieved at 20 mol. % of the MnO addition.

Tanaka et al. [65] showed that the interfacial tension between liquid Fe alloy and slag drastically decreases during chemical reactions and then it gradually increases reaching a steady value at equilibrium between metal and slag. It was pointed out that the amount of oxygen absorbed at the interface is the main reason for the interfacial tension change. Thus, an increase in the adsorbed oxygen at the interface leads to a decrease in the interfacial tension between the metal and the slag.

# Part III

# Methodology

# Chapter 6

# Material preparation and experimental setup

In all experiments, synthetic ferroalloys and slags have been prepared from pure powders for studying surface and interfacial tension in the sessile drop furnace as indicated in Figure 6.1. Compositions of the ferroalloys and the slags [3, 33, 66, 67] have been selected based on the composition of industrial materials [68]. In addition, the synthetic slags have been selected to cover the most relevant slags for ferroalloys production.

The pure powders for material preparation were mixed and melted separately in graphite crucibles in an induction furnace in Ar atmosphere at 1773-1883 K and holding time of 60 min for the ferroalloys and 5 min for master slags. The holding time was chosen to ensure carbon saturation in ferroalloys and prevent reduction of oxides in slag by carbon, while ensuring mixing of all oxides in slag. After the first melting, the ferroalloys and the master slags were cooled down in the crucibles and then ground in a ball mill. The ground master slags were divided into batches of 20 g and additional amounts of oxide powders has been added based on the composition of the final slag. In experiments with sulfur, FeS was added to 50 g batches of the ferroalloys, depending on the required sulfur content. Both the ferroalloys and the master slags were then remelted in the in-

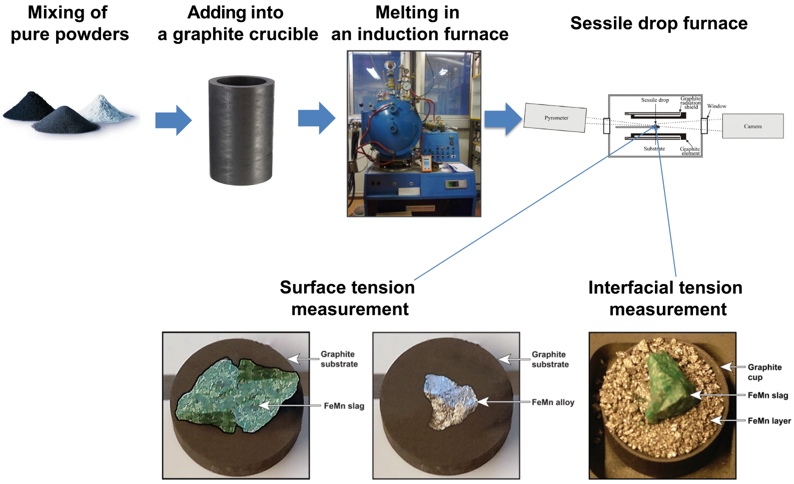

**Figure 6.1:** Procedure for material preparation and investigation of surface and interfacial tension in the sessile drop furnace.

duction furnace using the same operational parameters to ensure better mixing. Carbon was not added as a raw material for the preparation of the ferroalloys, since it is contained in the graphite crucible, which allows ferroalloys to be saturated with the required amount of carbon up to the saturation point. It should be noted that pure powders do not react significantly using the proposed operational parameters for materials preparation, which allows to produce ferroalloys and slags that are close to the calculated composition with high precision. Since this is a general description of the methodology, more details on the composition of prepared ferroalloys and slags as well as experimental matrix in each study are given in the following sections and the published papers [3, 33, 66, 67].

The sessile drop furnace, as sketched in Figure 6.2, was used for investigating the interfacial interaction between ferroalloys and slags. The sessile drop furnace was equipped with a pyrometer and a C-type thermocouple for measuring temperature, and with a digital video camera (Allied Vision Prosilica GT2000, Edmund Optics Inc., Barrington, USA) with a telecentric lens (Navitar 1-50993D)

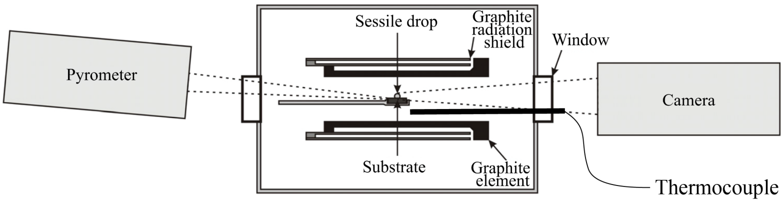

**Figure 6.2:** Schematic overview of the sessile drop furnace. Modified and reprinted from Bao et al. [69] under the terms of the Creative Commons CC BY license.

for recording images of molten samples with the resolution of 2048x1088 pixels at one frame per second after reaching melting temperature of the ferroalloys and the slags. Every 10-15 experiments, the thermocouple was calibrated by melting pure Fe in Ar and assessing its melting temperature from recorded images. The experiments were performed using graphite substrates or cups (ISO-88) in Ar atmosphere (6N grade) at temperatures above the melting point and variable holding time, depending on the experiment. In order to avoid erroneous results due to dust or other solid particles on the surface of the graphite substrates and cups, they were cleaned with a paper towel dipped in ethanol or acetone and then dried using compressed air. The experimental parameters used in the experiments are presented in Table 6.1.

Two main experimental methods (Figure 6.3), were employed for studying interfacial interaction between the ferroalloys and the slags:

- Method A (Figure 6.4(a)), allowing to measure apparent contact angles between metal and slag. This method was used for studying interfacial behaviour in SiMn-slag systems as it was found that SiMn has a poor wetting towards graphite, forming a SiMn droplet instead of a molten layer in the graphite cup.
- Method B (Figure 6.4(b)), allowing to determine both interfacial tension

**Table 6.1:** Experimental conditions in the sessile drop furnace.

| Parameter | Value in measurement of | |
|---|---|---|
| | Surface tension | Interfacial tension and contact angle |
| Weight of FeMn slag, g | 0.120 | 0.050 - 0.060 |
| Weight of FeMn alloy, g | 0.115 | 0.300 - 0.350 or<br>0.740 - 0.850* |
| Weight of SiMn slag, g | 0.110 | ≈0.110 |
| Weight of SiMn alloy, g | 0.115 | 0.053 - 0.061 |
| Ar flow, NLPM | 0.1 | 0.1 |
| Pressure inside the chamber, Pa | 101325 | 101325 |
| Holding temperature for FeMn-slag, K | 1723 | 1623, 1673, 1723 |
| Holding temperature for SiMn-slag, K | 1923 | 1823, 1873, 1923 |
| Holding time, min | 5 | 5, 10, 15 |
| Heating rate to 1473 K, K/min | 300 | 300 |
| Heating rate from 1473 K to maximum temperature, K/min | ≈25 | ≈25 |

[*] The amount of metal depends upon the volume of the graphite cup used in the experiments.

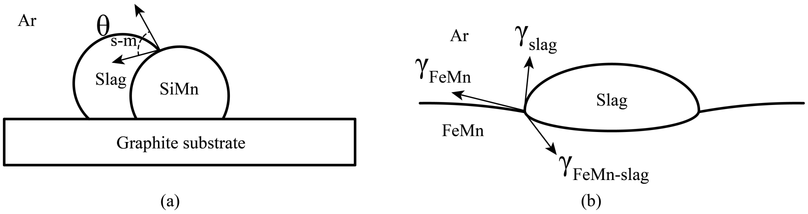

**Figure 6.3:** Schematic demonstrating slag and ferroalloys at fully molten state in experiments. Image (a) shows slag and SiMn droplets in Ar atmosphere. $\theta_{s-m}$ is the contact angle between slag and SiMn. Image (b) shows the slag droplet floating on top of molten FeMn in Ar atmosphere. $\gamma_{FeMn}$ is surface tension of FeMn, $\gamma_{slag}$ is surface tension of slag, $\gamma_{FeMn-slag}$ is interfacial tension between FeMn and slag. Reprinted from Bublik et al. [67] under the terms of the Creative Commons CC BY license.

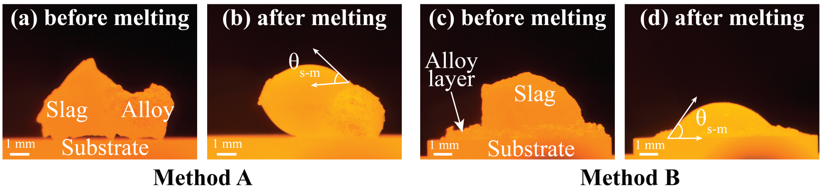

**Figure 6.4:** Methods used for investigation of interfacial properties. In method A, ferroalloy and slag were placed on a graphite substrate. In method B, slag was placed on top of a ferroalloy layer in contact with a graphite cup. The interaction between slag and ferroalloy before melting for method A and B, respectively, is shown in images (a) and (c), while the interaction at the molten state is shown in images (b) and (d). Note that the roughness on the surface of the droplets is related to the formation of solid carbon particles during the melting. Reprinted from Bublik et al. [67] under the terms of the Creative Commons CC BY license.

and apparent contact angle between metal and slag.

After the experiments, the ferroalloys and the slags were cast in epoxy, sectioned in the centre of the slag droplet, re-cast into epoxy, polished and coated with carbon prior to analysis in EOL JXA-8500F EPMA at the Department of Materials Science and Engineering at NTNU. The composition of ferroalloy and slag phases were measured in several points and then average composition of each phase was calculated. In experiments with sulfur, elemental mapping was performed for several samples in order to show sulfur distribution between metal and slag. Additionally, the chemical composition of the ferroalloys and the slags prior to experiments was determined by XRF and the combustion infrared detection technique at SINTEF Norlab AS. The ferroalloys were analyzed for Mn, Fe, Si, S and C, whereas slags were analyzed for MnO, CaO, MgO, $SiO_2$, $Al_2O_3$, FeO and S.

In order to determine the surface tension of the ferroalloys and the slags, the sessile drop technique was applied, where small pieces of the ferroalloys and the slags were melted on a graphite substrate in Ar atmosphere. Surface tension for FeMn and FeMn slag was measured at 1723 K and at 1923 K for SiMn and SiMn slag.

# Chapter 7

# Methodology for determination of surface and interfacial tension

The methodology for determination of interfacial tension between metal and slag is based on calculation or experimental determination of surface tension, followed by a comparison of geometrical features obtained from multiphase CFD simulations using OpenFOAM and experiments in the sessile drop furnace.

## 7.1 Calculation of slag density

The density of molten slag can be calculated from partial molar volumes of each component in the slag [70]:

$$V_{T,liq} = \frac{M}{\rho_{T,liq}} \Rightarrow \rho_{T,liq} = \frac{M}{V_{T,liq}}, \tag{7.1}$$

$$V_{T,liq} = V_{1773} + 0.01(T_{liq} - 1773), \tag{7.2}$$

$$V_{1773} = \sum_{i=1}^{N} x_i V_{1773,i}. \tag{7.3}$$

The partial molar volumes at 1773 K are taken from Table 7.1, which shows the partial molar volumes of each slag component found experimentally [70].

**Table 7.1:** Partial molar volumes used for the calculation of the liquid slag density.

| | $SiO_2$ | CaO | $Al_2O_3$ | MgO | $Na_2O$ | $K_2O$ | $Li_2O$ | FeO | MnO | $CaF_2$ | $TiO_2$ | $B_2O_3$ |
|---|---|---|---|---|---|---|---|---|---|---|---|---|
| $V_{1773}$ | $V_{SiO_2}$ | 20.7 | $V_{Al_2O_3}$ | 16.1 | 33 | 51.8 | 16 | 15.8 | 15.6 | 31.3 | 24 | 10 |

The effect of the $SiO_2$ and $Al_2O_3$ on the structure and molar volume can be represented by two equations derived from an analysis of density measurements [62]:

$$V_{SiO_2} = 19.55 + 7.97X_{SiO_2}, \tag{7.4}$$

$$V_{Al_2O_3} = 28.3 + 32X_{Al_2O_3} - 31.45X^2_{Al_2O_3}. \tag{7.5}$$

## 7.2 Calculation of slag surface tension

To reduce the number of experiments required for determining the slag surface tension and further validation of experimental results, the surface tension of liquid slag is calculated based on the numerical models by Mills et al. [70, 71]. The calculation accounts for the individual contribution of surfactants and bulk components to the surface tension, as well as the temperature dependence of the surface tension:

$$\gamma_{T,liq} = \gamma_{1773} + \frac{d\gamma}{dT}(T_{liq} - 1773), \tag{7.6}$$

$$\gamma_{1773} = \gamma_{bulk,1773} + \gamma_{surf,1773} = \left(\sum_{i=1}^{N} x_i\gamma_i\right)_{bulk} + \left(\sum_{i=1}^{N} x_i\gamma_i\right)_{surf}, \tag{7.7}$$

$$\frac{d\gamma}{dT} = \sum_{i=1}^{N} x_i \frac{d\gamma_i}{dT}, \tag{7.8}$$

where the surfactants are $Na_2O$, $K_2O$, $CaF_2$ and $B_2O_3$.

The surface tension and temperature coefficient of slag components [70] used in the calculation are shown in Table 7.2.

The surface tension change due to the surfactants is expressed as [72]:

- $Na_2O$ or $K_2O$:

$$x_i\gamma_i = 0.8 - 1388x_i + 6723x_i^2. \tag{7.9}$$

- $CaF_2$:

$$x_i\gamma_i = -2 - 934x_i + 4769x_i^2. \tag{7.10}$$

- $B_2O_3$:

$$x_i\gamma_i = -5.2 - 3454x_i + 22178x_i^2. \tag{7.11}$$

Note that these equations are valid for surfactants content up to 0.12 ($\sum x_{surf} = 0.12$). Any excess surfactant is treated as a bulk component.

**Table 7.2:** Values of surface tension and temperature coefficient of slag components.

| | $SiO_2$ | CaO | $Al_2O_3$ | MgO | $Na_2O$ | $K_2O$ | $Li_2O$ | FeO | MnO | $CaF_2$ | $TiO_2$ | $B_2O_3$ |
|---|---|---|---|---|---|---|---|---|---|---|---|---|
| $\gamma_{1773}$ | 260 | 625 | 655 | 635 | 297 | 160 | 300 | 645 | 530 | 290 | 350 | 110 |
| $d\gamma/dT$ | 0.031 | −0.094 | −0.177 | −0.130 | −0.110 | −0.110 | −0.110 | −0.100 | −0.100 | −0.070 | −0.150 | - |

## 7.3 Experimental determination of surface tension of ferroalloys and slags

The surface tension of the slags can be found by the elliptic solution of the Young-Laplace equation [73], implemented in MATLAB [74]. The surface tension (in N/m) is determined from the expression:

$$\gamma = \frac{a^2(\rho_{slag} - \rho_{Ar})g}{\frac{a^3}{b^3} + \frac{a}{b} - 2}, \tag{7.12}$$

where the values of the semi-major axis $a$ and the semi-minor axis $b$ are obtained from image analysis of slag droplets in experiments, after fitting an ellipse to the slag curvature (Fig. 7.1). The elliptic solution fails if contact angle between the droplet and the substrate is lower than 90°, giving wrong values of the surface tension. In addition, there is a significant uncertainty in values found by this method

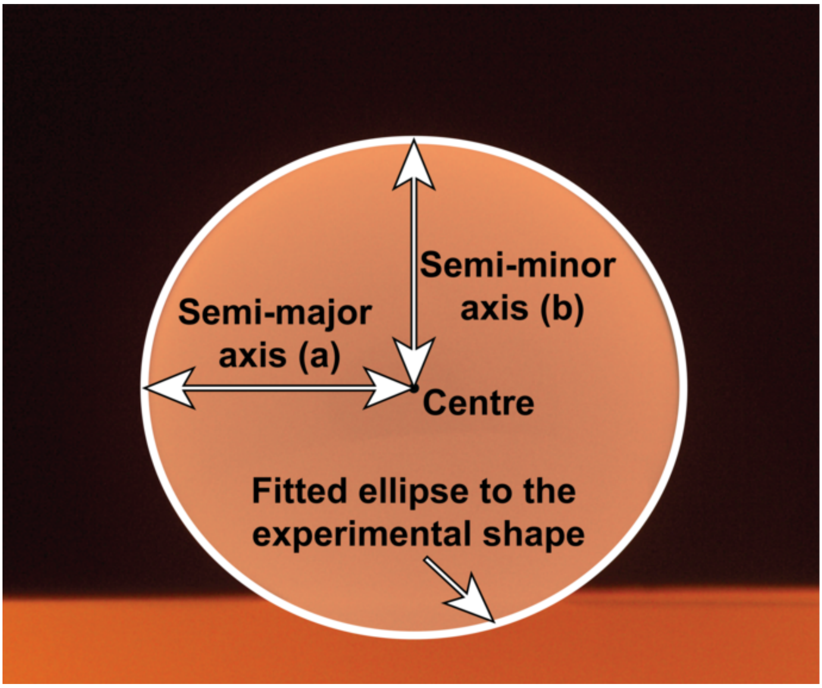

**Figure 7.1:** Ellipsoidal fitting to the slag droplet during experiments in the sessile drop furnace. Reprinted from Bublik and Einarsrud [3].

if the droplet is rough due to the presence of solid particles on the surface during experiments.

The contact angle between the ferroalloys and the graphite substrate is lower than 90°. For this reason, the surface tension of the ferroalloys is measured by a plugin for ImageJ [75], which is based on the low-bond axisymmetric drop shape analysis (LBADSA) [76]. The plugin extracts parameters of droplet's contour after the fitting of the Young-Laplace equation to the image data (Fig. 7.2), providing the capillary constant as the output. The capillary constant is related to the surface tension of metal through the equation:

$$c = \frac{(\rho_{metal} - \rho_{Ar})g}{\gamma}. \tag{7.13}$$

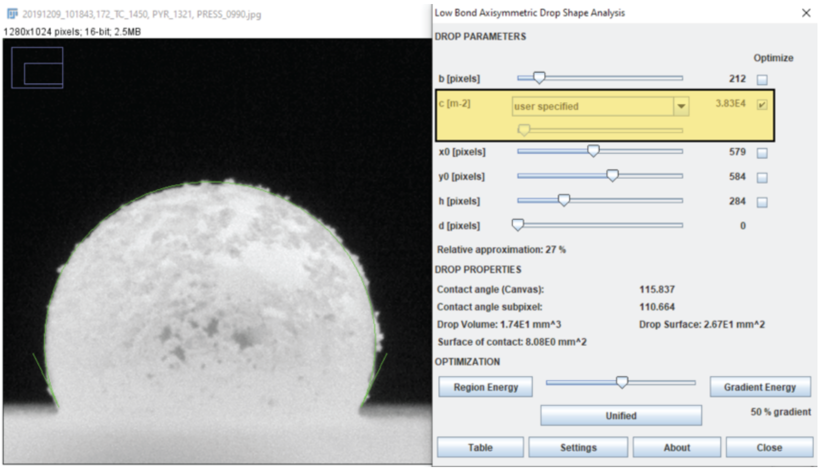

b [pixels] 212 ☐
c [m-2] user specified 3.83E4 ☑
x0 [pixels] 579 ☐
y0 [pixels] 584 ☐
h [pixels] 284 ☐
d [pixels] 0
Relative approximation: 27 %
DROP PROPERTIES
Contact angle (Canvas): 115.837
Contact angle subpixel: 110.664
Drop Volume: 1.74E1 mm^3
Drop Surface: 2.67E1 mm^2
Surface of contact: 8.08E0 mm^2
50 % gradient

**Figure 7.2:** Fitting and measurement of parameters of a ferroalloy droplet from images by LBADSA plugin in ImageJ. Reprinted from Bublik and Einarsrud [3].

where $c$ is the capillary constant in $m^{-2}$ (found from the plugin as an output based on the curve-fitting), $\rho_{metal}$ is the density of ferroalloys in liquid state - 5612 $kg/m^3$ for FeMn and 4449 $kg/m^3$ for SiMn [77].

After the capillary constant has been determined, the surface tension can be calculated from the equation:

$$\gamma = \frac{(\rho_{metal} - \rho_{Ar})g}{c}. \tag{7.14}$$

## 7.4 Determination of interfacial tension between metal and slag

The methodology for the determination of the interfacial tension involves multiple steps, where the fundamental idea is to compare geometric parameters of slag droplets observed during experiments with those obtained from parametric multiphase CFD simulations. A schematic illustrating the multiple steps for the determination of the interfacial tension is demonstrated in Figure 7.3.

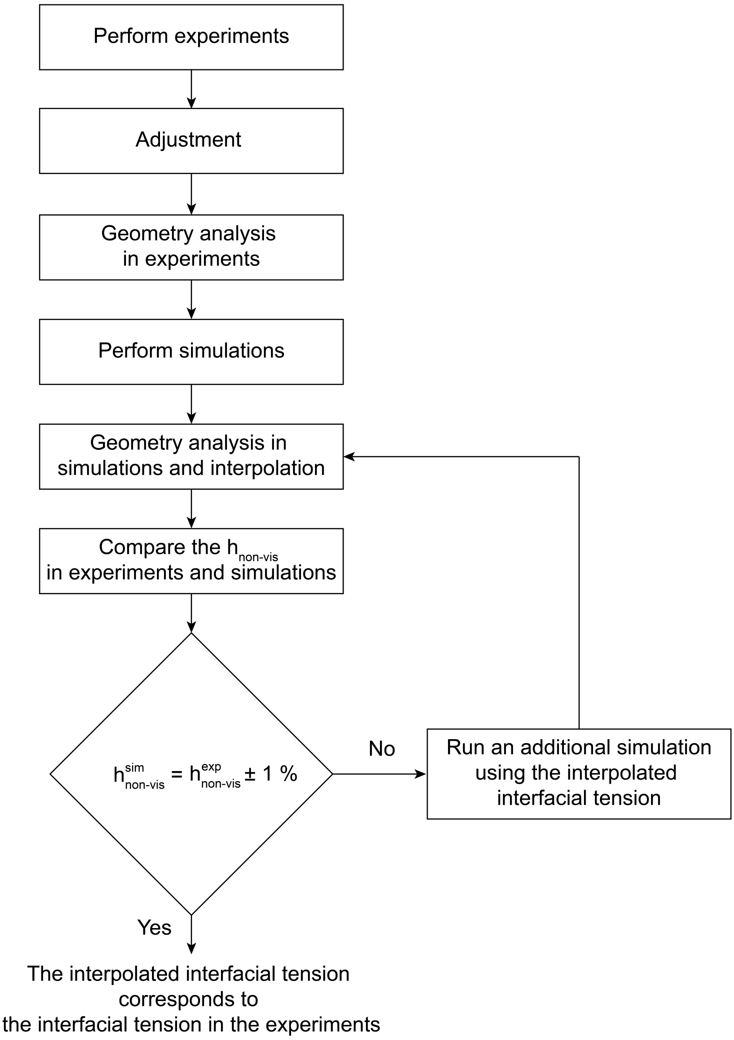

**Figure 7.3:** Main steps for the determination of the interfacial tension in the experiments based on the geometrical parameters of the slag droplet.

***Experimental step***

At this step, a series of three experiments are carried out with a slag droplet placed on top of a metal layer in a graphite cup, where images characterizing the interfacial interaction between slag and metal in the molten state are obtained. The methodology for this step is described previously in Chapter 6.

***Adjustment step***

During the experiments, the composition of the slag and metal changes, and thus the initial composition of the liquid slag phase must be adjusted to take into account the equilibrium between the metal and slag phases. The amount of liquid slag phase is calculated using the equilibrium module in FactSage 8.0 [78]. The obtained values are subsequently utilized for estimating surface tension and density of the slag droplet at the equilibrium using numerical models developed by Mills et al. [70, 71] as described in Section 7.1 and 7.2. The adjustment step consists of the following substeps:

a) Calculate composition of the liquid slag phase after interaction with the metal in the equilibrium module of FactSage using FactPS, FToxid and FT-misc databases.
b) Calculate the surface tension and the density of the slag droplet and its liquid slag phase using the numerical models developed by Mills et al. [70, 71]
c) Calculate the average surface tension and the average density, which can be found as the average values between the slag droplet and its liquid slag phase.

***Geometry analysis***

The geometrical parameters have to be assessed at the minimum volume expansion of the slag droplet, i.e. when the metal and the slag have reached equilibrium. This allows to reduce the influence of volume fluctuations due to chemical reactions and gas formation on experimental results. An example of the fluctuating volume of the slag droplet, which is expressed in terms of the visible height,

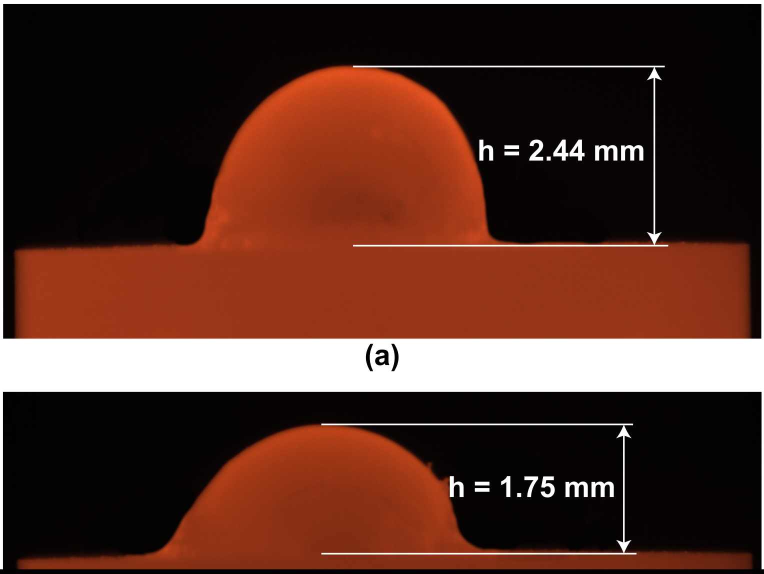

**Figure 7.4:** Visible height of the slag droplet: (a) in the beginning of the holding period (t = 0 min) at 1673 K, (b) in the end of the holding period (t = 5 min) at 1673 K.

is shown in Figure 7.4. Two other important sources of error in the experiments are the amount of metal layer in the graphite cup, and the surface roughness due to the formation of solid carbon, thus these two parameters must also be taken into account for more accurate results. The following substeps are conducted at this step:

a) Measure a surface roughness correction coefficient for each experiment ($k_R$) directly from the experimental images as the average size of solid particles found at the metal-gas and slag-gas interface. In all experiments, $k_R$ was up to 0.7 mm, depending on the surface roughness, which corresponds to 25

% of the typical droplet size.

b) Calculate total volume of the slag droplet, $V_{total}$, using slag density in the molten state and weight of the slag droplet measured before the experiments:

$$V_{total} = \frac{m_{slag}}{\rho_{slag}}. \tag{7.15}$$

c) Calculate visible volume of the slag droplet in the experiments, $V_{vis}^{exp}$. As discussed earlier by Calvo et al. [79], a drop of oil released onto water forms a perfect spherical cap both above and below the interface after reaching a steady state. Ferreira et al. [80] concluded a similar geometric relationship for the metal-slag system, where the total volume of a slag droplet resting on metal is the sum of the upper (in the gas) and lower (in the metal) parts of the droplet. Therefore, it has been assumed in all experiments that the slag droplet forms the spherical cap both above and below the metal-gas interface. In addition, $k_R$ is subtracted from visible height and radius of the slag droplet to address the effect of the surface roughness:

$$V_{vis}^{exp} = \frac{1}{6}\pi(h_{vis}^{exp} - k_R)(3(a^{exp} - k_R)^2 + (h_{vis}^{exp} - k_R)^2), \tag{7.16}$$

where $h_{vis}^{exp}$ is the visible height of the slag droplet and $a^{exp}$ is the measured radius of the slag droplet.

d) Calculate non-visible volume of the slag droplet in the experiments, $V_{non-vis}^{exp}$:

$$V_{non-vis}^{exp} = V_{total}^{exp} - V_{vis}^{exp}. \tag{7.17}$$

e) Calculate non-visible height of the slag droplet in the experiments, $h_{non-vis}^{exp}$, by expressing it from the equation:

$$V_{non-vis}^{exp} = \frac{1}{6}\pi h_{non-vis}^{exp}(3(a^{exp} - k_R)^2 + (h_{non-vis}^{exp})^2). \tag{7.18}$$

f) The metal layer does not completely fill the graphite cup, therefore, distance

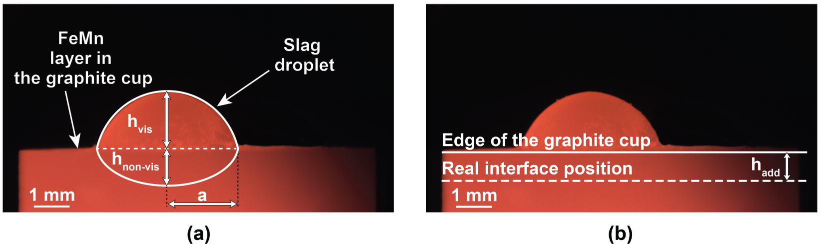

**Figure 7.5:** Geometrical parameters of the slag droplet (a) and the real position of the interface (b) used in the calculations. Reprinted from Bublik et al. [33] under the terms of the Creative Commons CC BY license.

from the metal-gas interface to the edge of the graphite cup has to be taken into account as well. It can be calculated using volume of the cup, density of the metal in the molten state and weight of the metal layer:

$$V_{cup} = \pi r_{cup}^2 h_{cup}, \tag{7.19}$$

$$V_{metal} = \frac{m_{metal}}{\rho_{metal}}, \tag{7.20}$$

$$h_{add} = \frac{V_{cup} - V_{metal}}{\pi r_{cup}^2}, \tag{7.21}$$

where $V_{cup}$ is the volume of the cup, $r_{cup}$ is the inner radius of the cup (4 mm), $h_{cup}$ is the inner height of the cup (3 mm), $V_{metal}$ is the volume of the metal layer, $m_{metal}$ is the weight of the metal layer, $\rho_{metal}$ is the density of the metal in the molten state, $h_{add}$ is the distance from the metal-gas interface to the edge of the graphite cup, correcting for the cup not being 100 % filled.

A visual explanation of these geometrical parameters is shown in Figure 7.5.

g) Considering $h_{add}$, calculate the non-visible height of the slag droplet in the experiments (in %):

$$h_{non-vis}^{exp}(\%) = \frac{h_{non-vis}^{exp} - h_{add}}{h_{non-vis}^{exp} + h_{vis}^{exp}} \cdot 100. \tag{7.22}$$

h) Calculate the average non-visible height for each experiment:

$$\overline{h}_{non-vis}^{exp}(\%) = \frac{\sum h_{non-vis}^{exp}(\%)}{n}, \tag{7.23}$$

where $n$ is the number of observations, considering the minimum volume expansion of the slag droplet.

### *Modelling step*

At the modelling step, simulations are performed using the physical properties and parameters from the experiments: the surface tension and the density of the metal in the molten state; the average surface tension and the average density of slag in the molten state; the weight of the slag droplet and the metal layer. As shown in Figure 7.6, the interfacial interaction between the ferroalloy and the slag droplet is simulated without walls of the graphite cup. However, the geometrical features of the slag droplet have to be calculated considering that a part of the slag droplet cannot be seen due to the walls. The non-visible height in the simulation is then compared to the non-visible height in the experiment, and if they differ by more than 1 %, a new simulation is started with a new value for the interfacial tension. Here, the following substeps are performed:

a) Perform three parallel simulations using the interfacial tension between the FeMn alloy and the slag droplet of 0.30, 1.15 and 2.00 N/m.
b) Knowing the apex position of the slag droplet on Y-axis ($Y_{slag\ apex}$) and the edge position of the graphite cup on Y-axis ($Y_{edge}$), visible height of the slag droplet in simulations can be obtained:

$$h_{vis}^{sim} = Y_{slag\ apex} - Y_{edge}. \tag{7.24}$$

$$h_{vis}^{sim}(\%) = \frac{h_{vis}^{sim}}{h_{droplet}^{sim}} \cdot 100. \tag{7.25}$$

c) Non-visible height is then expressed as:

$$h^{sim}_{non-vis}(\%) = 100 - h^{sim}_{vis}(\%) \tag{7.26}$$

Consequently, the average non-visible height of the slag droplet in a steady state is calculated (in %):

$$\overline{h}^{sim}_{non-vis}(\%) = \frac{\sum h^{sim}_{non-vis}(\%)}{n_t}, \tag{7.27}$$

where $h^{sim}_{non-vis}$ is calculated for each time step and the simulation is stopped when two conditions are met: a) simulation time is equal to twice the time required for reaching the steady state (0.8 s in this study) and b) $\overline{h}^{sim}_{non-vis}(\%)$ is almost constant (±2 %) during the last 0.4 s of the simulation, i.e. after the steady state is reached. $n_t$ is the number of time steps in the steady state corresponding to the last 0.4 s of the simulation.

d) Linearly interpolate $\overline{h}^{sim}_{non-vis}(\%)$ from the current set of simulations as a function of the interfacial tension and determine the corresponding value of the interfacial tension to $\overline{h}^{exp}_{non-vis}$.

e) Perform a simulation using the interpolated interfacial tension and calculate $\overline{h}^{sim}_{non-vis}(\%)$ as described in step c).

f) Repeat steps from c) to e) until $\overline{h}^{sim}_{non-vis}(\%)$ is ±1 % from the experimental value ($\overline{h}^{exp}_{non-vis}$).

The 80 % and 95 % confidence intervals were calculated for each set of three experiments based on the Student's t-distribution [81]:

$$CI = \overline{y} \pm t\frac{s}{\sqrt{n}}, \tag{7.28}$$

where $\overline{y}$ is the sample mean, $t$ is the critical value found from the confidence level and degrees of freedom of the sample (1.886 and 4.303 for a two-tailed test with a statistical significance of 0.2 and 0.05, respectively, and two degrees of freedom), $s$ is the sample standard deviation and $n$ is the number of experiments in a set.

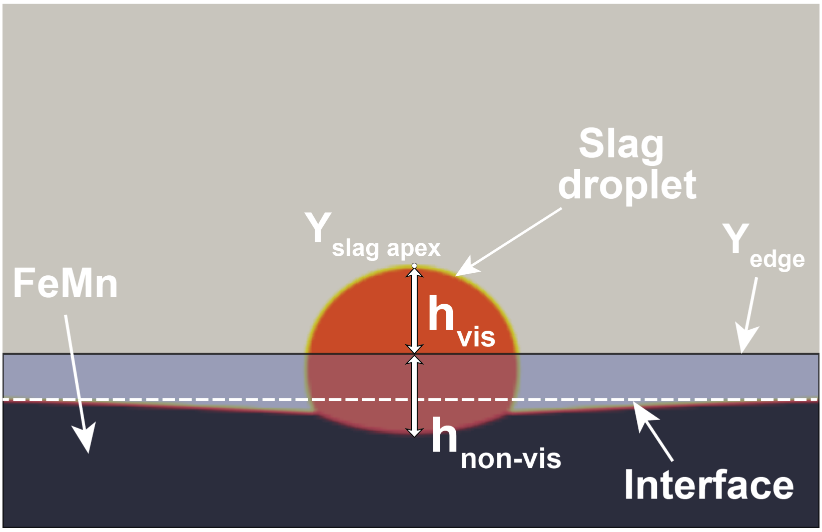

**Figure 7.6:** The slag droplet at the metal-gas (FeMn-Ar) interface in the steady state in the simulations. The semi-transparent blue filled area represents the walls of the graphite cup with $r_{cup}$ of 4 mm and $h_{cup}$ of 3 mm. Reprinted from Bublik et al. [33] under the terms of the Creative Commons CC BY license.

Here, $s$ is expressed as:

$$s = \sqrt{\frac{\sum_{i=1}^{n}(y_i - \overline{y})^2}{n-1}}, \tag{7.29}$$

where $y_i$ $\{y_1, y_2, ..., y_n\}$ represents one measured value of the sample (i.e. interfacial tension in a single experiment).

# Chapter 8

# Multiphase solver in OpenFOAM

Simulations of the interfacial interaction between metal and slag were carried out in OpenFOAM 6-8 [82] using the *multiphaseInterFoam* solver for *N* incompressible fluids, which captures interfaces and includes surface tension and contact angle effects for each phase, with optional mesh motion and topology changes.

OpenFOAM (Open Source Field Operation and Manipulation) is a free, open source CFD software under GNU General Public License. OpenFOAM was initially developed in the C++ programming language for solving problems in continuum mechanics, i.e. stresses, deformation and flow of solids, liquids and gases [83]. It has an extensive range of features to solve many problems from complex fluid flows involving chemical reactions, turbulence and heat transfer, to solid dynamics and electromagnetics. OpenFOAM, as an extensive tool for CFD modelling, includes many different solvers which can be used for solving physical problems, such as turbulence, heat and mass transfer, multiphase flows and wave modelling. In addition, it includes applications for mesh manipulation, setting boundary conditions, parallel processing, data extraction and post-processing [84]. By default, OpenFOAM uses ParaView [85] for post-processing and visualization of simulation results.

OpenFOAM is based on the finite volume method (FVM), which is a numerical method for the approximate solution of partial differential equations [86]. FVM can be applied for solving problems in 1D, 2D or 3D and for different systems of equations and can use both structured and unstructured meshes.

The *multiphaseInterFoam* solver employs the conventional volume of fluid (VOF) method demonstrated by Hirt and Nichols [87], where the transport equation is applied to determine the volume fraction $\alpha_n$ of each phase at each discrete position in space [88]. The transport equation is solved simultaneously with the continuity and momentum equation for each phase [89].

In the VOF method, fluid properties such as mixture density ($\rho$) or viscosity ($\mu$) are weight-averaged by the volume fraction of each phase [90]:

$$\rho = \sum_n \rho_n \alpha_n \tag{8.1}$$

and

$$\mu = \sum_n \mu_n \alpha_n. \tag{8.2}$$

As mentioned by Berberovic et al. [91], the conservation of the phase fraction is the most crucial point in the application of the VOF model for the numerical simulation of free surface flows. This becomes especially critical in the case of high density ratios, where even small errors in the volume fraction can lead to significant errors in calculations of physical properties. Therefore, an accurate calculation of the phase fraction is important for correct estimation of the surface curvature, which is then required for the calculation of surface tension force and pressure gradient across the free surface. The interface between two phases is not sharply defined and is therefore highly sensitive to grid resolution.

The continuity equation is defined as:

$$\nabla \cdot \mathbf{U} = 0. \tag{8.3}$$

The transport equation for $\alpha$ is:

$$\frac{\partial \alpha}{\partial t} + \nabla \cdot (\mathbf{U}\alpha) + \nabla \cdot [\mathbf{U}_r \alpha (1-\alpha)] = 0, \tag{8.4}$$

where $\nabla \cdot [\mathbf{U}_r \alpha(1-\alpha)]$ is an additional convective (compression) term for the interface compression which contributes to higher interface resolution. The compression term is valid only for the interface and disappears at a certain limit of the phase fraction, as well as at a sharp interface. Eq. 8.4 in this case reduces to:

$$\frac{\partial \alpha}{\partial t} + \nabla \cdot (\mathbf{U}\alpha) = 0. \tag{8.5}$$

The momentum equation is expressed as:

$$\frac{\partial(\rho \mathbf{U})}{\partial t} + \nabla \cdot (\rho \mathbf{U}\mathbf{U}) = -\nabla p + \mathbf{g} \cdot \mathbf{x} \nabla \rho + \mu \left[ \nabla \mathbf{U} + (\nabla \mathbf{U})^T \right] + \gamma \kappa \nabla \alpha, \tag{8.6}$$

where $\mu \left[ \nabla \mathbf{U} + (\nabla \mathbf{U})^T \right]$ is the viscous term, $\gamma \kappa \nabla \alpha$ is surface tension force per unit volume, which is based on the continuum surface force model [91], $\kappa$ is the mean curvature of the free surface:

$$\kappa = -\nabla \cdot \left( \frac{\nabla \alpha}{| \nabla \alpha |} \right). \tag{8.7}$$

## Chapter 9

# Multiphase simulations in OpenFOAM

### 9.1 Methodology and settings

Simulations were performed using an axisymmetric 2D geometry as shown in Fig. 9.1, allowing the computational domain to be halved, and thereby reducing the time required to reach steady state and obtain simulation results. For the right, top and bottom wall, it is assumed that the fluid flow has zero velocity relative to the wall (no-slip condition), as well as a fixed flux pressure (P = 0 Pa).

The initial number of cells in the simulations was set to 5000. 2D dynamic mesh refinement [92] was applied to increase the resolution at slag-Ar, metal-Ar and metal-slag interfaces, allowing to refine the interfaces and increase the total number of cells up to 18000.

All simulations were performed on resources provided by the NTNU IDUN computing cluster [93] using modified settings for damBreak4phase tutorial case [94] with multiphaseInterFoam solver, as shown in Table 9.1. Simulations were aiming to reach steady state conditions corresponding to a droplet at rest. The presence of so-called spurious currents in VOF simulations results in considerable challenges in obtaining a static steady state and therefore low values of under-

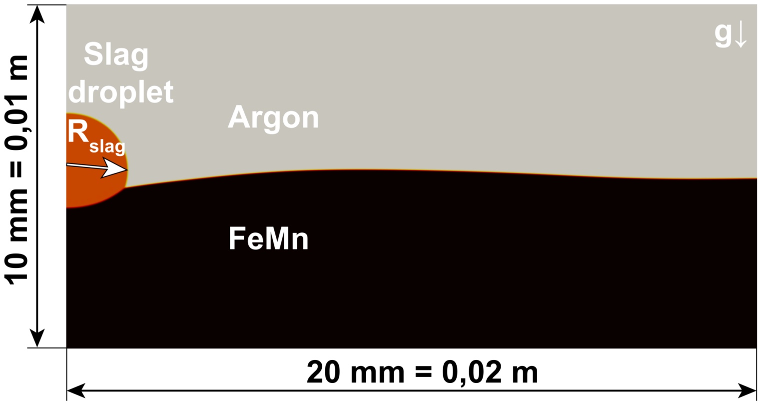

**Figure 9.1:** 2D axisymmetric geometry applied in simulations. $R_{slag}$ varied depending on the weight of a slag droplet, and $g$ is the gravity, acting in y-direction. Reprinted from Bublik and Einarsrud [3].

relaxation factors were applied to reduce spurious currents as it was proposed by Vachaparambil and Einarsrud [95]. As multiphaseInterFoam is a transient solver, transient simulations with dynamic time stepping from $10^{-3}$ to $10^{-6}$ s and the maximum Courant number up to 0.25 were performed. The simulations were initialized with a slag droplet with radius from ≈1.40 to 1.60 mm, depending on the weight of the slag droplet, initially positioned 1.50 mm above the alloy interface. The physical parameters used in the simulations are shown in Table 9.2.

The MPLIC method was applied in simulations as an interpolation scheme for interface capturing. This interpolation scheme represents an interface by performing multiple surface-cuts, splitting each cell to match the volume fraction of the phase in a given cell. The surface-cuts are oriented according to the point field of the local phase fraction. The phase fraction on each cell face (the interpolated value) is then calculated from the amount submerged below the surface-cut. MPLIC methods are more precise than standard interface compression schemes for meshes with refinement patterns; therefore, it is recommended to apply MPLIC together with dynamic mesh refinement, which makes it possible to almost com-

**Table 9.1:** Numerical solution parameters used in the simulation setup.

**Solution and algorithm control settings (fvSolution)**

| Parameter | Field | | | | | |
|---|---|---|---|---|---|---|
| | alpha | pcorr | p_rgh | p_rghFinal | U | UFinal |
| tolerance | $10^{-6}$ | $10^{-8}$ | $10^{-8}$ | $10^{-9}$ | $10^{-6}$ | $10^{-8}$ |
| relTor | 0 | 0 | 0 | 0 | 0 | 0 |
| maxIter | 100 | 100 | - | 50 | - | - |
| nAlphaSubCycles | 2 | - | - | - | - | - |
| nAlphaCorr | 2 | - | - | - | - | - |
| MULESCorr | false | - | - | - | - | - |
| cAlpha | 1 | - | - | - | - | - |
| nLimiterIter | 3 | - | - | - | - | - |
| smoother | GaussSeidel | - | - | - | - | - |
| nSweeps | 1 | - | - | - | - | - |
| solver | smoothSolver | - | - | - | - | - |
| relaxationFactors | - | 0.3 | 0.3 | 0.9 | 0.3 | - |

**PIMPLE loop**

| Parameter | Value |
|---|---|
| nCorrectors, nOuterCorrectors | 1 |
| momentumPredictor | false |

**Numerical schemes settings (fvSchemes)**

| Time derivatives | Value |
|---|---|
| ddtSchemes | CrankNicolson 0.50 |

| Surface interpolation scheme | Value |
|---|---|
| div(phi,alpha) | Gauss MPLIC* |

**Time and data input/output control settings (controlDict)**

| Parameter | Value |
|---|---|
| deltaT | $10^{-5}$ |
| maxDeltaT | $10^{-3}$ |
| maxCo, maxAlphaCo | <0.25 |

[*] Multicut Piecewise-Linear Interface Calculation.

**Table 9.2:** Physical parameters applied in simulations.

| Parameter | Value |
|---|---|
| $\rho_{slag}$, kg/m$^3$ | 3077 - 3395* |
| $\rho_{FeMn}$, kg/m$^3$ | 5612* |
| $\rho_{Ar}$, kg/m$^3$ | 1.66 |
| $\nu_{slag}$, m$^2$/s | varied |
| $\nu_{FeMn}$, m$^2$/s | varied |
| $\nu_{Ar}$, m$^2$/s | varied |
| $\gamma_{slag-Ar}$, N/m | 0.44 - 0.65 |
| $\gamma_{FeMn-Ar}$, N/m | 1.50 |
| $\gamma_{FeMn-slag}$, N/m | 0.30 - 2.00 |

*Density of slag [70] and FeMn alloy [77] in the molten state.

pletely reduce numerical oscillations of the interface [96].

In order to further reduce the effects of spurious currents and to reach the steady state more quickly in the simulations, the viscosity was set to an artificially elevated value, which does not affect the surface and interfacial forces, but reduces the numerical oscillations of the interface that can occur during simulations. Since the steady state is static, the actual value of the viscosity should not impact the final converged result. A parametric study was performed to determine a suitable value for the viscosity, in which the steady state solutions were compared, according to the values indicated below:

- $10^{-6} \leq \nu_{FeMn} \leq 10^{-2}$ m$^2$/s.
- $10^{-5} \leq \nu_{slag} \leq 10^{-3}$ m$^2$/s.
- $10^{-5} \leq \nu_{Ar} \leq 10^{-3}$ m$^2$/s.

In addition, a parametric study of the mesh resolution, geometry size and quality of the dynamic mesh refinement has been carried out to determine the most appropriate parameters to be used in the simulations without affecting the results and changing the convergence time significantly.

## 9.2 Optimization and automation

The multiphase simulations in OpenFOAM have been linked to a Python script for optimization and automation of simulations. The Python script allows automatically running simulations depending on provided input (experimental values), calculating the non-visible height of the slag droplet for each time step, and then comparing calculated values based on a given condition(s). The general logic of the script is presented in Figure 9.2.

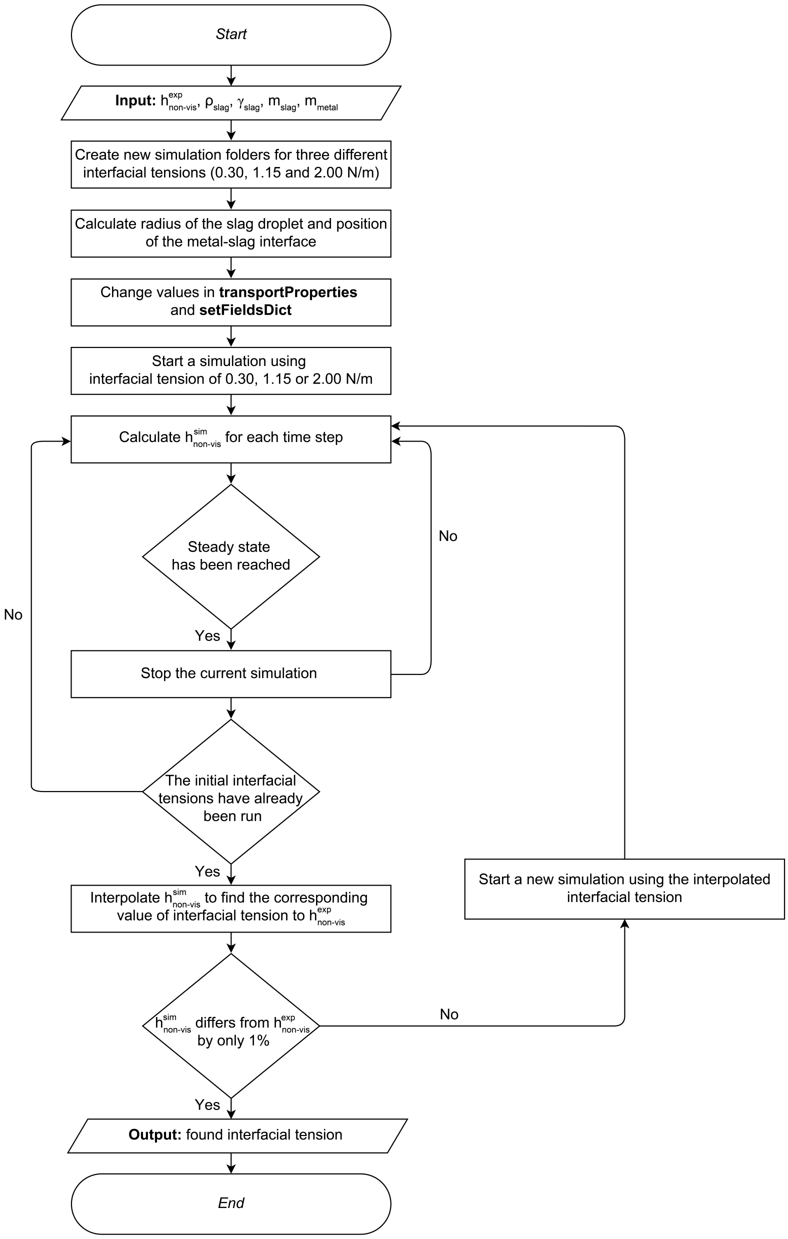

**Figure 9.2:** Schematic showing the general logic for optimizing and automating OpenFOAM simulations.

# Part IV

# Scientific dissemination

# Chapter 10

# Summary of scientific contributions

## Summary of paper I

**Slag-metal Interactions in the FeMn Tapping Process: Interfacial Properties and Wetting**

Sergey Bublik, Sarina Bao, Merete Tangstad, Kristian Etienne Einarsrud, *Proceedings of the Liquid Metal Processing & Casting Conference 2019*, Birmingham, UK, 2019.

***Author contributions***

The first author (Sergey Bublik) planned and performed the experiments, prepared the samples for electron microscopy and examined them by EPMA, evaluated and analyzed the results, wrote the paper and submitted it to LMPC2019, where the study was presented by him.

***Context to the work and objective***

FeMn and other ferroalloys are mostly produced in submerged arc furnaces at high temperatures during carbothermic reduction of oxide raw materials by carbon. In addition to the ferroalloy, a considerable amount of slag is also generated [97], therefore, both metal and slag have to removed from the furnace during tapping into ladles. The molten slag and metal subsequently separate based on their density difference in the first ladle, and the excess slag phase overflows to the following ladles. However, the tapping of molten materials into ladles results in the formation of small metal droplets in slag formed due to turbulence of the tapping flow and interfacial interaction between slag and metal. For this reason, it is important to study mechanisms of molten metal droplets entrainment by slag, which may be explained by interfacial phenomena and characterized by interfacial tension between metal and slag [46, 98–100].

The measurement of the interfacial tension between two molten phases is extremely challenging due to the high temperature and the complexity of phase composition. Specifically, the presence of dissolved surface active elements (oxygen, sulfur) at the interface between slag and metal could considerably modify the interfacial tension [22, 65]. Moreover, available methods for determining the interfacial tension are complex and do not allow studying interfacial phenomena with stable and reproducible results.

The primary objective of Paper I was to develop a methodology for characterizing the interfacial interaction in metal-slag systems. Synthetic high carbon FeMn alloy and $MnO$-$CaO$-$MgO$-$SiO_2$-$Al_2O_3$ slag were used for investigating in a sessile drop furnace at temperatures from 1583 to 1633 K in Ar atmosphere, and two different experimental methods, as shown in Figure 10.1, were presented and discussed:

- Method A - slag and FeMn pieces were placed on a graphite substrate with diameter of 10 mm, and then heated up to a high temperature.
- Method B - a slag piece was placed on top of the FeMn layer in a graphite cup with diameter of 10 mm and internal height of 1 mm.

***Main results***

Dynamic changes in relevant contact angles (slag-graphite, metal-graphite and slag-metal) and shape of droplets during melting in the sessile drop furnace were evaluated for both methods as presented in Figure 10.2 and 10.3.

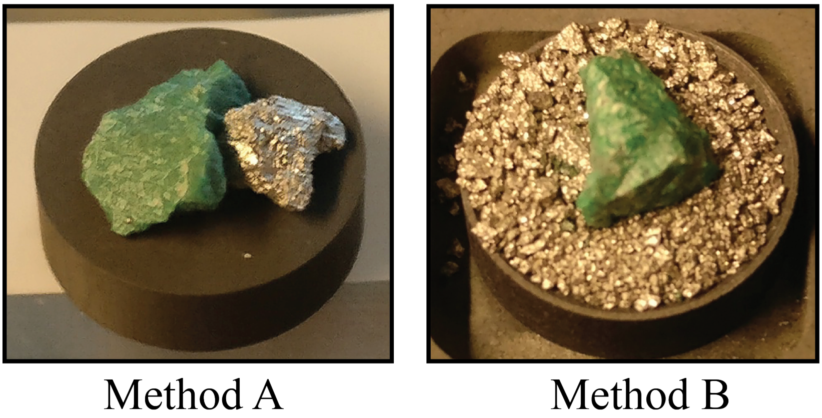

**Figure 10.1:** Raw materials before experiments in method A and B. Reprinted from Bublik et al. [66].

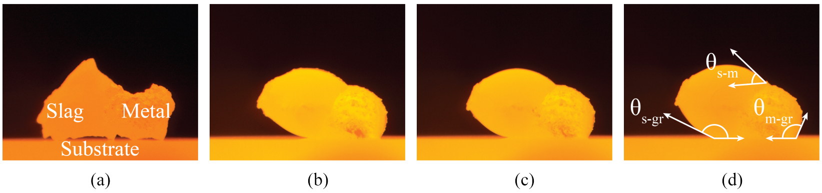

(a) (b) (c) (d)

**Figure 10.2:** Melting of slag (left) and FeMn (right) pieces in method A: (a) samples before melting at 1473 K (b) samples at 1573 K, (c) samples at 1598 K, (d) samples at 1623 K. Relevant contact angles are indicated in frame (d). Reprinted from Bublik et al. [66].

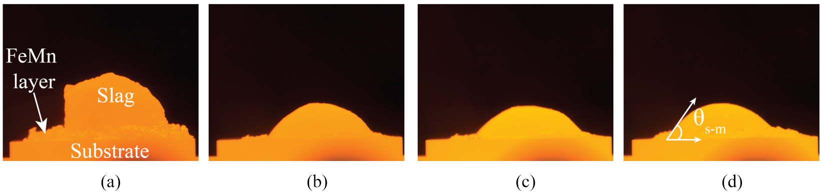

(a) (b) (c) (d)

**Figure 10.3:** Melting of slag (left) and FeMn (right) pieces in method B: (a) samples before melting at 1473 K (b) samples at 1573 K, (c) samples at 1598 K, (d) samples at 1623 K. The relevant contact angle is indicated in frame (d). Reprinted from Bublik et al. [66].

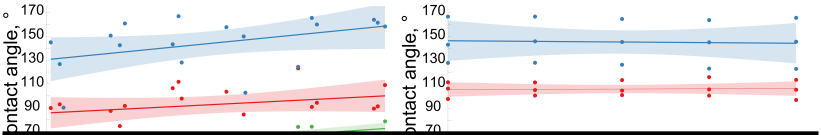

[redacted]

**Figure 10.4:** Measured contact angles in method A: (a) at different S/M ratios at 1583 K, (b) at different temperature at S/M ratio from 0.71 to 0.74. The lines and shaded areas represent linear regression with 95 % confidence interval.

In experiments using method A, it was found that the effect of temperature on the measured apparent contact angles is negligible, while the contact angles vary depending on the slag-to-metal (S/M) ratio in the range from 0.25 to 1.50 (Figure 10.4). Values of the contact angle between metal-graphite and slag-graphite are more randomly distributed, resulting in low adjusted R-squared values (0.05 and 0.13, respectively). In contrast, values of the contact angle between slag-metal have higher adjusted R-squared value (0.60), indicating a larger dependence from the S/M ratio. This might be explained by gravity, which becomes more pronounced when the slag droplet weight increases, while the weight of the FeMn droplet is fixed. Here, the effect of droplets volume or weight on the gravity contribution might be described by the capillary constant:

$$a^2 = \frac{V}{l} = \frac{\sigma}{\Delta \rho g}, \tag{10.1}$$

where $a$ is the capillary constant, $V$ is the volume of liquid phase, $l$ is the length of the capillary perimeter, $\sigma$ is the interfacial or surface tension, $\Delta \rho$ is the density difference between two phases, $g$ is gravitational acceleration.

In experiments using method B, the apparent interfacial tension between metal and slag was determined using the axisymmetric drop shape analysis (ADSA) [76], which is based on the balance between surface, interfacial tension and external forces. S/M ratio in these experiments was limited to 0.18-0.29 to reduce the in-

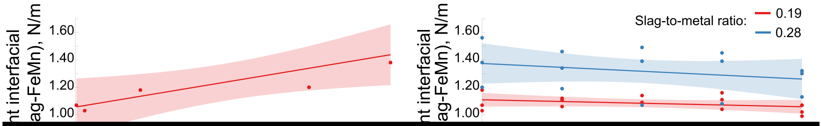

[redacted]

**Figure 10.5:** The apparent interfacial tension between slag and metal in method B: (a) at different S/M ratios at 1583 K, (b) at different temperature at S/M ratio of 0.19 and 0.28. The lines and shaded areas represent linear regression with 95 % confidence interval. Reprinted from Bublik et al. [66].

fluence of the gravity on the experimental results. However, even in this range of S/M ratio, the effect of gravity becomes more noticeable with increasing it up to 0.29, which increases the interfacial tension compared to low values of S/M ratio as shown in Figure 10.5. Therefore, it is necessary to keep the slag droplet weight as low as possible, depending upon the surface roughness and experimental considerations. The temperature seems to affect the interfacial tension very slightly, decreasing the interfacial tension as the temperature rises from 1583 to 1623 K. The apparent contact angle between slag and metal was found to be in the range of 43.3-64.6° for method B, which is in good correspondence with that found with method A.

The interface between slag and FeMn was investigated by EPMA and illustrated in Figure 10.6, where it can be seen that the metal-slag emulsion formed during the experiments and a considerable amount of slag inclusions was found near the metal-slag interface. Since the volume of the entrained molten slag is very small, it is expected that it will remain in the metal phase due to the interfacial forces. The variation in the phases composition is discussed in the attached papers (paper I and V).

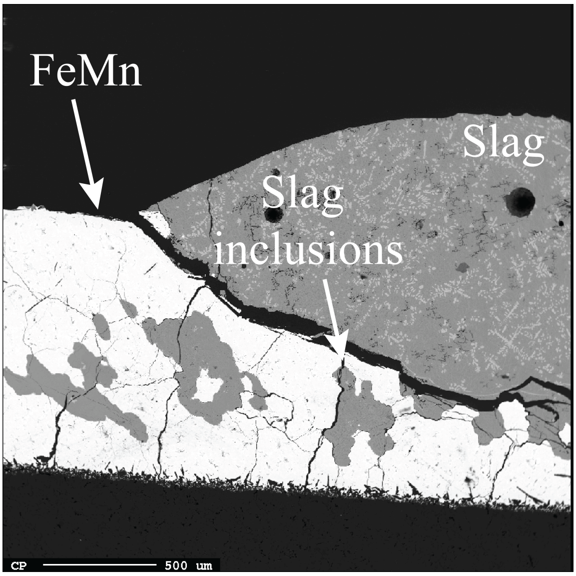

**Figure 10.6:** EPMA image of slag and metal after experiments using method B. Reprinted from Bublik et al. [66].

## Summary of paper II

### Inverse Modelling of Interfacial Tension Between Ferroalloy and Slag Using OpenFOAM

Sergey Bublik, Kristian Etienne Einarsrud, *Proceedings from the 14th International Conference on CFD in Oil & Gas, Metallurgical and Process Industries*, Trondheim, Norway, 2020.

***Author contributions***

The first author (Sergey Bublik) planned and performed the experiments and the simulations, evaluated and analyzed the results, wrote the paper and submitted it to CFD2020, where the study was presented by him.

***Context to the work and objective***

The interfacial tension plays an important role in the interaction between ferroalloy and slag due its ability to modify droplet shape and flow regime [15]. Experimentally, surface tension of a material or interfacial tension between two molten phases are determined by melting materials in a furnace equipped with an X-ray camera [32] or by applying the sessile drop technique with a digital camera [20]. After recording images from interfacial interaction between two different phases and gas, surface or interfacial tension are obtained by the numerical solution of the Young-Laplace equation. However, in most cases, the measurement of interfacial/surface tension is complicated due to high temperatures, complex composition and chemical interaction between materials.

The main objective in Paper II was to develop a methodology allowing to measuring interfacial tension between molten metal and slag in a sessile drop furnace with reproducible results. A new inverse modelling strategy has been developed, combining simulations and analysis of images from the sessile drop furnace. The model applicability and sensibility has been studied for a FeMn-slag system at 1623-1673 K and discussed by comparing different settings in OpenFOAM and the uncertainty in experimental data.

***Overview of the developed methodology***

The inverse modelling methodology consist of the followings steps:

a) Conduct experiments with a single slag or FeMn alloy droplet, and determine the *surface tension* of each phase using the elliptic solution to the Young-Laplace equation and the LBADSA methodology.

b) Conduct experiments in the sessile drop furnace with FeMn layer and a slag piece on top.

c) Conduct simulations in OpenFOAM with the geometry as shown in Figure 10.7 for a certain range of interfacial tension using densities of FeMn alloy and slag in the molten state, weight of the slag droplet and surface tensions determined from step *a)*.

d) Calculate visible (or non-visible) height of the slag droplet (in %), as shown in Figure 10.8 and 10.9, both for experiments and simulations. Compare experimental and simulation values to determine *interfacial tension*.

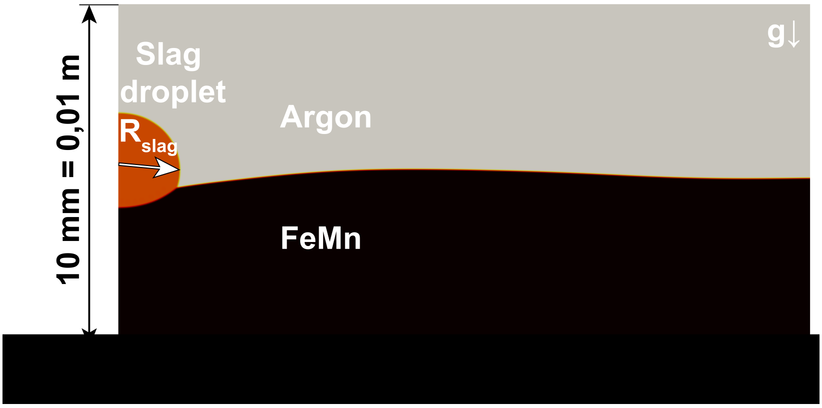

**Figure 10.7:** 2D axisymmetric geometry applied in simulations. $R_{slag}$ varies from 0.00147 to 0.00163 m (from 1.47 to 1.63 mm), depending on the weight of a slag droplet, and $g$ is the gravity, acting in y-direction. Reprinted from Bublik and Einarsrud [3].

### *Main results*

The experimentally measured values surface tension of FeMn alloy and slag are shown in Figure 10.10. Surface tension of FeMn alloy was found to be 1.50

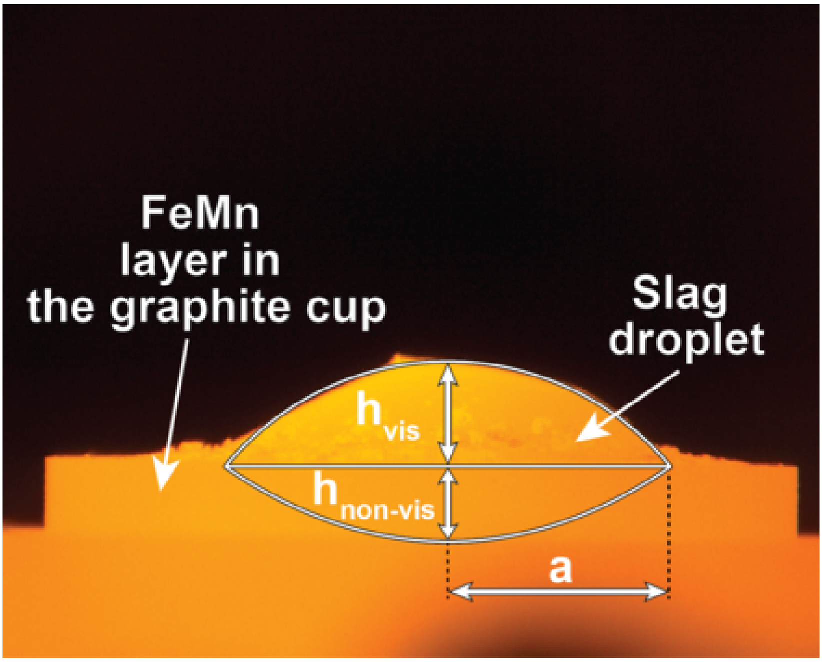

**Figure 10.8:** Slag droplet on top of FeMn layer in experiments: $a$ is the base radius of the spherical cap, $h_{vis}$ and $h_{non-vis}$ are the height of the spherical cap above and below the interface, respectively. Reprinted from Bublik and Einarsrud [3].

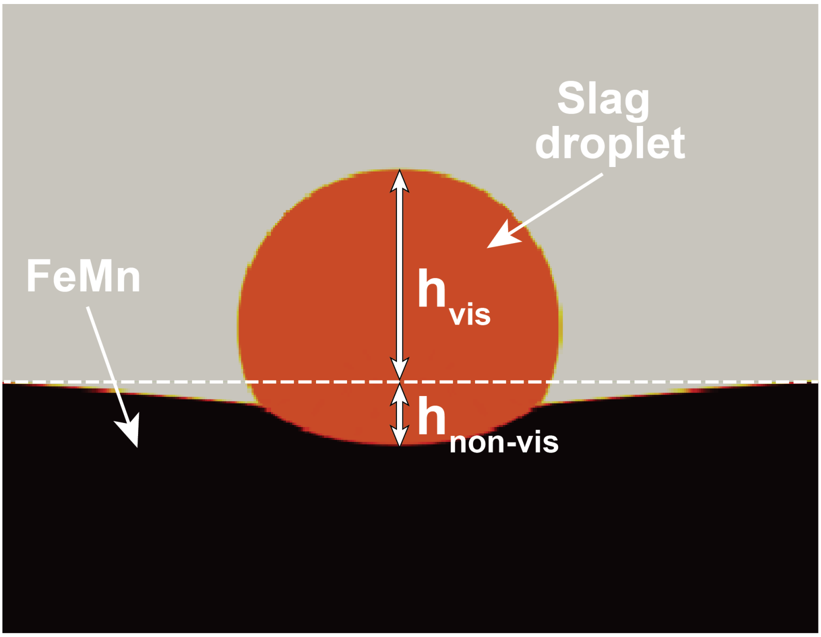

**Figure 10.9:** Slag droplet on top of FeMn bath in simulations. Reprinted from Bublik and Einarsrud [3].

± 0.05 N/m, while surface tension of slag was considerably lower (0.65 ± 0.01 N/m). From the confidence intervals, it is evident that the LBADSA methodology, which was applied for the measurement of surface tension of FeMn has higher deviation (±0.05 N/m) than the ellipsoidal solution of the Young-Laplace equation, where the confidence interval for surface tension of slag was ±0.01 N/m.

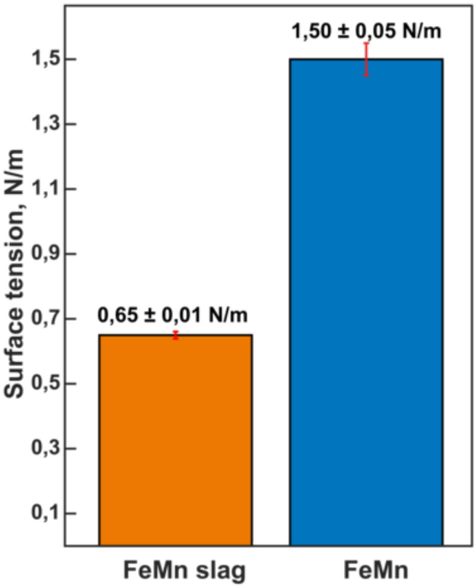

**Figure 10.10:** Surface tension of FeMn alloy and slag measured experimentally in the sessile drop furnace. Red lines on top of bars are 95 % confidence intervals. Reprinted from Bublik and Einarsrud [3].

Figure 10.11 shows the simulation matrix obtained after performing multiphase simulations in OpenFOAM with various values of interfacial tension and physical parameters corresponding to the experiments in the sessile drop furnace. The corresponding non-visible height to the values of interfacial tension from 0.85 to 1.50 N/m is illustrated in Figure 10.12. The results demonstrate that the slag droplet remains above the interface at relatively high values of interfacial tension (≈1.20 - 1.50 N/m), promoting better separation of FeMn alloy and slag and therefore less metal losses. The slag droplet begins to sink down below the interface at intermediate interfacial tension (≈0.85 - 1.15 N/m), contributing to emulsification of FeMn and slag.

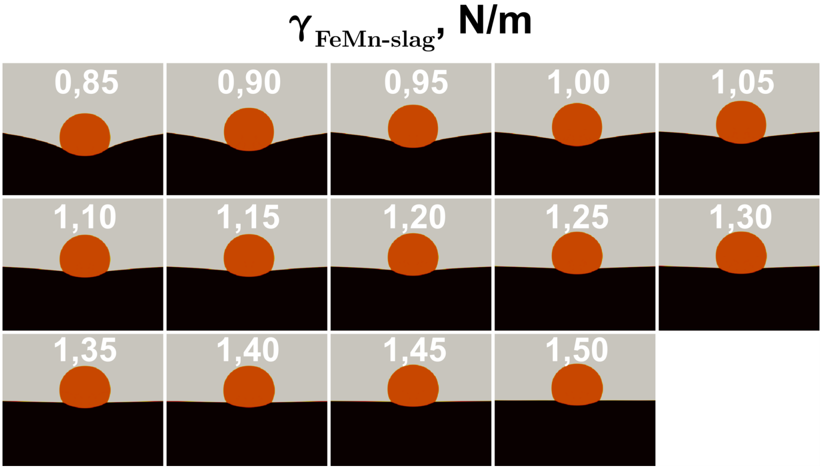

**Figure 10.11:** The simulations results depending on interfacial tension between FeMn alloy and slag from 0.85 to 1.50 N/m. Reprinted from Bublik and Einarsrud [3].

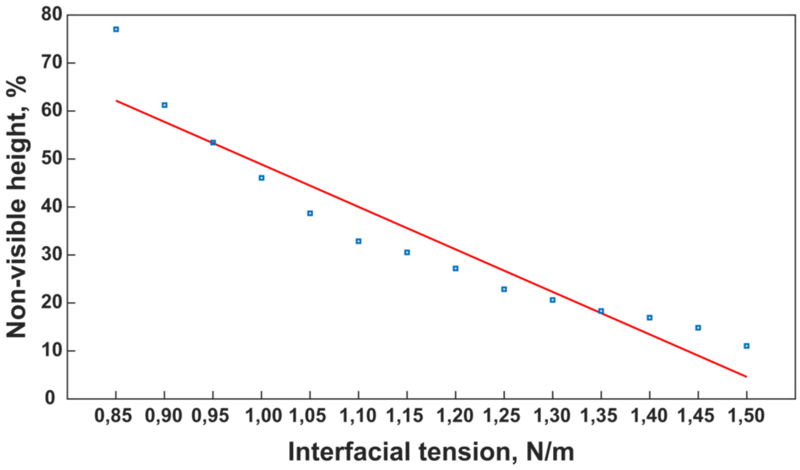

**Figure 10.12:** Influence of interfacial tension on the non-visible height in the simulations. Reprinted from Bublik and Einarsrud [3].

## Summary of paper III

### A Review of Ferroalloy Tapping Models

Sergey Bublik, Jan Erik Olsen, Varun Loomba, Quinn Gareth Reynolds, Kristian Etienne Einarsrud, *Metallurgical and Materials Transactions B,* 52, pp. 2038-2047, 2021.

***Author contributions***

The first author (Sergey Bublik) planned the structure of the review together with other authors, wrote the following chapters: introduction, physical and numerical models, collected all the chapters from other authors in LaTeX format, submitted the paper to Metallurgical and Materials Transactions B and was responsible for the correspondence with reviewers and addressing the feedback received from them.

***Context to the work and objective***

Tapping is an important furnace operation in the ferroalloy industry and poses a number of complex and coupled challenges of both practical and economical importance. Owing to the hazardous high-temperature conditions surrounding the tap hole, the application of various modelling techniques allows for development and acquisition of both scientific and engineering knowledge of the process through physical or numerical proxies.

Different aspects related to tapping of SAFs can be investigated using mathematical models and computational fluid dynamics (CFD) [77, 101, 102]. Such approaches can provide great insight to the operation, and the knowledge gained from properly constructed studies with such tools can ultimately improve the consistency of tapping.

The main objectives of Paper III were as follows:

- review and summarize earlier studies on modelling of ferroalloy tapping.
- discuss main principles of the tapping process and multiphase interaction of slag and metal.
- discuss advantages and disadvantages of various tapping modelling approaches,

and assess their general applicability.

The main focus in this paper was on drainage of slag and alloys, but metal loss, metal overflow and issues related to health, safety and environment were considered as well. Selected studies on blast furnace tapping models were also discussed in addition to tapping modelling of SAFs, since the drainage mechanisms are very similar in both furnaces.

***Physical and numerical models***

Different approaches to modelling of the tapping process in ferroalloy production have been conducted; categorized as physical or mathematical modelling. An experimental setup with a physical representation of the process or phenomena to be studied defines a physical model. For ferroalloy tapping this should in principle involve a drainage experiment with at least one liquid phase and a particle bed. Although several physical drainage experiments have been reported in the literature, few have considered the particle bed [103, 104].

Mathematical models can relate to many aspects of the process including thermochemical properties, material erosion and wear and more [105, 106]. In this paper, the main focus were on mathematical models for the drainage of slag and metal from the furnace. In addition, it is necessary to differentiate between reduced order modelling and CFD. In principle, CFD can be defined to include all mathematical models describing flow, but here CFD is limited to mathematical models solving the full 3D (or 2D) set of conservation equations for mass and momentum by a numerical algorithm. Reduced order modelling refers to a modelling scheme where the model complexity is reduced through various assumptions allowing for reduction in solution time and/or data storage.

***Reduced order modelling***

In modelling the draining flow from a furnace, Bernoulli's equation provides a reasonable representation of the flow between two points in a geometry. The equation is based on conservation of mechanical energy along a flow line. Models based on this principle are used in textbooks in Fluid Dynamics with drainage as an example, and all known reduced order models for furnace tapping apply Bernoulli's equation.

The tapping rate for a tank with a liquid can be estimated by Bernoulli's equation (see e.g. Guthrie [103]):

$$\dot{m} = \frac{\rho C_D \pi d^2}{4} \sqrt{2gH} \tag{10.2}$$

where $d$ is the diameter of the tap-hole, $\rho$ is the density of liquid, $C_D$ is the drag coefficient, $g$ is the acceleration due to gravity. Here, the hydrostatic head $H$ provides a pressure which is the driving force of tapping. In a furnace, a viscous resistance will be present due to the particle bed of carbon material and ore. The driving force will also be affected by the furnace pressure. The tapping of a submerged arc furnace is therefore more complex than tapping of water through a hole in a tank.

Another important expression is the Kozeny-Carman expression, typically applied in laminar flow, to account for the pressure drop due to the particle bed:

$$\Delta P = \frac{180\mu}{\Phi^2 d_p^2} \frac{(1-\epsilon)^2}{\epsilon^3} v_t r_t \tag{10.3}$$

where $\mu$ is liquid viscosity, $v_t$ is tapping velocity, $r_t$ is tap-hole radius, $\epsilon$ is particle bed porosity, $d_p$ is particle diameter and $\Phi$ is particle sphericity. The particle bed resistance is therefore accounted for in a similar manner as for a porous material.

Olsen and Reynolds [104] have suggested that the Ergun equation, which is applicable to turbulent flow, can be applied for calculating the pressure drop due to particle bed in slag and metal tapping:

$$\Delta P = \frac{150\mu}{\Phi^2 d_p^2} \frac{(1-\epsilon)^2}{\epsilon^3} v_t r_t + \frac{1.75\rho_m}{3\Phi d_p} \frac{(1-\epsilon)}{\epsilon^3} v_t^2 r_t \tag{10.4}$$

The results of Olsen and Reynolds [104] indicate that the Ergun equation is more reliable for this application than the Kozeny-Carman equation, since the Reynolds number in the tapping process indicates turbulent flow. Results obtained using the Ergun equation were superior to those obtained with the Kozeny-Carman equation when comparing with physical models (Vango et al. [106]).

***CFD modelling***

Computational fluid dynamics (CFD) is the method of numerically solving the equations for conservation of mass, momentum and energy in order to compute fluid and heat flow [107]. These equations are mathematically represented as follows [108]:

- **Conservation of mass**

$$\frac{\partial \rho}{\partial t} + \nabla \cdot (\rho u) = 0. \tag{10.5}$$

- **Conservation of momentum**

$$\frac{\partial \rho u}{\partial t} + \nabla \cdot (\rho u u) = -\nabla P + \nabla \cdot \left[\mu_{eff}(\nabla u + (\nabla u)^T)\right] + \rho g + S_u. \tag{10.6}$$

- **Conservation of energy**

$$\frac{\partial \rho h}{\partial t} + \nabla \cdot (\rho h u) = -\frac{DP}{Dt} + \nabla \cdot (k \nabla T) + S_h. \tag{10.7}$$

where $u$ and $\rho$ are the fluid velocity and density, $\mu_{eff}$ is the effective viscosity - accounting also for turbulence, $P$ is the pressure in the fluid, $S_u$ is a momentum source term, $h$ is the enthalpy, $T$ is the temperature, $k$ is the thermal conductivity of the fluid and $S_h$ is a source/sink term accounting for instance for radiation. The effect of the particle bed resistance in the furnace can be included by adding the pressure drop across the bed calculated by the Kozeny-Carman equation (Eq. 10.3) or the Ergun equation (Eq. 10.4) as the source term $S_u$ to Eq. 10.6 without affecting the simulation complexity considerably.

CFD has been applied to metallurgical processes since the 1980s but the first work on metal tapping dates to 2001, when Dash et al. [109] optimized the length of the tap-hole block inside the furnace to reduce the peak shear stress in the furnace hearth which occurs at the tap-hole due to high velocity of metal. The authors included the effect of porosity via the Kozeny-Carman formulation, i.e. excluding inertial effects in the porous zone. In 2004, Dash et al. [110] expanded their research and optimized the angle of tap-block to the horizontal axis to minimize the peak shear stress. Since then, CFD modelling has been extensively used for modelling of different tapping aspects, as such Nishioka et al. [111] studied the effect of the particle diameter in the packed bed on tapping rates, Kadkhodabeigi et al. [112] studied tapping of molten silicon and flow in the tap-hole depending on different conditions inside the furnace, Reynolds et al. [113, 114] performed optimization of the geometry of tap-hole inlet and the launder, and analyzed the sensitivity of material properties on tapping rates.

***Application to tapping***

The potential inherent in modelling of tapping processes is considerably wider in scope. With the advent of the fourth industrial revolution (4IR) modelling methods constitute a powerful toolbox that can be leveraged by high-level software automation for design, optimization, and control purposes. This can take several forms:

- Virtual prototyping, in which numerous variations of equipment and process designs are tested extensively using computer models as front-line engineering tools, in order to arrive at an optimized final design [115, 116].
- Digital twinning, in which predictive numerical or computational models are integrated with live data from furnace plants in order to provide model-based control, operator guidance, and early warning systems.
- Inverse modelling and soft sensors, in which models are used to infer and interpolate between real measurements (such as those obtained from furnace feed and electrical systems, thermocouples, sidewall cooling elements, etc.) in order to provide virtual sensors which can be used by plant control systems as though they were real instruments [117, 118].
- Industrial Internet of Things (IIoT) applications, in which knowledge obtained from modelling (or even simple models themselves) are directly integrated into instruments and support equipment installed on the tapping

system, facilitating the development of more distributed and self-organizing control strategies [119].

- Data-driven modelling, in which large quantities of measured tapping data for a particular furnace operation are analyzed using data science and machine learning tools in order to support and augment more traditional empirical or fundamental modelling [120].

## Summary of paper IV

### Interfacial Behaviour in Ferroalloys: The Influence of Sulfur in FeMn and SiMn Systems

Sergey Bublik, Sarina Bao, Merete Tangstad, Kristian Etienne Einarsrud, *Metallurgical and Materials Transactions B*, 52, pp. 3624-3645, 2021.

***Author contributions***

The first author (Sergey Bublik) developed and verified the mentioned methodologies, planned and performed the experiments, prepared the samples for electron microscopy and examined them by EPMA, evaluated and analyzed the results, wrote the paper, submitted it to Metallurgical and Materials Transactions B and was responsible for the correspondence with reviewers and addressing the feedback received from them.

***Context to the work and objective***

Interfacial phenomena are vital for ferroalloy production, as a better understanding of entrainment mechanisms can significantly help reduce ferroalloy losses with slag. The interfacial interaction between metal and slag and the stability of the interface between them are characterized by interfacial tension [35]. High interfacial tension promotes better separation, while the opposite is true for low interfacial tension [6, 14]. In metal-slag systems where surface-active elements such as sulfur, oxygen, selenium and tellurium are present, interfacial tension decreases as a result of higher mass transfer rates, leading to problems with the separation of metal and slag due to the formation of metal-slag emulsion [121]. In ferroalloys production, major elements which represent surface-active elements are sulfur and oxygen. For such systems, the thermodynamic equilibrium between ferroalloy and slag can be described by the reaction [122]:

$$[S] + (O^{2-}) \Leftrightarrow (S^{2-}) + [O]. \tag{10.8}$$

The study in Paper IV is based on methodologies for the measurement of interfacial tension and apparent contact angles between ferroalloy and slag, which were developed and verified by the authors previously in Paper I and II [3, 66]. Interfacial interaction in synthetic FeMn-slag and SiMn-slag systems, both with and without sulfur addition to ferroalloy, has been investigated by combining analysis of images from a sessile drop furnace and multiphase flow simulations in OpenFOAM v6 [82], and discussed together with the assessment of the sensitivity of the results by comparing different experiments.

***Main results***

The experimentally measured average values of surface tension are shown in Figure 10.13. As it is expected for metals, FeMn and SiMn have higher values of surface tension of 1.50 and 1.20 N/m, respectively, while slags have considerably lower surface tensions of 0.65 N/m for FeMn slag and 0.50 N/m for SiMn slag. Besides, sulfur addition to ferroalloys seems to have no significant effect on surface tension of FeMn and SiMn, which results in the same surface tension as corresponding alloys without sulfur addition. The LBADSA methodology, which was used for determination of surface tension of FeMn alloy, has a higher deviation in values of surface tension for FeMn, ±0.05 N/m. In contrast, the LBADSA methodology used for SiMn alloy and the ellipsoidal solution of the Young-Laplace equation used for slags result in a smaller deviation, ±0.02 N/m. The difference can be explained by a rough surface of FeMn compared to other materials, as shown in Figure 10.14, which gives greater variation in measurements. The observed roughness of FeMn could be attributed to a higher C content, and hence more C can precipitate or dissolve during experiments with FeMn.

The effect of sulfur content in the SiMn alloy ($S_{SiMn}$) on the average apparent contact angle between SiMn and slag has been studied at constant maximum temperature of 1873 K and constant holding time of 5 min and is shown in Figure 10.15. The increase of $S_{SiMn}$ from 0.02 to 0.90 wt. % decreases the average apparent contact angle from 37.8 to 29.6°. The largest change of -6.7° is observed between $S_{SiMn}$ of 0.02 and 0.25 wt. %, while the change between $S_{SiMn}$ of 0.25 and 0.62 wt. %, and between $S_{SiMn}$ of 0.62 and 0.90 wt. % was only -1.1° and

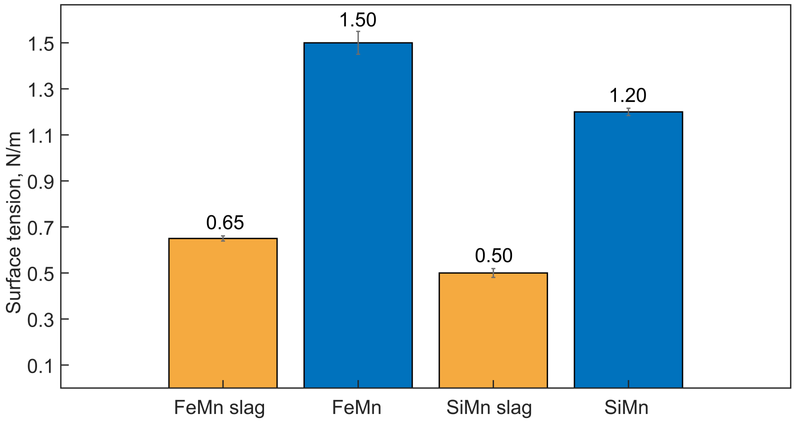

**Figure 10.13:** Average values of surface tension of FeMn, SiMn and slags measured experimentally. Grey lines on top of bars represent the 95 % confidence interval for the sample mean. Reprinted from Bublik et al. [67] under the terms of the Creative Commons CC BY license.

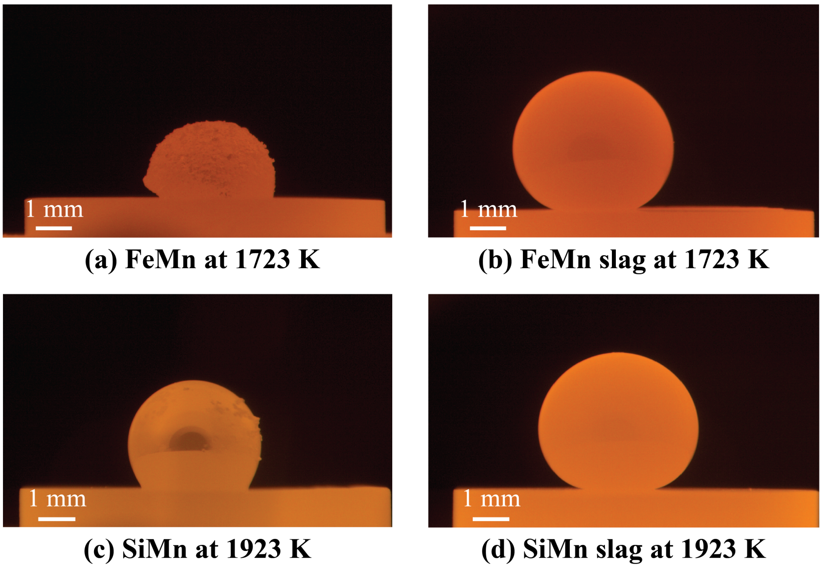

**(a) FeMn at 1723 K**

**(b) FeMn slag at 1723 K**

**(c) SiMn at 1923 K**

**(d) SiMn slag at 1923 K**

**Figure 10.14:** Surface of FeMn, SiMn and slags during melting in the sessile drop furnace: (a) FeMn droplet at 1723 K, (b) FeMn slag droplet at 1723 K, (c) SiMn droplet at 1923 K, (d) SiMn slag droplet at 1923 K. Reprinted from Bublik et al. [67] under the terms of the Creative Commons CC BY license.

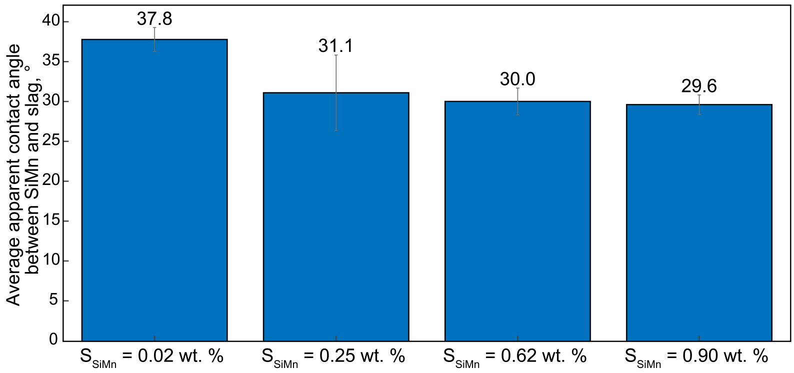

**Figure 10.15:** Effect of sulfur content in SiMn on average apparent contact angle between SiMn and slag at temperature of 1873 K and holding time of 5 min. Grey lines on top of bars represent the 95 % confidence interval for the sample mean. Reprinted from Bublik et al. [67] under the terms of the Creative Commons CC BY license.

-0.4°.

The average interfacial tension between FeMn and slag changes depending upon sulfur content in the FeMn alloy ($S_{FeMn}$), as shown in Figure 10.16. The largest change of -0.30 N/m is noted when $S_{FeMn}$ increases from 0.03 to 0.31 wt. %, which indicates that the equilibrium in the FeMn-slag-S system is reached in this range of $S_{FeMn}$. The further increase of $S_{FeMn}$ to 0.93 wt. % decreases interfacial tension only slightly from 0.96 N/m to 0.88 N/m. However, the measurements for $S_{FeMn}$ of 0.31 and 0.57 wt. % have a larger deviation described by confidence intervals of ±0.09 and ±0.05 N/m, respectively, which may be attributed to significant fluctuations in surface area of droplets during experiments due to the gas evolution.

After reaching equilibrium between ferroalloy and slag and finishing the experiments, sulfur was mainly found in the slag phase as illustrated in Figure 10.17 and 10.18, even though sulfur was initially added only to FeMn or SiMn. The sulfur distribution to the slag phase was confirmed further by calculating the sulfur distribution between FeMn/SiMn and slag in FactSage [78] (Figure 10.19), from

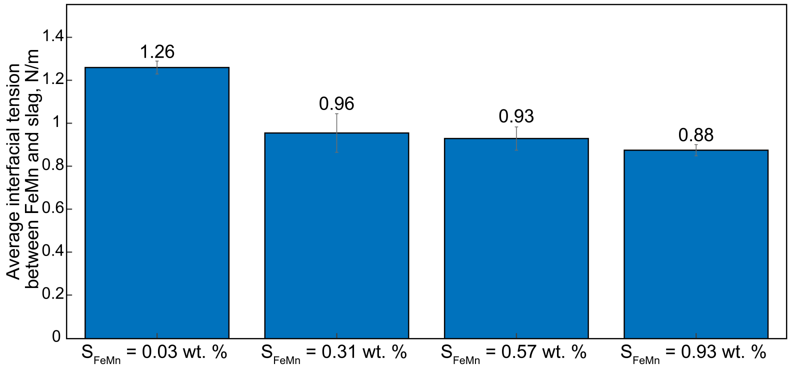

**Figure 10.16:** Effect of sulfur content in FeMn on average interfacial tension between FeMn and slag at temperature of 1673 K and holding time of 5 min. Grey lines on top of bars represent the 95 % confidence interval for the sample mean. Reprinted from Bublik et al. [67] under the terms of the Creative Commons CC BY license.

which it is evident that sulfur tends to be distributed in slag, whether added to FeMn or SiMn.

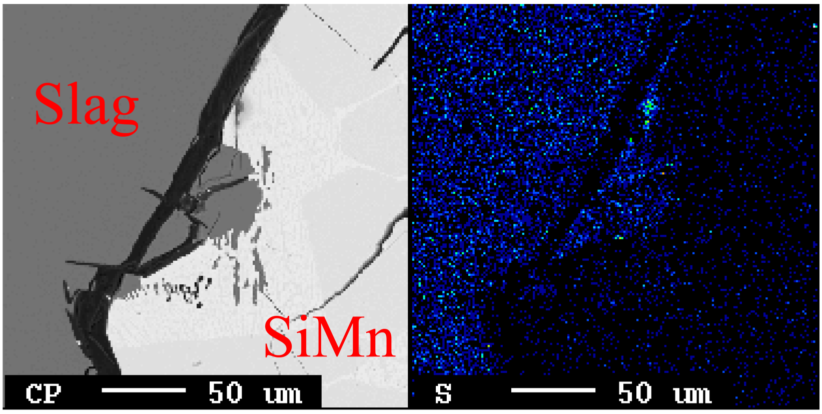

(a) BSE image (b) S distribution

**Figure 10.17:** EPMA results of the sample from experiment 15 (0.62 wt. % $S_{SiMn}$, 1873 K, 5 min holding time). (a) SiMn and slag on the BSE image, (b) EPMA elemental mapping showing sulfur distribution between SiMn and slag. Reprinted from Bublik et al. [67] under the terms of the Creative Commons CC BY license.

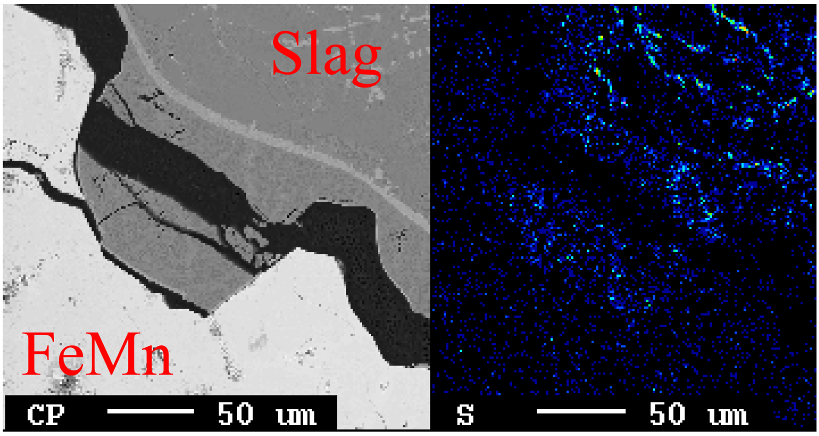

(a) BSE image (b) S distribution

**Figure 10.18:** EPMA results of the sample from experiment 2 (0.31 wt. % $S_{FeMn}$, 1673 K, 5 min holding time). (a) FeMn and slag on the BSE image, (b) EPMA elemental mapping showing sulfur distribution between FeMn and slag. Reprinted from Bublik et al. [67] under the terms of the Creative Commons CC BY license.

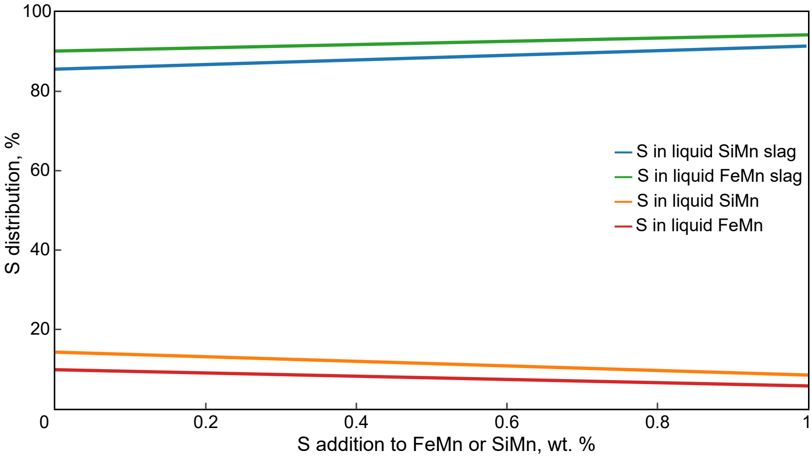

**Figure 10.19:** Sulfur distribution between phases in the FeMn-slag-S-Ar and SiMn-slag-S-Ar systems at 1673 and 1873 K, respectively. Calculated using FactSage 7.3. Reprinted from Bublik et al. [67] under the terms of the Creative Commons CC BY license.

## Summary of paper V

### Interfacial Behaviour in Ferroalloys: The Influence of FeMn Slag Composition

Sergey Bublik, Merete Tangstad, Kristian Etienne Einarsrud, *Submitted to Metallurgical and Materials Transactions B*.

***Author contributions***

The first author (Sergey Bublik) developed the mentioned methodologies, planned and performed the experiments, prepared the samples for electron microscopy and examined them by EPMA, evaluated and analyzed the results, wrote the paper, submitted it to Metallurgical and Materials Transactions B and was responsible for the correspondence with reviewers and addressing the feedback received from them.

***Context to the work and objective***

The carbothermic reduction of manganese ores for producing FeMn alloy in submerged arc furnaces is related to the formation of a significant amount of molten slag, which is then tapped simultaneously with FeMn to ladles, where a metal-slag emulsion is formed. Small FeMn droplets are entrained in the slag phase due to the intensive mixing of FeMn and slag. This decreases efficiency of the ferroalloy production process because further removal of metal from slag may cause logistics difficulties and is heavily time- and energy-consuming [68, 123]. Interfacial tension between molten metal and slag characterizes the metal-slag separation [41] and thus it is important for ferroalloy production. High interfacial tension promotes a high degree of separation of metal and slag, while a low interfacial tension will promote formation of metal-slag emulsion and small metal droplets in slag [40]. Several studies have shown that the interfacial tension is greatly dependent upon the slag composition due to chemical reactions at the metal-slag interface and the mass transfer across the interface [19, 20, 22, 37, 39, 61, 64, 65]. In FeMn production, the FeMn alloy is highly saturated with carbon, which results in reduction of oxides such as MnO, FeO or $SiO_2$ at the interface between FeMn and slag, and subsequently in the mass transfer of Mn, Fe and Si to the

FeMn alloy. The thermodynamic equilibrium between ferroalloy and slag can be described by several reduction reactions [124]:

$$(MnO) + [C] = [Mn] + CO_{(g)}, \tag{10.9}$$

$$(SiO_2) + 2[C] = [Si] + 2CO_{(g)}, \tag{10.10}$$

$$(FeO) + [C] = [Fe] + CO_{(g)}, \tag{10.11}$$

$$(MnO) + [Fe] = [Mn] + (FeO), \tag{10.12}$$

$$(SiO_2) + 2[Mn] = [Si] + 2(MnO). \tag{10.13}$$

In Paper V, the interfacial interaction between FeMn alloy and slags of different compositions was investigated in a sessile drop furnace using the methodology developed by the authors previously in Paper I and II [3, 66, 125], which was improved in this study to improve reproducibility and reduce uncertainty due to the precipitation of solid carbon during melting of FeMn alloy and slag. The improved methodology combines analysis of images from experiments in the sessile drop furnace, numerical data obtained in multiphase flow simulations in OpenFOAM v8 [82], the numerical models for calculation of density and surface tension of slag developed by Mills et al. [70, 71] and results of equilibrium calculations in FactSage 7.3 [78]. In addition, the sensitivity of the results was assessed by comparing different experiments.

***Main results***

The surface tension and density of the slags were calculated considering the composition of the initial slag and the liquid slag phase calculated in FactSage. The surface tension between the initial slag and the liquid slag phase has the maximum variation of 0.025 N/m (5.5 %), meaning that its values does not vary significantly between the initial slag and the liquid slag phase. Higher values of the surface tension at higher basicities may be related to the composition change during which the content of CaO increases while $SiO_2$ decreases. CaO has a high surface tension of 0.625 N/m in its pure form, whereas surface tension of pure $SiO_2$ (0.260 N/m) is substantially lower [70]. In addition, slags without $Al_2O_3$ addition have lower surface tension due to the low content of $Al_2O_3$ which has a high surface tension of 0.655 N/m. However, the variation in the density between the initial slag and the liquid slag phase is higher, reaching a maximum difference of 301 $kg/m^3$ or 9.6 % for slag C3. The density for the initial slags is almost constant regardless of the slag basicity, but it increases when MnO and $Al_2O_3$ content in the slags increases as they have a higher density of 5370 and 3965 $kg/m^3$, respectively, in their pure form compared with CaO (3340 $kg/m^3$), MgO (3580 $kg/m^3$) and $SiO_2$ (2650 $kg/m^3$) [126]. For the liquid slag phase, the density decreases with the slag basicity due to the significant change in the composition of the liquid phase after reaction with the FeMn alloy, which leads to a lower MnO content.

The interfacial tension between the FeMn alloy and the slags with and without $Al_2O_3$ addition is shown in Figures 10.20 and 10.21, respectively. It can be seen from the figures that the interfacial tension sharply increases with the slag basicity for both groups of slags and that the interfacial tension change for the slags with $Al_2O_3$ addition is more pronounceable at higher higher basicities. As such, the average interfacial tension for the slags with $Al_2O_3$ addition is 0.21-0.40 N/m higher at the basicity of 0.8, and 0.05-0.36 N/m higher for the basicity of 1.2. In addition, the 80 % confidence intervals overlap greatly in each group of basicities due to the low number of experiments in parallels; however, the measured values of the interfacial tension fall within the proposed ranges of the confidence intervals. Increasing MnO content in slag from 30.0 to 45.0 wt. % does not show statistically significant differences in the interfacial tension for all slags. Here, it is important to note that due to the fluctuations of the slag droplet during reaction with the FeMn alloy, which can influence the experimental results, the non-visible height and, accordingly, the interfacial tension were measured only at local minimum expansion of the slag droplet as shown in Figure 10.22.

Chung and Cramb [39] suggested that the emulsification phenomena are closely

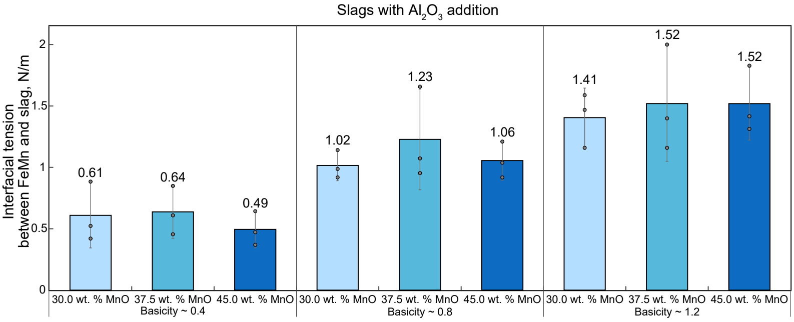

**Figure 10.20:** The interfacial tension between the FeMn alloy and the slag with the addition of $Al_2O_3$ at different slag basicities and MnO content at 1673 K. The top part of the bars corresponds to the average interfacial tension between the FeMn alloy and the slag. The grey lines on top of bars represent the 80 % confidence interval, and the circle markers represent the experimental measurements. Reprinted from Bublik et al. [33] under the terms of the Creative Commons CC BY license.

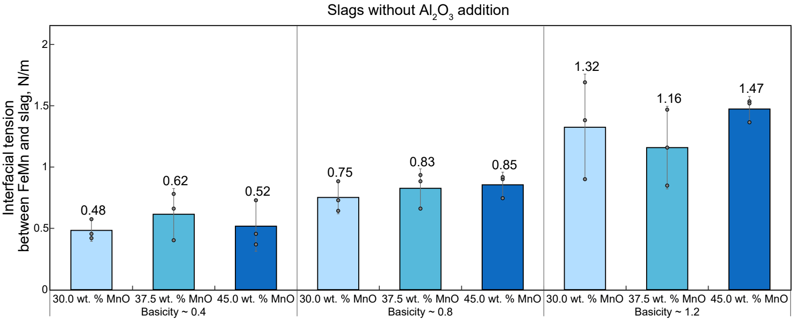

**Figure 10.21:** The interfacial tension between the FeMn alloy and the slag without the addition of $Al_2O_3$ at different slag basicities and MnO content at 1673 K. The top part of the bars corresponds to the average interfacial tension between the FeMn alloy and the slag. The grey lines on top of bars represent the 80 % confidence interval, and the circle markers represent the experimental measurements. Reprinted from Bublik et al. [33] under the terms of the Creative Commons CC BY license.

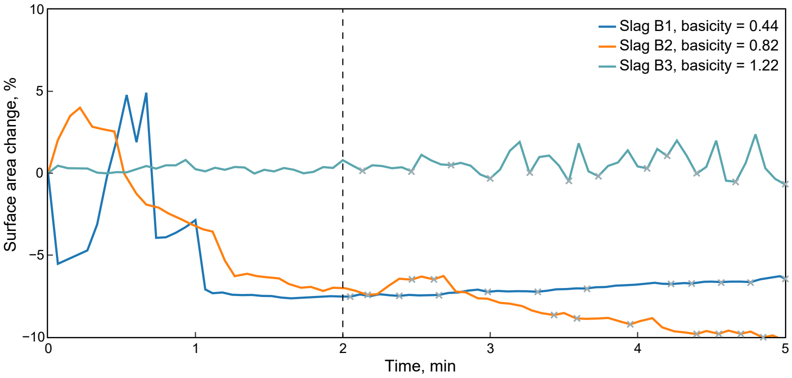

**Figure 10.22:** Temporal change in visible surface area for slags B1-B3 during holding at 1673 K. The grey cross markers correspond to the local minimum expansion of the slag droplet in the experiments. Note that interfacial tension was measured only after two minutes of holding time as indicated with the vertical dashed line. Reprinted from Bublik et al. [33] under the terms of the Creative Commons CC BY license.

related to the interaction of fluids at the interface and that the driving force for fluid flow across the interface depends on reactions in the system under isothermal conditions due to the concentration gradient at the interface. In case of the concentration gradient and the fluid flow driven by the interfacial reaction, the interface eventually becomes unstable and the metal-slag interfacial area increases (the Kelvin-Helmholtz interfacial instability). Based on the Kelvin-Helmholtz model, Gopal [41] discussed the mechanism of small droplet formation and emulsification of slag and metal during reactions between them. If the mass transfer rate of elements or compounds across the interface is low, it results in a slight destabilization of the interface (Figure 10.23(a)), corresponding to the high slag basicity of 1.2 in this study. At higher mass transfer rates, the destabilization of the interface is more severe as shown in Figure 10.23(b-c), which results in the formation of the metal-slag emulsion and droplets of one phase into another as it was observed for the low slag basicities from 0.4 to 0.8.

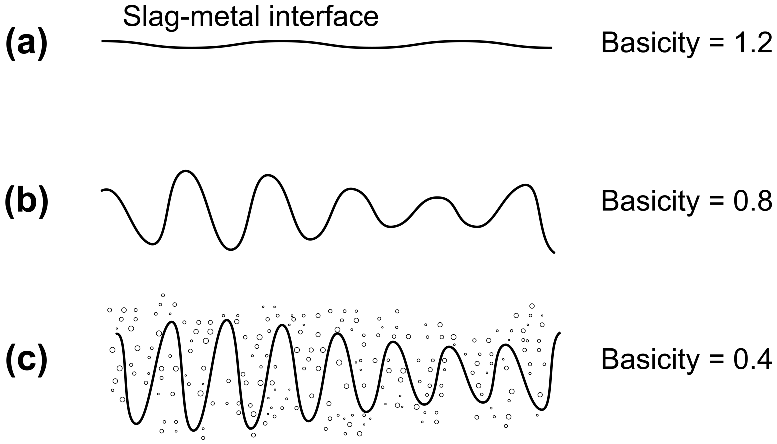

**Figure 10.23:** Emulsification of slag and metal and formation of small droplets due to the Kelvin-Helmholtz instability. Images (a)-(c) represent disturbances of the interface between slag and metal at different slag basicities. Reprinted from Bublik et al. [33] under the terms of the Creative Commons CC BY license.

## Summary of paper VI

### Slag Properties in the Primary Production Process of Mn-Ferroalloys

Merete Tangstad, Sergey Bublik, Shokouh Haghdani, Kristian Etienne Einarsrud, Kai Tang, *Metallurgical and Materials Transactions B,* 52, pp. 3688-3707, 2021.

***Author contributions***

The second author (Sergey Bublik) planned the structure of the review together with other authors, wrote the sections: density, surface and interfacial tension.

***Context to the work and objective***

Mn-ferroalloys are alloys containing mostly Mn, Fe, Si and C. Manganese is the main element and typically accounts for between 60 and 80 wt. % of the alloy. Practically, all iron from raw materials will end up in the alloy, while the Si content is usually less than 1 wt. % in FeMn alloy and from 16 to 30 wt. % in SiMn alloy. Mn-ferroalloys are always saturated with carbon from raw materials and electrodes, thereby the C content in the FeMn alloy is around 7 wt. % and up to 2 wt. % for the SiMn alloy, depending on the amount of Si.

Temperatures in closed Mn-ferroalloy furnaces can be from 200 °C to 600 °C on the top of the charge and from 1500 °C to 1600 °C in the tapped slag. This means that in the upper part of the furnace, the low temperature zone, the raw materials are solid, and when they descend to the area on top of the coke-bed with temperature from 1200 °C to 1400 °C, the raw materials will melt into a primary slag. This slag will coexist with the solid carbon materials added to the furnace.

Paper VI discusses MnO-slags and their properties in the primary production of FeMn or SiMn alloys in SAFs. The mechanisms of slag formation, thermodynamics, kinetics, slag structure are considered and a summary of the key slag properties is given. These key properties include viscosity, density, interfacial tension and wetting properties, and electrical conductivity. The pathway of the slag considered in this work starts with the production of primary slag from the raw materials, followed by the reduction of valuable elements into Mn-alloy and finally tapping of slag and Mn-alloy from the furnace.

***Slag structure***

The structure of silicate melts is of fundamental importance in metallurgical processes because the melt structure is closely linked to transport properties such as viscosity, density, and electrical conductivity [127, 128]. The degree of polymerization (DOP) of silicate networks has been introduced as the most influential parameter for linking these properties and slag structure. DOP and viscosity are proportional, while density and electrical conductivities are inversely proportional to DOP [129, 130]. In silicate slags, the presence of network-former and network-modifier elements determines the DOP of the silicate structure. $SiO_2$ is among the network-former oxides, while alkali and alkali-earth oxides, such as $Na_2O$ and CaO (basic oxides), contribute to depolymerization of the silicate network as network-modifying components. Amphoteric oxides, such as $Al_2O_3$, can act as either network-former or network-modifier oxide based on the availability of basic oxides in the silicate network [131].

Other important parameters are oxygen species, namely bridging oxygen ($O^0$), non-bridging oxygen ($O^-$), and free oxygen ($O^{2-}$). In silicate networks, $O^0$ is connected to two network-former cations (Si-$O^0$-Si or Si-$O^0$-Al), $O^-$ is bounded to only one network-former cations (Ca-$O^-$-Si), while $O^{2-}$ is connected to only network-modifier cations (Ca-$O^{2-}$-Ca). By increasing $O^{2-}$ through dissociation of basic oxides, the DOP of silicate networks decrease because $O^{2-}$ reacts with $O^0$ in the silicates to split the highly complex structures of Si-O into low polymerized units. There are various types of Si-O units called $Q^n$ species where n is the number of $O^0$ in the unit and can be 0 to 4. These units are monomer structure ($Q^0$), dimer structure ($Q^1$), chain structure ($Q^2$), sheet structure ($Q^3$), and 3-dimensional structure ($Q^4$) [132]. The DOP parameter can be found both experimentally and theoretically through $Q^n$ species obtained by Raman analysis and slag compositions, respectively. Oxygens species are also given experimentally using X-ray photoelectron spectroscopy and theoretically using slag compositions [133].

***Slag viscosity***

The viscosity of slag contributes to the metal-slag separation efficiency and tapping process, and is thus closely related to operation efficiency and minimizing the energy usage [134]. Slag viscosity depends on temperature and slag composition as the viscosity decreases with increasing temperature and basic oxide contents.

Viscosity measurements for the slag system with MnO-CaO-MgO-$SiO_2$-$Al_2O_3$ have been carried out for various industrial applications [135–138]. In general, the results of these studies have revealed the effect of both temperature and MnO content. These findings suggest that slag viscosity decreases by increasing temperature and reduces by increasing the MnO content. The latter can be understood by considering the fact that MnO is a basic oxide and acts as a network breaker in the silicate network.

***Slag density***

There is a lack of density data on slags in Mn-ferroalloy production, but some insight may be gained by considering slags in steel production. Particularly, so-called mould slags in steel production consist of similar components as slags in Mn-ferroalloy production, MnO, CaO, MgO, $SiO_2$, $Al_2O_3$, while the main difference is the content of these components in both types of slags [139].

In general, slag density can be determined by (a) numerical calculations based on previously established models [70] and (b) experimental methods, such as the sessile drop technique [59], the Archimedes principle [140] or electrostatic levitation method [141].

Results of the experimentally measured density by Lee at al. [142] and the calculated density by the model from Mills et al. [70] for MnO-CaO-$SiO_2$-MgO-$Al_2O_3$ and MnO-CaO-$SiO_2$ slags have shown that the density estimated using the model shows fairly close values to those determined by Lee et al., and in addition, the calculated densities show the expected increase when MnO content is increased, which may indicate that the model of Mills et al. can be applied for slags in ferroalloy production with high reproducibility.

### *Surface and interfacial tension*

Surface and interfacial tensions govern important phenomena such as wetting, foaming, refractory infiltration and slag-metal separation [143–145]. Interfacial behaviour depends upon the content of chemical elements and components interacting at the slag-metal interface, and thus interfacial tension changes as a function of slag composition. As with other properties of slags in ferroalloy production, there are few published data on surface tension of multicomponent slags and interfacial tension between slag and ferroalloys. However, studies on slags in steel production have shown that surface tension of most multicomponent slags lies in the range from 0.30 to 0.70 N/m [56, 57, 60]. Bublik et al. [67] have found that surface tension of slags corresponding to FeMn and SiMn production is 0.65 and 0.50 N/m, respectively. Mills et al. [70] have reported that surface tension of multicomponent slags can be calculated assuming that surface tension is temperature-dependent and that all slag components modify surface tension depending on their content in the bulk or at the surface.

## Summary of paper VII

### SlagCalculator: A Framework for Slag and Metallurgical Properties

Sergey Bublik, Sylvain Gouttebroze, Terence Coudert, Merete Tangstad, Kristian Etienne Einarsrud, *Proceedings of the 16th International Ferro-Alloys Congress (INFACON XVI) 2021*, Trondheim, Norway, 2021.

***Author contributions***

The first author (Sergey Bublik) planned the code structure and developed the framework using Python, planned the interface of the publicly available version, wrote the paper (except the "Overview of digital solutions"), and submitted it to INFACON XVI.

***Context to the work and objective***

Metallurgical processes are complex, therefore their modelling is important for advanced process control and optimization. There are many models which describe slag properties and processes, but these models are not gathered in one place, and thus it is of great importance to have a framework that integrates all available models to obtain and manipulate data in a more convenient and accessible way. Many properties can be extracted from commercial codes as for example FactSage [78] or HSC Chemistry [146], but often it is required to have access to tools that are more user-friendly. A web-based application for calculating electrolyte properties [147], ElProp, has shown that it is completely possible to use advanced frameworks to create easily accessible interactive dashboards.

The main goal of Paper VII was to develop a web-based application for calculation and search of slag properties. The publicly available version of the application is based on models and data published in previous studies on multicomponent slag systems. In addition, the architecture of the application was designed taking into consideration interoperability and data security. The stored data and results generated by the models share a common representation that enables data exchange, comparison, and visualization. Moreover, access to data sets and models is restricted by user authorization to be relevant for the process industry. To further

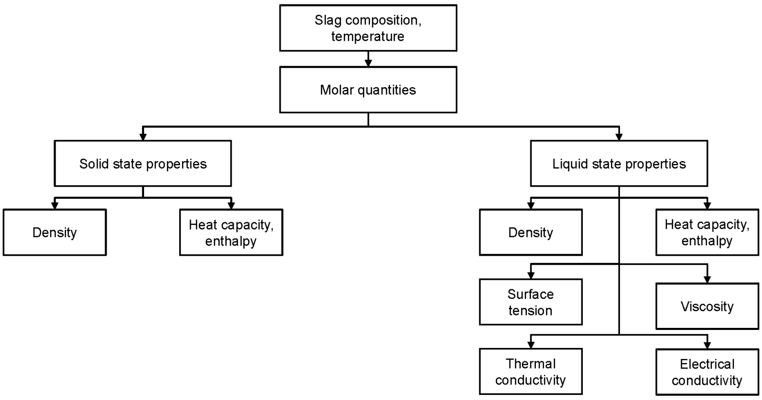

**Figure 10.24:** Schematic of slag properties in the solid and the liquid state. Reprinted from Bublik et al. [153].

increase the modularity, the web-based application relies on micro-services called via a standardized application programming interface (REST API), which allows to facilitate the addition of new models or dashboard presentation in the future.

***Overview of models used for calculation of slag properties***

A schematic describing physical properties of slags for solid and liquid state calculated in the application is shown in Figure 10.24. All applied models are described in detail in previous studies:

- density, heat capacity, surface tension - Mills et al., 2016 [70].
- viscosity - Riboud et al., 1981 [148]; Urbain, 1987 [149]; Iida et al., 2000 [150].
- thermal conductivity - Mills et al., 2011 [71].
- electrical conductivity - Zhang and Chou, 2010 [151]; Zhang et al. 2011 [152].

Density, heat capacity and enthalpy are calculated both for the solid and the liquid state, depending on slag composition and temperature range provided by the user, while surface tension, viscosity, thermal and electrical conductivity are calculated only for the liquid state.

***Density***

The density (in kg/m$^3$) is expressed from partial molar volumes of each component in the slag:

$$\rho_{T,sol} = \frac{M}{V_{T,sol}}, \tag{10.14}$$

$$\rho_{T,liq} = \frac{M}{V_{T,liq}}, \tag{10.15}$$

where $\rho_{T,sol}$ is density of the slag in the solid state, $\rho_{T,liq}$ is density of the slag in the liquid state, $M$ is molecular weight of the slag, $V_{T,sol}$ and $V_{T,liq}$ is partial molar volume of the slag at the specified temperature for the solid and liquid state, respectively.

***Heat capacity and enthalpy***

The calculation for the heat capacity (in J/(mol · K) or J/(kg · K)) and the enthalpy (in J/mol or J/kg) is based on molar heat capacity and molecular weight of the slag:

$$C_{p,sol} = \frac{C_{m,sol} \cdot 1000}{M}, \tag{10.16}$$

$$C_{p,liq} = \frac{C_{m,liq} \cdot 1000}{M}, \tag{10.17}$$

$$\Delta H_{p,sol} = \frac{\Delta H_{m,sol} \cdot 1000}{M}, \tag{10.18}$$

$$\Delta H_{p,liq} = H_{T,liq} - H_{298} = (\Delta H_{m,sol})_{T_m} + \Delta H^{fus} + C_{p,liq}(T_{liq} - T_m), \tag{10.19}$$

where $C_{p,sol}$ is specific heat capacity in the solid state, $C_{p,liq}$ is specific heat capacity in the liquid state, $C_{m,sol}$ is molar heat capacity in the solid state, $C_{m,liq}$ is molar heat capacity in the liquid state, $\Delta H_{p,sol}$ is molar enthalpy in the solid state, $H_{T,liq}$ is the enthalpy at the specified temperature for the liquid state, $\Delta(H_{m,sol})_{T_m}$ is the enthalpy at the liquidus temperature (T$_m$) for the solid state, $\Delta H^{fus}$ is enthalpy of fusion, $\Delta H_{p,liq}$ is specific enthalpy in the liquid state.

***Surface tension***

The surface tension (in mN/m) of the slag in the liquid state is calculated considering the individual contribution of surfactants and bulk components to the surface tension, as well as the temperature dependence of the surface tension:

$$\gamma_{T,liq} = \gamma_{1773} + \frac{d\gamma}{dT}(T_{liq} - 1773), \tag{10.20}$$

$$\gamma_{1773} = \gamma_{bulk,1773} + \gamma_{surf,1773}, \tag{10.21}$$

where $\gamma_{T,liq}$ is the surface tension at the specified temperature for the liquid state, $\gamma_{bulk,1773}$ is the surface tension of bulk components at 1773 K, $\gamma_{surf,1773}$ is the surface tension of surfactants ($B_2O_3$, $K_2O$, $Na_2O$, $CaF_2$) at 1773 K [70], $\gamma_{1773}$ is the surface tension at 1773 K, $\frac{d\gamma}{dT}$ is the temperature dependence of the surface tension.

***Viscosity***

The viscosity of the slag in the liquid state is calculated from Riboud, Urbain and Iida models:

- Riboud model:

  $$\eta = A \cdot T_{liq} \cdot \exp(\frac{B}{T_{liq}}), \tag{10.22}$$

  where $\eta$ is the viscosity, A and B are experimental parameters.
- Urbain model:

  $$\eta = A \cdot T_{liq} \cdot \exp(\frac{10^3 \cdot B}{T_{liq}}), \tag{10.23}$$

- Iida model:

  $$\eta = A \cdot \eta_0 \cdot \exp(\frac{E}{B_i}), \tag{10.24}$$

  where $A$ is the pre-exponential term, $B_i$ is the basicity index, $E$ is the activation energy, $\eta_0$ is the sum of hypothetical viscosity for each component in the slag.

***Thermal conductivity***

The thermal conductivity (in W/(m · K)) can be calculated from three methods, where it can be expressed from the viscosity and/or structural parameters of the slag:

- relation with viscosity:

$$k = \exp(-2.178 + 0.282 \cdot \ln(\eta)), \tag{10.25}$$

  where $k$ is the thermal conductivity of the slag, $\eta$ is the viscosity calculated from Riboud, Urbain or Iida models.

- relation to structure and viscosity:

$$k = \exp(-1.8755 - 0.0893 \ln(\eta) + 0.0352 \ln(\eta)^2), \tag{10.26}$$

$$\eta = 0.165 \exp(\frac{Q}{0.817}), \tag{10.27}$$

$$Q = 4 - NBO/T, \tag{10.28}$$

  where $Q$ and $NBO/T$ are measures of slag polymerization and depolymerization [70], respectively.

- relation to structure:

$$k = \exp(-1.914 + 0.00037 \cdot \exp(\frac{Q}{0.402})). \tag{10.29}$$

***Electrical conductivity***

The electrical conductivity (in $\Omega^{-1} \cdot \mathrm{m}^{-1}$) is calculated from the viscosity or the structure-viscosity relation if the slag contains alkali metal oxides.

- relation with viscosity:

$$\kappa = \exp(\frac{-0.08 - \ln(\eta)}{1.18}), \tag{10.30}$$

  where $\kappa$ is the electrical conductivity of the slag, $\eta$ is the viscosity calculated from Riboud, Urbain or Iida models.

- relation with structure and viscosity for alkali-containing slags:

$$\kappa = \exp(0.15 + 3.87 \cdot r - \frac{\ln(\eta)}{1.1 + 1.77 \cdot r}), \tag{10.31}$$

$$r = \frac{2\sum X_{M^{+}}}{\sum(2X_{M^{+}} + X_{M^{2+}} + 0.667X_{M^{3+}} + 0.5X_{M^{4+}})}. \tag{10.32}$$

# Part V

# Final conclusions and further work

# Chapter 11

# Conclusions

The research work in this PhD thesis was aimed at studying the interfacial interaction and phenomena in ferroalloy-slag systems and evaluating the surface and interfacial tension relevant to these systems. The proposed thesis is of relevance for the ferroalloy industry because the separation of slag and metal is strongly influenced by interfacial phenomena and represents an important problem for the efficiency and sustainability of the ferroalloy production process. It is expected that the results can be practically used in the ferroalloy industry to improve slag-metal separation and will find application in CFD studies of the molten fluid flow in submerged arc furnaces and tapping.

The main key points and conclusions arising from this thesis are summarized below:

1. A novel methodology for assessing the interfacial tension between metal and slag has been developed by combining experiments in the sessile drop furnace and multiphase modelling in OpenFOAM.
2. The developed inverse modelling methodology has several advantages over the sessile drop and X-ray techniques because it completely avoids the need to use X-rays and complex experimental setups. In addition, multiphase simulations in OpenFOAM and further data analysis can be fully automated. However, the presence of solid particles at the surface and chemical reac-

tions can affect results both from the inverse modelling methodology and the sessile drop technique, which may require special consideration for interpretation of experimental results.

3. The surface tension of ferroalloys and slags used in the proposed methodology can be found either experimentally or numerically. The values of surface tension determined in this study by experiments in the sessile drop furnace were 1.50 N/m for FeMn alloy, 1.20 N/m for SiMn alloy, 0.65 N/m for FeMn slag and 0.50 N/m for SiMn slag. In addition, the surface tension of slags of different composition have been assessed by applying the numerical models proposed by Mills et al. [70, 71]. The surface tension of the slags obtained from calculations varied from 0.45 to 0.53 N/m depending on the slag composition.
4. There is a maximum of the extent to which sulfur can change the interfacial tension and the apparent contact angle between ferroalloy and slag. The largest change in the apparent contact angle between SiMn and slag of -6.7° (from 37.8 to 31.1°) is noted when the sulfur content in SiMn increases from 0.02 to 0.25 wt. %. The interfacial tension between FeMn and slag changes in a similar way – the largest change of -0.30 N/m (from 1.26 to 0.96 N/m) is observed when the sulfur content in FeMn increases from 0.03 to 0.31 wt. %. For all sulfur additions to ferroalloys, it is observed that sulfur distributes mainly to the slag after reaching equilibrium and the amount of sulfur remaining in the metal phase is less than 15 %.
5. It has been found that the effect of temperature on the interfacial tension and the apparent contact angle is more noticeable in ferroalloy-slag systems with the sulfur addition, which can be explained by a higher mass transfer rate and a larger interfacial area in such systems.
6. The interfacial tension between FeMn alloy and slag increases when the slag basicity changes from 0.4 to 1.2. It was also found that the addition of $Al_2O_3$ to the slag with basicity of 0.8 and 1.2 increases the interfacial tension, while increasing MnO content from 30.0 to 45.0 wt. % does not

have any statistically significant influence on the interfacial tension.

7. EPMA analysis has revealed an important phenomenon which contributes to the understanding of interfacial tension drop at low slag basicity. $SiO_2$ in the slag is reduced by the saturated carbon from the FeMn alloy at the interface and afterwards Si distributes to the metal phase. The mass transfer of Si across the interface creates the interface instability due to the growing interfacial area between slag and FeMn, leading to the formation of small metals droplets in slag and a metal-slag emulsion.
8. The above-mentioned interfacial phenomena related to the mass transfer of species or elements across the interface is crucial for the separation of metal and slag as it causes a change in the interfacial energy at the metal-slag interface and thus to additional metal losses with slag.

Table 11.1 shows the main results of the publications and how each publication answers the research questions.

**Table 11.1:** Research questions and findings of the thesis.

| № | Question | Paper | Main findings |
|---|---|---|---|
| 1 | How can the interfacial interaction between two molten phases be studied at the laboratory scale? | Paper I | Interfacial interaction between FeMn and FeMn slag can be studied using the sessile drop technique. It is possible to measure both contact angle and interfacial tension at high temperatures. In addition, the microstructure of metal and slag phases can be studied by EPMA. |
| 2 | How can Computational Fluid Dynamics (CFD) facilitate the determination of interfacial tension? | Paper II | OpenFOAM can be applied for investigating multiphase flow between two molten materials (FeMn-slag). The developed methodology also allows determining values of interfacial tension between slag and metal at different operational conditions. |
| | | Paper III | The paper discusses modelling strategies and suggests that molten flow and slag-metal separation can be investigated by applying physical and numericals models, as well as CFD methods. |
| 3 | How does the interfacial interaction change depending on the sulfur concentration, slag composition and experimental conditions? | Paper IV | The influence of sulfur and operational parameters on interfacial tension and contact angle has been studied in the sessile drop furnace. Sulfur and temperature have a significant influence on both interfacial tension and apparent contact angle, decreasing both values and promoting the formation of a metal-slag mixture. Holding time does not affect interfacial interaction after reaching equilibrium between ferroalloy and slag. |
| | | Paper V | The influence of slag composition on interfacial tension has been studied in the sessile drop furnace. Interfacial tension between FeMn alloy and slag increases with slag basicity. $Al_2O_3$ addition to slag increases interfacial tension, while MnO content from 30 to 45 wt. % does not have any statistically significant influence. |
| 4 | How does the interfacial tension affect metal losses with slag? | Paper II, IV, V, VI | Lower values of interfacial tension lead to higher metal losses with slag. Elements changing interfacial energy at the interface result in formation of metal-slag emulsion due to interfacial instability, and therefore additional losses of metal with slag. |
| 5 | What are the main properties of the slag affecting the interfacial interaction and how can the be estimated? | Paper VII | Density, surface tension and viscosity are the most important properties of slag which affect slag-metal separation. These slag properties can be modelled numerically. |

# Chapter 12

# Topics for future research

The proposed methodology allows to determine the interfacial tension between metal and slag and investigate interfacial phenomena in these systems. However, the methodology can be further refined to improve the reproducibility of results, as well as for its application to metal-slag systems outside of ferroalloy production. Given below are some suggestions for improving this methodology:

1. Solid carbon particles observed around the surface of the ferroalloys and the slags, therefore, the improvement of the materials preparation methodology might be necessary to reduce the influence of surface roughness on experimental results. A possible solution to this problem could be the use of crucibles made of materials other than graphite or the use of more pure reagents for material preparation.
2. A study of substrates and cups used in the sessile drop furnace made of different materials can also expand the range of systems in which interfacial tension or surface tension can be determined, as this will allow more flexibility in controlling wettability in a desired system.
3. Further experiments, using a broader range of MnO content in the slag, could provide more data on the effect of MnO influence on the interfacial tension between slag and metal, which might be crucial for the ferroalloy industry.

4. Study the effect of oxygen on the surface tension of ferroalloys.
5. The modelling framework for multiphase simulations in OpenFOAM can be further extended from 2D to 3D geometry, which will improve the sensitivity of simulation results and provide more comprehensive sight on the interfacial interaction between metal and slag.
6. The proposed values of the interfacial and surface tension can be directly applied in CFD modelling of tapping into ladles to improve the slag-metal separation.
7. Further development of the inverse modelling methodology to determine the interfacial tension between metal and slag droplets, which will also allow obtaining interfacial tension in SiMn-slag systems.

# Bibliography

[1] S. E. Olsen, M. Tangstad and T. Lindstad, *Production of Manganese Ferroalloys*. Tapir Academic Press, 2007, 256 pp., ISBN: 978-82-519-2191-6.

[2] S. Bublik, J. E. Olsen, V. Loomba, Q. G. Reynolds and K. E. Einarsrud, 'A Review of Ferroalloy Tapping Models,' *Metall Mater Trans B*, vol. 52, no. 4, pp. 2038–2047, 1st Aug. 2021, ISSN: 1543-1916. DOI: `10.1007/s11663-021-02134-5`.

[3] S. Bublik and K. E. Einarsrud, 'Inverse modelling of interfacial tension between ferroalloy and slag using OpenFOAM,' in *14th International Conference on CFD in Oil & Gas, Metallurgical and Process Industries*, Trondheim, Norway: SINTEF Academic Press, 2020, pp. 28–38, ISBN: 978-82-536-1684-1. [Online]. Available: `https://sintef.brage.unit.no/sintef-xmlui/handle/11250/2720839` (visited on 15/01/2021).

[4] M. Tangstad, M. Ksiazek, J. E. Olsen, Q. Reynolds and E. Ringdalen, 'Controlled Tapping—The Research Project,' in *Furnace Tapping 2022*, J. D. Steenkamp, D. Gregurek, Q. G. Reynolds, G. Alvear Flores, H. Joubert and P. J. Mackey, Eds., ser. The Minerals, Metals & Materials Series, Cham: Springer International Publishing, 2022, pp. 3–14, ISBN: 978-3-030-92544-4. DOI: `hnn6`.

[5] K.-i. Ohno, S. Natsui, S. Sukenaga, K. Tonya, T. Maeda and K. Kunitomo, 'Numerical Approach to Comprehend for Effect of Melts Physical Proper-

ties on Iron-slag Separation Behaviour in Self-reducing Pellet,' *ISIJ International*, vol. 60, no. 12, pp. 2695–2704, 2020. DOI: `hnn5`.

[6] K. Mukai, T. Matsushita and S. Seetharaman, 'Motion of fine particles in liquid caused by interfacial tension gradient in relation to metals separation technologies,' *Scandinavian Journal of Metallurgy*, vol. 34, no. 2, pp. 137–142, 2005, ISSN: 1600-0692. DOI: `10.1111/j.1600-0692.2005.00729.x`. [Online]. Available: `https://onlinelibrary.wiley.com/doi/abs/10.1111/j.1600-0692.2005.00729.x` (visited on 06/02/2022).

[7] P. K. Iwamasa and R. J. Fruehan, 'Separation of Metal Droplets from Slag,' *ISIJ International*, vol. 36, no. 11, pp. 1319–1327, 1996. DOI: `10.2355/isijinternational.36.1319`.

[8] Q. G. Reynolds and J. E. Olsen, 'Modelling of Metal Loss in Ferromanganese Furnace Tapping Operations,' in *Materials Processing Fundamentals 2021*, J. Lee, S. Wagstaff, A. Anderson, F. Tesfaye, G. Lambotte and A. Allanore, Eds., ser. The Minerals, Metals & Materials Series, Cham: Springer International Publishing, 2021, pp. 83–92, ISBN: 978-3-030-65253-1. DOI: `10.1007/978-3-030-65253-1_7`.

[9] E. de WILDE, I. Bellemans, M. Campforts, M. Guo, B. Blanpain, N. Moelans and K. Verbeken, 'Sessile drop evaluation of high temperature copper-/spinel and slag/spinel interactions,' *Transactions of Nonferrous Metals Society of China*, vol. 26, no. 10, pp. 2770–2783, 1st Oct. 2016, ISSN: 1003-6326. DOI: `hnn7`.

[10] T. Matsushita, I. Belov, D. Siafakas, A. E. W. Jarfors and M. Watanabe, 'Interfacial phenomena between molten iron and molten slag–Effect of nitrogen on the Marangoni convection,' *J Mater Sci*, vol. 56, no. 13, pp. 7811–7822, May 2021, ISSN: 0022-2461, 1573-4803. DOI: `10.1007/s10853-020-05730-z`. [Online]. Available: `http://link.springer.com/10.1007/s10853-020-05730-z` (visited on 03/01/2022).

[11] Q. Wang, Y. Liu, F. Wang, Y. Cao and G. Li, 'Study on Sulfur Transfer Behavior during Refining of Rejected Electrolytic Manganese Metal,' *Metals*, vol. 9, no. 7, p. 751, Jul. 2019. DOI: `10.3390/met9070751`. [Online]. Available: `https://www.mdpi.com/2075-4701/9/7/751` (visited on 29/11/2019).

[12] J. Strandh, K. Nakajima, R. Eriksson and P. Jönsson, 'A Mathematical Model to Study Liquid Inclusion Behavior at the Steel-Slag Interface,' *ISIJ International*, vol. 45, no. 12, pp. 1838–1847, 2005. DOI: `10.2355/isijinternational.45.1838`.

[13] I. Bellemans, E. De Wilde, N. Moelans and K. Verbeken, 'Metal losses in pyrometallurgical operations - A review,' *Advances in Colloid and Interface Science*, Multiscale Applications of Surface Tension and Capillary Forces, vol. 255, pp. 47–63, 1st May 2018, ISSN: 0001-8686. DOI: `10.1016/j.cis.2017.08.001`. [Online]. Available: `https://www.sciencedirect.com/science/article/pii/S0001868616303001` (visited on 10/09/2021).

[14] X. Zhang, S. Pirker and M. Saeedipour, 'Numerical investigation of particle motion at the steel—slag interface in continuous casting using VOF method and dynamic overset grids,' *Exp. Comput. Multiph. Flow*, 14th Jan. 2022, ISSN: 2661-8869, 2661-8877. DOI: `10.1007/s42757-021-0130-6`. [Online]. Available: `https://link.springer.com/10.1007/s42757-021-0130-6` (visited on 27/01/2022).

[15] R. Clift, J. R. Grace and M. E. Weber, *Bubbles, Drops, and Particles*. Academic Press, 1978.

[16] J. R. Grace, T. Wairegi and J. Brophy, 'Break-up of drops and bubbles in stagnant media,' *Can. J. Chem. Eng.*, vol. 56, no. 1, pp. 3–8, Feb. 1978, ISSN: 00084034, 1939019X. DOI: `10.1002/cjce.5450560101`. [Online]. Available: `https://onlinelibrary.wiley.com/doi/10.1002/cjce.5450560101` (visited on 27/03/2022).

[17] J. Steenkamp and P. Pistorius, ‘Tap-hole wear: Analysis of daily average slag and metal compositions of a single SiMn smelter,’ 31st May 2015.

[18] R. Sripriya and C. V. G. K. Murty, ‘Recovery of metal from slag/mixed metal generated in ferroalloy plants—a case study,’ *International Journal of Mineral Processing*, vol. 75, no. 1, pp. 123–134, 6th Jan. 2005, ISSN: 0301-7516. DOI: `10.1016/j.minpro.2004.08.013`. [Online]. Available: `https://www.sciencedirect.com/science/article/pii/S0301751604000821` (visited on 02/07/2022).

[19] S.-C. Park, H. Gaye and H.-G. Lee, ‘Interfacial tension between molten iron and CaO–$SiO_2$–MgO–$Al_2O_3$–FeO slag system,’ *Ironmaking Steelmaking*, vol. 36, pp. 3–11, 1st Jan. 2009. DOI: `10.1179/174328108X358622`.

[20] E.-J. Jung, W. Kim, I. Sohn and D.-J. Min, ‘A study on the interfacial tension between solid iron and CaO–$SiO_2$–MO system,’ *J. Mater. Sci.*, vol. 45, no. 8, pp. 2023–2029, 1st Apr. 2010, ISSN: 1573-4803. DOI: `10.1007/s10853-009-3946-1`. [Online]. Available: `https://doi.org/10.1007/s10853-009-3946-1` (visited on 08/11/2018).

[21] H. Sun, K. Nakashima and K. Mori, ‘Interfacial Tension between Molten Iron and CaO-$SiO_2$ Based Fluxes*,’ *ISIJ Int.*, vol. 37, no. 4, pp. 323–331, 1997. DOI: `10.2355/isijinternational.37.323`.

[22] L. Muhmood, N. N. Viswanathan and S. Seetharaman, ‘Some Investigations into the Dynamic Mass Transfer at the Slag–Metal Interface Using Sulfur: Concept of Interfacial Velocity,’ *Metall. Mater. Trans. B*, vol. 42, no. 3, pp. 460–470, 1st Jun. 2011, ISSN: 1543-1916. DOI: `10.1007/s11663-011-9482-9`. [Online]. Available: `https://doi.org/10.1007/s11663-011-9482-9` (visited on 09/10/2019).

[23] R. Hagemann, H.-P. Heller, S. Lachmann, S. Seetharaman and P. R. Scheller, ‘Slag entrainment in continuous casting and effect of interfacial tension,’ *Ironmaking & Steelmaking*, vol. 39, no. 7, pp. 508–513, 1st Oct. 2012,

ISSN: 0301-9233. DOI: `10.1179/1743281212Y.0000000018`. [Online]. Available: `https://doi.org/10.1179/1743281212Y.0000000018` (visited on 26/01/2022).

[24] M. A. Rhamdhani, G. A. Brooks and S. A. Nightingale, 'Characterisation of interfacial phenomena in metal-slag reactions,' p. 11,

[25] P. V. Riboud and L. D. Lucas, 'Influence of Mass Transfer Upon Surface Phenomena in Iron and Steelmaking,' *Canadian Metallurgical Quarterly*, vol. 20, no. 2, pp. 199–208, 1st Apr. 1981, ISSN: 0008-4433. DOI: `10.1179/cmq.1981.20.2.199`. [Online]. Available: `https://doi.org/10.1179/cmq.1981.20.2.199` (visited on 04/01/2022).

[26] P. Ni, T. Tanaka, M. Suzuki, M. Nakamoto and P. G. Jönsson, 'A Kinetic Model on Oxygen Transfer at a Steel/Slag Interface under Effect of Interfacial Tension,' *ISIJ Int.*, vol. 58, no. 11, pp. 1979–1988, 2018. DOI: `10.2355/isijinternational.ISIJINT-2018-303`.

[27] J. Vermaak, C. Mays and D. Kuhlmann-Wilsdorf, 'On surface stress and surface tension,' *Surface Science*, vol. 12, no. 2, pp. 128–133, Oct. 1968, ISSN: 00396028. DOI: `10.1016/0039-6028(68)90118-0`. [Online]. Available: `https://linkinghub.elsevier.com/retrieve/pii/0039602868901180` (visited on 05/01/2022).

[28] F. M. Borodich, 'The Hertz-Type and Adhesive Contact Problems for Depth-Sensing Indentation,' in *Advances in Applied Mechanics*, vol. 47, Elsevier, 2014, pp. 225–366, ISBN: 978-0-12-800130-1. DOI: `hnn8`.

[29] S. Banerjee, 'Simple derivation of Young, Wenzel and Cassie-Baxter equations and its interpretations,' 11th Aug. 2008. arXiv: `0808.1460 [cond-mat]`. [Online]. Available: `http://arxiv.org/abs/0808.1460` (visited on 05/01/2022).

[30] C.-Y. Hui and A. Jagota, 'Surface Tension, Surface Energy, and Chemical Potential Due to Their Difference,' *Langmuir*, vol. 29, no. 36, pp. 11 310–

11 316, 10th Sep. 2013, ISSN: 0743-7463. DOI: `10.1021/la400937r`. [Online]. Available: `https://doi.org/10.1021/la400937r` (visited on 05/01/2022).

[31] A. Jakobsson, M. Nasu, J. Mangwiru, K. C. Mills and S. Seetharaman, 'Interfacial tension effects on slag—metal reactions,' *Philosophical Transactions of the Royal Society of London. Series A: Mathematical, Physical and Engineering Sciences*, vol. 356, no. 1739, E. D. Hondros, M. McLean and K. C. Mills, Eds., pp. 995–1001, 15th Apr. 1998, ISSN: 1471-2962. DOI: `bxksmj`. [Online]. Available: `http://www.royalsocietypublishing.org/doi/10.1098/rsta.1998.0203` (visited on 15/04/2019).

[32] A. Jakobsson, D. Sichen, S. Seetharaman and N. N. Viswanathan, 'Interfacial phenomena in some slag-metal reactions,' *Metall. Mater. Trans. B*, vol. 31, no. 5, pp. 973–980, 1st Oct. 2000, ISSN: 1543-1916. DOI: `10.1007/s11663-000-0073-4`. [Online]. Available: `https://doi.org/10.1007/s11663-000-0073-4` (visited on 03/12/2020).

[33] S. Bublik, M. Tangstad and K. E. Einarsrud, 'Interfacial Behaviour in Ferroalloys: The Influence of FeMn Slag Composition,' *Metall Mater Trans B*, 19th Aug. 2022, ISSN: 1073-5615, 1543-1916. DOI: `10.1007/s11663-022-02605-3`. [Online]. Available: `https://link.springer.com/10.1007/s11663-022-02605-3` (visited on 12/09/2022).

[34] P. Kozakevitch, G. Urbain and M. Sage, 'Sur la tension interfaciale fonte/laitier et le mécanisme de désulfuration,' *Rev. Met. Paris*, vol. 52, no. 2, pp. 161–172, Feb. 1955, ISSN: 0035-1563, 1156-3141. DOI: `10.1051/metal/195552020161`. [Online]. Available: `http://www.metallurgical-research.org/10.1051/metal/195552020161` (visited on 04/01/2022).

[35] H. Ooi, T. Nozaki and H. Yoshii, 'The Effect of Chemical Reactions on the Interfacial Tension between Iron and CaO-$SiO_2$-$Al_2O_3$ Slag,' *Trans. Iron Steel Inst. Jpn.*, vol. 14, no. 1, pp. 9–16, 1974, ISSN: 0021-1583, 1881-1183. DOI: `10.2355/isijinternational1966.14.9`. [Online]. Available:

`https://www.jstage.jst.go.jp/article/isijinternational1966/14/1/14_9/_article` (visited on 21/12/2020).

[36] D. J. Kim and J. H. Park, ‘Interfacial Reaction Between CaO-SiO2-MgO-Al2O3 Flux and Fe-xMn-yAl (x = 10 and 20 mass pct, y = 1, 3, and 6 mass pct) Steel at 1873 K (1600 °C),’ *Metall and Materi Trans B*, vol. 43, no. 4, pp. 875–886, Aug. 2012, ISSN: 1073-5615, 1543-1916. DOI: `10.1007/s11663-012-9667-x`. [Online]. Available: `http://link.springer.com/10.1007/s11663-012-9667-x` (visited on 27/01/2022).

[37] P. Ni, T. Tanaka, M. Suzuki, M. Nakamoto and P. G. Jönsson, ‘A Kinetic Model of Mass Transfer and Chemical Reactions at a Steel/Slag Interface under Effect of Interfacial Tensions,’ *ISIJ Int.*, vol. 59, no. 5, pp. 737–748, 2019. DOI: `10.2355/isijinternational.ISIJINT-2018-496`.

[38] M. A. Rhamdhani, K. S. Coley and G. A. Brooks, ‘Analysis of the source of dynamic interfacial phenomena during reaction between metal droplets and slag,’ *Metall and Materi Trans B*, vol. 36, no. 5, pp. 591–604, Oct. 2005, ISSN: 1073-5615, 1543-1916. DOI: `10.1007/s11663-005-0050-z`. [Online]. Available: `http://link.springer.com/10.1007/s11663-005-0050-z` (visited on 06/01/2022).

[39] Y. Chung and A. W. Cramb, ‘Dynamic and equilibrium interfacial phenomena in liquid steel-slag systems,’ *Metall. Mater. Trans. B*, vol. 31, no. 5, pp. 957–971, 1st Oct. 2000, ISSN: 1543-1916. DOI: `10.1007/s11663-000-0072-5`. [Online]. Available: `https://doi.org/10.1007/s11663-000-0072-5` (visited on 05/08/2021).

[40] P. R. Scheller, J. Lee and T. Tanaka, ‘Chapter 1.8 - Stability of Interface Between Liquid Steel and Molten Slag,’ in *Treatise on Process Metallurgy*, S. Seetharaman, Ed., Boston: Elsevier, 1st Jan. 2014, pp. 111–118, ISBN: 978-0-08-096984-8. DOI: `10.1016/B978-0-08-096984-8.00021-5`. [Online]. Available: `https://www.sciencedirect.com/science/article/pii/B9780080969848000215` (visited on 04/06/2021).

[41] E. S. R. Gopal, 'Principles of emulsion formation,' in Academic Press, London, 1968, pp. 1–75.

[42] K. Krishnapisharody and G. A. Irons, 'The Fluid Mechanics of Slag-Metal Interactions in Ladle Metallurgy,' *Journal for Manufacturing Science and Production*, vol. 12, no. 3-4, pp. 139–146, 14th Dec. 2012, ISSN: 2191-0375. DOI: `10.1515/jmsp-2012-0016`. [Online]. Available: `https://www.degruyter.com/document/doi/10.1515/jmsp-2012-0016/html` (visited on 04/01/2022).

[43] S. Chandrasekhar, *Hydrodynamic and Hydromagnetic Stability*. New York: Dover Publications, 1981, ISBN: 978-0-486-64071-6.

[44] L. Zhang, Y. Li, Q. Wang and C. Yan, 'Prediction model for steel/slag interfacial instability in continuous casting process,' *Ironmaking & Steelmaking*, vol. 42, no. 9, pp. 705–713, 21st Oct. 2015, ISSN: 0301-9233, 1743-2812. DOI: `10.1179/1743281215Y.0000000023`. [Online]. Available: `http://www.tandfonline.com/doi/full/10.1179/1743281215Y.0000000023` (visited on 04/01/2022).

[45] R. Fatehi, M. S. Shadloo and M. T. Manzari, 'Numerical investigation of two-phase secondary Kelvin–Helmholtz instability,' *Proceedings of the Institution of Mechanical Engineers, Part C: Journal of Mechanical Engineering Science*, vol. 228, no. 11, pp. 1913–1924, Aug. 2014, ISSN: 0954-4062, 2041-2983. DOI: `10.1177/0954406213512630`. [Online]. Available: `http://journals.sagepub.com/doi/10.1177/0954406213512630` (visited on 28/03/2022).

[46] G. Irons, A. Senguttuvan and K. Krishnapisharody, 'Recent Advances in the Fluid Dynamics of Ladle Metallurgy,' *ISIJ Int.*, vol. 55, no. 1, pp. 1–6, 15th Jan. 2015, ISSN: 0915-1559, 1347-5460. DOI: `hnpb`.

[47] S. Seetharaman, *Fundamentals of Metallurgy*. Elsevier, 10th Oct. 2005, 589 pp., ISBN: 978-1-84569-094-6. Google Books: `5wikAgAAQBAJ`.

[48] G. S. Bainbridge and H. Sawistowski, 'Surface tension effects in sieve plate distillation columns,' *Chemical Engineering Science*, vol. 19, no. 12, pp. 992–993, 1st Dec. 1964, ISSN: 0009-2509. DOI: `fprq35`. [Online]. Available: `https://www.sciencedirect.com/science/article/pii/0009250964851083` (visited on 02/01/2022).

[49] J. Lee, L. Thu Hoai and M. Shin, 'Density and Surface Tension of Liquid Fe-Mn Alloys,' *Metall. Mater. Trans. B*, vol. 42, no. 3, pp. 546–549, Jun. 2011, ISSN: 1073-5615, 1543-1916. DOI: `10.1007/s11663-011-9490-9`. [Online]. Available: `http://link.springer.com/10.1007/s11663-011-9490-9` (visited on 13/11/2019).

[50] K. Mukai, T. Matsushita, K. C. Mills, S. Seetharaman and T. Furuzono, 'Surface Tension of Liquid Alloys—A Thermodynamic Approach,' *Metall. Mater. Trans. B*, vol. 39, no. 4, pp. 561–569, Aug. 2008, ISSN: 1073-5615, 1543-1916. DOI: `10.1007/s11663-008-9164-4`. [Online]. Available: `http://link.springer.com/10.1007/s11663-008-9164-4` (visited on 21/12/2020).

[51] J. Lee and K. Morita, 'Effect of carbon and sulphur on the surface tension of molten iron,' *Steel Res.*, vol. 73, no. 9, pp. 367–372, Sep. 2002, ISSN: 01774832. DOI: `10.1002/srin.200200001`. [Online]. Available: `http://doi.wiley.com/10.1002/srin.200200001` (visited on 04/12/2020).

[52] Y. Su, K. C. Mills and A. Dinsdale, 'A model to calculate surface tension of commercial alloys,' *J Mater Sci*, vol. 40, no. 9-10, pp. 2185–2190, May 2005, ISSN: 0022-2461, 1573-4803. DOI: `10.1007/s10853-005-1930-y`. [Online]. Available: `http://link.springer.com/10.1007/s10853-005-1930-y` (visited on 06/02/2022).

[53] K. Morohoshi, M. Uchikoshi, M. Isshiki and H. Fukuyama, 'Effects of Carbon and Oxygen on Fe–C–O Melt Surface Tension,' *ISIJ Int.*, vol. 53, no. 8, pp. 1315–1319, 2013, ISSN: 0915-1559, 1347-5460. DOI: `f476vz`.

[54] B. J. Keene, 'Review of data for the surface tension of iron and its binary alloys,' *Int. Mater. Rev.*, vol. 33, no. 1, pp. 1–37, Jan. 1988, ISSN: 0950-6608, 1743-2804. DOI: `10.1179/imr.1988.33.1.1`. [Online]. Available: `http://www.tandfonline.com/doi/full/10.1179/imr.1988.33.1.1` (visited on 07/12/2020).

[55] R. Zhang, Y. Meng, Z. Wang, S. Jiao, J. Jia, Y. Min and C. Liu, 'Surface Tension Prediction of Multicomponent Slags of the CaO-SiO2-All2O3-FeO-Fe2O3 System Based on Microstructure Analysis,' *Metall Mater Trans B*, vol. 53, no. 1, pp. 571–583, Feb. 2022, ISSN: 1073-5615, 1543-1916. DOI: `10.1007/s11663-021-02394-1`. [Online]. Available: `https://link.springer.com/10.1007/s11663-021-02394-1` (visited on 26/03/2022).

[56] J. Xin, N. Wang, M. Chen and L. Gan, 'Surface Tension Calculation of Molten Slag in SiO2–Al2O3–CaO–MgO Systems Based on a Statistical Modelling Approach,' *ISIJ Int.*, vol. 59, pp. 759–767, 15th May 2019. DOI: `10.2355/isijinternational.ISIJINT-2018-746`.

[57] M. Hanao, T. Tanaka, M. Kawamoto and K. Takatani, 'Evaluation of Surface Tension of Molten Slag in Multicomponent Systems,' *ISIJ Int.*, vol. 47, pp. 935–939, 1st Jan. 2007. DOI: `10.2355/isijinternational.47.935`.

[58] M. Nakamoto, A. Kiyose, T. Tanaka, L. Holappa and M. Hämäläinen, 'Evaluation of the Surface Tension of Ternary Silicate Melts Containing Al2O3, CaO, FeO, MgO or MnO,' *ISIJ Int.*, vol. 47, no. 1, pp. 38–43, 2007, ISSN: 0915-1559, 1347-5460. DOI: `10.2355/isijinternational.47.38`.

[59] M. A. Duchesne and R. W. Hughes, 'Slag density and surface tension measurements by the constrained sessile drop method,' *Fuel*, vol. 188, pp. 173–181, 15th Jan. 2017, ISSN: 0016-2361. DOI: `10.1016/j.fuel.2016.10.023`. [Online]. Available: `http://www.sciencedirect.com/science/article/pii/S0016236116309711` (visited on 28/01/2021).

[60] M. Wegener, L. Muhmood, S. Sun and A. V. Deev, 'Surface Tension Measurements of Calcia-Alumina Slags: A Comparison of Dynamic Methods,' *Metall and Materi Trans B*, vol. 46, no. 1, pp. 316–327, 1st Feb. 2015, ISSN: 1543-1916. DOI: `10.1007/s11663-014-0174-0`. [Online]. Available: `https://doi.org/10.1007/s11663-014-0174-0` (visited on 25/03/2019).

[61] K. Nakashima and K. Mori, 'Interfacial Properties of Liquid Iron Alloys and Liquid Slags Relating to Iron- and Steel-making Processes,' *ISIJ Int.*, vol. 32, no. 1, pp. 11–18, 1992. DOI: `10.2355/isijinternational.32.11`.

[62] K. C. Mills and B. J. Keene, 'Physical properties of BOS slags,' *Int. Mater. Rev.*, vol. 32, no. 1, pp. 1–120, 1st Jan. 1987, ISSN: 0950-6608. DOI: `10.1179/095066087790150296`. [Online]. Available: `https://doi.org/10.1179/095066087790150296` (visited on 28/01/2021).

[63] H. Gaye, L. D. Lucas, M. Olette and P. V. Riboud, 'Metal-Slag Interfacial Properties: Equilibrium Values and "Dynamic" Phenomena,' *Canadian Metallurgical Quarterly*, vol. 23, no. 2, pp. 179–191, Apr. 1984, ISSN: 0008-4433, 1879-1395. DOI: `10.1179/cmq.1984.23.2.179`. [Online]. Available: `http://www.tandfonline.com/doi/full/10.1179/cmq.1984.23.2.179` (visited on 15/04/2019).

[64] H. Sun, K. Nakashima and K. Mori, 'Influence of Slag Composition on Slag–Iron Interfacial Tension,' *ISIJ Int.*, vol. 46, no. 3, pp. 407–412, 2006, ISSN: 0915-1559, 1347-5460. DOI: `10.2355/isijinternational.46.407`. [Online]. Available: `http://joi.jlc.jst.go.jp/JST.JSTAGE/isijinternational/46.407?from=CrossRef` (visited on 28/05/2020).

[65] T. Tanaka, H. Goto, M. Nakamoto, M. Suzuki, M. Hanao, M. Zeze, H. Yamamura and T. Yoshikawa, 'Dynamic Changes in Interfacial Tension between Liquid Fe Alloy and Molten Slag Induced by Chemical Reactions,' *ISIJ Int.*, vol. 56, no. 6, pp. 944–952, 2016, ISSN: 0915-1559, 1347-5460.

DOI: `10.2355/isijinternational.ISIJINT-2015-654`. [Online]. Available: `https://www.jstage.jst.go.jp/article/isijinternational/56/6/56_ISIJINT-2015-654/_article` (visited on 20/03/2019).

[66] S. Bublik, S. Bao, M. Tangstad and K. E. Einarsrud, 'Slag-metal interactions in the FeMn tapping process: Interfacial properties and wetting,' in *Proceedings of the Liquid Metal Processing & Casting Conference 2019*, Birmingham, UK, 2019, pp. 375–384.

[67] S. Bublik, S. Bao, M. Tangstad and K. E. Einarsrud, 'Interfacial Behaviour in Ferroalloys: The Influence of Sulfur in FeMn and SiMn Systems,' *Metall Mater Trans B*, vol. 52, no. 6, pp. 3624–3645, 1st Dec. 2021, ISSN: 1543-1916. DOI: `10.1007/s11663-021-02323-2`. [Online]. Available: `https://doi.org/10.1007/s11663-021-02323-2` (visited on 06/02/2022).

[68] M. Tangstad, 'Chapter 7 - Manganese Ferroalloys Technology,' in *Handbook of Ferroalloys*, Oxford: Butterworth-Heinemann, 2013, ISBN: 978-0-12-805500-7. Google Books: `HDLPCwAAQBAJ`.

[69] S. Bao, K. Tang, A. Kvithyld, M. Tangstad and T. A. Engh, 'Wettability of Aluminum on Alumina,' *Metall. Mater. Trans. B*, vol. 42, no. 6, pp. 1358–1366, 1st Dec. 2011, ISSN: 1543-1916. DOI: `10.1007/s11663-011-9544-z`. [Online]. Available: `https://doi.org/10.1007/s11663-011-9544-z` (visited on 25/03/2019).

[70] K. C. Mills, S. Karagadde, P. D. Lee, L. Yuan and F. Shahbazian, 'Calculation of Physical Properties for Use in Models of Continuous Casting Process-Part 1: Mould Slags,' *ISIJ Int.*, vol. 56, no. 2, pp. 264–273, 2016, ISSN: 0915-1559, 1347-5460. DOI: `10.2355/isijinternational.ISIJINT-2015-364`. [Online]. Available: `https://www.jstage.jst.go.jp/article/isijinternational/56/2/56_ISIJINT-2015-364/_article` (visited on 28/01/2021).

[71] K. C. Mills, Y. Lang and R. T. Jones, 'Estimating the physical properties of slags,' *J. South. Afr. Inst. Min. Metall.*, vol. 111, pp. 649–658, 2011.

[72] K. C. Mills, 'Estimation of Physicochemical Properties of Coal Slags and Ashes,' in *Mineral Matter and Ash in Coal*, ser. ACS Symposium Series 301, vol. 301, 0 vols., American Chemical Society, 2nd Apr. 1986, pp. 195–214, ISBN: 978-0-8412-0959-6. DOI: `10.1021/bk-1986-0301.ch015`. [Online]. Available: `https://doi.org/10.1021/bk-1986-0301.ch015` (visited on 17/01/2022).

[73] E. Hernández-Baltazar and J. Gracia-Fadrique, 'Elliptic solution to the Young–Laplace differential equation,' *J. Colloid Interface Sci.*, vol. 287, no. 1, pp. 213–216, 1st Jul. 2005, ISSN: 0021-9797. DOI: `10.1016/j.jcis.2005.01.102`. [Online]. Available: `http://www.sciencedirect.com/science/article/pii/S0021979705001128` (visited on 04/12/2020).

[74] *MATLAB version 9.8 (R2020a)*, Manual, Natick, Massachusetts, 2020. [Online]. Available: `https://www.mathworks.com`.

[75] C. A. Schneider, W. S. Rasband and K. W. Eliceiri, 'NIH Image to ImageJ: 25 years of image analysis,' *Nat. Methods*, vol. 9, pp. 671–675, 28th Jun. 2012, ISSN: 1548-7105. DOI: `10.1038/nmeth.2089`. [Online]. Available: `https://www.nature.com/articles/nmeth.2089` (visited on 25/03/2019).

[76] A. F. Stalder, T. Melchior, M. Müller, D. Sage, T. Blu and M. Unser, 'Low-bond axisymmetric drop shape analysis for surface tension and contact angle measurements of sessile drops,' *Colloids Surf., A*, vol. 364, no. 1-3, pp. 72–81, Jul. 2010, ISSN: 09277757. DOI: `10.1016/j.colsurfa.2010.04.040`. [Online]. Available: `https://linkinghub.elsevier.com/retrieve/pii/S0927775710002761` (visited on 16/04/2019).

[77] J. Muller, J. H. Zietsman and P. C. Pistorius, 'Modeling of Manganese Ferroalloy Slag Properties and Flow During Tapping,' *Metall. Mater. Trans. B*,

vol. 46, no. 6, pp. 2639–2651, Dec. 2015, ISSN: 1073-5615, 1543-1916. DOI: `10.1007/s11663-015-0426-7`. [Online]. Available: `http://link.springer.com/10.1007/s11663-015-0426-7` (visited on 27/03/2019).

[78] C. W. Bale, E. Bélisle, P. Chartrand, S. A. Decterov, G. Eriksson, A. E. Gheribi, K. Hack, I. .-. Jung, Y. .-. Kang, J. Melançon, A. D. Pelton, S. Petersen, C. Robelin, J. Sangster, P. Spencer and M.-A. Van Ende, 'FactSage thermochemical software and databases, 2010–2016,' *CALPHAD: Comput. Coupling Phase Diagrams Thermochem.*, vol. 54, pp. 35–53, 1st Sep. 2016, ISSN: 0364-5916. DOI: `10.1016/j.calphad.2016.05.002`. [Online]. Available: `http://www.sciencedirect.com/science/article/pii/S0364591616300694` (visited on 04/01/2021).

[79] E. Calvo, E. De Malmazet, F. Risso and O. Masbernat, 'Coalescence of Water Drops at an Oil–Water Interface Loaded with Microparticles and Surfactants,' *Industrial and engineering chemistry research*, vol. 58, no. 34, pp. 15 573–15 587, Aug. 2019. DOI: `10.1021/acs.iecr.9b02524`. [Online]. Available: `https://hal.archives-ouvertes.fr/hal-02342106` (visited on 23/01/2022).

[80] M. E. Ferreira, P. C. Pistorius and R. J. Fruehan, 'Liquid Inclusion Distortion by Lens Shape Effect: In Situ Observation and Quantification on LCAK Steels Using HT-CSLM,' *Metall Mater Trans B*, vol. 50, no. 6, pp. 2498–2501, Dec. 2019, ISSN: 1073-5615, 1543-1916. DOI: `10.1007/s11663-019-01673-2`. [Online]. Available: `http://link.springer.com/10.1007/s11663-019-01673-2` (visited on 27/01/2022).

[81] D. C. Montgomery, *Design and Analysis of Experiments*, Eighth edition. Hoboken, NJ: John Wiley & Sons, Inc, 2013, 730 pp., ISBN: 978-1-118-14692-7.

[82] H. G. Weller, G. Tabor, H. Jasak and C. Fureby, 'A tensorial approach to computational continuum mechanics using object-oriented techniques,'

*Comput. Phys.*, vol. 12, no. 6, pp. 620–631, 1st Nov. 1998, ISSN: 0894-1866. DOI: `10.1063/1.168744`.

[83] *Programmer's Guide. Version v2112.* 20th Dec. 2021. [Online]. Available: `https://jztkft.dl.sourceforge.net/project/openfoam/v2112/ProgrammersGuide.pdf`.

[84] 'OpenFOAM: User Guide: OpenFOAM®: Open source CFD : Documentation.' (), [Online]. Available: `https://www.openfoam.com/documentation/guides/latest/doc/` (visited on 07/01/2022).

[85] C. D. Hansen and C. R. Johnson, Eds., *The Visualization Handbook*. Amsterdam ; Boston: Elsevier-Butterworth Heinemann, 2005, 962 pp., ISBN: 978-0-12-387582-2.

[86] D. Causon, C. Mingham and L. Qian, *Introductory Finite Volume Methods for PDEs*. 1st Jan. 2011, ISBN: 978-87-7681-882-1.

[87] C. W. Hirt and B. D. Nichols, 'Volume of fluid (VOF) method for the dynamics of free boundaries,' *Journal of Computational Physics*, vol. 39, no. 1, pp. 201–225, 1st Jan. 1981, ISSN: 0021-9991. DOI: `10.1016/0021-9991(81)90145-5`. [Online]. Available: `https://www.sciencedirect.com/science/article/pii/0021999181901455` (visited on 07/01/2022).

[88] P. Andersson, *Tutorial multiphaseInterFoam*, 2010. [Online]. Available: `http://www.tfd.chalmers.se/~hani/kurser/OS_CFD_2010/patrikAndersson/patrikAnderssonReport.pdf`.

[89] S. M. Damian, 'Description and utilization of interFoam multiphase solver,' *International Center for Computational Methods in Engineering*, 2012.

[90] K. E. Einarsrud, *A Treatise on Interpolar Transport Phenomena*. Norges teknisk-naturvitenskapelige universitet, Fakultet for ingeniørvitenskap og teknologi, Institutt for energi- og prosessteknikk, 2012, ISBN: 978-82-471-3699-7. [Online]. Available: `https://ntnuopen.ntnu.no/ntnu-xmlui/handle/11250/235008` (visited on 26/03/2022).

[91] E. Berberović, N. P. van Hinsberg, S. Jakirlić, I. V. Roisman and C. Tropea, 'Drop impact onto a liquid layer of finite thickness: Dynamics of the cavity evolution,' *Phys. Rev. E*, vol. 79, no. 3, p. 036 306, 18th Mar. 2009. DOI: `10.1103/PhysRevE.79.036306`. [Online]. Available: `https://link.aps.org/doi/10.1103/PhysRevE.79.036306` (visited on 07/01/2022).

[92] CFD Online Discussion Forums, *Main forum*, 2018. [Online]. Available: `https://www.cfd-online.com/Forums/openfoam-community-contributions/118870-2d-adaptive-mesh-refinement-2.html#post703369/`.

[93] M. Själander, M. Jahre, G. Tufte and N. Reissmann, *EPIC: An Energy-Efficient, High-Performance GPGPU Computing Research Infrastructure*, 2019.

[94] C. Greenshields. 'OpenFOAM v8 User Guide: 2.3 Breaking of a dam,' CFD Direct. (21st Jul. 2020), [Online]. Available: `https://cfd.direct/openfoam/user-guide/v8-dambreak/` (visited on 18/01/2022).

[95] K. J. Vachaparambil and K. E. Einarsrud, 'Comparison of Surface Tension Models for the Volume of Fluid Method,' *Processes*, vol. 7, no. 8, p. 542, 8 Aug. 2019. DOI: `10.3390/pr7080542`. [Online]. Available: `https://www.mdpi.com/2227-9717/7/8/542` (visited on 18/01/2022).

[96] C. Greenshields. 'Interface Capturing in OpenFOAM,' CFD Direct. (2nd Jul. 2020), [Online]. Available: `https://cfd.direct/openfoam/free-software/multiphase-interface-capturing/` (visited on 19/01/2022).

[97] '2015 Minerals Yearbook, Ferroalloys [Advance Release],' U.S. Department of the Interior, U.S. Geological Survey, May 2018. [Online]. Available: `https://minerals.usgs.gov/minerals/pubs/commodity/ferroalloys/myb1-2015-feall.pdf` (visited on 20/03/2022).

[98] H.-S. Jang, J. W. Ryu and I. Sohn, 'FeMn Metal Droplet Behavior in the MnO-SiO2-CaO Slag System,' *Metallurgical and Materials Transactions B*, vol. 46, no. 2, pp. 606–614, Apr. 2015, ISSN: 1073-5615, 1543-1916.

DOI: `10.1007/s11663-014-0234-5`. [Online]. Available: `http://link.springer.com/10.1007/s11663-014-0234-5` (visited on 25/03/2019).

[99] A. F. Yang, A. Karasev and P. G. Jönsson, 'Characterization of Metal Droplets in Slag after Desulfurization of Hot Metal,' *ISIJ Int.*, vol. 55, no. 3, pp. 570–577, 15th Mar. 2015, ISSN: 0915-1559, 1347-5460. DOI: `f3n3m6`. [Online]. Available: `https://www.jstage.jst.go.jp/article/isijinternational/55/3/55_570/_article/-char/ja/` (visited on 25/03/2019).

[100] Z. Han and L. Holappa, 'Mechanisms of Iron Entrainment into Slag due to Rising Gas Bubbles.,' *ISIJ International*, vol. 43, no. 3, pp. 292–297, 2003, ISSN: 0915-1559. DOI: `10.2355/isijinternational.43.292`. [Online]. Available: `http://joi.jlc.jst.go.jp/JST.Journalarchive/isijinternational1989/43.292?from=CrossRef` (visited on 25/03/2019).

[101] M. Kadkhodabeigi, H. Tveit and S. T. Johansen, 'Modelling the Tapping Process in Submerged Arc Furnaces Used in High Silicon Alloys Production,' *ISIJ International*, vol. 51, no. 2, pp. 193–202, 2011. DOI: `10.2355/isijinternational.51.193`.

[102] M. Vångö, C. Feilmayr, S. Pirker and T. Lichtenegger, 'Data-assisted CFD modeling of transient blast furnace tapping with a dynamic deadman,' *Applied Mathematical Modelling*, vol. 73, pp. 210–227, 1st Sep. 2019, ISSN: 0307-904X. DOI: `10.1016/j.apm.2019.04.024`.

[103] R. I. L. Guthrie, *Engineering in Process Metallurgy*, ser. Oxford Science Publications. Oxford : New York: Clarendon Press ; Oxford University Press, 1992, 528 pp., ISBN: 978-0-19-856367-9.

[104] J. E. Olsen and Q. G. Reynolds, 'Mathematical Modeling of Furnace Drainage While Tapping Slag and Metal Through a Single Tap-Hole,' *Metall Mater Trans B*, vol. 51, no. 4, pp. 1750–1759, 1st Aug. 2020, ISSN: 1543-1916. DOI: `10.1007/s11663-020-01873-1`. [Online]. Available: `https://doi.org/10.1007/s11663-020-01873-1` (visited on 09/12/2021).

[105] T. Nouchi, A. Yu and K. Takeda, 'Experimental and numerical investigation of the effect of buoyancy force on solid flow,' *Powder Technology*, vol. 134, no. 1-2, pp. 98–107, Aug. 2003, ISSN: 00325910. DOI: `10.1016/S0032-5910(03)00121-9`. [Online]. Available: `https://linkinghub.elsevier.com/retrieve/pii/S0032591003001219` (visited on 23/06/2022).

[106] M. Vångö, S. Pirker and T. Lichtenegger, 'Unresolved CFD–DEM modeling of multiphase flow in densely packed particle beds,' *Applied Mathematical Modelling*, vol. 56, pp. 501–516, 1st Apr. 2018, ISSN: 0307-904X. DOI: `10.1016/j.apm.2017.12.008`. [Online]. Available: `https://www.sciencedirect.com/science/article/pii/S0307904X17307370` (visited on 09/12/2021).

[107] H. H. Hu, 'Chapter 10 - Computational Fluid Dynamics,' in *Fluid Mechanics (Fifth Edition)*, P. K. Kundu, I. M. Cohen and D. R. Dowling, Eds., Boston: Academic Press, 1st Jan. 2012, pp. 421–472, ISBN: 978-0-12-382100-3. DOI: `10.1016/B978-0-12-382100-3.10010-1`. [Online]. Available: `https://www.sciencedirect.com/science/article/pii/B9780123821003100101` (visited on 09/12/2021).

[108] R. B. Bird, W. E. Stewart and E. N. Lightfoot, *Transport Phenomena*, Revised ed. New York: Wiley, 2007, ISBN: 978-0-470-11539-8.

[109] S. Dash, S. Ajmani, A. Kumar and H. Sandhu, 'Optimum taphole length and flow induced stresses,' *Ironmaking & Steelmaking*, vol. 28, no. 2, pp. 110–116, 1st Apr. 2001, ISSN: 0301-9233. DOI: `10.1179/030192301678019`.

[110] S. Dash, D. Jha, S. Ajmani and A. Upadhyaya, 'Optimisation of taphole angle to minimise flow induced wall shear stress on the hearth,' *Ironmaking & Steelmaking*, vol. 31, no. 3, pp. 207–215, 1st Jun. 2004, ISSN: 0301-9233. DOI: `10.1179/030192304225012114`.

[111] K. Nishioka, T. Maeda and M. Shimizu, 'A Three-dimensional Mathematical Modelling of Drainage Behavior in Blast Furnace Hearth,' *Isij Inter-*

*national - ISIJ INT*, vol. 45, pp. 669–676, 1st Jan. 2005. DOI: `10.2355/isijinternational.45.669`.

[112] M. Kadkhodabeigi, H. Tveit and S. Johansen, 'CFD modelling of the effect of furnace crater pressure on the melt and gas flows in the submerged arc furnaces used for silicon production,' *Progress in Computational Fluid Dynamics*, vol. 10, pp. 374–383, 1st Sep. 2010. DOI: `10.1504/PCFD.2010.035371`.

[113] Q. G. Reynolds and M. W. Erwee, 'Multiphase fluid flow modelling of furnace tap-holes,' *In Proceedings of the 12th International Conference on CFD in Oil & Gas, Metallurgical and Process Industries*, pp. 521–530, 2017.

[114] Q. G. Reynolds, J. E. Olsen, M. W. Erwee and O. F. Oxtoby, 'Phase effects in tap-hole flow - a computational modelling study,' *Journal of the Southern African Institute of Mining and Metallurgy*, vol. 119, no. 6, pp. 527–536, Jun. 2019, ISSN: 2225-6253. DOI: `10.17159/2411-9717/671/2019`. [Online]. Available: `http://www.scielo.org.za/scielo.php?script=sci_abstract&pid=S2225-62532019000600004&lng=en&nrm=iso&tlng=en` (visited on 02/10/2019).

[115] B. Ravary and S. Grådahl, 'Improving environment in the tapping area of a ferromanganese furnace,' presented at the INFACON XII, Helsinki, Finland, 2010.

[116] M. Kadkhodabeigi, H. Tveit and K. Berget, 'Silicon process-new hood design for tapping gas collection,' *In Twelfth International Ferroalloys Congress*, pp. 109–119, 2010.

[117] L. Shen, Z. Jiang, W. Gui, C. Yang, Y. Wang and B. Sun, 'Modelling of Inner Surface Temperature Field of Blast Furnace Wall Based on Inverse Heat Conduction Problems,' *IFAC-PapersOnLine*, 2019. DOI: `10.1016/j.ifacol.2019.09.167`.

[118] H. Ghorbani, M. Al-Dojayli and K. Chomyn, ‘Thermal Assessment and Identification of Wear Zones in Blast Furnace Hearth and Tapholes,’ in *SAIMM Furnace Tapping*, 2018.

[119] A. Sunyaev, ‘The Internet of Things,’ in *Internet Computing: Principles of Distributed Systems and Emerging Internet-Based Technologies*, A. Sunyaev, Ed., Cham: Springer International Publishing, 2020, pp. 301–337, ISBN: 978-3-030-34957-8. DOI: `10.1007/978-3-030-34957-8_10`. [Online]. Available: `https://doi.org/10.1007/978-3-030-34957-8_10` (visited on 09/12/2021).

[120] H. Saxen, C. Gao and Z. Gao, ‘Data-Driven Time Discrete Models for Dynamic Prediction of the Hot Metal Silicon Content in the Blast Furnace—A Review,’ *Industrial Informatics, IEEE Transactions on*, vol. 9, pp. 2213–2225, 1st Nov. 2013. DOI: `10.1109/TII.2012.2226897`.

[121] A. W. Cramb and I. Jimbo, ‘Calculation of the interfacial properties of liquid steel - slag systems,’ *Steel Res.*, vol. 60, no. 3-4, pp. 157–165, Mar. 1989, ISSN: 01774832. DOI: `10.1002/srin.198900893`. [Online]. Available: `http://doi.wiley.com/10.1002/srin.198900893` (visited on 30/10/2019).

[122] H. Saridikmen, C. S. Kucukkaragoz and R. H. Eric, ‘Sulphur behaviour in ferromanganese smelting,’ in *INFACON XI*, New Delhi, India, 2007, pp. 311–320.

[123] R. H. Eric, ‘Chapter 1.10 - Production of Ferroalloys,’ in *Treatise on Process Metallurgy*, S. Seetharaman, Ed., Boston: Elsevier, 1st Jan. 2014, pp. 477–532, ISBN: 978-0-08-096988-6. DOI: `10.1016/B978-0-08-096988-6.00005-5`. [Online]. Available: `http://www.sciencedirect.com/science/article/pii/B9780080969886000055` (visited on 02/10/2019).

[124] Y. E. Lee and L. Kolbeinsen, ‘Behavior of Slag in Ferromanganese and Silicomanganese Smelting Process,’ *Metall. Mater. Trans. B*, 29th Jun. 2021,

ISSN: 1073-5615, 1543-1916. DOI: `10.1007/s11663-021-02242-2`. [Online]. Available: `https://link.springer.com/10.1007/s11663-021-02242-2` (visited on 06/07/2021).

[125] S. Bao, M. Tangstad, K. Tang, K. E. Einarsrud, M. Syvertsen, M. Onsøien, A. Kudyba and S. Bublik, 'Investigation of Two Immiscible Liquids Wetting at Elevated Temperature: Interaction Between Liquid FeMn Alloy and Liquid Slag,' *Metall. Mater. Trans. B*, vol. 52, no. 5, pp. 2847–2858, 11th Jun. 2021, ISSN: 1543-1916. DOI: `10.1007/s11663-021-02222-6`. [Online]. Available: `https://doi.org/10.1007/s11663-021-02222-6` (visited on 05/08/2021).

[126] P. Patnaik, *Handbook of Inorganic Chemicals*. McGraw-Hill, 2003, 1134 pp., ISBN: 978-0-07-049439-8.

[127] B. O. Mysen, D. Virgo and F. A. Seifert, 'The structure of silicate melts: Implications for chemical and physical properties of natural magma,' *Reviews of Geophysics*, vol. 20, no. 3, pp. 353–383, 1982, ISSN: 1944-9208. DOI: `10.1029/RG020i003p00353`. [Online]. Available: `https://onlinelibrary.wiley.com/doi/abs/10.1029/RG020i003p00353` (visited on 20/12/2021).

[128] K. C. Mills, 'The Influence of Structure on the Physico-chemical Properties of Slags.,' *ISIJ International*, vol. 33, no. 1, pp. 148–155, 1993, ISSN: 0915-1559. DOI: `10.2355/isijinternational.33.148`.

[129] J. H. Park, 'Structure–Property Correlations of CaO–$SiO_2$–MnO Slag Derived from Raman Spectroscopy,' *ISIJ International*, vol. 52, no. 9, pp. 1627–1636, 2012. DOI: `10.2355/isijinternational.52.1627`.

[130] J. H. Park, 'Composition–structure–property relationships of CaO-MO-SiO2 (M=Mg2+, Mn2+) systems derived from micro-Raman spectroscopy,' *Journal of Non-Crystalline Solids*, vol. 358, no. 23, pp. 3096–3102, 1st Dec. 2012, ISSN: 0022-3093. DOI: `10.1016/j.jnoncrysol.2012.08.014`. [Online].

Available: `https://www.sciencedirect.com/science/article/pii/S0022309312004930` (visited on 20/12/2021).

[131] K. Mills, L. Yuan, Z. Li, G. Zhang and K. Chou, 'A Review of the Factors Affecting the Thermophysical Properties of Silicate Slags,' *High Temperature Materials and Processes*, vol. 31, no. 4-5, 30th Jan. 2012, ISSN: 2191-0324, 0334-6455. DOI: `10.1515/htmp-2012-0097`. [Online]. Available: `https://www.degruyter.com/view/j/htmp.2012.31.issue-4-5/htmp-2012-0097/htmp-2012-0097.xml` (visited on 25/10/2018).

[132] B. Mysen and P. Richet, *Silicate Glasses and Melts*. Elsevier, 27th Nov. 2018, 722 pp., ISBN: 978-0-444-63709-3. Google Books: `rslaDwAAQBAJ`.

[133] I. Sohn and D. J. Min, 'A Review of the Relationship between Viscosity and the Structure of Calcium-Silicate-Based Slags in Ironmaking,' *Steel Research International*, vol. 83, no. 7, pp. 611–630, 2012, ISSN: 1869-344X. DOI: `10.1002/srin.201200040`. [Online]. Available: `https://onlinelibrary.wiley.com/doi/abs/10.1002/srin.201200040` (visited on 20/12/2021).

[134] C. Han, 'Viscosity Studies of High-Temperature Metallurgical Slags Relevant to Ironmaking Process,' Ph.D. dissertation, The University of Queensland, 20th Oct. 2017. DOI: `10.14264/uql.2017.995`. [Online]. Available: `http://espace.library.uq.edu.au/view/UQ:689105` (visited on 22/12/2021).

[135] I. Tanabe, K. Oku and T. Honda, 'Effects of Magnesia on the Viscosity of High Carbon Ferro-Manganese Slag,' *Journal of The Electrochemical Society of Japan*, vol. 28, no. 10-12, E262–E266, 1960. DOI: `10.5796/jesj.28.10-12.E262`.

[136] L. C. Woollacott and D. D. Howat, 'The Viscosities and Electrical Conductivities of Slags Associated with the Production of High-carbon Ferromanganese Alloys,' p. 6,

[137] M. Persson, 'Investigations of Slag Properties and Reactions,' 2007. [Online]. Available: `http://urn.kb.se/resolve?urn=urn:nbn:se:kth:diva-4378` (visited on 22/12/2021).

[138] B. Yan, Y. Liu, Q. Shu, T. Deng and B. Glaser, 'Measurements and Model Estimations of Viscosities of the MnO-CaO-SiO2-MgO-Al2O3 Melts,' *Metall and Materi Trans B*, vol. 50, no. 1, pp. 376–384, Feb. 2019, ISSN: 1073-5615, 1543-1916. DOI: `10.1007/s11663-018-1454-x`. [Online]. Available: `http://link.springer.com/10.1007/s11663-018-1454-x` (visited on 22/12/2021).

[139] K. C. Mills and C.-Å. Däcker, *The Casting Powders Book*. Cham: Springer International Publishing, 2017, ISBN: 978-3-319-53616-3. DOI: `10.1007/978-3-319-53616-3`. [Online]. Available: `http://link.springer.com/10.1007/978-3-319-53616-3` (visited on 26/10/2018).

[140] L. Muhmood and S. Seetharaman, 'Density Measurements of Low Silica CaO-SiO2-Al2O3 Slags,' *Metall Mater Trans B*, vol. 41, no. 4, pp. 833–840, 1st Aug. 2010, ISSN: 1543-1916. DOI: `10.1007/s11663-010-9385-1`. [Online]. Available: `https://doi.org/10.1007/s11663-010-9385-1` (visited on 28/01/2021).

[141] T. Matsushita, T. Ishikawa, P.-F. Paradis, K. Mukai and S. Seetharaman, 'Density Measurements of Mould Flux Slags by Electrostatic Levitation Method,' *ISIJ International*, vol. 46, no. 4, pp. 606–610, 2006. DOI: `10.2355/isijinternational.46.606`.

[142] J. Lee, L. T. Hoai, J. Choe and J. H. Park, 'Density Measurements of CaO-MnO-$SiO_2$ Slags,' *ISIJ International*, vol. 52, no. 12, pp. 2145–2148, 2012. DOI: `10.2355/isijinternational.52.2145`.

[143] Y. Wanibe, H. Tsuchida, T. Fujisawa and H. Sakao, 'Fundamental Study on the Infiltration of Slags into Refractories with the Slagging Reaction,'

*Transactions of the Iron and Steel Institute of Japan*, vol. 23, no. 4, pp. 322–330, 1983. DOI: `10.2355/isijinternational1966.23.322`.

[144] J. Wikström, ‘A Mathematical and Experimental Study of Inclusion Behaviour at a Steel-Slag Interface,’ KTH, Stockholm, 2007. [Online]. Available: `http://urn.kb.se/resolve?urn=urn:nbn:se:kth:diva-4574` (visited on 05/02/2021).

[145] R. A. M. de Almeida, D. Vieira, W. V. Bielefeldt, A. C. F. Vilela, R. A. M. de Almeida, D. Vieira, W. V. Bielefeldt and A. C. F. Vilela, ‘Slag Foaming Fundamentals - A Critical Assessment,’ *Materials Research*, vol. 20, no. 2, pp. 474–480, Apr. 2017, ISSN: 1516-1439. DOI: `10.1590/1980-5373-mr-2016-0059`. [Online]. Available: `http://www.scielo.br/scielo.php?script=sci_abstract&pid=S1516-14392017000200474&lng=en&nrm=iso&tlng=en` (visited on 29/01/2021).

[146] ‘HSC Chemistry.’ (2021), [Online]. Available: `https://www.hsc-chemistry.com/` (visited on 09/07/2021).

[147] ‘Electrolyte Properties.’ (2021), [Online]. Available: `https://peter-entner.com/E/ElProp-2/ElProp-2.htm` (visited on 09/07/2021).

[148] P. V. Riboud, Y. Roux, L. D. Lucas and H. Gaye, ‘Improvement of Continuous Casting Powders,’ *Fachber Huttenprax Metallweiterverarb*, vol. 19, no. 10, pp. 859–869, 1981.

[149] G. Urbain, ‘Viscosity estimation of slags,’ *Steel Research*, vol. 58, no. 3, pp. 111–116, 1987, ISSN: 1869-344X. DOI: `10.1002/srin.198701513`. [Online]. Available: `https://onlinelibrary.wiley.com/doi/abs/10.1002/srin.198701513` (visited on 07/07/2021).

[150] T. Iida, H. Sakai, Y. Kita and K. Shigeno, ‘An Equation for Accurate Prediction of the Viscosities of Blast Furnace Type Slags from Chemical Composition,’ *ISIJ International*, vol. 40, S110–S114, Suppl 2000, ISSN: 0915-1559. DOI: `10.2355/isijinternational.40.Suppl_S110`.

[151] G.-H. Zhang and K.-C. Chou, ‘Simple Method for Estimating the Electrical Conductivity of Oxide Melts with Optical Basicity,’ *Metall and Materi Trans B*, vol. 41, no. 1, pp. 131–136, Feb. 2010, ISSN: 1073-5615, 1543-1916. DOI: `10.1007/s11663-009-9298-z`. [Online]. Available: `http://link.springer.com/10.1007/s11663-009-9298-z` (visited on 07/07/2021).

[152] G.-H. Zhang, B.-J. Yan, K.-C. Chou and F.-S. Li, ‘Relation Between Viscosity and Electrical Conductivity of Silicate Melts,’ *Metall and Materi Trans B*, vol. 42, no. 2, pp. 261–264, Apr. 2011, ISSN: 1073-5615, 1543-1916. DOI: `10.1007/s11663-011-9484-7`. [Online]. Available: `http://link.springer.com/10.1007/s11663-011-9484-7` (visited on 07/07/2021).

[153] S. Bublik, S. Gouttebroze, T. Coudert, M. Tangstad and K. E. Einarsrud, ‘SlagCalculator: A Framework for Slag and Metallurgical Properties,’ *SSRN Journal*, 2021, ISSN: 1556-5068. DOI: `10.2139/ssrn.3926702`.

# Paper I

# Slag-metal interactions in the FeMn tapping process: Interfacial properties and wetting

Sergey Bublik[1], Sarina Bao[2], Merete Tangstad[3], Kristian Etienne Einarsrud[4]

[1,3,4]Department of Materials Science and Engineering, Norwegian University of Science and Technology (NTNU), 7941 Trondheim, Norway
[2]Department of Metal Production and Processing, SINTEF Industry, 7941 Trondheim, Norway

**Keywords:** ferromanganese, ferromanganese slag, wetting, interfacial tension, surface tension

## Abstract

FeMn-alloys are produced by transforming ore and carbon materials into FeMn and slag at high temperatures in a furnace. Entrainment of FeMn in slag during tapping reduces the yield. Entrainment and subsequent separation are strongly influenced by slag-metal interfacial properties. In the current work, interfacial properties, including the contact angle, in the FeMn-slag graphite system have been investigated using the sessile drop technique at temperatures above 1573 K. Two experimental configurations are proposed: (a) slag and metal placed beside each other on graphite; and (b) slag placed on top of the metal layer. The average interfacial tension between slag and metal over the temperature interval was found to be 1.08±0.10 N/m for slag-to-metal weight ratio 0.19, and 1.30±0.32 N/m for slag-to-metal weight ratio 0.28. In addition, wetting properties are considerably influenced by the variation of slag-metal weight ratio in the range from 0.25 to 1.50 and only marginally by temperature.

## I. INTRODUCTION

At the present time, the production of ferromanganese and other types of ferroalloys is consistently growing, which is partly caused by the increased demand for steel and these alloys[1,2]. High carbon FeMn production (78 per cent Mn, 15 per cent Fe, 7 per cent C) reached the level of 4.2 million t in 2017[3]. FeMn and most of the ferroalloys (SiMn, FeSi, FeCr) are produced in submerged arc furnaces (SAF) during high-temperature reduction of the oxide raw materials by carbon (coke, anthracite, charcoal). In addition to the ferroalloy, a significant amount of slag is generated[4]. The slag-to-metal ratio depends upon the quality of raw materials and operational conditions: for FeMn production, the slag-to-metal ratio varies from 0.60 to 1.22[5]. There are several methods for tapping of products from the SAF, such as combined metal and slag tapping, dedicated metal-slag tapping and slag-only tapping[6]. In the ferroalloy production industry, the combined method is typically used, where both slag and metal are tapped periodically every 2-3 hours. The taphole can be changed in order to prevent operational difficulties and to stabilize the molten bath level[7]. As a consequence, slag and metal must be separated after tapping to obtain the required quality of FeMn. Typically, this is performed in a cascade of ladles, where the separation takes place due to the density difference between products, and liquid slag overflows to the following ladles. The slag overflow, nevertheless, entrains unseparated FeMn droplets, resulting in metal losses and thereby decreasing the process efficiency. The entrainment of the molten FeMn droplets by the slag phase is greatly affected by interfacial phenomena, which are mainly determined by the interfacial tension[8–11].

The measurement of the interfacial tension between two molten phases is extremely challenging due to the high temperature and the complexity of phase composition. Specifically, the presence of dissolved surface active elements (oxygen, sulphur) at the interface between slag and metal could considerably modify the interfacial tension[12,13]. Moreover, available methods for the determination the interfacial tension are complicated and do not allow to investigate interfacial phenomena with stable and reproducible results.

In the present work, the interfacial properties between high carbon FeMn and FeMn slag ($MnO$-$CaO$-$MgO$-$SiO_2$-$Al_2O_3$) have been studied using the sessile drop technique. Two different experimental methods are presented and discussed, aiming to determine their applicability to the current system.

## II. EXPERIMENTAL PROCEDURE

### *A. Materials preparation*

FeMn slag and HC FeMn compositions and densities were selected corresponding to that of industrial products, which are presented in **Table I**. Both FeMn and slag were made from pure powder materials. The purity of powders and the weight of powders are shown in **Table II**.

The powders were mixed and melted in a graphite crucible in a graphite tube furnace in argon at 1773 K. The obtained product after melting and solidification was then removed from the crucible and crushed.

It is noteworthy to mention that carbon materials were not added during the mixing of powders for HC FeMn due to the carbon available from the graphite crucible.

**Table I. Chemical composition of the industrial FeMn and FeMn slag.**

| Material | Chemical composition, wt. %[14] | | | | | | | | Density, kg/m$^3$[15] |
|---|---|---|---|---|---|---|---|---|---|
| | Mn | Fe | C | MnO | CaO | MgO | $SiO_2$ | $Al_2O_3$ | |
| HC FeMn | 78.0 | 15.0 | 7.0 | - | - | - | - | - | 5612 |
| FeMn slag | - | - | - | 38.0 | 23.0 | 6.0 | 23.0 | 10.0 | 3300 |

**Table II. The purity and the weight of powders for the mixing.**

| Material | Purity, % | | | | | | |
|---|---|---|---|---|---|---|---|
| | Mn | Fe | MnO | CaO | MgO | $SiO_2$ | $Al_2O_3$ |
| Powder | 99.99 | 98.00 | 99.00 | 98.00 | 98.00 | 99.99 | 95.00 (5 % $SiO_2$) |

| Synthetic material | Weight of mixed powders, g | | | | | | | | |
|---|---|---|---|---|---|---|---|---|---|
| | Mn | Fe | C | MnO | CaO | MgO | $SiO_2$ | $Al_2O_3$ | Total |
| HC FeMn | 41.94 | 8.23 | - | - | - | - | - | - | 50.17 |
| FeMn slag | - | - | - | 19.19 | 11.73 | 3.06 | 11.24 | 5.26 | 50.48 |

### *B. Experimental Setup*

In order to study the interfacial properties between synthetic FeMn slag and HC FeMn, the sessile drop technique was applied. The experimental equipment is illustrated schematically in **Fig. 1**.

Two experimental methods were made:

*Method A* – slag (15-125 mg) and FeMn (60-120 mg) placed beside each other on a graphite substrate (d = 1 cm);

*Method B* – slag (~60-90 mg) placed on the top of the FeMn layer (~300 mg), which is in contact with a graphite substrate (d = 1 cm).

Slag and FeMn pieces, as shown in **Fig. 2**, were located on a graphite substrate (ISO-88), which was cleaned by compressed air. Subsequently, the chamber of the sessile drop furnace was closed, evacuated, rapidly heated in argon atmosphere up to 1423 K in 3.75 minutes (300 K/min) and then heated up to 1623 K in 10 minutes (20 K/min). After reaching 1623 K, the furnace was turned off and samples cooled down. Thereafter the samples were cast in epoxy, sectioned in the centre and prepared for the electron microprobe analysis (EPMA) by wavelength-dispersive spectroscopy. The composition of slag and FeMn before and after the sessile drop test were measured in several points and then average composition of each phase was calculated. The experimental matrix for both methods is represented in **Table III**.

The chamber of the furnace was equipped with windows in order to allow a digital video camera (Sony XCD-SX910CR, Sony Corporation, Millersville, MD) with a telecentric lens (Navitar 1-50993D) to record images from the molten samples with the resolution of 1280x1024 pixels at one frame per second. This means three frames per degree of temperature increase from 1423 K and above.

The contact angles between different phases in method A were measured directly from the image using the image processing software (ImageJ[16]). Values for surface- and interfacial tension were not obtained for method A due to challenges in fitting regular shapes to the interfaces in question.

For method B, the interfacial and the surface tension were estimated from the contour of droplets during experiments in the sessile drop furnace using the axisymmetric drop shape analysis (ADSA)[17], which is based on the balance between surface, interfacial tension and external forces.

The figures after analysing the raw data were produced using a data visualization toolbox for MATLAB (Gramm[18]). The confidence bands for fitted lines are given by:

$$C = b \pm t\sqrt{S} \qquad [1]$$

where $b$ are the coefficients produced by the fit, $t$ is the value, which depends on the confidence level and is computed using the inverse of Student's $t$ cumulative distribution function, $S$ is a vector of the diagonal elements from the estimated covariance matrix of the coefficient estimates.

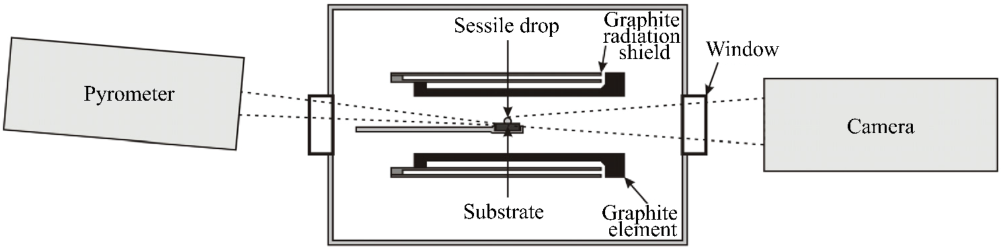

**Fig. 1** – Schematic illustration of the sessile drop technique[19].

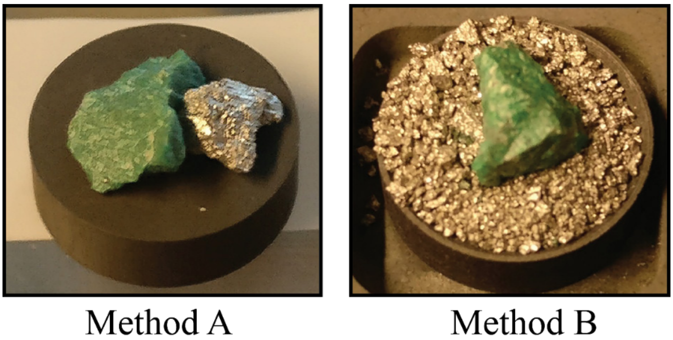

**Fig. 2** – Raw materials before experiments: A, slag and metal side by side on a graphite disk; B, slag on the metal layer in a graphite cup.

**Table III. The experimental matrix.**

| **Experiment** | **Slag-to-metal weight ratio (S/M)** | | |
|---|---|---|---|
| | **Average** | **Min** | **Max** |
| **Method A** | | | |
| **A1-A3** | 0.25 | 0.22 | 0.27 |
| **A4-A6** | 0.49 | 0.46 | 0.52 |
| **A7-A9** | 0.73 | 0.71 | 0.74 |
| **A10-A12** | 0.97 | 0.92 | 1.00 |
| **A13-A15** | 1.26 | 1.21 | 1.29 |
| **A16-A18** | 1.54 | 1.52 | 1.56 |
| **Method B** | | | |
| **B1-B3** | 0.19 | 0.18 | 0.20 |
| **B4-B6** | 0.28 | 0.26 | 0.29 |

## III. RESULTS AND DISCUSSION

The changes in the droplets shape during melting are presented for both methods in **Fig. 3** and **Fig. 4**, respectively, together with a schematic view of relevant contact angles. The contact angles were defined geometrically as described below:

- slag-graphite ($\theta_{s\text{-}gr}$) is the angle formed by the tangent to the slag-graphite interface;
- metal-graphite ($\theta_{m\text{-}gr}$) is the angle formed by the tangent to the metal-graphite interface;
- slag-metal ($\theta_{s\text{-}m}$) is the angle formed by two tangent lines from the contact point of slag and metal.

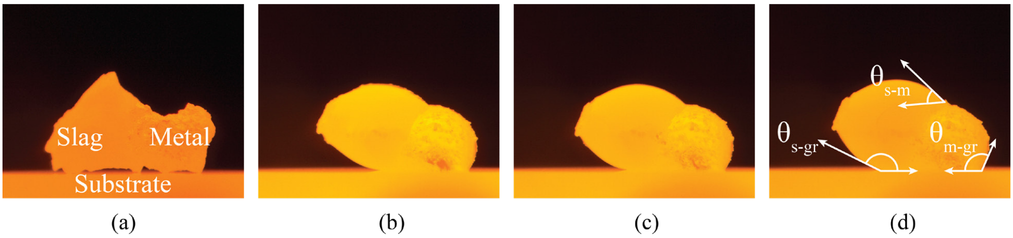

(a) (b) (c) (d)

**Fig. 3** – Experiment A9, S/M = 0.73, melting of the slag (left) and FeMn (right): (a) samples before melting, T = 1473 K; (b) T = 1573 K; (c) T = 1598 K; (d) T = 1623 K. Relevant contact angles are indicated in frame (d).

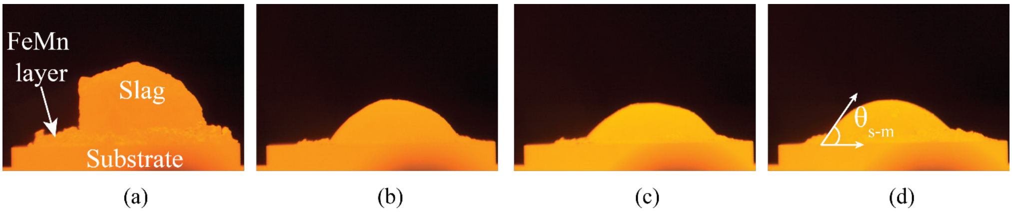

(a) (b) (c) (d)

**Fig. 4** – Experiment B4, S/M = 0.28, melting of slag placed on the FeMn layer: (a) slag before melting, T = 1473 K; (b) T = 1573 K; (c) T = 1598 K; (d) T = 1623 K. The relevant contact angle is indicated in frame (d).

### *A. Wetting according to the method A*

Melting points of FeMn and slag were found to be 1533 K and 1563 K, respectively. In order to represent conditions relevant to the tapping process, contact angles were determined between 1583 and 1623 K. The rate of reduction increases at higher temperatures, thereby contributing to uncertainties.

**Fig. 5(a)** shows that the measured contact angle varies, depending on the interface and the slag-to-metal ratio in the range from 0.25 to 1.50. Values of the contact angle between metal-graphite and slag-graphite are more randomly distributed, resulting in low adjusted R-squared values (0.05 and 0.13, respectively). In contrast, values of the contact angle between slag-metal have higher adjusted R-squared value (0.60), indicating a larger dependence within the limits of the plotted linear model.

The apparent contact angle at the metal-graphite interface changes considerably with the slag-to-metal ratio due to the gravity effect, which become more substantial with increasing the volume of the slag droplet, while the volume of the FeMn droplet is fixed.

Below a certain value of the drop volume, the dominant forces are capillary terms and any gravity effects in the system can be ignored. However, with increasing droplet volumes, the gravity influence becomes more pronounced, which contributes to a stronger effect of gravity[20] and a change in the apparent interfacial (or surface) tension, which is determined by[21]:

$$a^2 = \frac{V}{l} = \frac{\sigma}{\Delta\rho g} \qquad [2]$$

where $a$ is the capillary constant, $V$ is the volume of raised liquid, $l$ is the length of the capillary perimeter, $\sigma$ is the interfacial or surface tension of the liquid, $\Delta\rho$ is the density difference between two phases, $g$ is gravitational acceleration.

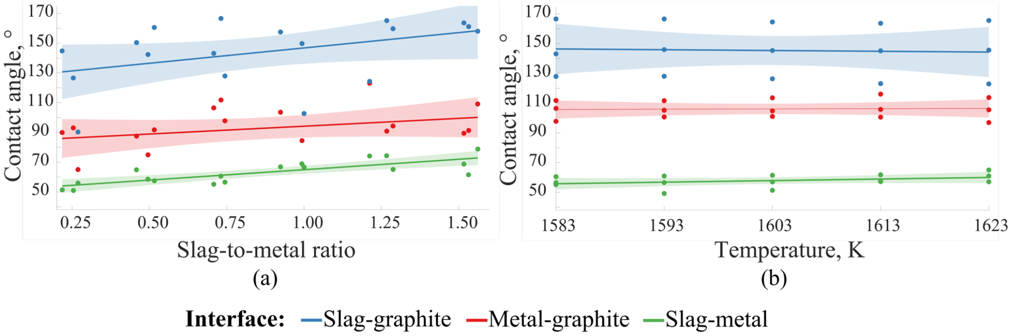

(a) (b)

**Fig. 5** – Experiments A1-A18: Measured contact angles and linear regression with 95 % confidence bands (lines and shaded areas): (a) at different slag-to-metal ratio at 1583 K, (b) at different temperature at S/M from 0.71 to 0.74.

The results of the contact angle at different temperatures and at fixed slag-to-metal ratio (close to 0.75) demonstrate that the effect of temperature in the range from 1583 to 1623 K is negligible (**Fig. 5(b)**). Values of the contact angle for different interfaces are:

- slag-graphite: 144.4–146.4°;
- metal-graphite: 105.8–106.5°;
- slag-metal: 55.8–60.0°.

### *B. Interfacial behaviour according to the method B*

The apparent interfacial tension between slag and metal at the slag metal ratio from 0.18 to 0.29 is demonstrated in **Fig. 6(a)**. The value of the interfacial tension, calculated based on the ADSA approach, is 1.03–1.18 N/m when the slag-to-metal ratio is in the range from 0.18 to 0.21, while increasing the slag-to-metal ratio to 0.26–0.29 leads to the higher values of the interfacial tension (1.20–1.56 N/m).

In case of higher values of the slag-to-metal ratio, the apparent interfacial tension has higher values due to the gravity effect, which becomes more pronounced with increasing the slag volume when the volume of the FeMn layer is fixed. According to the **Eq. [2]**, higher volume results in higher values of the interfacial tension. Calvimontes[22] has shown that the interfacial properties can be greatly modified by the gravitational force, resulting in increased apparent wetting and considerably lower measured contact angles. As indicated in **Fig. 6(b)**, the slag-Ar surface tension does not show a (statistically) significant influence from the slag-to-metal ratio, which is as expected as the curvature of the upper surface of the droplet is relatively straight forward to fit to an oblate. The mean value of the slag surface tension is found to be 1.14 N/m.

As presented in **Fig. 7**, both the interfacial and surface tension tend to slightly decrease as the temperature rises in the experimental range. Several studies[23–26] have shown a similar temperature dependence.

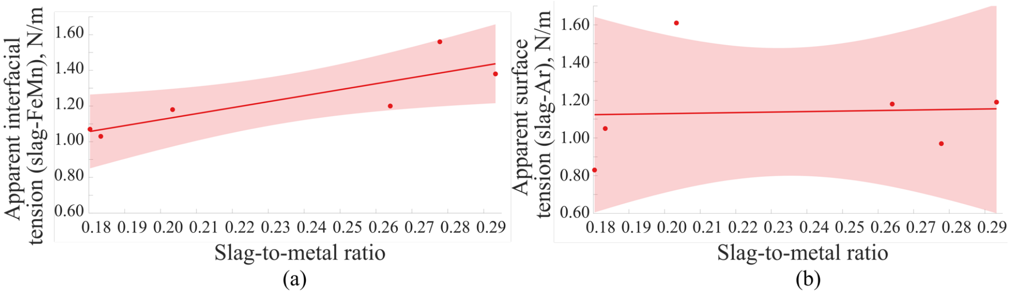

(a) (b)

**Fig. 6** – Experiments B1-B6: the interfacial tension between slag and metal (a) and the surface tension of slag in Ar (b) at different slag-to-metal ratio at 1583 K and linear regression with the 95 % confidence band (lines and the shaded areas).

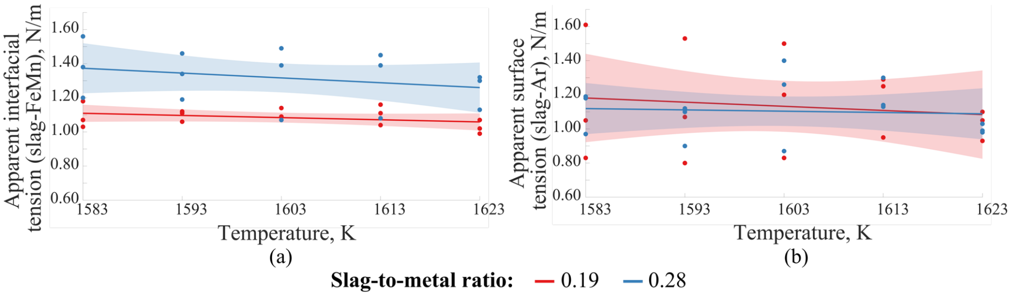

(a) (b)

**Fig. 7** – Experiments B1-B6: the interfacial tension between slag and metal (a) and the surface tension of slag in Ar (b) as a function of temperature and linear regression with the 95 % confidence bands (lines and shaded areas).

The apparent contact angle between slag and metal was found to be in the range of 43.3-64.6° for method B, determined by image analysis, in good correspondence with that found with method A.

### C. *EPMA of the raw materials and samples after the experiments*

The EPMA images with 200 times magnification both for FeMn slag and FeMn after melting in the graphite crucible are presented in **Fig. 8**. The initial average chemical compositions of slag and FeMn are summarized in **Table IV**. Comparing to the **Table I**, we can see that the raw materials are close in composition to the industrial FeMn slag and FeMn. According to the Kim et al. (2003)[27], the carbon solubility in Mn-Fe melts (15 % Fe) at 1773 K is 7.5 %. The graphite crucible introduced expected amounts of carbon into the FeMn.

The results from the point analysis by EPMA (**Table V**) demonstrates that the slag contains two phases: the matrix and dendrites (MnO and MgO). **Fig. 8(b)** shows that FeMn consists of four different phases, the composition of which is demonstrated in **Table VI.**

**Fig. 9(a)** shows the slag phase of the sample after experiment in the sessile drop furnace using method B. The point analysis by EPMA (**Table VII**) illustrates that the slag matrix has the similar composition to the slag prior the experiment, while dendrites contain slightly higher MgO content (mean value of 12.5 %) and lower MnO content (mean value of 84.5 %).

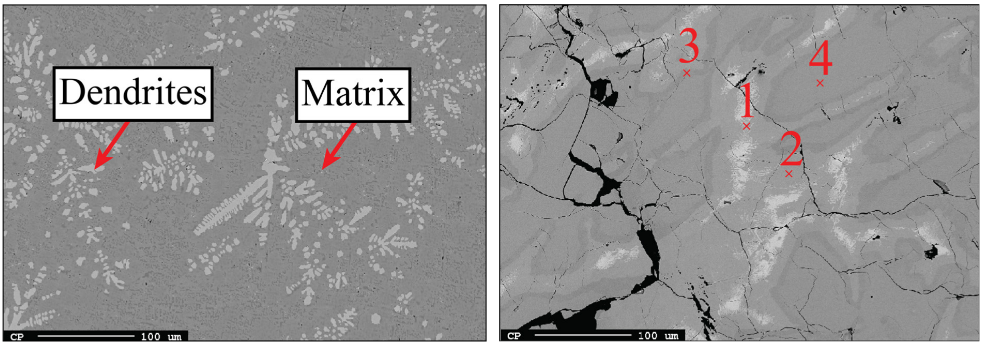

(a) (b)

**Fig. 8** – EPMA image of FeMn slag (a) and FeMn (b) before the experiments.

**Table IV. The average chemical composition of materials before the experiments in the sessile drop furnace.**

| **Material** | **Average chemical composition, wt. %** | | | | | | | | | |
|---|---|---|---|---|---|---|---|---|---|---|
| | **Mn** | **Fe** | **C** | **MnO** | **CaO** | **MgO** | **$SiO_2$** | **$Al_2O_3$** | **FeO** | **Total** |
| FeMn | 80.4 | 14.9 | 6.7 | - | - | - | - | - | - | 102.0 |
| FeMn slag | - | - | - | 35.2 | 22.7 | 5.6 | 23.0 | 10.5 | 0.1 | 97.1 |

**Table V. Chemical composition of slag phases, measured at different points.**

| **Phase** | **Average chemical composition, wt. %** | | | | | | |
|---|---|---|---|---|---|---|---|
| | **MnO** | **CaO** | **MgO** | **$SiO_2$** | **$Al_2O_3$** | **FeO** | **Total** |
| Dendrites | 87.1 | 1.5 | 8.8 | 0.0 | 0.4 | 0.2 | 97.9 |
| Matrix | 27.0 | 26.7 | 5.3 | 22.7 | 12.7 | 0.0 | 94.4 |

**Table VI. Chemical composition of FeMn phases, measured at different points.**

| **No.** | **Average chemical composition, wt. %** | | | |
|---|---|---|---|---|
| | **Mn** | **Fe** | **C** | **Total** |
| 1 | 75.5 | 28.0 | 2.8 | 106.3 |
| 2 | 79.0 | 18.4 | 5.6 | 103.1 |
| 3 | 80.0 | 15.0 | 6.3 | 101.3 |
| 4 | 79.6 | 14.4 | 6.4 | 100.5 |

However, it has been observed that the metal phase of the sample after experiment B6 (**Fig. 9(b)**) consist of only two phases, the chemical analysis of which is presented in **Table VIII**, compared to the FeMn sample before the experiment, which has four phases. This was found for all samples considered.

The interface between slag and FeMn is shown in **Fig. 9(c)**. As demonstrated, the slag penetrates the metal, resulting in a significant amount of slag inclusions near the interface. The point analysis of the inclusions, obtained from samples after experiments B1-B5, is presented in **Table IX**.

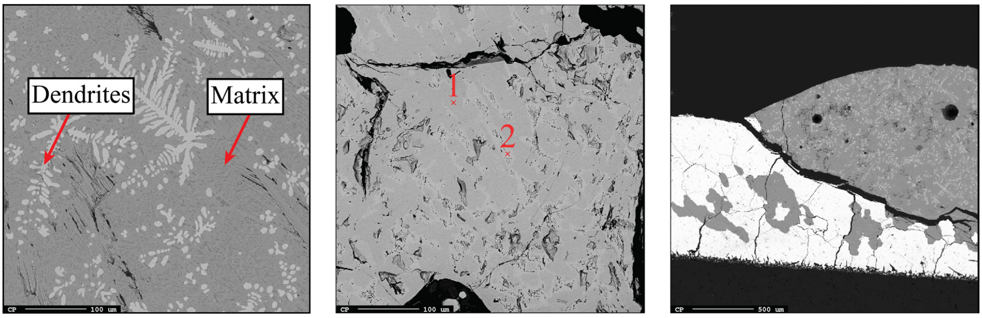

(a) (b) (c)

**Fig. 9** – EPMA images of the sample after experiment B6: (a) slag phase, (b) metal phase, (c) the interface between slag and metal phase.

**Table VII. Chemical composition of the slag phase of the sample after experiment B6.**

| **No.** | **Average chemical composition, wt. %** | | | | | | |
|---|---|---|---|---|---|---|---|
| | **MnO** | **CaO** | **MgO** | **$SiO_2$** | **$Al_2O_3$** | **FeO** | **Total** |
| Dendrites | 84.5 | 1.4 | 12.5 | 0.0 | 0.4 | 0.2 | 98.9 |
| Matrix | 28.8 | 26.0 | 5.2 | 24.3 | 11.2 | 0.1 | 95.5 |

**Table VIII. Chemical composition of the metal phase of the sample after experiment B6.**

| **No.** | **Average chemical composition, wt. %** | | | |
|---|---|---|---|---|
| | **Mn** | **Fe** | **C** | **Total** |
| 1 | 78.3 | 19.0 | 5.6 | 102.8 |
| 2 | 78.8 | 17.2 | 6.2 | 102.2 |

**Table IX. Chemical composition of the slag inclusions in the metal phase.**

| **Average chemical composition, wt. %** | | | | | | |
|---|---|---|---|---|---|---|
| **MnO** | **CaO** | **MgO** | **$SiO_2$** | **$Al_2O_3$** | **FeO** | **Total** |
| 27.0 | 26.8 | 4.6 | 27.5 | 11.1 | 0.2 | 97.2 |

## IV. CONCLUSIONS

Two methods for the measurement of the interfacial properties between FeMn and FeMn slag were studied in the sessile drop furnace at temperature from 1583 to 1623 K under Ar atmosphere. Both methods are suitable for the investigation of interfacial properties, however, method B allows for easier determination of the droplet shape, thereby enabling estimates of interfacial and surface tensions. The average interfacial tension between slag and metal over the temperature interval was found to be 1.08±0.10 N/m for S/M 0.19, and 1.30±0.32 N/m for S/M 0.28, whereas the surface tension of slag in Ar is 1.13±0.52 N/m for S/M 0.19, and 1.10±0.30 N/m for S/M 0.28. Both interfacial and surface tension was found to decrease slightly with increasing temperature. Moreover, it has been observed that both methods are sensitive to the slag-to-metal ratio, which modifies the gravity effect and therefore the force balance in the system. Future work aims to improve the processing procedure so that the true tensions can be determined from the apparent values presented here as well as taking actions to reduce the uncertainty in measurements.

## REFERENCES

1 *World Steel in Figures 2018*, World Steel Association, 2018.
2 A. Figueiredo, A. Werner, C.A. Miller, F. Mascarenhas, S. Bassil, B. Siqueira, C. Couri, and R. Capanema: *Vale's Production and Sales in 3Q18*, Investor Relations Department, Vale, 2018.
3 *IMnI Statistics 2018*, International Manganese Institute, 2018.
4 *2015 Minerals Yearbook, Ferroalloys [Advance Release]*, U.S. Department of the Interior, U.S. Geological Survey, 2018.
5 A.V. Zhdanov, V.I. Zhuchkov, V.Y. Dashevskiy, and L.I. Leontyev: in *Advanced Methods and Technologies in Metallurgy in Russia*, S. Syngellakis and J.J. Connor, eds., Springer International Publishing, Cham, 2018, pp. 113–20.
6 L.R. Nelson and R.J. Hundermark: *J. South. Afr. Inst. Min. Metall.*, 2016, vol. 116, pp. 465–90.
7 M. Kadkhodabeigi: Modeling of Tapping Processes in Submerged Arc Furnaces, NTNU, 2011.
8 H.-S. Jang, J.W. Ryu, and I. Sohn: *Metall. Mater. Trans. B*, 2015, vol. 46, pp. 606–14.
9 G. Irons, A. Senguttuvan, and K. Krishnapisharody: *ISIJ Int.*, 2015, vol. 55, pp. 1–6.
10 A.F. Yang, A. Karasev, and P.G. Jönsson: *ISIJ Int.*, 2015, vol. 55, pp. 570–7.
11 Z. Han and L. Holappa: *ISIJ Int.*, 2003, vol. 43, pp. 292–7.
12 L. Muhmood, N.N. Viswanathan, and S. Seetharaman: *Metall. Mater. Trans. B*, 2011, vol. 42, pp. 460–70.
13 T. Tanaka, H. Goto, M. Nakamoto, M. Suzuki, M. Hanao, M. Zeze, H. Yamamura, and T. Yoshikawa: *ISIJ Int.*, 2016, vol. 56, pp. 944–52.
14 M. Tangstad: *Handbook of Ferroalloys: Chapter 7. Manganese Ferroalloys Technology*, Elsevier Inc. Chapters, 2013.
15 J. Muller, J.H. Zietsman, and P.C. Pistorius: *Metall. Mater. Trans. B*, 2015, vol. 46, pp. 2639–51.
16 C.A. Schneider, W.S. Rasband, and K.W. Eliceiri: *Nat. Methods*, 2012, vol. 9, pp. 671–5.
17 S.M.I. Saad and A.W. Neumann: *Adv. Colloid Interface Sci.*, 2016, vol. 238, pp. 62–87.
18 P. Morel: Gramm, http://joss.theoj.org, (accessed 25 March 2019).
19 S. Bao, K. Tang, A. Kvithyld, M. Tangstad, and T.A. Engh: *Metall. Mater. Trans. B*, 2011, vol. 42, pp. 1358–66.
20 K. GmbH: *Effect of Drop Volume on Static Contact Angles*, 2004.
21 V.V. Kashin, K.M. Shakirov, and A.I. Poshevneva: *Steel Transl.*, 2011, vol. 41, pp. 795–8.
22 A. Calvimontes: DOI:10.20944/preprints201708.0062.v2.
23 Hondros E. D., McLean M., Mills K. C., Hibiya Taketoshi, Nakamura Shin, Mukai Kusuhiro, Niu Zheng–Gang, Imaishi Nobuyuki, Nishizawa Shin–ichi, Yoda Shin–ichi, and Koyama Masato: *Philos. Trans. R. Soc. Lond. Ser. Math. Phys. Eng. Sci.*, 1998, vol. 356, pp. 899–909.
24 R. Brooks, I. Egry, S. Seetharaman, and D. Grant: *High Temp.-High Press.*, 2001, vol. 33, pp. 631–7.
25 M. Wegener, L. Muhmood, S. Sun, and A.V. Deev: *Metall. Mater. Trans. B*, 2015, vol. 46, pp. 316–27.
26 L. Muhmood, N.N. Viswanathan, and S. Seetharaman: *Metall. Mater. Trans. B*, 2011, vol. 42, pp. 460–70.
27 E.-J. Kim, B.-D. You, and J.-J. Pak: *Metall. Mater. Trans. B*, 2003, vol. 34, pp. 51–9.

# Paper II

*14th International Conference on CFD In Oil & Gas, Metallurgical and Process Industries*
*SINTEF, Trondheim, NORWAY*
*October 12-14, 2020*

# INVERSE MODELLING OF INTERFACIAL TENSION BETWEEN FERROALLOY AND SLAG USING OPENFOAM

**Sergey BUBLIK**[1*], **Kristian Etienne EINARSRUD**[1†]
[1]Department of Materials Science and Engineering, Norwegian University of Science and Technology (NTNU), Trondheim, NORWAY

[*] E-mail: sergey.bublik@ntnu.no
[†] E-mail: kristian.e.einarsrud@ntnu.no

## ABSTRACT

The entrainment of molten ferroalloy droplets in slag during tapping operations is strongly related to turbulence and interfacial forces between alloy and slag. Therefore, interfacial phenomena are of great importance for the ferroalloys industry and a better understanding of entrainment mechanisms can reduce ferroalloy losses with slag flow. The interfacial tension plays an important role in the interaction between ferroalloy and slag due to the ability to modify droplets shape and the flow regime. However, the measurement of interfacial tension between two molten phases is challenging due to high temperatures and complex composition. In particular, surface active elements significantly influence the interfacial tension. Available methods for determining the interfacial tension are often based on using complex equipment (e.g. a furnace equipped with an X-ray camera) and tend to have significant uncertainty in measurements. In this study, a methodology for inverse modelling of interfacial tension between ferroalloys and slag was developed and investigated by combining experimental measurements, reduced order modelling and simulations in OpenFOAM. The proposed method relies upon experimental determination of the shape of single droplets, from which surface tension can be determined using numerical procedures such as elliptic fitting and the low-bond axisymmetric drop shape technique. Given relevant material properties for single phases, parameters governing the interactions between the phases, e.g. interfacial tension, can be determined by comparing parametric simulations to experiments in which interactions are present. Simulations are realized using multiphaseInterFoam for a slag droplet at rest on molten metal in an inert atmosphere. The current work describes the modelling strategy and demonstrates its applicability to recent experiments for the FeMn-slag system. The uncertainty and sensibility of the method are assessed by comparing different available simulation settings, resolution and the uncertainty in the experimental data.

**Keywords:** Inverse modelling, interfacial phenomena, interfacial tension, slag metal separation.

## NOMENCLATURE

*Greek Symbols*

| | |
|---|---|
| $\alpha$ | Phase fraction within the range $0 < \alpha < 1$. |
| $\gamma$ | Surface or interfacial tension, $[N/m]$. |
| $\theta$ | Contact angle, $[°]$. |
| $\mu$ | Dynamic viscosity, $[Pa \cdot s]$. |
| $\nu$ | Kinematic viscosity, $[m^2/s]$. |
| $\rho$ | Density, $[kg/m^3]$. |
| $\Delta\rho$ | Density difference between two phases, $[kg/m^3]$. |

*Latin Symbols*

| | |
|---|---|
| $a$ | Length of the semi-major axis of an ellipse, $[m]$. |
| $b$ | Length of the semi-minor axis of an ellipse, $[m]$. |
| $c$ | Capillary constant, $[m^{-2}]$. |
| $g$ | Gravitational acceleration, 9,81, $[m/s^2]$. |
| $h$ | Height, $[m]$. |
| $m$ | Weight, $[kg]$. |
| $P$ | Pressure, $[Pa]$. |
| $\Delta P$ | Pressure difference across the interface, $[Pa]$. |
| $\Delta P_0$ | Pressure difference at a reference plane, $[Pa]$. |
| $R_0$ | Radius of curvature at the droplet apex, $[m]$. |
| $R_1, R_2$ | Principal radii of curvature, $[m]$. |
| $U$ | Fluid velocity, $[m/s]$. |
| $U_r$ | Compression velocity, $[m/s]$. |
| $V$ | Volume, $[m^3]$. |
| $x$ | Position vector, $[m]$. |

*Sub/superscripts*

| | |
|---|---|
| $n$ | Phase. |
| $exp$ | Corresponding to experiments. |
| $sim$ | Corresponding to simulations. |
| $vis$ | Visible. |
| $non-vis$ | Non-visible. |
| $slag$ | Corresponding to slag. |
| $FeMn$ | Corresponding to FeMn. |
| $Ar$ | Corresponding to argon atmosphere. |
| $slag-Ar$ | Interface between slag and Ar. |
| $FeMn-Ar$ | Interface between FeMn and Ar. |
| $FeMn-slag$ | Interface between FeMn and slag. |

## INTRODUCTION

Ferroalloys are widely used to improve various properties of steels and alloys, for example, hardness, ductility and corrosion resistance (Holappa, 2013). Ferroalloys are produced mainly by carbothermic reduction in submerged arc furnaces (SAFs), where raw materials are heated up by applying the electric current to electrodes. Raw materials in the production of ferroalloys are complex in chemical composition and therefore all other elements, which do not end up in the alloy phase, need to be separated from the alloy and removed as the slag. The removal of molten material (a mixture of slag and alloy) is carried out through an operation which is called tapping. During this operation, the SAF is opened by a drilling machine and thereafter the molten material comes out from the furnace into a cascade of ladles (Tangstad, 2013). The first ladle in the cascade is used for separation of slag and alloy due to the density differences, and storing the alloy, while the following ladles are used only for the slag (Fig. 1). The molten flow typically disintegrates after the impact with either the surface of the alloy ladle or the molten material due to turbulence and interfacial forces between alloy and slag (Lee, 2016). It results in the formation and entrainment of small alloy droplets in slag phase, which then overflows to slag ladles, contributing to the alloy losses. For this reason, the interfacial phenomena are vital for the ferroalloys industry and a better understanding of entrainment mechanisms can reduce ferroalloy losses with slag flow.

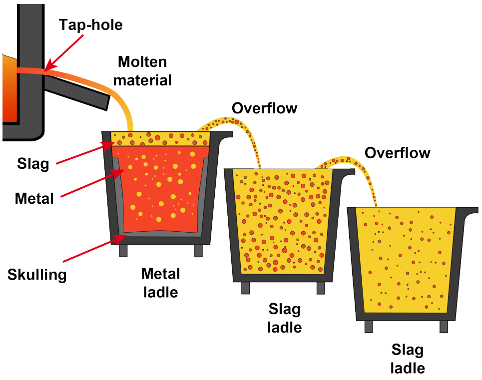

**Figure 1:** Tapping of the SAF.

The interfacial tension characterizes the interaction between slag and metal and the stability of the interface between slag and alloy (Ooi *et al.*, 1974). High interfacial tension results in better separation, while its lower values promote the formation of slag-metal emulsion. Furthermore, surface active elements, which can significantly reduce the interfacial tension, are typically present in molten systems (Li *et al.*, 2003). In ferroalloys production, the surface active elements are represented by sulphur and oxygen. The thermodynamic equilibrium between alloy and slag is described by the reaction (Saridikmen *et al.*, 2007):

$$[S] + (O^{2-}) \Leftrightarrow (S^{2-}) + [O], \qquad (1)$$

where $[S], [O]$ are sulphur and oxygen in alloy, $(S^{2-}), (O^{2-})$ are sulphur and oxygen in slag.

In addition, the interfacial tension can affect the terminal (settling) velocity of alloy droplets in slag phase. Droplets can have various regimes (Clift *et al.*, 1978), which are based on physical properties such as density, interfacial tension and viscosity. Hence, depending on the regime, the surface area of a droplet can be significantly different from its initial shape, meaning that the drag force which acts in the flow direction will also be affected by the regime.

Experimentally, surface and interfacial tension between two molten materials are determined by melting materials in a furnace equipped with an X-ray camera (Jakobsson *et al.*, 2000) or by applying the sessile drop technique with a digital camera (Kim *et al.*, 2010). After recording images from interfacial interaction between two different phases and a gas, surface or interfacial tension are obtained by the numerical solution of the Young-Laplace equation. However, in most cases, the measurement of interfacial/surface tension is extremely complicated due to high temperatures and complex composition of materials.

The equilibrium in the three-fluid interaction is described schematically as shown in Fig. 2a and consequently the surface and interfacial tension vectors are characterized by applying the Neumann vectorial triangle (Fig. 2b). At the equilibrium the sum of surface forces equals to zero, therefore the force balance for all interfaces (αβ, αδ, βδ) is written as (Rowlinson and Widom, 2002):

$$\begin{aligned} \gamma_{\alpha\beta} + \gamma_{\beta\delta}\cos\beta + \gamma_{\alpha\delta}\cos\alpha &= 0 \\ \gamma_{\alpha\beta}\cos\beta + \gamma_{\beta\delta} + \gamma_{\alpha\delta}\cos\delta &= 0 \qquad (2) \\ \gamma_{\alpha\beta}\cos\alpha + \gamma_{\beta\delta}\cos\delta + \gamma_{\alpha\delta} &= 0, \end{aligned}$$

where $\gamma_{\alpha\beta}$, $\gamma_{\alpha\delta}$, $\gamma_{\beta\delta}$ is the tension of the $\alpha\beta$, $\alpha\delta$, $\beta\delta$ interface, respectively.

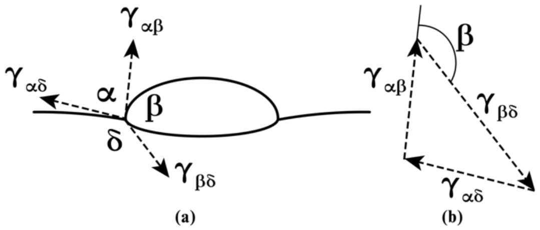

(a) (b)

**Figure 2:** (a) The equilibrium between a fluid droplet, resting on the interface between two fluids of different densities, (b) the Neumann's triangle; $\gamma_{\alpha\beta}$ corresponds to surface tension between slag and gas, $\gamma_{\alpha\delta}$ corresponds to surface tension between FeMn alloy and gas, $\gamma_{\beta\delta}$ corresponds to interfacial tension between FeMn alloy and slag.

Based on the law of cosines, the force balance can be rewritten in order to obtain a numerical value of $\cos\beta$:

$$\cos\beta = \frac{\gamma_{\alpha\delta}^2 - \gamma_{\alpha\beta}^2 - \gamma_{\beta\delta}^2}{2\gamma_{\alpha\beta}\gamma_{\beta\delta}}. \qquad (3)$$

A methodology allowing for the observations of interfacial flow between ferromanganese alloys (FeMn) and slag, was developed by the authors (Bublik *et al.*, 2019), based on experiments using a sessile drop furnace and recording of images.

In this work, the interfacial tension between FeMn alloy and slag has been determined based on a new inverse modelling strategy, combining simulations with analysis of images from the sessile drop furnace. The model applicability and sensibility has been studied and discussed by comparing different settings in OpenFOAM and the uncertainty in experimental data.

## METHOD DESCRIPTION

### *A. Materials preparation*

The synthetic FeMn alloy and slag for experiments in the sessile drop furnace were prepared from pure powders according to the industrial composition (Table 1). The powders were mixed and melted separately in a graphite crucible in an induction furnace in Ar atmosphere at 1773 K, 60 min of holding for FeMn and 5 min of holding for slag. After the first melting, both FeMn and slag were removed from the crucible, ground into small pieces in a ball mill and then remelted in the graphite crucible in the induction furnace at the same operational parameters.

**Table 1:** Chemical composition of materials used for the experiments in the sessile drop furnace.

| Material | Chemical composition, wt. % | | | | | | | |
|---|---|---|---|---|---|---|---|---|
| | Mn | Fe | C | MnO | CaO | MgO | $SiO_2$ | $Al_2O_3$ |
| HC FeMn | 78 | 15 | 7 | - | - | - | - | - |
| FeMn slag | - | - | - | 38 | 23 | 6 | 23 | 10 |

*B. Experimental setup*

The sessile drop technique was applied in order to determine surface tension of alloy/slag and to investigate the interfacial behaviour between FeMn and slag:

- In experiments, where *surface tension* was measured, a piece of slag or FeMn alloy was placed on a graphite substrate (ISO-88) as shown in Fig. 3 and Fig. 4, the furnace is heated up and images of interaction between slag-graphite or alloy-graphite were recorded. Thereafter, the images were analyzed by means of the Young-Laplace equation.

- In experiments for measurement of *interfacial interaction*, small FeMn pieces were placed in a graphite cup (Fig. 5) and a slag piece was placed on top of the FeMn layer. Subsequently, the interfacial tension is measured by inverse modelling in OpenFOAM.

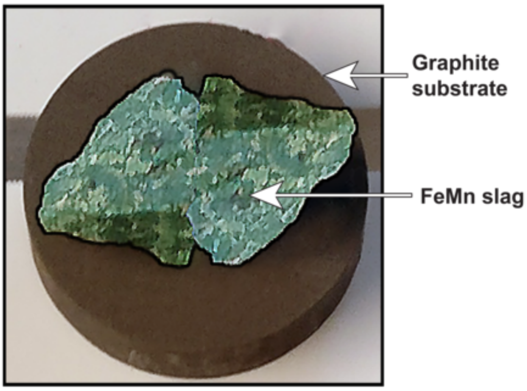

**Figure 3:** Slag on a graphite substrate before experiments for measurement of surface tension in the sessile drop furnace.

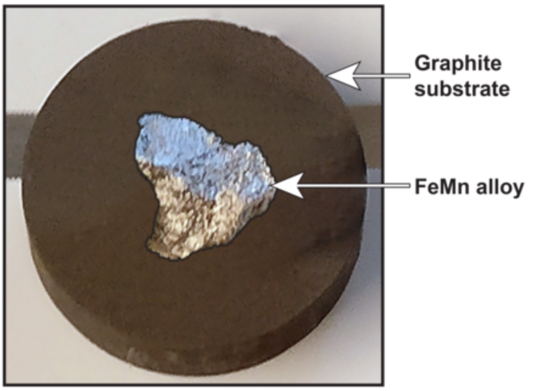

**Figure 4:** FeMn alloy on a graphite substrate before experiments for measurement of surface tension in the sessile drop furnace.

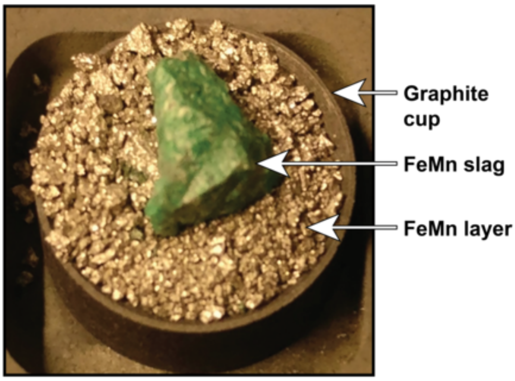

**Figure 5:** Slag on top of FeMn pieces in a graphite cup before experiments for measurement of interfacial tension in the sessile drop furnace.

The sessile drop furnace (Fig. 6) was equipped with a digital video camera (Sony XCD-SX910CR, Sony Corporation, Millersville, MD) with a telecentric lens (Navitar 1-50993D) to record images from the molten samples with the resolution of 1280x1024 pixels. The experiments were done at the maximum temperature of 1623, 1673, 1723 K and holding time of 5, 10, 15 min.

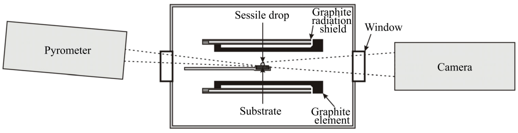

**Figure 6:** Schematic illustration of the sessile drop furnace.

*C. Methodology for inverse modelling*

The methods consist of the followings steps:

a) Conduct experiments with a single slag or FeMn alloy droplet and determine the *surface tension* of each phase.

b) Conduct experiments in the sessile drop furnace with FeMn layer and a slag piece on top.

c) Conduct simulations in OpenFOAM for a certain range of interfacial tension using densities of FeMn alloy and slag in the molten state, weight of the slag droplet and surface tensions determined from step *a)*.

d) Calculate visible (or non-visible) height of the slag droplet (in %) both for experiments and simulations. Compare experimental and simulation values to determine *interfacial tension*.

## Determination of surface tension

The Young-Laplace equation describes the relationship between the curvature of a droplet and surface tension:

$$\Delta P = \gamma \left( \frac{1}{R_1} + \frac{1}{R_2} \right). \tag{4}$$

If external forces are not applied on a droplet, except of the gravity, the pressure difference is expressed as:

$$\begin{aligned} \Delta P &= \Delta P_0 + \Delta \rho g h \\ &= \frac{2\gamma}{R_0} + \Delta \rho g h. \end{aligned} \tag{5}$$

a) Surface tension of slag is determined by the elliptic solution of the Young-Laplace equation (Hernandez-Baltazar and Gracia-Fadrique, 2005), implemented in MATLAB. Surface tension (in N/m) is determined from the expression:

$$\gamma = \frac{a^2 (\rho_{slag} - \rho_{Ar}) g}{\frac{a^3}{b^3} + \frac{a}{b} - 2}, \tag{6}$$

where the values of the semi-major axis $a$ and the semi-minor axis $b$ are obtained from image analysis of slag droplets in experiments, after fitting an ellipse to the slag curvature (Fig. 7). The elliptic solution fails if contact angle ($\theta$) between the droplet and the substrate is lower than 90°, giving wrong values for surface tension. In addition, there is a significant uncertainty in measurements by this method if droplet's surface during experiments is rough.

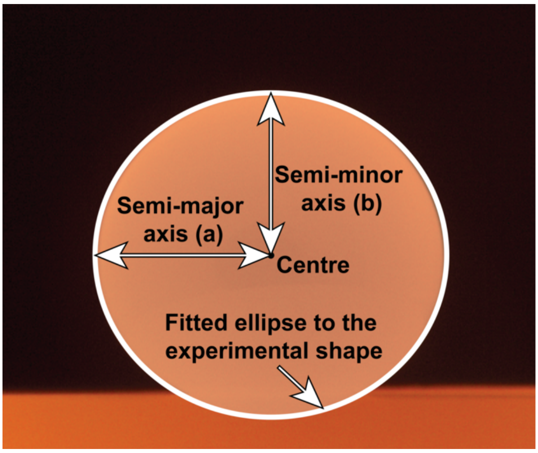

**Figure 7:** Ellipsoidal fitting to the slag droplet during experiments in the sessile drop furnace.

b) The contact angle between FeMn alloy and the graphite substrate is lower than 90°, and the surface roughness is high (Fig. 8). For this reason, surface tension of FeMn alloy is measured by a plugin for ImageJ (Rueden *et al.*, 2017), which is based on the low-bond axisymmetric drop shape analysis (LBADSA) (Stalder *et al.*, 2010). The plugin extracts parameters of droplet's contour after the fitting of the Young-Laplace equation to the image data (Fig. 9). The output from the plugin is the capillary constant $c$, which is related to surface tension of FeMn ($\gamma$) through the equation:

$$c = \frac{(\rho_{FeMn} - \rho_{Ar}) g}{\gamma}. \tag{7}$$

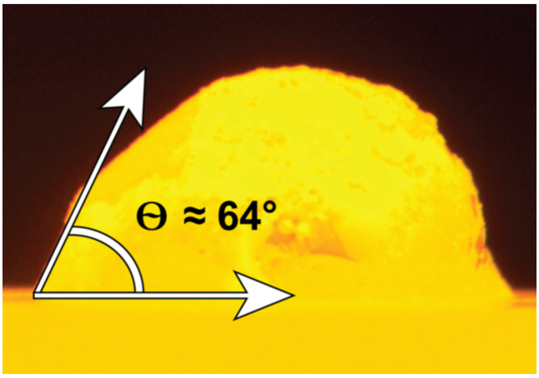

**Figure 8:** FeMn alloy surface during experiments in the sessile drop furnace.

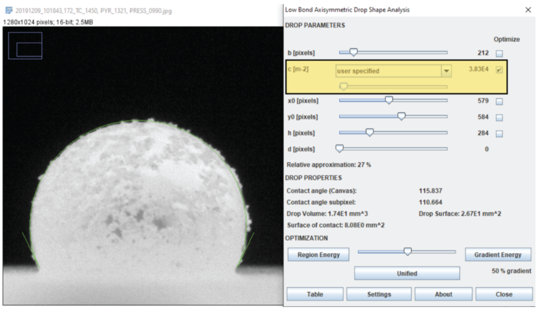
20191209_101843,172_TC_1450, PYR_1321, PRESS_0990.jpg
1280x1024 pixels; 16-bit; 2.5MB

Low Bond Axisymmetric Drop Shape Analysis

DROP PARAMETERS

| | | Optimize |
|---|---|---|
| b [pixels] | 212 | ☐ |
| c [m-2] user specified | 3.83E4 | ☑ |
| x0 [pixels] | 579 | ☐ |
| y0 [pixels] | 584 | ☐ |
| h [pixels] | 284 | ☐ |
| d [pixels] | 0 | |

Relative approximation: 27 %

DROP PROPERTIES

Contact angle (Canvas): 115.837
Contact angle subpixel: 110.664
Drop Volume: 1.74E1 mm^3
Drop Surface: 2.67E1 mm^2
Surface of contact: 8.08E0 mm^2

OPTIMIZATION

50 % gradient

**Figure 9:** Fitting and measurement of parameters of a FeMn droplet from the image data by LBADSA plugin for ImageJ.

## Simulations using multiphaseInterFoam

Simulations were carried out in OpenFOAM 6 (Weller *et al.*, 1998) using *multiphaseInterFoam*, a solver for $N$ incompressible fluids which captures the interfaces and includes surface tension and contact angle effect for each phase, with optional mesh motion and topology changes.

multiphaseInterFoam is based on the volume-of-fluid (VOF) method (Hirt and Nichols, 1981), where a transport equation is applied to define the volume fraction $\alpha_n$ of each of the phases (Andersson, 2010). The transport equation is solved with the continuity and momentum equation for each phase (Damian, 2012). The continuity equation is defined as:

$$\nabla \cdot \mathbf{U} = 0. \tag{8}$$

The transport equation for $\alpha$ is:

$$\frac{\partial\alpha}{\partial t} + \nabla\cdot(\mathbf{U}\alpha) + \nabla\cdot[\mathbf{U}_r\alpha(1-\alpha)] = 0, \tag{9}$$

and the momentum equation is expressed as:

$$\frac{\partial(\rho\mathbf{U})}{\partial t} + \nabla\cdot(\rho\mathbf{U}\mathbf{U}) = -\nabla p + \mathbf{g}\cdot\mathbf{x}\nabla\rho + \mu\left[\nabla\mathbf{U} + (\nabla\mathbf{U})^T\right] + \gamma\kappa\nabla\alpha, \tag{10}$$

where $\mu\left[\nabla\mathbf{U} + (\nabla\mathbf{U})^T\right]$ is the viscous term, $\gamma\kappa\nabla\alpha$ is surface tension force per unit volume, which is based on the continuum surface force model (Berberovic *et al.*, 2009), $\kappa$ is the mean curvature of the free surface:

$$\kappa = -\nabla\cdot\left(\frac{\nabla\alpha}{|\nabla\alpha|}\right). \tag{11}$$

The mixture density ($\rho$) and viscosity ($\mu$) are calculated as weighted averages based on the phase fraction in a control volume, i.e.:

$$\rho = \sum_n \rho_n\alpha_n \tag{12}$$

and

$$\mu = \sum_n \mu_n\alpha_n. \tag{13}$$

Evidently, cells with only a single phase, retain the material properties of the phase in question.

## Reduced order modelling

In order to determine the interfacial tension between slag and alloy, the non-visible height of droplets (in %) both in experiments and simulations was calculated by the following procedure:

*A. Procedure for slag droplets in experiments*

1. Measure the weight of the slag droplet before experiments, $m_{slag}$.

2. Calculate the (total) volume of the slag droplet in molten state, $V^{slag}_{total}$:

$$V^{slag}_{total} = \frac{m_{slag}}{\rho_{slag}}. \tag{14}$$

3. The slag droplet resting on top of the FeMn layer is assumed to be a spherical cap both above and below the FeMn-Ar interface as shown in Fig. 10. According to the geometric properties of the spherical cap, $a$ and $h^{exp}_{vis}$ can be obtained directly by measuring corresponding distances, while the height below the interface, $h^{exp}_{non-vis}$, is unknown, and therefore it has to be determined via additional calculations.

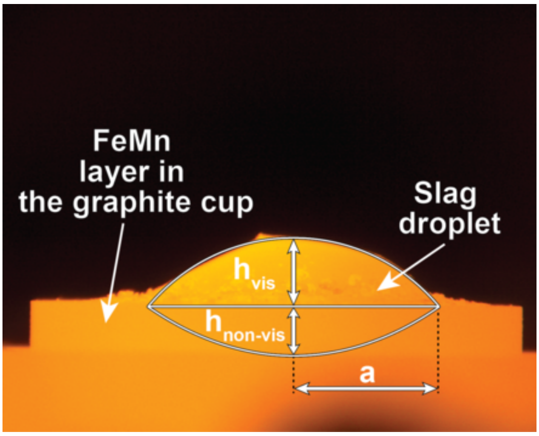

**Figure 10:** Slag droplet on top of FeMn layer in experiments: $a$ is the base radius of the spherical cap, $h_{vis}$ and $h_{non-vis}$ are the height of the spherical cap above and below the interface, respectively.

4. Calculate the visible volume of the slag droplet, $V^{slag}_{vis}$:

$$V^{slag}_{vis} = \frac{1}{6}\pi h^{exp}_{vis}\left(3(a^{exp})^2 + (h^{exp}_{vis})^2\right). \tag{15}$$

5. Calculate the non-visible volume of the slag droplet, $V^{slag}_{non-vis}$:

$$V^{slag}_{non-vis} = V^{slag}_{total} - V^{slag}_{vis}. \tag{16}$$

6. Determine the height of the spherical cap below the interface in *meters*, $h^{exp}_{non-vis}$. In this study, a MATLAB script has been developed, allowing to solve the equation for the volume of a spherical cap (eq. 17) and calculate $h^{exp}_{non-vis}$, given that $a$, $h^{exp}_{vis}$, $V^{slag}_{non-vis}$ are known.

$$V^{slag}_{non-vis} = \frac{1}{6}\pi h^{exp}_{non-vis}\left(3(a^{exp})^2 + (h^{exp}_{non-vis})^2\right). \tag{17}$$

7. Calculate the non-visible height of the slag droplet in %:

$$h^{exp}_{non-vis}(\%) = \frac{h^{exp}_{non-vis}}{h^{exp}_{non-vis} + h^{exp}_{vis}}\cdot 100. \tag{18}$$

*B. Procedure for slag droplets in simulations*

1. In simulations, the height of slag droplets both below and above the interface can be obtained directly from measuring distances as shown in Fig. 11.

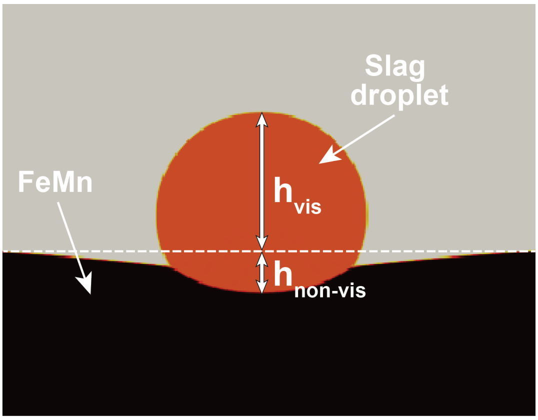

**Figure 11:** Slag droplet on top of FeMn bath in simulations.

2. Calculate the non-visible height of the slag droplet in %:

$$h^{sim}_{non-vis}(\%) = \frac{h^{sim}_{non-vis}}{h^{sim}_{non-vis} + h^{sim}_{vis}} \cdot 100. \tag{19}$$

3. The non-visible height of the slag droplet in simulations obtained from equation *19* is compared with experimental values from equation *18* to find the corresponding non-visible height and thereby also the corresponding interfacial tension, which in the simulations was varied according to a range of expected values.

## EXPERIMENTAL CONDITIONS AND NUMERICAL SETTINGS

### Experimental conditions

The experimental parameters used in experiments in the sessile drop furnace are shown in Table 2.

**Table 2:** Experimental conditions in the sessile drop furnace.

| **Parameter** | **Value in measurement of** | |
|---|---|---|
| | **Surface tension** | **Interfacial tension** |
| $m_{slag}$, g | 0,120 | ≈0,050 - 0,060 |
| $m_{FeMn}$, g | 0,120 | ≈0,300 - 0,350 |
| Ar flow, NLPM | 0,1 | 0,1 |
| Pressure inside the chamber, Pa | 101325 | 101325 |
| Maximum temperature, K | 1723 | 1623, 1673, 1723 |
| Holding time at maximum temperature, min | 5 | 5, 10, 15 |
| Heating rate to 1473 K, K/min | 300 | 300 |
| Heating rate from 1473 K to maximum temperature, K/min | ≈25 | ≈25 |

### Numerical settings and simulation procedure

Simulations were carried out on an axisymmetric 2D geometry as shown in Fig. 12, where the following boundary conditions were applied:

- Left wall - symmetry.
- Right, top and lower wall - no-slip condition with a fixed flux pressure (P = 0 Pa).

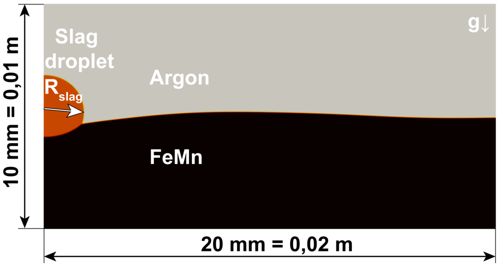

**Figure 12:** 2D axisymmetric geometry applied in simulations. $R_{slag}$ varies from 0,00147 to 0,00163 m (from 1,47 to 1,63 mm), depending on the weight of a slag droplet, and $g$ is the gravity, acting in y-direction.

The initial number of cells in the simulations was 5000. In order to increase the resolution at the interfaces (slag-Ar, FeMn-Ar, FeMn-slag), 2D dynamic mesh refinement (CFD Online Discussion Forums, 2018) was applied, which allows increasing the number of cells up to 20000 for the given simulation setup. All simulations were performed on resourses provided by the NTNU IDUN computing cluster (Sjalander *et al.*, 2019) using modified settings for damBreak4phase tutorial case (cf. The OpenFOAM Foundation, 2016) with multiphaseInterFoam solver, as shown in Table 3. The presence of so-called spurious currents in VOF simulations results in considerable challenges when aiming to reach a static steady state and therefore low values of under-relaxation factors were applied to reduce spurious currents as it was proposed by Vachaparambil and Einarsrud, 2019. Simulations were aiming to reach steady state conditions corresponding to a droplet at rest. As multiphaseInterFoam is a transient solver, transient simulations with dynamic time stepping from $10^{-5}$ to $10^{-6}$ s and the maximum Courant number of 0,25 until 1 s flow time was attained - sufficient to obtain a (quasi) steady state for all simulations considered. The simulations were initialized with a slag droplet with radius from 1,47 to 1,63 mm, depending on the weight of the slag droplet, initially positioned 1,50 mm above the alloy interface.

In addition, a numerical calculation using equation *3* has been carried out to evaluate a relevant range of interfacial tension for the simulations. Values of $\cos\beta$, as illustrated in Fig. 13, are greater than 1 when interfacial tension is smaller than 0,85 N/m. Interfacial tension of 0,85 N/m has therefore been used as the minimum value in simulations, while the maximum interfacial tension is assumed to be identical to surface tension of FeMn - 1,50 N/m.

The physical parameters used in simulations are shown in Table 4.

In order to reduce the effects of spurious currents even more, the viscosity was set to an (artificial) elevated value. Since the steady state is static - the actual value of the viscosity should not impact the final converged result. In order to determine a suitable value for the viscosity - a parametric study was performed, in which the steady state solutions (if found) were compared, according to the values indicated below.

- $10^{-6} \leq \nu_{FeMn} \leq 10^{-2}$ m$^2$/s.

**Table 3:** Numerical solution parameters used in the simulation setup.

**Solution and algorithm control settings (fvSolution)**

| Parameter | Field | | | | | |
|---|---|---|---|---|---|---|
| | **alpha** | **pcorr** | **p_rgh** | **p_rghFinal** | **U** | **UFinal** |
| tolerance | $10^{-6}$ | $10^{-8}$ | $10^{-8}$ | $10^{-9}$ | $10^{-6}$ | $10^{-8}$ |
| relTor | 0 | 0 | 0 | 0 | 0 | 0 |
| maxIter | 100 | - | - | 50 | - | - |
| nAlphaSubCycles | 2 | - | - | - | - | - |
| nAlphaCorr | 2 | - | - | - | - | - |
| MULESCorr | false | - | - | - | - | - |
| cAlpha | 1 | - | - | - | - | - |
| nLimiterIter | 3 | - | - | - | - | - |
| smoother | GaussSeidel | - | - | - | - | - |
| nSweeps | 1 | - | - | - | - | - |
| solver | smoothSolver | - | - | - | - | - |
| relaxationFactors | - | 0,3 | 0,3 | 0,9 | 0,3 | - |

**PIMPLE loop**

| Parameter | Value |
|---|---|
| nCorrectors | 1 |
| nOuterCorrectors | 1 |
| momentumPredictor | false |

**Numerical schemes settings (fvSchemes)**

| Time derivatives | Value |
|---|---|
| ddtSchemes | CrankNicolson 0,50 |

**Time and data input/output control settings (controlDict)**

| Parameter | Value |
|---|---|
| deltaT | $10^{-6}$ |
| maxDeltaT | $10^{-5}$ |
| maxCo | 0,25 |
| maxAlphaCo | 0,25 |

- $10^{-5} \leq \nu_{slag} \leq 10^{-3}$ m²/s.
- $10^{-5} \leq \nu_{Ar} \leq 10^{-3}$ m²/s.

In addition, a parametric study of the mesh resolution, quality of the dynamic mesh refinement (DMR) and geometry size has been carried out to determine the most appropriate parameters to be used in simulations without affecting the results and changing the convergence time significantly. For all simulations in the parametric study, $\gamma_{slag-Ar}$, $\gamma_{FeMn-Ar}$ and $\gamma_{FeMn-slag}$ were 0,70, 1,00 and 0,70 N/m, respectively.

## RESULTS AND DISCUSSION

*A. Surface tension of FeMn alloy and slag*

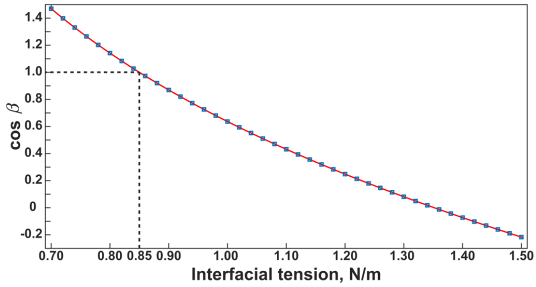

**Figure 13:** Values of $\cos\beta$ calculated by equation *3*.

**Table 4:** Physical parameters applied in simulations.

| Parameter | Value |
|---|---|
| $\rho_{slag}$, kg/m$^3$ | 3300* |
| $\rho_{FeMn}$, kg/m$^3$ | 5612* |
| $\rho_{Ar}$, kg/m$^3$ | 1,66 |
| $\nu_{slag}$, m$^2$/s | varied |
| $\nu_{FeMn}$, m$^2$/s | varied |
| $\nu_{Ar}$, m$^2$/s | varied |
| $\gamma_{slag-Ar}$, N/m | 0,65 |
| $\gamma_{FeMn-Ar}$, N/m | 1,50 |
| $\gamma_{FeMn-slag}$, N/m | 0,85 - 1,50 |

*Density of slag and FeMn alloy in molten state (Muller *et al.*, 2015)

The values surface tension of FeMn alloy and slag, obtained after the experimental measurement, are shown in Fig. 14. Surface tension of FeMn alloy was found to be 1,50 ± 0,05 N/m, while surface tension of slag was considerably lower (0,65 ± 0,01 N/m). From the confidence intervals, it is evident that the LBADSA methodology, which was applied for the measurement of surface tension of FeMn has higher deviation (±0,05 N/m), that the ellipsoidal solution of the Young-Laplace equation, where the confidence interval for surface tension of slag was ±0,01 N/m.

*B. Parametric study: influence of viscosity*

For simulations with $\nu_{FeMn} \leq 10^{-6}$ m²/s, the alloy interface failed to stabilize as indicated in Fig. 15. For values of $10^{-4} \leq \nu_{FeMn} \leq 10^{-2}$ m²/s, the interface was stable, also for a wide range of viscosities for the remaining phases; $10^{-4} \leq \nu_{slag} \leq 10^{-5}$ m²/s and $10^{-3} \leq \nu_{Ar} \leq 10^{-5}$ m²/s, indicated in Fig. 16. Increasing the viscosity further led to unphysical numerical artifacts.

From the parametric study, it was concluded to choose $\nu_{FeMn} = 10^{-4}$ m²/s, $\nu_{slag} = 10^{-5}$ m²/s and $\nu_{Ar} = 10^{-5}$ m²/s. The kinematic viscosity of FeMn differs from the real kinematic viscosity of FeMn, which is usually in the order of $10^{-6}$ m²/s; however, the assumed kinematic viscosity of FeMn should not influence the steady state of the simulations as discussed earlier.

*C. Parametric study: influence of mesh resolution and geometry size*

Studied settings of DMR and mesh resolution, total number

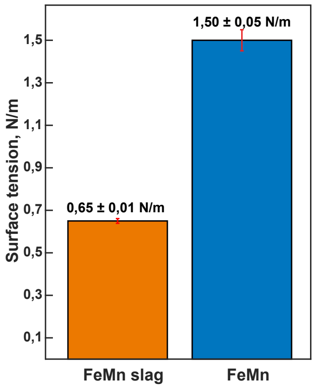

**Figure 14:** Surface tension of FeMn alloy and slag measured experimentally in the sessile drop furnace. Red lines on top of bars are 95 % confidence intervals.

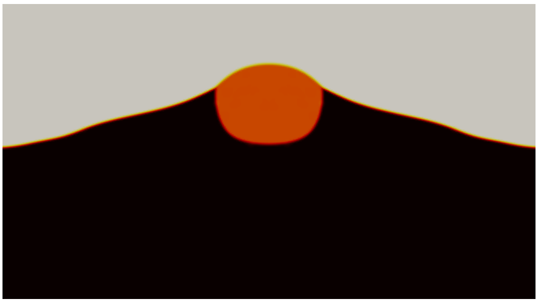

**Figure 15:** Surface instabilities induced by spurious currents.

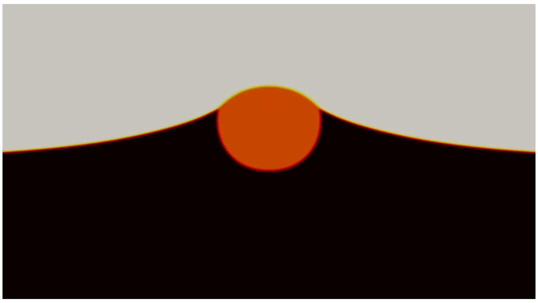

**Figure 16:** The simulation results for the kinematic viscosity: $\nu_{FeMn} = 10^{-4}$ m$^2$/s, $\nu_{slag} = 10^{-4}$-$10^{-5}$ m$^2$/s, $\nu_{Ar} = 10^{-3}$-$10^{-5}$ m$^2$/s.

of cells before and after DMR as well as maximum time step and convergence time are presented in Table 5. In addition, the influence of geometry size has been studied with the parameters as shown in Table 6. Since the non-visible height of the slag droplet is crucial for obtaining the interfacial tension based on the inverse modelling strategy, it has been applied for comparing the steady state in various simulations.

The non-visible height obtained at different time steps in tests of different mesh resolution and DMR quality is shown in Fig. 17. In test A1 and A2, the slag droplet has reached a steady state as represented in Fig. 18, while the convergence time increases with increasing the quality of DMR as well as the total number of mesh cells after DMR increases up to 2,0 and 3,6 times for low (A1) and average (A2) quality of DMR, respectively. On the contrary, test A3 with the highest quality of DMR and test A5 with the highest number of cells after DMR, have instabilities in achieving the steady state, which leads to higher values of the average non-visible height. Similarly to tests A1 and A2, the increasing of mesh resolution in test A4 does not have any influence on the simulation results, however, the convergence time increases to 24784 s. For the proposed simulation setup, the settings from test A2 with average quality of DMR has been chosen as optimal since it requires slightly higher convergence time compared to test A1 with low quality.

The influence of geometry size in x- and y-direction on the non-visible height of the slag droplet is demonstrated in Fig. 19. Tests B2-B5 have shown similar steady results with relatively close values of the average non-visible height, while test B1 has instabilities at the FeMn-Ar interface, resulting in the average non-visible height two times higher compared to other simulations. Test B2 has been chosen as optimal since it requires the lowest convergence time compared to tests B3-B5 with higher geometry size.

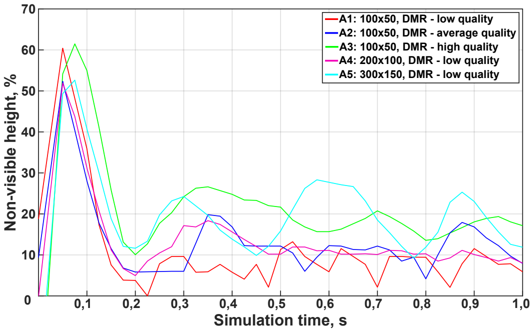

**Figure 17:** Effect of mesh resolution and DMR quality on the non-visible height of slag droplet in the parametric study. The average non-visible height in percent at the steady state (after 0,2 s of simulation time) for each test is: A1 - 7,4; A2 - 11,2; A3 - 18,9; A4 - 11,2; A5 - 18,4.

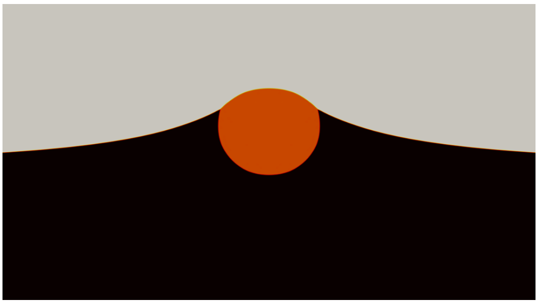

**Figure 18:** The steady state of slag droplet reached in simulations in the parametric study.

### *D. Interfacial tension between FeMn alloy and slag*

Fig. 20 shows the simulation matrix obtained after performing simulations with various values of interfacial tension and parameters as shown in Table 4, with viscosities and resolution as determined in previous sections. The corresponding non-visible height to the values of interfacial tension from 0,85 to 1,50 N/m is illustrated in Fig. 21. The results demon-

**Table 5:** Settings for mesh resolution and DMR quality used in the parametric study.

| Mesh | DMR quality | Mesh resolution, mm$^2$ | Initial total number of cells | Total number of cells after DMR | Maximum time step, s | Convergence time, s |
|---|---|---|---|---|---|---|
| A1 | Low | 0,200 x 0,200 | 5000 | 10000 | $10^{-5}$ | 8541 |
| A2 | Average | 0,200 x 0,200 | 5000 | 18000 | $10^{-5}$ | 14009 |
| A3 | High | 0,200 x 0,200 | 5000 | 44000 | $10^{-5}$ | 52366 |
| A4 | Low | 0,100 x 0,100 | 20000 | 31800 | $10^{-5}$ | 24784 |
| A5 | Low | 0,066 x 0,066 | 45000 | 66500 | $10^{-5}$ | 64886 |

**Table 6:** Geometry size used in the parametric study.

| Mesh | DMR quality | Mesh resolution, mm$^2$ | Geometry size in x-direction, mm | Geometry size in y-direction, mm | Surface area of the geometry, mm$^2$ | Maximum time step, s | Convergence time, s |
|---|---|---|---|---|---|---|---|
| B1 | Low | 0,200 x 0,200 | 10 | 10 | 100 | $10^{-5}$ | 5013 |
| B2 | Low | 0,200 x 0,200 | 20 | 10 | 200 | $10^{-5}$ | 8375 |
| B3 | Low | 0,200 x 0,200 | 20 | 20 | 400 | $10^{-5}$ | 11189 |
| B4 | Low | 0,200 x 0,200 | 20 | 40 | 800 | $10^{-5}$ | 21703 |
| B5 | Low | 0,200 x 0,200 | 50 | 10 | 500 | $10^{-5}$ | 17822 |

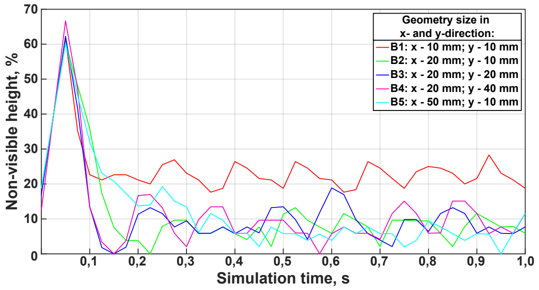

**Figure 19:** Effect of the geometry size on the non-visible height of slag droplet in the parametric study. The average non-visible height in percent at the steady state (after 0,2 s of simulation time) for each test is: B1 - 22,3; B2 - 7,4; B3 - 9,0; B4 - 8,8; B5 - 7,4.

strate that the slag droplet remains above the interface at relatively high values of interfacial tension (≈1,20 - 1,50 N/m), which promotes better separation of FeMn alloy and slag and therefore less metal losses. The slag droplet begins to sink down below the interface at intermediate interfacial tension (≈0,85 - 1,15 N/m), contributing to emulsification of FeMn and slag.

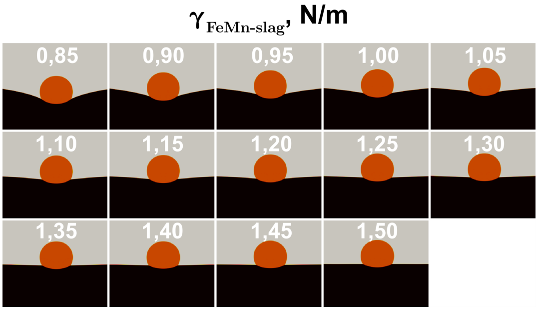

**Figure 20:** The simulations results, depending on interfacial tension between FeMn alloy and slag from 0,85 to 1,50 N/m.

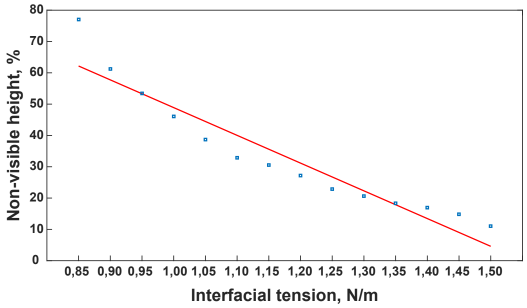

**Figure 21:** Effect of interfacial tension on the non-visible height in the simulations.

The simulations shown in Fig. 20 were compared to the non-visible part of slag droplets from corresponding experiments, from which the interfacial tension could be estimated under various conditions. Figure 22 shows a comparison of the non-visible surface to that obtained under simulations under similar conditions. The estimated interfacial tension between FeMn alloy and slag at different temperatures and holding time is presented in Fig. 23 and Fig. 24, respectively. According to Fig. 23, the interfacial tension gradually decreases from 1,50 ± 0,05 N/m to 1,15 ± 0,04 N/m when temperature increases. Fig. 24 shows that the holding time of 5 and 10 min has no effect on the interfacial tension; however, interfacial tension slightly decreases to 1,25 N/m when the holding time is 15 min.

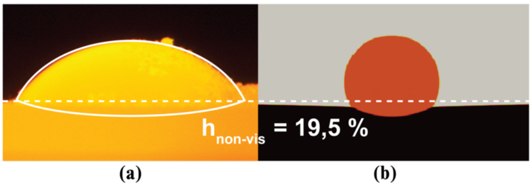

(a) (b)

**Figure 22:** Comparison of the slag surface obtained experimentally at 1673 K (a) and in simulations (b), corresponding to interfacial tension of 1,30 N/m.

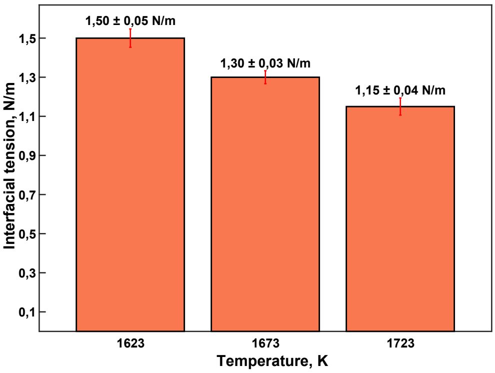

**Figure 23:** Effect of the temperature on interfacial tension between FeMn alloy and slag. Red lines on top of bars are 95 % confidence intervals.

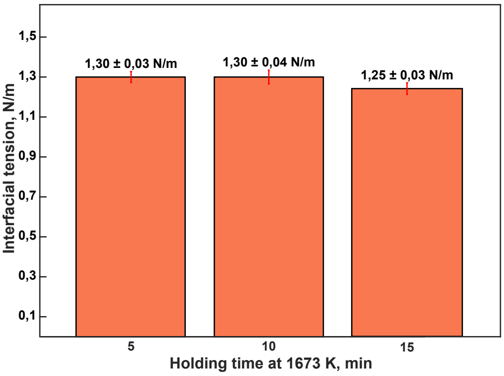

**Figure 24:** Effect of the holding time on interfacial tension between FeMn alloy and slag at constant temperature. Red lines on top of bars are 95 % confidence intervals.

### *F. Previous research on surface tension of FeMn alloy and slag*

Lee *et al.*, 2011 have reported that the surface tension of FeMn alloys without carbon decreases with increasing the Mn content - from ≈1,90 N/m for a pure Fe-system to ≈1,00 N/m for a pure Mn-system. According to their data, the corresponding value of surface tension is 1,10 N/m for the composition used in this study, assuming that no carbon is present in FeMn alloy (≈84 wt. % Mn, ≈16 wt. % Fe). However, they have not studied the influence of carbon on the Fe-Mn system, which can explain the difference in the surface tension of FeMn alloy - 1,10 N/m in Lee *et al.*, 2011 compared to 1,50 N/m in the present work for high-carbon saturated FeMn alloy. Xin *et al.*, 2019 developed a numerical model for calculation of the surface tension of molten slags which predicts that molten slags generally have surface tension in the range from 0,30 to 0,70 N/m, depending on the composition, again corresponding well to that identified in the current work.

While there to our best knowledge is no data for interfacial tension between FeMn alloy and slag, Park *et al.*, 2009 have reported interfacial tension between molten iron and CaO-$SiO_2$-MgO-$Al_2O_3$-FeO slag between 0,72 and 1,44 N/m, depending on slag composition and oxygen content in iron. Surface tension of FeMn slag (0,65 N/m) and interfacial tension between FeMn alloy and FeMn slag (1,15-1,50 N/m), again in the range of that found in the current work.

## SUMMARY AND CONCLUSIONS

The current paper presents a method in which images from a sessile drop furnace are combined with multiphase simulations in order to determine material properties which otherwise are not easily accessible. The method is demonstrated for a FeMn-slag system with constant composition.

The proposed method estimates interfacial tensions of 1,50 ± 0,05 N/m, 1,30 ± 0,03 N/m and 1,15 ± 0,04 N/m at temperatures of 1623, 1673 and 1723 K, respectively. Furthermore, it has been found that changing the holding times from 5 to 15 minutes does not affect the interfacial tension significantly. Surface active elements, such as S, can have a considerable impact on interfacial tension. Although it is not addressed in the current work, experiments considering such effects have been carried out recently, and will be published in the near future (Bublik *et al.*, 2021).

The methodology developed here is demonstrated only for FeMn; however, it is expected that it could also be applied for other processes, i.e. metal refining and for other metals, for instance, SiMn, FeSi, Si and Fe. Future work will explore these possibilities as well as the influence of slag composition for the FeMn system.

## REFERENCES

ANDERSSON, P. (2010). “Tutorial multiphaseInterFoam”. `http://www.tfd.chalmers.se/~hani/kurser/OS_CFD_2010/patrikAndersson/patrikAnderssonReport.pdf`. Accessed: 24.08.2020.

BERBEROVIC, E., VAN HINSBERG, N.P., JAKIRLIC, S., ROISMAN, I.V. and TROPEA, C. (2009). “Drop impact onto a liquid layer of finite thickness: Dynamics of the cavity evolution”. *Phys. Rev. E*, **79**, 036306.

BUBLIK, S., BAO, S., TANGSTAD, M. and EINARSRUD, K.E. (2019). “Slag-metal interactions in the FeMn tapping process: Interfacial properties and wetting”. *Proceedings of the Liquid Metal Processing & Casting Conference 2019*. Birmingham, UK.

BUBLIK, S., BAO, S., TANGSTAD, M. and EINARSRUD, K.E. (2021). “Influence of sulphur on the interfacial behaviour between FeMn alloy-slag and SiMn alloy-slag”. To be presented at MOLTEN 2021.

CFD Online Discussion Forums (2018). “Main Forum”. `https://www.cfd-online.com/Forums/openfoam-community-contributions/118870-2d-adaptive-mesh-refinement-2.html#post703369/`. Accessed: 24.08.2020.

CLIFT, R., GRACE, J. and WEBER, M. (1978). *Bubbles, Drops, and Particles*. Academic Press.

DAMIAN, S.M. (2012). “Description and utilization of interFoam multiphase solver”. *International Center for Computational Methods in Engineering*.

HERNANDEZ-BALTAZAR, E. and GRACIA-FADRIQUE, J. (2005). “Elliptic solution to the Young–Laplace differential equation”. *Journal of Colloid and Interface Science*, **287(1)**, 213 – 216.

HIRT, C. and NICHOLS, B. (1981). “Volume of fluid (VOF) method for the dynamics of free boundaries”. *Journal of Computational Physics*, **39(1)**, 201 – 225.

HOLAPPA, L. (2013). “Chapter 2 - Basics of Ferroalloys”. M. Gasik (ed.), *Handbook of Ferroalloys*. Butterworth-Heinemann, Oxford.

JAKOBSSON, A., SICHEN, D., SEETHARAMAN, S. and NURNI, V. (2000). "Interfacial phenomena in some slag-metal reactions". *Metallurgical and Materials Transactions B*, **31**, 973–980.

KIM, H., KIM, J. and SASAKI, Y. (2010). "The role of molten slag in iron melting process for the direct contact carburization: Wetting and separation". *ISIJ international*, **50**, 1099–1106.

LEE, J.J.E. (2016). "Droplet formation mechanisms in metallurgical processes".

LEE, J., SHIN, M. *et al.* (2011). "Density and surface tension of liquid Fe-Mn alloys". *Metallurgical and Materials Transactions B*, **42(3)**, 546–549.

LI, Z., ZEZE, M. and MUKAI, K. (2003). "Surface tension and wettability of liquid Fe-16 mass%Cr-S alloy with alumina". *Materials Transactions*, **44(10)**, 2108–2113.

MULLER, J., ZIETSMAN, J. and PISTORIUS, P. (2015). "Modeling of manganese ferroalloy slag properties and flow during tapping". *Metallurgical and Materials Transactions B*, **46**.

OOI, H., NOZAKI, T. and YOSHII, H. (1974). "The effect of chemical reactions on the interfacial tension between iron and CaO-$SiO_2$-$Al_2O_3$ slag". *Transactions of the Iron and Steel Institute of Japan*, **14(1)**, 9–16.

PARK, S.C., GAYE, H. and LEE, H.G. (2009). "Interfacial tension between molten iron and CaO–$SiO_2$–MgO–$Al_2O_3$–FeO slag system". *Ironmaking & Steelmaking*, **36(1)**, 3–11.

ROWLINSON, J. and WIDOM, B. (2002). *Molecular Theory of Capillarity*. Dover books on chemistry. Dover Publications.

RUEDEN, C.T., SCHINDELIN, J., HINER, M.C., DEZONIA, B.E., WALTER, A.E., ARENA, E.T. and ELICEIRI, K.W. (2017). "ImageJ2: ImageJ for the next generation of scientific image data". *BMC bioinformatics*, **18(1)**, 529.

SARIDIKMEN, H., KUCUKKARAGOZ, C.S. and ERIC, R.H. (2007). "Sulphur behaviour in ferromanganese smelting".

SJALANDER, M., JAHRE, M., TUFTE, G. and REISSMANN, N. (2019). "EPIC: An energy-efficient, high-performance GPGPU computing research infrastructure".

STALDER, A.F., MELCHIOR, T., MULLER, M., SAGE, D., BLU, T. and UNSER, M. (2010). "Low-bond axisymmetric drop shape analysis for surface tension and contact angle measurements of sessile drops". *Colloids and Surfaces A: Physicochemical and Engineering Aspects*, **364(1)**, 72 – 81.

TANGSTAD, M. (2013). *Handbook of Ferroalloys: Chapter 7. Manganese Ferroalloys Technology*. Elsevier Science.

The OpenFOAM Foundation (2016). "OpenFOAM v6 User Guide". `https://cfd.direct/openfoam/user-guide-v6/`. Accessed: 24.08.2020.

VACHAPARAMBIL, K.J. and EINARSRUD, K.E. (2019). "Comparison of surface tension models for the volume of fluid method". *Processes*, **7(8)**, 542.

WELLER, H.G., TABOR, G., JASAK, H. and FUREBY, C. (1998). "A tensorial approach to computational continuum mechanics using object-oriented techniques". *Computers in Physics*, **12(6)**, 620–631.

XIN, J., WANG, N., CHEN, M. and GAN, L. (2019). "Surface tension calculation of molten slag in $SiO_2$–$Al_2O_3$–CaO–MgO systems based on a statistical modelling approach". *ISIJ International*, **59(5)**, 759–767.

# Paper III

ORIGINAL RESEARCH ARTICLE

# A Review of Ferroalloy Tapping Models

SERGEY BUBLIK, JAN ERIK OLSEN, VARUN LOOMBA,
QUINN GARETH REYNOLDS, and KRISTIAN ETIENNE EINARSRUD

Tapping is an important furnace operation in the ferroalloy industry and poses a number of complex and coupled challenges of both practical and economical importance. Owing to the hazardous high-temperature conditions surrounding the tap hole, the application of various modeling techniques allows for development and acquisition of both scientific and engineering knowledge of the process through physical or numerical proxies. In this review, earlier work on modeling of ferroalloy tapping is summarized and main principles of the tapping process and multiphase interaction of slag and metal are discussed and summarized. The main focus is on drainage of slag and alloys, but some attention will also be given to metal loss, metal overflow and health, safety and environment. Our review shows that although considerable progress has been made in computational capability over the last decades, However, it is clear that research and development in the field of ferroalloy furnace tapping remains at a relatively nascent stage. The most progress up to date has happened in the area of so called reduced-order models. Such models are robust and simple, and may be easily fitted to process data from a particular operation in order to develop tailored solutions. Such models are more easily combined with software and instruments, ultimately enabling improved automation, process control and ultimately improved tapping consistency.

https://doi.org/10.1007/s11663-021-02134-5
© The Author(s) 2021

## I. INTRODUCTION

FERROALLOYS refer to different alloys of iron with high content of other elements (*i.e.* Mn, Si, Cr, Ti), used in the production of steels and alloys to improve properties such as strength, ductility, and fatigue or corrosion resistance. The ferroalloy production volume is greatly dependent on steel production, which means that the production of ferroalloys changes alongside steel production. In the period from 1990 to 2010, the total world steel production has increased from 770 to 1400 million tones and, similarly, ferroalloy production has risen from 20 to 45 million tones.[1]

Ferroalloys are mostly produced in submerged arc furnaces (SAF) during carbothermic reduction of oxide raw materials at high temperatures, where the main smelting products are molten metal and slag. A ferroalloy producing furnace is shown in Figure 1 with a schematic of the entire production process as presented in Figure 2.

The processes taking place in the SAF are typically a combination of solid-gas, solid-solid, solid-liquid and liquid-liquid reactions, with an overall reaction "$MO + C \rightarrow M + CO$", *i.e.* producing metal from the corresponding metal oxide, which often can be in multiple oxidation states. In addition to metal, slag is also produced as a by-product in the SAF. The slag in ferroalloy production consists of a mixture of different oxides (*e.g.* MnO, CaO, MgO, $SiO_2$, $Al_2O_3$). The overall process is endothermic, meaning that heat must be supplied to the furnace. The heat required for endothermic reactions, heating the coke bed and to compensate for heat losses is supplied by electrodes, which are submerged in the coke bed. Heating in the SAF takes place by the flow of electricity between the electrodes, through the coke bed and slag to molten metal.[2]

The removal of the molten material from a furnace is performed through a process called tapping. Tapping is the transitional process step where the alloys are transferred from a furnace in which they are produced into a ladle or a set of ladles where further processing may take place. The furnace tapping can be illustrated

---

SERGEY BUBLIK, VARUN LOOMBA, KRISTIAN ETIENNE EINARSRUD are with the Department of Materials Science and Engineering, Norwegian University of Science and Technology (NTNU), 7491 Trondheim, Norway. Contact e-mail: sergey.bublik@ntnu.no JAN ERIK OLSEN is with SINTEF Industry, 7034 Trondheim, Norway. QUINN GARETH REYNOLDS is with the Pyrometallurgy Division, Mintek, Randburg, 2125, South Africa and the Department of Process Engineering at the University of Stellenbosch, Stellenbosch, 7602, South Africa.

Manuscript submitted October 5, 2020; accepted February 22, 2021.

Published online: 23 April 2021

schematically as shown in Figure 3. In the ferroalloy production industry, tap-holes are made from carbon, silicon carbide or other refractory materials.[3–5] Some furnaces operate with a continuous tapping scheme, but most of them are tapped every 2 to 4 hours.[5,6] The tapping operation usually lasts 10-15 min, depending on the size of the furnace and ladles, and consist of several stages:

(A) Tap-hole opening by an automatic or semi-automatic tap-hole drill. Besides that, oxygen lancing can be carried out in case of viscous flow or clogging of the tap-hole. This auxiliary operation supplies oxygen as a source of heat to the tap-hole, thereby melting and penetrating the materials clogging the tap-hole.[7] Excessive lancing is highly undesirable and must be used only when drilling fails because it results in difficulties during next tapping and extensive wear of the tap-hole refractory. This stage often involves manual work of operators near the tap-hole area and therefore is considered a most dangerous operation.[8]

(B) Filling of metal and slag ladles. At this stage, the tapping flow rate is determined by physico-chemical properties of the molten material and the geometry of the furnace and the tap-hole.[9] In addition, the hydrostatic equilibrium plays an important role because it acts as the driving mechanism of tapping. It can be characterized as the balance between three forces: downward force due to the pressure from fluid above in the furnace (pressure), weight of fluid contained in volume (gravity), and upward force due to pressure from fluid below, physical barriers and solid particles (resistance). In the metal ladle, the slag and alloy separate from each other due to density differences, and as soon as it is filled, liquid slag overflows to the slag ladle, often involving a significant amount of alloy droplets.[4]

(C) After the metal ladle is filled with molten alloy, the tap-hole is plugged by a mudgun loaded with a tap-hole clay (mixture of $Al_2O_3$, $SiO_2$ and C).[2,10]

(D) Post-tap-hole processing: slag remaining on top in the metal ladle has to be removed by manual tilting the ladle and skimming off the slag with a mechanical rake.[11] This stage results in additional losses of ferroalloy with slag.

There are several alternative methods for tapping of products from the SAF; combined metal and slag tapping, dedicated metal-slag tapping and slag-only tapping.[4] Each of these methods have different operational difficulties, which may result in non-stable furnace operation and hazardous environmental conditions. This includes, for example, challenges with tap-hole opening due to viscous flow or a significant amount of solid coke particles in the molten flow.

Another important aspect of the furnace tapping is the entrainment of ferroalloy droplets by slag.[13] The interactions between metal and slag are governed by interfacial phenomena, which are characterized by the interfacial tension.[14–16] Surface-active elements (*e.g.* oxygen, sulphur) in the ferroalloy-slag system result in intensive reactions at the alloy-slag interface,[17] which

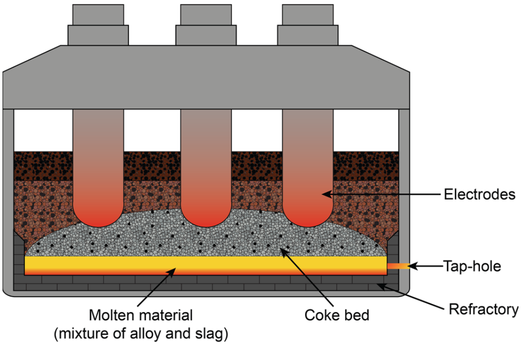

Fig. 1—Schematic of a submerged arc furnace for production of ferroalloys.

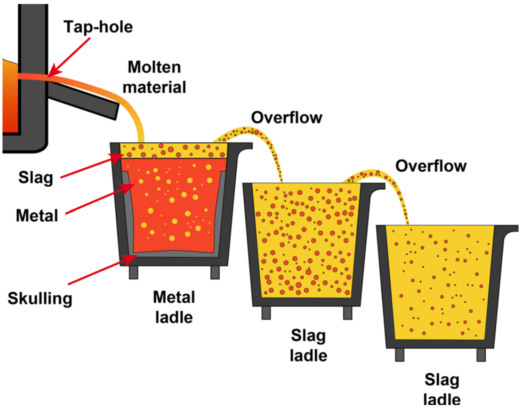

Fig. 3—Tapping of SAF.[12]

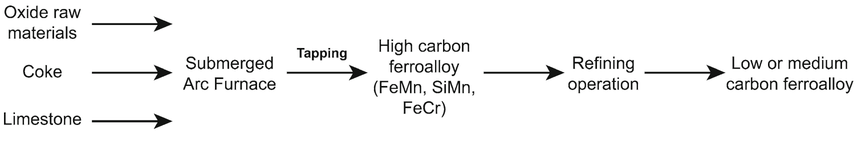

Fig. 2—Simplified ferroalloy production flowsheet.

contribute to a dynamic change of the interfacial tension between alloy and slag until thermodynamic equilibrium is reached.[18,19] This affects metal loss to the slag phase during cascade tapping—see Figure 3.

Different aspects related to tapping of SAFs can be investigated using mathematical models and computational fluid dynamics (CFD).[9,20,21] Such approaches can provide great insight to the operation, and the knowledge gained from properly constructed studies with such tools can ultimately improve the consistency of tapping.

In this review, earlier work on modeling of ferroalloy tapping is summarized and main principles of the tapping process and multiphase interaction of slag and metal are discussed. Moreover, advantages and disadvantages of various approaches are given, followed by an assessment of their general applicability. The main focus is on drainage of slag and alloys, but some attention will also be given to metal loss, metal overflow and issues related to health, safety and environment (HSE). Although the focus of the current work is modeling of ferroalloy tapping SAFs, selected studies on blast furnace tapping models are also discussed, since the drainage mechanisms are very similar. However, this is not a full review of blast furnace tapping models.

## II. PHYSICAL AND NUMERICAL MODELS

Different approaches to modeling of the tapping process in ferroalloy production have been conducted; categorized as physical or mathematical modeling. We will mainly focus on mathematical modeling since the work on physical modeling is very scarce. An experimental setup with a physical representation of the process or phenomena to be studied defines a physical model. For ferroalloy tapping this should in principle involve a drainage experiment with at least one liquid phase and a particle bed. Although several physical drainage experiments have been reported in the literature, few have considered the particle bed.

Nouchi *et al.*[22] performed a drainage experiment resembling a scaled down version of a blast furnace with two liquids (paraffin and fluoride) in a particle bed of plastic beads, highlighting that liquid drainage velocities are dominated by the permeability in front of tap-hole.

A similar study was performed by Vango *et al.*,[23] considering a water tank experiment with spherical wood particles. They designed the experiment such that the particle bed could be sitting or floating. The results showed that a floating particle bed adds weight and thus driving pressure, resulting in faster drainage.

Mathematical models can relate to many aspects of the process including thermochemical properties, material erosion and wear and more. In this paper, we focus on mathematical models for the drainage of slag and metal from the furnace. In addition, it is necessary to differentiate between reduced order modeling and CFD. In principle, CFD can be defined to include all mathematical models describing flow, but here we limit CFD to mathematical models solving the full 3D (or 2D) set of conservation equations for mass and momentum by a numerical algorithm. With reduced order modeling we refer to a modeling scheme where the model complexity is reduced through various assumptions allowing for reduction in solution time and/or data storage. An overview of published work is discussed in the following sections.

### A. *Reduced Order Modeling*

In modeling the draining flow from a furnace, Bernoulli's equation provides a reasonable representation of the flow between two points in a geometry. The equation is based on conservation of mechanical energy along a flow line. Models based on this principle are used in textbooks in Fluid Dynamics with drainage as an example, and all known reduced order models for furnace tapping apply Bernoulli's equation to our best knowledge.

The tapping rate for a tank with a liquid can be estimated by Bernoulli's equation (see *e.g.* Guthrie[24]):

$$\dot{m} = \frac{\rho C_D \pi d^2}{4}\sqrt{2gH} \qquad [1]$$

where $d$ is the diameter of the tap-hole, $\rho$ is the density of liquid, $C_D$ is the drag coefficient, $g$ is the acceleration due to gravity. Here, the hydrostatic head $H$ provides a pressure which is the driving force of tapping. In a furnace, a viscous resistance will be present due to the particle bed of carbon material and ore. The driving force will also be affected by the furnace pressure. The tapping of a submerged arc furnace is therefore more complex than tapping of water through a hole in a tank. Mitsui *et al.*[25] modified the above expression by accounting for a furnace pressure (crater pressure) and by applying the idealized pressure drop through a channel for the pressure drop through the tap-hole:

$$\dot{m} = \frac{\rho \pi d^2}{4}\sqrt{\frac{2gH + P/\rho}{1 + \lambda l/d}} \qquad [2]$$

where $\lambda$ is the wall friction constant of the tap-hole and $l$ is the length of the tap-hole. They did not account for the pressure drop due to the particle bed. The particle bed pressure drop was included in the reduced order model of Nouchi *et al.*[22] and Iida *et al.*[26] for iron and slag tapping from a blast furnace. They also accounted for two liquids (metal and slag) with a mixture model which in principle is a single-phase model, but material properties are derived by an average of the two liquids' properties. Shao and Saxen[27] derived a drainage model for blast furnaces treating the two liquids as segregated immiscible phases. This allowed for separated estimates of metal and slag tapping rates, whereas earlier models only provided a total tapping rate.

All of the above-mentioned work on reduced order modeling was applied towards blast furnaces and steel production. Muller *et al.*[9] applied the modeling concept of Iida *et al.*[26] to manganese ferroalloy tapping and included a substantial study on slag properties. Metal and slag were treated as a mixture and thus a total tapping rate was calculated, not the individual tapping rates of slag and metal. They applied the Kozeny–Carman expression, typically applied in laminar flow, to account for the pressure drop due to the particle bed:

$$\Delta P = \frac{180\mu}{\Phi^2 d_p^2}\frac{(1-\varepsilon)^2}{\varepsilon^3} v_t r_t \qquad [3]$$

where $\mu$ is liquid viscosity, $v_t$ is tapping velocity, $r_t$ is tap-hole radius, $\varepsilon$ is particle bed porosity, $d_p$ is particle diameter and $\Phi$ is particle sphericity. The particle bed resistance is, therefore, accounted for in a similar manner as for a porous material. Olsen and Reynolds[28] also focused on tapping of manganese alloys and published a model for slag and metal tapping where slag and metal were treated as separate phases providing individual tapping rates for these immiscible phases. The Ergun equation, which is applicable to turbulent flow, was used for calculating the pressure drop due to the particle bed:

$$\Delta P = \frac{150\mu}{\Phi^2 d_p^2}\frac{(1-\varepsilon)^2}{\varepsilon^3} v_t r_t + \frac{1.75\rho_m}{3\Phi d_p}\frac{(1-\varepsilon)}{\varepsilon^3} v_t^2 r_t \qquad [4]$$

The results of Olsen and Reynolds[28] indicate that the Ergun equation is more reliable for this application than the Kozeny–Carman equation, since the Reynolds number in the tapping process indicates turbulent flow. Results obtained using the Ergun equation were superior to those obtained with the Kozeny–Carman equation when comparing with the experiments of Vango *et al.*[23]

Table I summarizes the work done in reduced order modeling of tapping flow.

### B. *CFD Modeling*

Computational fluid dynamics (CFD) is the method of numerically solving the equations for conservation of mass, momentum and energy to compute fluid and heat flow.[29] These equations are mathematically represented as follows[30]:

- Conservation of mass

$$\frac{\partial \rho}{\partial t} + \nabla \cdot (\rho u) = 0 \qquad [5]$$

- Conservation of momentum

$$\frac{\partial \rho u}{\partial t} + \nabla \cdot (\rho u u) = -\nabla P + \nabla \cdot \left[\mu_{eff}(\nabla u + (\nabla u)^T)\right] + \rho g + S_u \qquad [6]$$

- Conservation of energy

$$\frac{\partial \rho h}{\partial t} + \nabla \cdot (\rho h u) = -\frac{DP}{Dt} + \nabla \cdot (k \nabla T) + S_h \qquad [7]$$

where $u$ and $\rho$ are the fluid velocity and density, $\mu_{eff}$ is the effective viscosity—accounting also for turbulence, $P$ is the pressure in the fluid, $S_u$ is a momentum source term, $h$ is the enthalpy, $T$ is the temperature, $k$ is the thermal conductivity of the fluid and $S_h$ is a source/sink term accounting for instance for radiation. The effect of the particle bed resistance in the furnace can be included by adding the pressure drop across the bed calculated by the Kozeny–Carman equation (Eq. [3]) or the Ergun equation (Eq. [4]) as the source term $S_u$ to Eq. [6] without affecting the simulation complexity considerably. The interface between the different fluids is often tracked using a Volume of Fluid (VOF) method. Other multiphase flow approaches, such as Euler-Euler and Euler-Lagrangian, are rarely used in tap-hole flow simulations as the interface between the immiscible fluids (metal and slag) is not traced. The Euler-Lagrangian approach, which is also called discrete element method (DEM), has however been used to study the movement of solid particles forming the porous zone.[23]

There are several commercial and open source CFD software available in the market such as Ansys® Fluent,[31] OpenFOAM®,[32] FLOW-3D®,[33] COMSOL Multiphysics®[34] and STAR-CCM+®.[35] Many of them are user-friendly packages with a graphical user interface (GUI), reducing the mathematical and programming complexity. On the other hand, open source software often requires, more programming and mathematical skills, but can provide better control over parameters that need to be solved, as the source code is available and can be modified according to requirements.

CFD has been applied to metallurgical processes since the 1980s but the first work on metal tapping dates to 2001, when Dash *et al.*[36] optimized the length of the tap-hole block inside the furnace to reduce the peak shear stress in the furnace hearth which occurs at the tap-hole due to high velocity of metal. The authors included the effect of porosity *via* the Kozeny–Carman formulation, *i.e.* excluding inertial effects in the porous

**Table I. Overview Over Work Done and Strategies Employed in Reduced Order Modeling of Tapping**

| Article | Entry Losses | Channel Losses | Interface Deformation | Ferroalloy | Porous Model | Phase Model |
|---|---|---|---|---|---|---|
| Mitsui *et al.*[25] | | + | | | | single |
| Nouchi *et al.*[22] | | | + | | Kozeny–Carman | mixed |
| Iida *et al.*[26] | | + | | | Kozeny–Carman | mixed |
| Shao & Saxen[27] | + | + | | | Kozeny–Carman | immiscible |
| Muller *et al.*[9] | | + | | + | Kozeny–Carman | mixed |
| Olsen & Reynolds[28] | + | + | + | + | Ergun | immiscible |

zone. In 2004, Dash *et al.*[37] expanded their research and optimized the angle of tap-block to the horizontal axis to minimize the peak shear stress. Their results showed that a tap-hole block length of 0.75 m and an angle of 15 deg with the horizontal led to minimum peak stress during tapping.

The effect of the particle diameter in the packed bed on tapping rates was studied in 2005 by Nishioka *et al.*[38] As in previous studies, the effect of the particle bed was included using the Kozeny–Carman formulation. The authors reported that the tapping flow rate increases by up to five times when doubling the diameter of the tap-hole. At a constant porosity, changing the particle size from 15 to 60 mm led to a maximum difference of 13 pct for overall tapping rate, while the maximum metal tapping rate decreased by 16 pct and slag tapping rate increased by almost 50 pct. Nishioka *et al.*[39] further simulated the effect of other parameters such as porosity, particle diameter distribution, the presence of an impermeable zone, slag viscosity and presence of a coke free zone on the tapping rates. Changing the porosity from 0.2 to 0.5, resulted in a maximum difference of 12 pct in the overall tapping rate, while the maximum slag tapping rate increased by approximately 10 pct. The metal flow rate decreased insignificantly by these changes. The presence of a coke free zone or impermeable zone of 2.2 m height from the bottom had no effect on the tapping rates. Viscosity was found to have an strong effect on the tapping rates, increasing with 11 pct when the slag viscosity was reduced by 75 pct.

Kadkhodabeigi *et al.*[40] studied tapping of molten silicon and found that the flow in the tap-hole is highly dependent on the conditions inside the furnace. They found an increase in tapping flow rates with increasing crater pressure in a submerged-arc furnace. This study was extended by Kadkhodabeigi *et al.*[20] to include the influence of other parameters such as metal column height and permeability of the packed bed on the tapping flow rate, gassing and tapping time. The effect of the porous particle bed on the flow was considered using the Ergun equation (Eq. [4]). The mass flow rate was almost doubled by increasing the crater pressure from 30 to 200 mbar, while the effect of metal height was less significant as the mass flow rate increased by only 33 pct on increasing the metal column from 4.5 to 12 cm. Finally, a reduction of 60 pct in the permeability of the packed bed (only reducing particle diameter) did not lead to a significant change in the flow rates.

Shao *et al.*[41] simulated the two-phase flow in the tap-hole of a blast furnace for a short period (10 seconds) during which the slag-iron interface falls from above to below the tap-hole. The results show tap-hole flow of iron and slag with a well-defined interface between them during the middle stages of tapping (2-5 seconds). In the beginning and the end of tapping, largely one phase dominates with a wavy interface. A developing velocity profile for iron and slag in the entrance region and fully developed flow in the rest of the tap-hole is also observed.

In 2017, Reynolds and Erwee[42] performed an optimization of the shape of the tap-hole inlet and the launder and visualized their effect on the flow of metal and slag in the tap-hole and ladle respectively. The authors utilized large eddy simulation (LES) to better understand the turbulent effects in the tap-hole and the transition from laminar to turbulent flow. Their results showed that a rounded entrance showed delayed onset of turbulence and v-shaped launder resulted in narrower cross-section of metal falling into the ladle compared to rectangular shaped launder, reducing the chances of re-oxidation. The importance of the tap hole shape was also considered by Kirschen *et al.*,[43] aiming to optimize the design of the tap-hole in an electric arc furnace used for steel production. A conical shaped tap-hole was found to lead to a more stable flow of metal compared to standard cylindrical channel.

Reynolds *et al.*[44] extended their work from 2017[42] by including the presence of a particle bed and analyzed the sensitivity of material properties on tapping rates. The presence of a particle bed in either phase reduced the tapping rates of the respective phase. The particle bed parameters affected the flow rates the most, slag viscosity and metal density were also found to have a significant effect, while the effect of metal viscosity was insignificant. Varying the design parameters such as increasing tap-hole diameter led to a considerable increase in the mass flow rate of the metal and slag, while the length of the tap-hole did not contribute significantly.

Vango *et al.*[23] in 2018 applied the VOF method to solve the flow and interface of a single liquid phase and coupled this to the discrete element method (DEM) in order to account for the particle bed. Their results were validated against their own experimental data. In 2019, the authors extended the study in Vango *et al.*[21] and prepared a database of packed bed states consisting of the bed porosity, mass of the metal/slag and Sauter-mean diameter of the bed particles from the information of metal/slag height, weight of the burden and particle size distribution of the packed bed using the CFD-DEM coupling approach. This database was then used to obtain dynamic packed bed void fraction and solid phase configuration for simulating the flow during tapping. The effect of porosity was modelled by the Koch and Hill drag relation, which has similar properties to the Kozeny–Carman formulation.

Olsen *et al.*[45] demonstrated coupled heat and fluid flow simulation to understand the factors affecting the temperature profile in the tap block and the surrounding region. They reported high effectiveness of water-cooled system compared to natural cooling and high temperatures in the tap block with convection (when metal is being tapped) compared to heat conduction of the refractory material (no tapping).

In addition to the above-mentioned studies on fluid drainage in the tapping process, work has also been conducted on other aspects of tapping. In 2018, Johansen *et al.*[46] modified the tap-hole and the ladle configuration in cascade tapping of ferrochrome to reduce the loss of metal overflowing from the metal- to slag ladles. By reducing the fall height and increasing the angle of the ladle outlet, the metal loss could be reduced by up to a factor of 30. This is consistent with experimental studies from the steel industry by Kim *et al.*[47] and the review of Lee.[48] Some work has also been on safety and environmental issues around the tap-hole. Metal droplets may disperse and re-oxidize during tapping, and suspend as oxides in the air leading to pollution in the working area around the furnace. This issue was addressed by Ravary *et al.*[49] in 2010, suggesting design modifications to the tapping area with an objective of preserving the health of workers, leading to an improved ventilation of dust and process gases. In 2015, the flow patterns of the pollutants exiting from the tap-hole were studied by Ma *et al.*,[50] utilizing CFD-DEM coupling to visualize the dispersion of suspended particles. They observed that high winds in the furnace area leads to faster reduction of the particle content in the environment and compared the effect of different wind speeds and direction.

Table II highlights the application of CFD in the pyrometallurgical field for determination of fluid and heat flow in the furnace hearth as well as in the tap-holes. Fluid flow simulation are frequently performed compared to heat flow simulation because many of the factors affecting the furnace operation are fluid flow related. It can be seen in Table II that the Ergun equation has been applied in recent work as an alternative to Kozeny–Carman, thereby allowing for inclusion of inertial effects on the flow in the packed bed. ANSYS Fluent has historically been the most commonly used simulation software, while open source CFD software such as OpenFOAM and CFDEM[51] have received attention more recently.

### C. *Conceptual Model for Tapping*

From the knowledge and findings given in the literature cited above, it is possible to design an outline of a conceptual model for furnace tapping. There are still details which have to be studied, but the main principles are starting to be revealed.

For drainage of slag and metal through a tap-hole, it is known from the models that the hydrostatic pressure head is the driving mechanism of drainage and therefore the molten bath level as well as gas pressure are of great importance for tapping. Pressure created from gas producing reactions vary between different ferroalloy production processes, meaning that the gas contribution is insignificant for certain ferroalloys, while for others it should not be neglected. However, the hydrostatic pressure head from slag and metal is the dominating driving force. This has been shown by several CFD studies, but it can also be seen from Eq. [1] based on Bernoulli's principle for the tapping rate. It is evident from this equation that liquid density is the most significant material property affecting the tapping process—heavy liquids will drain faster from the tap-hole than light liquids owing to gravity. Moreover, the tapping rate directly depends on the tap-hole diameter—a bigger opening will naturally promote a higher tapping rate.

For tapping of slag and metal from a furnace, we need to look beyond Bernoulli's equation in its simplest form since two immiscible liquids are present and they reside in a particle bed. The particle bed forms a resistance to the flow which reduces the tapping flow rate. The resistance is given by the particle size, particle packing (*i.e.* bed porosity), the liquid viscosity and the liquid density. It is much easier for a gas than a highly viscous slag to flow through a particle bed. The resistance increases with decreasing particle size and decreasing porosity. Studies with both CFD and reduced order models show that most of the particle bed resistance is found in the region near the tap-hole. This is explained by the acceleration of slag and metal happening in that region as it converges into a narrow tap-hole.

Since the two liquids are immiscible, they will drain with different tapping rates. Normally the lower liquid, which for most smelting processes is metal, will drain first. It will stop draining once the level goes beneath the tap-hole level. However, if the level of the metal is below the tap-hole upon the start of the tapping, metal may

**Table II. Overview Over Work Done and Strategies Employed in CFD Simulations of the Tapping Process**

| | Flow | | | | | | | |
|---|---|---|---|---|---|---|---|---|
| Article | Fluid | Heat | 3D | Transient | Multiphase | Ferroalloy | Software | Porosity |
| Dash *et al.*[36] | + | | + | | | | Phoenics | Kozeny–Carman |
| Dash *et al.*[37] | + | | + | | | | Phoenics | Kozeny–Carman |
| Nishoka *et al.*[38] | + | | + | + | + | | | Kozeny–Carman |
| Nishoka *et al.*[39] | + | | + | + | + | | | Kozeny–Carman |
| Kirschen *et al.*[43] | + | | + | + | + | | Ansys Fluent | |
| Kadkhodabeigi *et al.*[40] | + | | + | + | + | + | Ansys Fluent | Ergun |
| Ravary *et al.*[49] | + | | + | + | | + | Ansys Fluent | |
| Kadkhodabeigi *et al.*[20] | + | | + | + | + | + | Ansys Fluent | Ergun |
| Shao *et al.*[41] | + | | + | + | + | | Ansys Fluent | |
| Ma *et al.*[50] | + | | + | + | + | + | Ansys Fluent | |
| Johansen *et al.*[46] | + | | + | + | | + | Ansys Fluent | |
| Olsen *et al.*[45] | + | + | + | + | + | + | Ansys Fluent | |
| Vango *et al.*[23] | + | | + | + | + | | CFDEM®coupling | |
| Reynolds *et al.*[44] | + | | | + | + | + | OpenFOAM | Ergun |
| Vango *et al.*[21] | + | | | + | + | | OpenFOAM | Koch and Hill |

not be tapped at all. The upper liquid, *i.e.* slag, will normally start draining after metal starts to drain. It should be noted that slag and metal will drain simultaneously if the interface between them is somewhat close to the height levels covered by the tap-hole. This feature is illustrated in Figure 4,[28] where tapping rates for slag and metal in a FeMn furnace are plotted for a case with initial metal and slag levels of 30 cm each. Both slag and metal are tapped simultaneously throughout the given time interval, while their tapping rates are not equal. Metal has a higher tapping rate in the beginning of the tap, and towards the end, the metal tapping stops while slag continuous to be tapped. This applies to slag and metal being tapped through a single tap-hole.

It should also be noted that the interface between slag and metal and slag and gas is not flat. Due to the drainage velocities a suction force (*i.e.* dynamic pressure) causes the interface to deform towards the tap-hole. This will cause slag to tap earlier than expected from its average level, while metal tapping will take longer. This is illustrated in Figure 5 which is created from a CFD simulation. This will result in slag tapping occurring earlier than expected from its average level, and metal tapping will take longer.

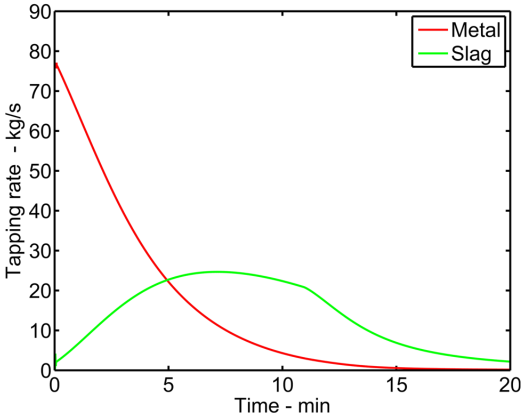

Fig. 4—Tapping rates for slag and metal in a FeMn furnace as a function of time.[28]

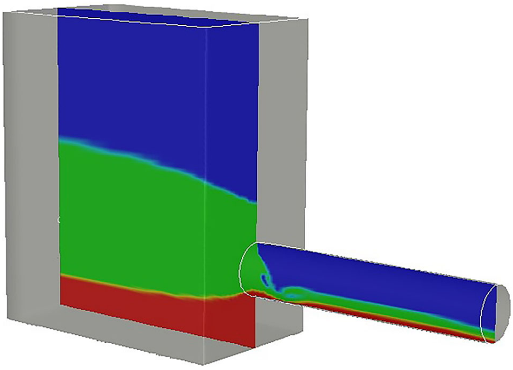

Fig. 5—Example of slag (green) and metal (red) phases during tapping from a FeMn furnace. The tap-hole diameter is 10 cm (Color figure online).

The mechanisms mentioned here can be explained and calculated with the models cited in the preceding sub-chapters. The knowledge and techniques associated with the models can be applied to enhance tapping as discussed in the following chapter.

## III. APPLICATION TO TAPPING

The application of modeling methods to real-world problems in the ferroalloy industry remains at an early stage of development. As is clear from the previous sections, the majority of work in this field has so far been focused in two main areas. The first is specific design verification or modification, in which a physical or numerical model of an individual component of the tapping system is constructed after it has been designed using more traditional engineering methods. The second is broad fundamental studies of various aspects and phenomena in generic tapping systems, in which the parameter spaces of simplified models are explored in order to build deeper understanding of the tapping process in general.

While these approaches have been largely successful to date, the potential inherent in modeling of tapping processes is considerably wider in scope. With the advent of the fourth industrial revolution (4IR) modeling methods constitute a powerful toolbox that can be leveraged by high-level software automation for design, optimization, and control purposes. This can take several forms:

- Virtual prototyping, in which numerous variations of equipment and process designs are tested extensively using computer models as front-line engineering tools, in order to arrive at an optimized final design,
- Digital twinning, in which predictive numerical or computational models are integrated with live data from furnace plants in order to provide model-based control, operator guidance, and early warning systems,
- Inverse modeling and soft sensors, in which models are used to infer and interpolate between real measurements (such as those obtained from furnace feed and electrical systems, thermocouples, sidewall cooling elements, *etc.*) in order to provide virtual sensors which can be used by plant control systems as though they were real instruments,
- Industrial Internet of Things (IIoT) applications, in which knowledge obtained from modeling (or even simple models themselves) are directly integrated into instruments and support equipment installed on the tapping system, facilitating the development of more distributed and self-organizing control strategies,
- Data-driven modeling, in which large quantities of measured tapping data for a particular furnace operation are analyzed using data science and ma-

chine learning tools in order to support and augment more traditional empirical or fundamental modeling.

The utility of virtual prototyping has already been demonstrated in the HSE field for the development of new equipment and operational procedures for managing gas and dust emissions during ferroalloy tapping.[49,52] Advanced models of other parts of furnace tapping systems are potentially able to predict a wide range of phenomena relevant in HSE applications including tap-hole wear and damage, splashing and accidental overflows from tapping runners and ladles, thermal radiation loads from molten metal and slag surfaces, outcomes of different equipment failure modes, and so forth. In the more general virtual prototyping space it is expected that computational modeling of ferroalloy furnace tapping systems will be able to provide tangible economic benefits by suggesting design optimizations that improve phase separation efficiencies, increase robustness and tolerance to tapping variability, and reduce maintenance and consumables.

Digital twinning is expected to evolve naturally from developments in virtual prototyping as models become more sophisticated and available computational power advances. It is expected that while virtual prototyping focuses on the detailed design of individual components of the furnace tapping system, digital twin models will unify component models into a single framework in order to account for interaction effects. An example of this is shown in Figure 6, in which information from various sub-models carries through a simple flowsheet for a ferroalloy furnace tapping system. The availability of powerful software integration and automation tools in high-level general purpose languages like Python is expected to be a key driver of digital twin development in the future.

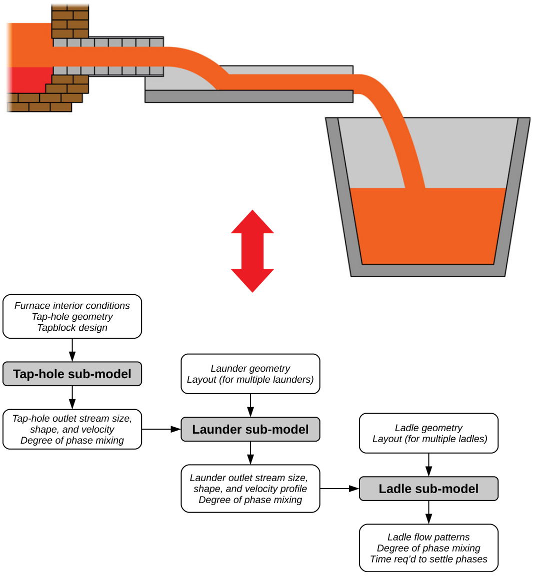

Fig. 6—Furnace tapping system (top) with corresponding integrated modeling flowsheet (bottom).

The use of inverse modeling and soft sensors to expand measurements from instrumentation is already quite commonplace in blast furnace operations for hearth and sidewall integrity monitoring.[53,54] It is anticipated that extension of such techniques to furnace tapping systems will give plant operators a clearer picture of the interior condition of tap-holes and tapblock lining assemblies in particular, facilitating efficient just-in-time maintenance practices and averting catastrophic failures.

IIoT applications[55] are still in their infancy in the ferroalloy industry. However, it is expected that with ongoing advances of instruments and sensors, modeling technologies from virtual prototyping and digital twinning will trickle down to this level in due course. A network of smart instrumentation and equipment will be capable of not only communicating and sharing information with each other, but also running simulations to enhance their knowledge of the tapping system and improve their actions. Automation and control of tapping systems are therefore likely to become considerably more distributed in such environments, requiring only supervisory monitoring and high-level objectives to be provided by plant operators.

Data-driven modeling is expected to see greatly increased application in the control and management of furnace tapping systems in the future. The enabling technologies of data science and machine learning are already seeing significant adoption in other areas of pyrometallurgy such as quality monitoring and control.[56] By combining the top-down approach of data science methods with bottom-up models based on process fundamentals, powerful augmented modeling frameworks can be conceived which are fitted optimally to large dynamic real-world datasets while remaining flexible enough to extrapolate realistically beyond the bounds of that data. Together with IIoT, such techniques are also expected to feed back into the development of more advanced modeling methods for virtual prototyping and digital twinning, closing the loop of new applications for modeling in furnace tapping systems.

## IV. CONCLUSIONS AND OUTLOOK

Tapping is a ubiquitous and cross-cutting furnace operation in the ferroalloy industry, and poses a number of challenges ranging from the complexity of the physics involved to the extreme hazards faced by the personnel who work on it. It would, therefore, seem to be an ideal subject for the application of modeling techniques, which are able to build scientific and engineering knowledge of a process *via* physical or numerical proxies. However, it is clear from the present review that research and development in the field of ferroalloy furnace tapping remains at a relatively nascent stage.

Arguably, the most progress to date has happened in the area of reduced-order models, with refinements and advances in the state of the art contributed by many different authors over a number of years. Such models are robust and simple, and may be easily fitted to process data from a particular operation in order to develop tailored solutions. They also lend themselves naturally to new applications in software automation and control.

Applications in physical modeling have been somewhat limited in recent times, despite the fact that this can add significant value to other types of modeling work; very little industrial data on furnace tapping are available in the open literature, and as such physical experiments are frequently the only accessible datasets against which to test and validate numerical models.

Computational modeling methods have great potential and are seeing rapid growth in both research and engineering environments. The high level of multi-physics coupling in the tapping problem together with limited data for parameters and validation means that they are primarily useful in gaining an understanding of general trends and phenomena rather than performing detailed equipment and process design at this time—but this area of tapping modeling will evolve rapidly in the future. Although we already have obtained good insight from CFD studies, more information about the conditions inside the furnace can be obtained when simulations are linked to new and better knowledge. Most modeling studies assumes uniform conditions in the particle bed, while in reality the particle bed is non-uniform with varying particle size, cracks and impermeable zones. If CFD can include such defects into the simulations, we might be able to explain inconsistency between taps. This will, however, require a deeper knowledge of the furnace internal conditions, which can be gathered from furnace excavations,[10,57] but more details are needed, especially on the conditions near the tap-hole.

It is anticipated that the adoption of methods and technologies from 4IR (including virtual prototyping and digital experimentation, digital twinning, the Internet of Things and data science) will be a strong driver for modeling of ferroalloy tapping processes. These applications are already gaining acceptance in many other parts of pyrometallurgical furnace operations, and they offer a unique opportunity to repurpose many traditional modeling methods in new and interesting ways.

Finally, it is important to appreciate that many similarities exist between tapping operations for different types of furnaces and commodities, and this should be explored further in order to build better knowledge, models, and toolsets with reduced effort and cost. modeling research from the iron and steel industry has already been used extensively in many aspects of ferroalloy smelting, and tapping is no exception. Going forward, building on such synergies to expand the capabilities and applications of modeling methods in ferroalloy furnace tapping is likely to continue to the benefit of all parties.

## ACKNOWLEDGMENTS

This publication has been funded by the Research Council of Norway (KPN Project, 267621). The authors gratefully acknowledge the financial support from the Research Council of Norway and the Norwegian Ferroalloy Producers Research Association (FFF). This paper is published by permission of Mintek.

## FUNDING

Open access funding provided by NTNU Norwegian University of Science and Technology (incl St. Olavs Hospital - Trondheim University Hospital).

## OPEN ACCESS

This article is licensed under a Creative Commons Attribution 4.0 International License, which permits use, sharing, adaptation, distribution and reproduction in any medium or format, as long as you give appropriate credit to the original author(s) and the source, provide a link to the Creative Commons licence, and indicate if changes were made. The images or other third party material in this article are included in the article's Creative Commons licence, unless indicated otherwise in a credit line to the material. If material is not included in the article's Creative Commons licence and your intended use is not permitted by statutory regulation or exceeds the permitted use, you will need to obtain permission directly from the copyright holder. To view a copy of this licence, visit http://creativecommons.org/licenses/by/4.0/.

## REFERENCES

1. L. Holappa: Handbook of Ferroalloys: Chapter 2—Basics of Ferroalloys, 2013, pp. 9–28.
2. R.H. Eric: Treatise on Process Metallurgy: Chapter 1.10—Production of Ferroalloys, 2014, pp. 477–532.
3. I.Mc Dougall: Handbook of Ferroalloys: Chapter 4—Ferroalloys Processing Equipment, 2013, pp. 83–138.
4. L. Nelson and R. Hundermark: *J. S. Afr. Inst. Min. Metall.*, 2016, vol. 116, pp. 465–90.
5. J. Sutherland and J. Gous: *J. S. Afr. Inst. Min. Metall.*, 2019, vol. 119, pp. 563–71.
6. M. Tangstad: Handbook of Ferroalloys: Chapter 7. Manganese Ferroalloys Technology, 2013, pp. 221–66.
7. M.W. Erwee, Q. Reynolds, and J.H. Zietsman: *JOM*, 2016, vol. 68, pp. 1556–62.
8. B. Beek, T. Goff, P. Nel, and E. Rex: *J. S. Afr. Inst. Min. Metall.*, 2016, vol. 116, pp. 27–34.
9. J. Muller, J.H. Zietsman, and P.C. Pistorius: *Metall. Trans. B*, 2015, vol. 46, pp. 2639–51.
10. J. Steenkamp, P. Pistorius, and M. Tangstad: *J. S. Afr. Inst. Min. Metall.*, 2015, vol. 115, pp. 199–208.
11. S.E. Olsen, M. Tangstad, T. Lindstad: Production of Manganese Ferroalloys, Tapir Akademisk Forlag 2007. https://www.worldcat.org/title/production-of-manganese-ferroalloys/oclc/271336213.
12. S. Bublik, K.E. Einarsrud: Inverse modelling of interfacial tension between ferroalloy and slag using OpenFOAM. 14th International Conference on CFD in Oil & Gas, Metallurgical and Process Industries SINTEF, Trondheim, Norway, October 12–14, 2020, SINTEF Academic Press, 2020, pp. 28–38.

13. I. Bellemans, E.D. Wilde, N. Moelans, and K. Verbeken: *Adv. Colloid Interface Sci.*, 2018, vol. 255, pp. 47–63.
14. H.-S. Jang, J.W. Ryu, and I. Sohn: *Metall. Trans. B*, 2015, vol. 46, pp. 606–14.
15. A.F. Yang, A. Karasev, and P.G. Jönsson: *ISIJ Int.*, 2015, vol. 55, pp. 570–77.
16. Z. Han and L. Holappa: *ISIJ Int.*, 2003, vol. 43, pp. 292–97.
17. Z. Li, M. Zeze, and K. Mukai: *Mater. Trans.*, 2003, vol. 44, pp. 2108–13.
18. L. Muhmood, N.N. Viswanathan, and S. Seetharaman: *Metall. Trans. B*, 2011, vol. 42, pp. 460–70.
19. A. Jakobsson, M. Nasu, J. Mangwiru, K.C. Mills, S. Seetharaman: Philos. Trans. R. Soc., A, 1998, vol. 356, pp. 995–1001.
20. M. Kadkhodabeigi, H. Tveit, and S.T. Johansen: *ISIJ Int.*, 2011, vol. 51, pp. 193–202.
21. M. Vango, C. Feilmayr, S. Pirker, and T. Lichtenegger: *Appl. Math. Model.*, 2019, vol. 73, pp. 210–27.
22. T. Nouchi, M. Yasui, and K. Takeda: *ISIJ Int.*, 2003, vol. 43, pp. 175–80.
23. M. Vango, S. Pirker, and T. Lichtenegger: *Appl. Math. Model.*, 2018, vol. 56, pp. 501–16.
24. R. Guthrie: Engineering in Process Metallurgy, 1992. https://global.oup.com/academic/product/engineering-in-process-metallurgy-9780198563679?cc = no&lang = en&.
25. H. Mitsui, Y. Toritani, T. Yamane, S. Yamasaki, Y. Oguchi, T. Kawakami: Interceram(Aachen Proc. 1988) 38, 98-102, 1989, (1988).
26. M. Iida, K. Ogura, and T. Hakone: *ISIJ Int.*, 2008, vol. 48, pp. 412–19.
27. L. Shao and H. Saxen: *ISIJ Int.*, 2011, vol. 51, pp. 228–35.
28. JE. Olsen and Q.G. Reynolds: *Metall. Trans. B*, 2020, vol. 51B, pp. 1750–59.
29. H.H. Hu: Fluid Mechanics: Chapter 10—Computational Fluid Dynamics, Fifth Edition, 2012, pp. 421–72.
30. R. Bird, W. Stewart, E. Lightfoot, Transport Phenomena, 2006.
31. ANSYS, Inc.: ANSYS Fluent. https://www.ansys.com. Accessed 17 Feb 2021.
32. The OpenFOAM Foundation: OpenFOAM. https://openfoam.org. Accessed 17 Feb 2021.
33. Flow Science, Inc.: FLOW-3D. https://www.flow3d.com. Accessed 17 Feb 2021.
34. COMSOL, Inc.: COMSOL Multiphysics. https://www.comsol.com. Accessed 17 Feb 2021.
35. Siemens: STAR-CMM + . https://www.plm.automation.siemens.com/global/en/products/simcenter/STAR-CCM.html. Accessed 17 Feb 2021.
36. S. Dash, S. Ajmani, A. Kumar, and H. Sandhu: *Ironmak. Steelmak.*, 2001, vol. 28, pp. 110–16.
37. S. Dash, D. Jha, S. Ajmani, and A. Upadhyaya: *Ironmak. Steelmak.*, 2004, vol. 31, pp. 207–15.
38. K. Nishioka, T. Maeda, and M. Shimizu: *ISIJ Int.*, 2005, vol. 45, pp. 669–76.
39. K. Nishoka, T. Maeda, and M. Shimizu: *ISIJ Int.*, 2005, vol. 45, pp. 1496–1505.
40. M. Kadkhodabeigi, H. Tveit, and S.T. Johansen: *Prog. Comput. Fluid Dyn.*, 2010, vol. 10, pp. 374–83.
41. L. Shao and H. Saxen: *ISIJ Int.*, 2013, vol. 53, pp. 988–94.
42. Q.G. Reynolds, M.W. Erwee: Multiphase fluid flow modelling of furnace tap-holes. Proceedings of the 12th International Conference on CFD in Oil & Gas, Metallurgical and Process Industries, 2007, pp. 521–30.
43. M. Kirschen, C. Rahm, J. Jeitler, and G. Hackl: *Arch. Metall. Mater.*, 2008, vol. 53, pp. 365–71.
44. Q.G. Reynolds, J.E. Olsen, M.W. Erwee, and O.F. Oxtoby: *J. S. Afr. Inst. Min. Metall.*, 2019, vol. 119, pp. 527–36.
45. J.E. Olsen, Q.G. Reynolds, M.W. Erwee: Temperature field at the tap hole in a manganese furnace-a computational modelling study. SAIMM Furnace Tapping 2018, Southern African Institute of Mining and Metallurgy, Kruger National Park, 2018, pp. 223–30.
46. S. Johansen, E. Ringdalen: Reduced metal loss to slag in HC FeCr production-by redesign based on mathematical modelling. SAIMM Furnace Tapping 2018, Southern African Institute of Mining and Metallurgy, Kruger National Park, 2018, pp. 29–38.
47. H. Kim, B. Ozturk, and R.J. Fruehan: *ISIJ Int.*, 1998, vol. 38, pp. 430–39.
48. J.J.E. Lee: Droplet Formation Mechanisms in Metallurgical Processes. https://www.maths.ox.ac.uk/system/files/attachments/Lee%20Eramet%20MP1.pdf.
49. B. Ravary, S. Grådahl: Improving Environment in the Tapping Area of a Ferromanganese Furnace. INFACON XII, Helsinki, Finland, 2010, pp. 99–108.
50. W. Ma, W. Liu, L. Li, G. Huang, B. Su, and C. Yu: *Indoor Built Environ.*, 2015, vol. 24, pp. 1069–81.
51. C. Goniva, C. Kloss, N.G. Deen, J.A. Kuipers, and S. Pirker: *Particuology*, 2012, vol. 10, pp. 582–91.
52. M. Kadkhodabeigi, H. Tveit, K.H. Berget: Silicon process—new hood design for tapping gas collection. INFACON XII, Helsinki, Finland, 2010.
53. L. Shen, Z. Jiang, W. Gui, C. Yang, Y. Wang, and B. Sun: *IFAC-PapersOnLine*, 2019, vol. 52, pp. 78–83.
54. H. Ghorbani, M. Al-Dojali, K. Chomyn: Thermal assessment and identification of wear zones in a blast furnace hearth and tapholes, in SAIMM Furnace Tapping 2018, Skukuza, South Africa, 2018.
55. A. Sunyaev: Internet Computing: The Internet of Things 301–337, 2020.
56. H. Saxen, C. Gao, and Z. Gao: *IEEE Trans. Ind. Inform.*, 2013, vol. 9, pp. 2213–25.
57. E. Ringdalen and M. Ksiazek: *SAIMM Furn. Tapping*, 2018, vol. 2018, pp. 167–78.

**Publisher's Note** Springer Nature remains neutral with regard to jurisdictional claims in published maps and institutional affiliations.

# Paper IV

TOPICAL COLLECTION: TOPICAL COLLECTION: SCIENCE AND TECHNOLOGY OF MOLTEN SLAGS, FLUXES, AND SALTS

# Interfacial Behaviour in Ferroalloys: The Influence of Sulfur in FeMn and SiMn Systems

SERGEY BUBLIK, SARINA BAO, MERETE TANGSTAD,
and KRISTIAN ETIENNE EINARSRUD

The present study has investigated the influence of sulfur content in synthetic FeMn and SiMn from 0 to 1.00 wt pct on interfacial properties between these ferroalloys and slags. The effect of experimental parameters such as temperature and holding time was evaluated. Interfacial interaction between ferroalloys and slags was characterized by interfacial tension and apparent contact angle between metal and slag, measured based on the Young–Laplace equation and an inverse modelling approach developed in OpenFOAM. The results show that sulfur has a significant influence on both interfacial tension and apparent contact angle, decreasing both values and promoting the formation of a metal-slag mixture. Despite the fact that sulfur was added only to the ferroalloys, most of sulfur is distributed into slag after reactions with the metal phase. Increasing the maximum experimental temperature in the sessile drop furnace also resulted in a decrease of both interfacial properties, resulting in higher mass transfer rates and intensive reactions between metal and slag. The effect of holding time demonstrated that after reaching equilibrium in FeMn-slag and SiMn-slag systems (both with and without sulfur), interfacial tension and apparent contact angle remain constant.

https://doi.org/10.1007/s11663-021-02323-2
© The Author(s) 2021

## I. INTRODUCTION

HIGH-CARBON FeMn and SiMn are produced in submerged arc furnaces (SAF) by carbothermic reduction of manganese ores with the addition of carbon materials and fluxes. The main products generated in SAFs in ferroalloy production are molten metal and slag which accumulate during smelting and, therefore, must be removed from the furnace by performing an operation called tapping. During tapping, molten materials flow out through a tap-hole and into ladles, where the first ladle usually serves as a metal reservoir and subsequent ladles are used as slag reservoirs. Since the separation of metal and slag in the metal ladle occurs naturally due to their difference in density, slag tends to accumulate at the top of the metal ladle while metal settles to the bottom. Due to the turbulence of the tapping flow and interfacial interaction of metal and slag, metal droplets are formed in slag, forming a so-called metal-slag emulsion.[1] After the first ladle is completely filled, slag begins to overflow to the slag ladles, entraining a large number of metal droplets. Metal entrained in slag is considered a loss, and this generally reduces the process efficiency,[2,3] mainly for the reason that further post-processing of slag with entrained metal droplets requires additional costs.

Interfacial phenomena are vital for ferroalloy production, as a better understanding of entrainment mechanisms can significantly help reduce ferroalloy losses with slag. The interfacial interaction between metal and slag and the stability of the interface between them are characterized by interfacial tension.[4] High interfacial tension promotes better separation, while the opposite is true for low interfacial tension. In metal-slag systems where surface-active elements such as sulfur, oxygen, selenium and tellurium are present, interfacial tension decreases as a result of higher mass transfer rates, leading to problems with the separation of metal and slag due to the formation of metal-slag emulsion.[5] In ferroalloys production, major elements which represent surface-active elements are sulfur and oxygen. For such systems, the thermodynamic equilibrium between ferroalloy and slag can be described by the reaction[6]:

$$[S] + (O^{2-}) \Leftrightarrow (S^{2-}) + [O], \qquad [1]$$

where $[S]$, $[O]$ are sulfur and oxygen in alloy, $(S^{2-})$, $(O^{2-})$ are sulfur and oxygen in slag.

---

SERGEY BUBLIK, MERETE TANGSTAD, KRISTIAN ETIENNE EINARSRUD are with the Department of Materials Science and Engineering, Norwegian University of Science and Technology (NTNU), Trondheim, 7491, Norway. SARINA BAO is with SINTEF Industry, Trondheim, 7034, Norway. Contact e-mail: sergey.bublik@ntnu.no

Manuscript submitted January 22, 2021; accepted September 5, 2021.

Published online: 03 November 2021

Experimentally, the interfacial tension between two molten materials is typically determined by melting materials in a furnace equipped with an X-ray camera[7] or by applying the sessile drop technique with a digital camera.[8] After recording images of the interfacial interaction between two phases, interfacial tension is obtained by solving the Young–Laplace equation (Eq. [2]) numerically,

$$\Delta P = \gamma\left(\frac{1}{R_1} + \frac{1}{R_2}\right), \qquad [2]$$

where $\Delta P$ is the pressure difference at the interface, $\gamma$ is interfacial tension, $R_1$ and $R_2$ are the principal radii of curvature,[9] which describes the relationship between interfacial tension and the shape of the interface. However, in most cases, the measurement of interfacial tension is extremely complicated due to high temperatures and complex composition of molten materials.

The present study is based on methodologies for the measurement of interfacial tension and apparent contact angles between ferroalloy and slag, which were developed and verified by the authors previously.[10,11] Interfacial interaction in synthetic FeMn-slag and SiMn-systems, both with and without sulfur addition to ferroalloy, has been investigated by combining analysis of images from a sessile drop furnace and multiphase flow simulations in OpenFOAM v6,[12] and discussed together with the assessment of the sensitivity of the results by comparing different experiments.

## II. EXPERIMENTAL

### A. *Material Preparation*

Synthetic FeMn, SiMn and their corresponding slags have been prepared from pure powders for studying interfacial interactions in the sessile drop furnace. The composition of the synthetic materials has been chosen according to the composition of the industrial materials[2] as shown in Table I. The purity of chemicals used for material preparation is specified in Table II. The amount of each chemical required to produce corresponding synthetic materials has been calculated taking into account both the purity of chemicals and the composition of industrial materials and is presented in Table III.

The powders were mixed and melted separately in a graphite crucible in an induction furnace in Ar atmosphere at temperatures up to 1773 K for FeMn and 1873 K for SiMn. The holding time for preparation of FeMn and SiMn was 60 min, and for slags—5 min. After the melting, both ferroalloys and slags were ground in a ball mill and divided into batches of 50 g. Iron(II) sulfide

**Table I. Chemical composition of industrial FeMn, SiMn and Slags[2]**

| | Chemical Composition (Wt Pct) | | | | | | | | |
|---|---|---|---|---|---|---|---|---|---|
| Material | Mn | Fe | Si | C | MnO | CaO | MgO | $SiO_2$ | $Al_2O_3$ |
| FeMn | 78 | 15 | – | 7 | – | – | – | – | – |
| SiMn | 68 | 12 | 18 | 2 | – | – | – | – | – |
| FeMn Slag | – | – | – | – | 38 | 23 | 6 | 23 | 10 |
| SiMn Slag | – | – | – | – | 11 | 23 | 6 | 43 | 17 |

**Table II. Purity of Chemicals**

| | Purity (Pct) | | | | | | | | |
|---|---|---|---|---|---|---|---|---|---|
| Material | Mn | Fe | Si | MnO | CaO | MgO | $SiO_2$ | $Al_2O_3$ | FeS |
| Chemicals | 99.90 | 99.98 | 99.90 | 99.00 | 95.00 | 99.00 | 99.50 | 98.00 | 99.90 |

**Table III. Weight of Pure Chemicals Used for Producing Synthetic FeMn, SiMn and Slags**

| | Weight of Pure Chemicals (g) | | | | | | | | |
|---|---|---|---|---|---|---|---|---|---|
| Material | Mn | Fe | Si | MnO | CaO | MgO | $SiO_2$ | $Al_2O_3$ | Total |
| FeMn | 209.89 | 40.33 | — | — | — | — | — | — | 250.22 |
| SiMn | 173.64 | 30.62 | 45.96 | — | — | — | — | — | 250.22 |
| FeMn Slag | — | — | — | 95.96 | 60.53 | 15.15 | 57.79 | 25.51 | 254.94 |
| SiMn Slag | — | — | — | 27.78 | 60.53 | 15.15 | 108.04 | 43.37 | 254.87 |

powder has been added to batches of FeMn and SiMn to provide 0.33, 0.66 and 1.00 wt pct of sulfur as shown in Table IV. Thereafter, both ferroalloys and slag were remelted at the same operational parameters in the induction furnace. Note that the carbon has not been added as a raw material for melting as it is contained in the graphite crucible, which allows ferroalloys to be saturated with the required amount of carbon—7 and 2 wt pct for FeMn and SiMn, respectively.

### B. *Experimental Setup*

The sessile drop furnace, as sketched in Figure 1, has been applied for investigating the interfacial interaction between FeMn-slag and SiMn-slag. The sessile drop furnace was equipped with a pyrometer and a C-type thermocouple for measuring temperature, and with a digital video camera (Sony XCD-SX910CR, Sony Corporation, Millersville, MD) with a telecentric lens (Navitar 1-50993D) for recording images of the molten samples with the resolution of 1280 × 1024 pixels at one frame per second after reaching the melting point of ferroalloys and slags. Every 10 to 15 experiments, the thermocouple was calibrated by melting pure Fe in Ar and assessing its melting temperature from recorded images. The experiments were performed using graphite substrates or cups in Ar atmosphere (6 N grade) according to the experimental matrices as demonstrated in Tables V and VI. Additionally, the surface of the graphite substrates and cups was cleaned with a paper towel dipped in ethanol or acetone and then dried using compressed air.

Two experimental methods (Figure 2), were employed in this study:

- Method A (Figure 3(a)), allowing to measure apparent contact angles between metal and slag.
- Method B (Figure 3(b)), allowing to determine both interfacial tension and apparent contact angle between metal and slag.

Initially, it was planned to apply only method B for studying interfacial interaction for both FeMn-slag and SiMn-slag systems, but subsequently it was found that SiMn has a poor wetting towards graphite, forming a SiMn droplet instead of a molten layer in the graphite cup as it is illustrated in Figure 4. Therefore, method A was adopted for the SiMn-slag system.

After the experiments, the ferroalloys and slags were cast in epoxy, sectioned in the centre of the slag droplet, re-cast into epoxy, polished and coated with carbon prior to analysis in EOL JXA-8500F Electron Probe Micro Analyzer (EPMA). The composition of the ferroalloy and slag phases were measured in several points and then average composition of each phase was calculated. Elemental mapping was performed for several samples to show sulfur distribution between metal and slag. Additionally, the chemical composition of ferroalloys and slags prior to experiments was determined by X-ray fluorescence (XRF) and the combustion infrared detection technique (combustion-IR). The ferroalloys were analyzed for Mn, Fe, Si, S and C, whereas slags were analyzed for MnO, CaO, MgO, $SiO_2$, $Al_2O_3$ and FeO.

In addition, the surface tension of FeMn, SiMn and slags was measured using the sessile drop furnace by melting ferroalloy or slag pieces on a graphite substrate. Surface tension for FeMn and FeMn slag was measured at temperature of 1723 K and at 1923 K for SiMn and SiMn slag.

### C. *Methodology for Measurement of Surface and Interfacial Tension*

The methodology for determination of slag-metal interfacial tension is based on measurements of surface tension, followed by a comparison of geometrical features obtained from multiphase computational fluid dynamics (CFD) simulations using OpenFOAM[12] and experiments in the sessile drop furnace. The complete procedure is described in Reference 11, with a summary is given in the following for reference.

The elliptic solution of the Young–Laplace equation[14] has been applied for measurements of slag surface tension. Here, surface tension is expressed as:

**Table IV. Weight of Iron(II) Sulfide Added to FeMn and SiMn (in g)**

| | Corresponding to | | |
|---|---|---|---|
| Material | 0.33 wt pct S | 0.66 wt pct S | 1.00 wt pct S |
| FeS | 0.45 | 0.90 | 1.37 |

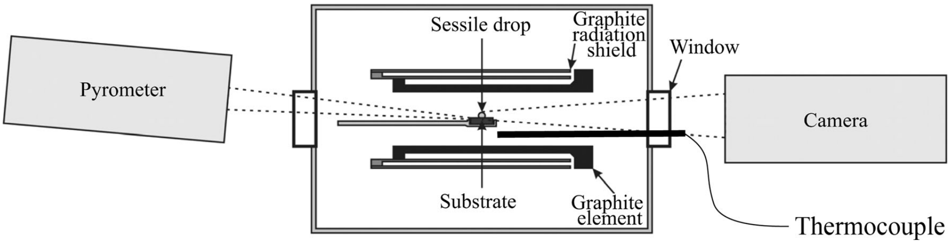

Fig. 1—Schematic overview of the sessile drop furnace. Modified from Ref. 13 under the terms of the Creative Commons CC BY license.

**Table V. Experimental Matrix Used in Experiments for the FeMn-Slag System**

| Experiment | Calculated S Content (Wt Pct) | Maximum Temperature (K) | Holding Time at Maximum Temperature (Min) |
|---|---|---|---|
| 1 | 0 | 1673 | 5 |
| 2 | 0.33 | 1673 | 5 |
| 3 | 0.66 | 1673 | 5 |
| 4 | 1.00 | 1673 | 5 |
| 5 | 0 | 1623 | 5 |
| 6 | 0 | 1723 | 5 |
| 7 | 0.66 | 1623 | 5 |
| 8 | 0.66 | 1723 | 5 |
| 9 | 0 | 1673 | 10 |
| 10 | 0 | 1673 | 15 |
| 11 | 0.66 | 1673 | 10 |
| 12 | 0.66 | 1673 | 15 |

**Table VI. Experimental Matrix Used in Experiments for the SiMn-Slag System**

| Experiment | Calculated S Content (Wt Pct) | Maximum Temperature (K) | Holding Time at Maximum Temperature (Min) |
|---|---|---|---|
| 13 | 0 | 1873 | 5 |
| 14 | 0.33 | 1873 | 5 |
| 15 | 0.66 | 1873 | 5 |
| 16 | 1.00 | 1873 | 5 |
| 17 | 0 | 1823 | 5 |
| 18 | 0 | 1923 | 5 |
| 19 | 0.66 | 1823 | 5 |
| 20 | 0.66 | 1923 | 5 |
| 21 | 0 | 1873 | 10 |
| 22 | 0 | 1873 | 15 |
| 23 | 0.66 | 1873 | 10 |
| 24 | 0.66 | 1873 | 15 |

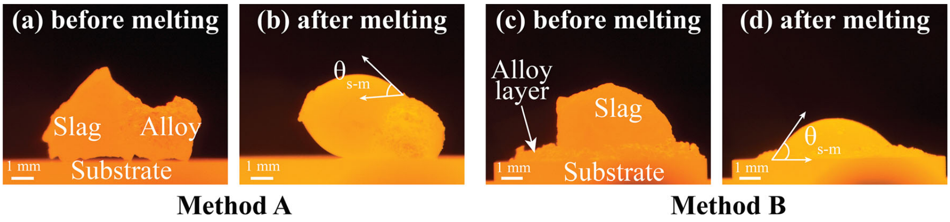

Fig. 2—Methods used for investigation of interfacial properties. In method A, ferroalloy and slag were placed on a graphite substrate. In method B, slag was placed on top of a ferroalloy layer in contact with a graphite cup. The interaction between slag and ferroalloy before melting for method A and B, respectively, is shown in images (*a*) and (*c*), while the interaction at the molten state is shown in images (*b*) and (*d*). Please note that the roughness on the surface of the droplets is related to the formation of solid carbon particles during the melting, which will be discussed further in Sect. III.B.

$$\gamma = \frac{a^2(\rho_{\text{slag}} - \rho_{\text{Ar}})g}{\frac{a^3}{b^3} + \frac{a}{b} - 2}, \qquad [3]$$

where $g$ is the gravitational acceleration, $\rho_{\text{Ar}}$ is the density of Ar ($1.66\,\text{kg/m}^3$), $\rho_{\text{slag}}$ is the density of slag in liquid state ($3300\,\text{kg/m}^3$) for FeMn slag and $2700\,\text{kg/m}^3$ for SiMn slag.[15] Values of $a$ and $b$ are the length of the semi-minor and semi-major axis—respectively—found by fitting an ellipse to the slag contour. The elliptic solution results in a significant error in measurements in case if the droplet has a high wettability towards the substrate (contact angle $< 90°$) or if the surface of the droplet does not form a perfect circle or ellipse.

Surface tension of ferroalloys was measured by a plugin for ImageJ[16] based on low-bond axisymmetric drop shape analysis (LBADSA), which allows to fit the Young—Laplace equation to images and extract parameters of droplet's contour.[17] The main output from the plugin is the capillary constant $c$, which is used then to calculate the surface tension *via* the equation:

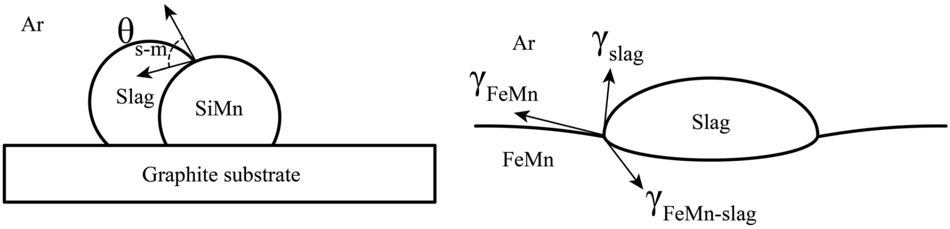

(a) (b)

Fig. 3—Schematic demonstrating slag and ferroalloys at fully molten state in experiments. Image (*a*) shows slag and SiMn droplets in Ar atmosphere. $\theta_{s-m}$ is the contact angle between slag and SiMn. Image (*b*) shows the slag droplet floating on top of molten FeMn in Ar atmosphere. $\gamma_{FeMn}$ is surface tension of FeMn, $\gamma_{slag}$ is surface tension of slag, $\gamma_{FeMn-slag}$ is interfacial tension between FeMn and slag.

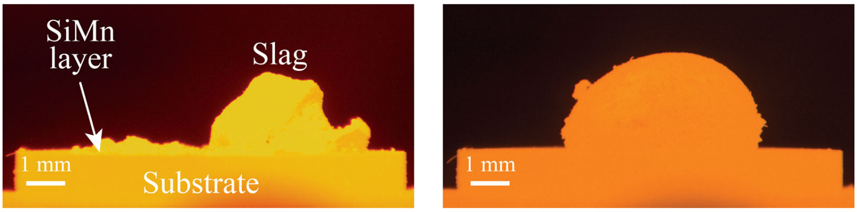

**(a) before melting, 1475 K** **(b) after melting, 1671 K**

Fig. 4—Melting of SiMn layer and slag in the graphite cup in the sessile drop furnace. Image (*a*) shows the slag droplet and the SiMn layer before melting at 1475 K. Image (*b*) illustrates formation of a droplet rather than a layer.

$$c = \frac{(\rho_{\mathrm{metal}} - \rho_{\mathrm{Ar}})g}{\gamma}, \qquad [4]$$

where $c$ is the capillary constant in $\mathrm{m}^{-2}$, $\rho_{\mathrm{metal}}$ is the density of ferroalloys in liquid state $-$ 5612 $\mathrm{kg/m^3}$ for FeMn and 4449 $\mathrm{kg/m^3}$ for SiMn.[15]

The apparent contact angle between SiMn and slag has been measured every 30 to 60 seconds after 30 seconds of holding time—directly from images using the open source image processing software (ImageJ[18]).

The interfacial tension between FeMn and slag has been measured by method B approximately every 30 seconds after 2 minutes of holding time at minimum volume expansion of slag droplet to minimize the influence of volume fluctuations on the results. Method B, which is essentially based on comparing geometrical features obtained from simulations and experiments, consists of the following steps[11]:

(a) Conduct experiments in the sessile drop furnace with a single ferroalloy or slag droplet and determine surface tension of each material.
(b) Conduct experiments in the sessile drop furnace with a slag droplet placed on top of ferroalloy.
(c) Perform simulations in OpenFOAM for a defined range of interfacial tension using densities of ferroalloy and slag in the molten state, weight of the slag droplet and surface tensions determined at the first step. Calculate the non-visible height of the slag droplet (in pct) in the simulations.
(d) Measure the surface roughness correction coefficient ($k_R$) directly from experimental images as the average size of solid particles found at the FeMn-gas and slag-gas interface. In this study, $k_R$ was up to 0.25 mm, depending on the surface roughness.
(e) Calculate the total volume of the slag droplet using slag density in the molten state and weight of the slag droplet measured before experiments:

$$V_{\mathrm{total}} = \frac{m_{\mathrm{slag}}}{\rho_{\mathrm{slag}}}, \qquad [5]$$

where $m_{\mathrm{slag}}$ is weight of the slag droplet.

(f) Calculate the visible volume of the slag droplet ($V_{\mathrm{vis}}$) in experiments assuming that the slag droplet forms a spherical cap both above and below the FeMn-gas interface and subtracting $k_R$ from the visible height and the radius of the slag droplet:

$$V_{\mathrm{vis}} = \frac{1}{6}\pi(h_{\mathrm{vis}} - k_R)(3(a - k_R)^2 + (h_{\mathrm{vis}} - k_R)^2), \qquad [6]$$

where $h_{\mathrm{vis}}$ is visible height of the slag droplet and $a$ is radius of the slag droplet.

Table VII. Measured Chemical Composition (In Wt Pct) of FeMn and SiMn Alloys Before the Experiments in the Sessile Drop Furnace

| Calculated S Content | Mn | Fe | Si | C | S | Total |
|---|---|---|---|---|---|---|
| FeMn Alloy | | | | | | |
| 0 wt pct | 76.60 | 15.20 | 0.81 | 7.26 | 0.03 | 99.90 |
| 0.33 wt pct | 75.50 | 15.70 | 0.57 | 7.22 | 0.04 | 99.03 |
| 0.66 wt pct | 75.90 | 16.40 | 0.20 | 7.18 | 0.05 | 99.73 |
| 1.00 wt pct | 74.50 | 17.10 | 0.20 | 7.18 | 0.11 | 99.09 |
| SiMn Alloy | | | | | | |
| 0 wt pct | 67.30 | 12.50 | 17.80 | 1.80 | 0.02 | 99.42 |
| 0.33 wt pct | 67.40 | 12.90 | 16.30 | 2.00 | 0.25 | 98.85 |
| 0.66 wt pct | 66.80 | 13.50 | 16.50 | 1.80 | 0.62 | 99.22 |
| 1.00 wt pct | 66.80 | 14.00 | 16.50 | 1.70 | 0.90 | 99.90 |

Table VIII. Measured Chemical Composition (In Wt Pct) of FeMn and SiMn Slags Before the Experiments in the Sessile Drop Furnace

| Material | MnO | CaO | MgO | $SiO_2$ | $Al_2O_3$ | FeO | Total |
|---|---|---|---|---|---|---|---|
| FeMn Slag | 36.13 | 23.82 | 6.76 | 23.54 | 10.41 | 1.42 | 102.32 |
| SiMn Slag | 13.02 | 21.38 | 6.43 | 42.80 | 16.84 | 1.85 | 102.32 |

(g) Calculate the non-visible volume of the slag droplet ($V_{\text{non-vis}}$):

$$V_{\text{non-vis}} = V_{\text{total}} - V_{\text{vis}}, \quad [7]$$

(h) Calculate the non-visible height of the slag droplet ($h_{\text{non-vis}}$) in the experiments:

$$V_{\text{non-vis}} = \frac{1}{6}\pi h_{\text{non-vis}}(3(a - k_R)^2 + h^2_{\text{non-vis}}), \quad [8]$$

(i) Calculate the non-visible height of the slag droplet in pct:

$$h_{\text{non-vis}}(\text{pct}) = \frac{h_{\text{non-vis}}}{h_{\text{non-vis}} + h_{\text{vis}}} \cdot 100. \quad [9]$$

(j) Compare experimental and simulation values to determine interfacial tension.

The 95 pct confidence interval for the sample mean was calculated based on the Student's t-distribution[19]:

$$CI = \overline{y} \pm t\frac{s}{\sqrt{n}}, \quad [10]$$

where $\overline{y}$ is the sample mean, $t$ is the critical value found from the confidence level and degrees of freedom of the sample, $s$ is unknown sample standard deviation and $n$ is the number of observations—from 6 to 31 in this study. Here, $s$ is expressed as:

$$s = \sqrt{\frac{\sum_{i=1}^{n}(y_i - \overline{y})^2}{n-1}}, \quad [11]$$

where $y_i$ $\{y_1, y_2, \ldots, y_n\}$ represents one measured value of the sample (*i.e.* single observation).

## III. RESULTS AND DISCUSSION

### A. *Chemical Composition of Synthetic Ferroalloys and Slags*

The chemical composition of ferroalloys before experiments was analyzed by XRF and combustion-IR and is summarized in Table VII, while the chemical composition of slags before experiments was analyzed by XRF and is given in Table VIII. Due to formation of FeMn dust and $MnO_2$ particles during combustion which then settle in the filter and lead to substantially lower sulfur values in the samples, sulfur content in FeMn could not reliably be determined by XRF and combustion-IR. Consequently, sulfur content in FeMn was estimated by EPMA from BSE images based on the surface area of the sulfide phase to the total area of the sample. The estimated sulfur content by EPMA is provided in Table IX.

Comparing the composition of the synthetic ferroalloys and slags with the composition of the industrial materials given in Table I, it is obvious that their compositions are close to a large extent, which indicates the correctness of the methodology used for the materials preparation in the current work.

### B. *Surface Tension of FeMn, SiMn and Corresponding Slags*

The experimentally measured average values of surface tension by employing the aforementioned methodologies are presented in Figure 5. As it is expected for metals, FeMn and SiMn have higher values of surface tension – 1.50 and 1.20 N/m, respectively, while slags have considerably lower surface tensions – 0.65 N/m for FeMn slag and 0.50 N/m for SiMn slag. Besides, sulfur addition to ferroalloys seems to have no significant effect on surface tension of FeMn and SiMn, which results in the same surface tension as corresponding alloys without sulfur addition. The LBADSA methodology, as it can be concluded from the confidence intervals, has a higher deviation in measurements of surface tension for FeMn, ±0.05 N/m. In contrast, the LBADSA for SiMn and the ellipsoidal solution of the Young-Laplace equation for slags result in smaller deviation, ±0.02 N/m. The difference can be explained by a rough surface of FeMn compared to other materials, as shown in Figure 6, which gives greater variation in measurements. The observed roughness of FeMn could be attributed to a higher C content, and hence more C can precipitate or dissolve during experiments with FeMn.

In all experiments with FeMn, solid carbon particles have been observed on top of FeMn layer as illustrated in Figure 7. Their formation may be caused by different temperatures during the materials preparation and the experiments. As it can be seen from Figure 8, the carbon saturation in FeMn is estimated to be 7.4 wt pct at melting temperature of 1773 K used in the induction furnace. However, at experimental temperatures of 1623 to 1723 K used in the sessile drop furnace, the carbon saturation decreases down to 7.0–7.3 wt pct and the rest of carbon remains in solid state, which can consequently be observed on top of the FeMn layer in the experiments. A similar phenomenon of floating carbon particles on top of the FeMn melt was suggested by Hoel,[20] where it was discussed that excess carbon precipitates as graphite from the supersaturated melt as the temperature decreases. Figure 6(c) demonstrates that the amount of solid carbon precipitation on surface of the SiMn alloy is significantly lower compared to the FeMn alloy, since the melting of SiMn in the induction furnace at 1873 K and holding time of 60 minutes allowed to dissolve only ≈2 wt pct of carbon in the SiMn alloy and, as shown in Figure 9, this amount of carbon is completely dissolved in liquid SiMn at 1873 K.

It is worth mentioning that the evaporation of slag and metal droplets was not observed at the proposed temperatures (Figure 6) in the experiments for measurements of surface tension. The sample size over time only increased in all experiments due to thermal expansion. For instance, the volume change of the FeMn droplet was up to 10 pct higher after increasing temperature from the melting point (≈ 1533 K) to 1773 K, when surface tension was measured. The given sample size in this study was chosen to reduce the effect of solid carbon particles precipitation on the surface of FeMn, as decreasing the sample size is expected to introduce more uncertainty associated with the surface roughness. On the contrary, the variation in the droplet size (e.g. an

Table IX. **Sulfur Content in FeMn Estimated by EPMA**

| Calculated S Content (Wt Pct) | MnS in the Total Area (Pct) | Chemical Composition of MnS Phase (Wt Pct) | | | S in FeMn (Wt Pct) |
|---|---|---|---|---|---|
| | | Mn | S | Total | |
| 0 | 0.08 | 62.62 | 38.27 | 100.90 | 0.03 |
| 0.33 | 0.80 | 63.33 | 38.87 | 102.20 | 0.31 |
| 0.66 | 1.48 | 63.36 | 38.70 | 102.50 | 0.57 |
| 1.00 | 2.40 | 63.21 | 38.62 | 101.83 | 0.93 |

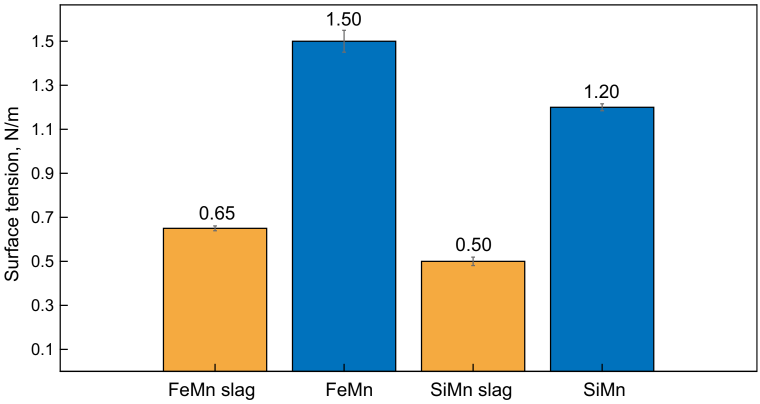

Fig. 5—Average values of surface tension of FeMn, SiMn and slags measured experimentally. Grey lines on top of bars represent the 95 pct confidence interval for the sample mean.

unreasonably big droplet) will also affect surface tension, as it can be inferred from Eq. [12], where the Eötvös number characterizes the balance between the gravitational force and the surface tension force,[21] and therefore the surface profile of a liquid droplet. However, no surface tension change was observed in the present study either using a droplet twice smaller or the given droplet size.

$$Eo = \frac{\Delta\rho g D^2}{\gamma}\left(\frac{\text{gravitational force}}{\text{surface tension force}}\right) \qquad [12]$$

where $Eo$ is the Eötvös number, $\Delta\rho$ is the density difference between two phases, $D$ is the diameter of the droplet. High values of Eo specify that the droplet is strongly affected by the gravitational force, flattening the droplet, while low Eo values indicate that the droplet has the spherical shape.[22]

As it is has been reported by Lee *et al.*,[23] the surface tension of a pure Fe-system is 1.90 N/m, while Mn addition decreases the surface tension,[24] reaching surface tension of 1.00 N/m for a pure Mn-system without C addition. Assuming that there is no carbon present in FeMn used in the current work, which corresponds to 84 wt pct Mn and 16 wt pct Fe, the surface tension of FeMn of this composition according to Lee *et al.* is 1.10 N/m compared to 1.50 N/m measured experimentally for the high-carbon saturated FeMn alloy. There is no data published on surface tension of SiMn; therefore, as an analogue of the Fe-Mn

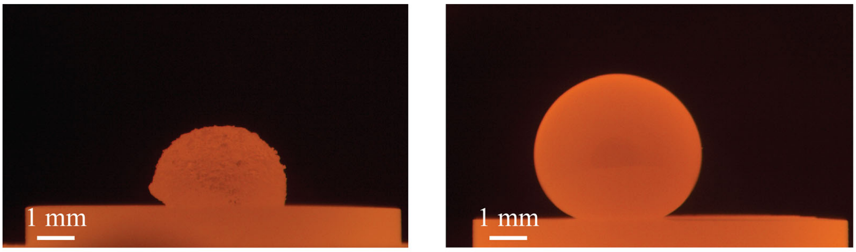

**(a)** FeMn at 1723 K

**(b)** FeMn slag at 1723 K

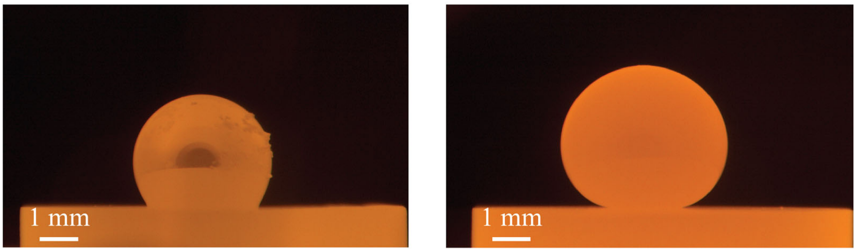

**(c)** SiMn at 1923 K

**(d)** SiMn slag at 1923 K

Fig. 6—Surface of FeMn, SiMn and slags during melting in the sessile drop furnace: (*a*) FeMn droplet at 1723 K, (*b*) FeMn slag droplet at 1723 K, (*c*) SiMn droplet at 1923 K, (*d*) SiMn slag droplet at 1923 K.

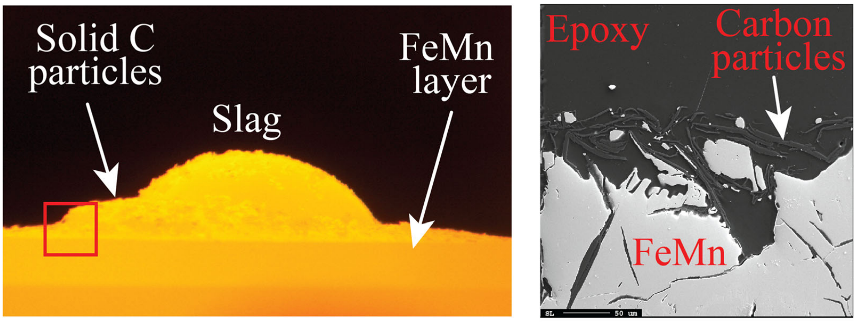

**(a)** FeMn and slag in experiments

**(b)** EPMA analysis

Fig. 7—(*a*) Slag droplet and solid carbon particles on top of FeMn layer during experiments. (*b*) EPMA image of the area indicated by the red box after experiments (Color figure online).

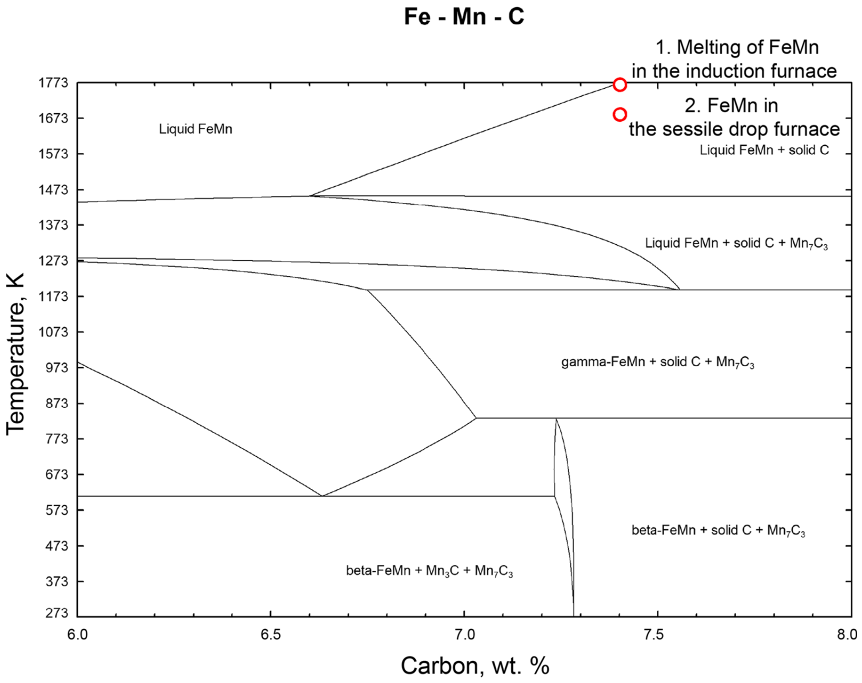

Fig. 8—Fe-Mn-C phase diagram calculated in FactSage 7.3 for constant Fe content of 15 wt pct.

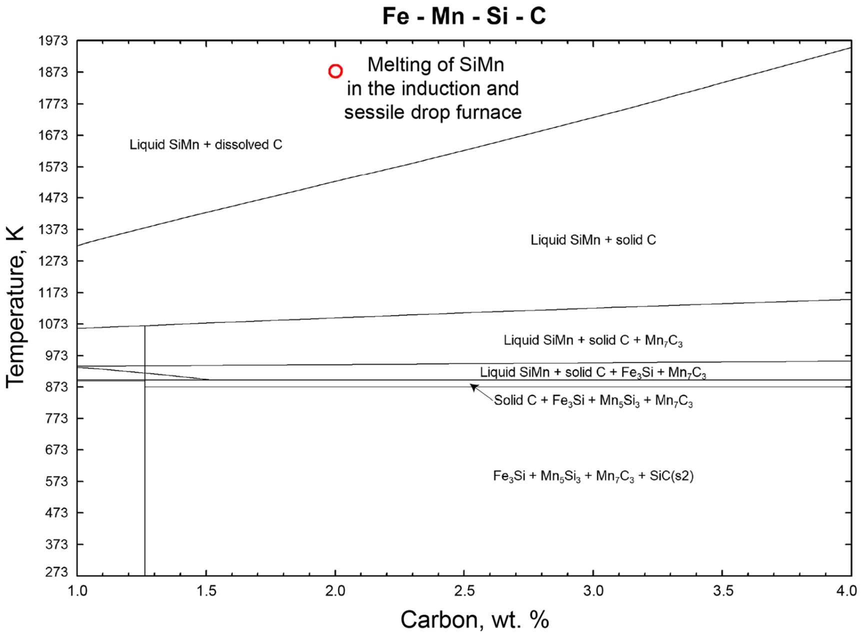

Fig. 9—Fe-Mn-Si-C phase diagram calculated in FactSage 7.3 for constant Fe and Mn content of 12 and 68 wt pct, respectively.

system, surface tension can be alternatively described only for the Fe-Si system. The similar negative trend of Si on surface tension has been observed for a Fe-Si system,[25,26] where the addition of Si to pure Fe decreases surface tension from ≈ 1.80–1.90 to 0.70 N/m.

Lee and Morita[27] studied the surface tension of a Fe-C-S system, where they found that surface tension of a pure Fe gradually decreases with sulfur addition, which is caused by a high concentration of sulfur at the surface. In the present study, even though sulfur acts as a surface-active element, there is no interaction between sulfur in ferroalloys, the graphite substrate and Ar during melting in the sessile drop furnace. In addition, the applied LBADSA methodology is not able to determine small changes in surface tension due to the uneven surface of ferroalloy droplets. These two factors can explain constant surface tension with increasing sulfur content in ferroalloys from 0 to 1.00 wt pct.

Besides that, Lee and Morita[27] showed that C addition to pure Fe on alumina or aluminium nitride substrates increases surface tension. As it can be adopted for ferroalloys studied in this work, both FeMn and SiMn, being completely saturated with carbon after melting in the graphite crucible in the induction furnace, do not react with the graphite substrate, which results in a higher surface tension compared to non-carbon ferroalloy systems.

Depending on the composition, multicomponent slags generally have surface tension in the range from 0.30 to 0.70 N/m,[28,29] which corresponds to the ranges of surface tension found in the present study.

### C. *Effect of Sulfur Addition to Ferroalloy-Slag Systems*

The effect of sulfur content in the SiMn alloy ($S_{SiMn}$) on the average apparent contact angle between SiMn and slag has been studied at constant maximum temperature of 1873 K and constant holding time of 5 minutes and is shown in Figure 10. The increase of $S_{SiMn}$ from 0.02 to 0.90 wt pct decreases the average apparent contact angle from 37.8 to 29.6°. The largest change of − 6.7° is observed between $S_{SiMn}$ of 0.02 and 0.25 wt pct, while the change between $S_{SiMn}$ of 0.25 and 0.62 wt pct , and between $S_{SiMn}$ of 0.62 and 0.90 wt pct was only − 1.1° and − 0.4°.

The average interfacial tension between FeMn and slag changes depending upon sulfur content in the FeMn alloy ($S_{FeMn}$), as shown in Figure 11. The largest change of − 0.30 N/m is noted when $S_{FeMn}$ increases from 0.03 to 0.31 wt pct, which indicates that the equilibrium in the FeMn-slag-S system is reached in this range of $S_{FeMn}$. The further increase of $S_{FeMn}$ to 0.93 wt pct decreases interfacial tension only slightly from 0.96 N/m to 0.88 N/m. However, the measurements for $S_{FeMn}$ of 0.31 and 0.57 wt pct have a larger deviation described by confidence intervals of ±0.09 and ±0.05 N/m, respectively. As illustrated in Figure 12, these two experiments have significant fluctuations in surface area due to the gas evolution after 2 minutes of holding time at the maximum temperature, which most likely contributes to the variance observed in the experiments.

Sulfur, as a surface-active element, mainly concentrates at the surface or the interface and therefore the concentration of sulfur in the bulk does not play a significant role on the interfacial mass transfer, which reasonably means that the maximum concentration of sulfur at the interface is reached at $S_{SiMn}$ of 0.25 wt pct and $S_{FeMn}$ of 0.31 wt pct and the further increase of sulfur content in ferroalloys does not affect interfacial interaction in the FeMn-slag-S and SiMn-slag-S systems significantly. Suzuki *et al.*[30] have studied the effect of sulfur in a Fe-slag system on the dynamic change of apparent contact angle, where they found that sulfur absorbs at the Fe-slag interface and the apparent contact angle gradually decreases during reactions between metal and slag which is more pronounced with sulfur addition. Kim and Tangstad[31] studied the reduction kinetics of FeMn and SiMn slags in CO atmosphere at temperatures up to 1873 K. The authors

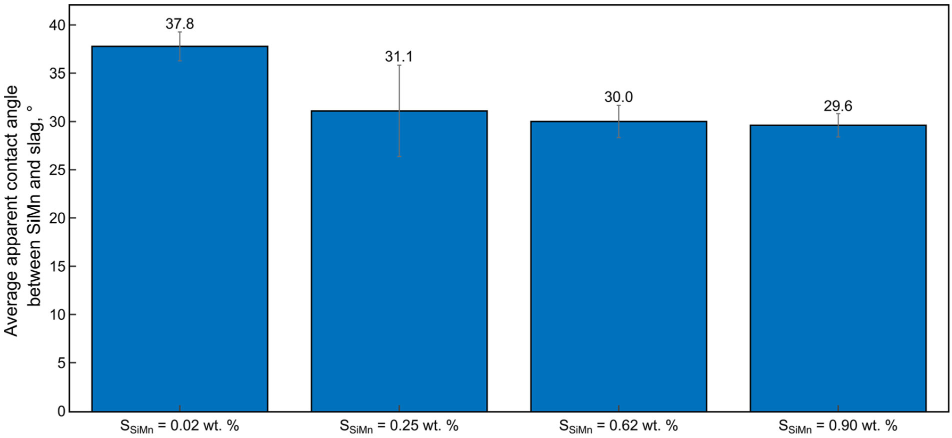

Fig. 10—Effect of sulfur content in SiMn on average apparent contact angle between SiMn and slag at temperature of 1873 K and holding time of 5 min. Grey lines on top of bars represent the 95 pct confidence interval for the sample mean.

reported that the initial sulfur content in slags changes the rate constant non-linearly, meaning that the rate constant reaches a maximum at a certain sulfur content in slag – 0.29 wt pct in their work. This may explain the surface area fluctuations in the experiments with $S_{FeMn}$ from 0.31 to 0.57 wt pct in the given study, which are caused by higher reaction rates and thereby faster reactions between FeMn and slag.

Even though sulfur has not been added in experiment 13, sulfur is found to be evenly distributed between SiMn and slag as shown in Figure 13. This may indicate that sulfur was introduced to the SiMn-slag system from the powders or the graphite crucible during materials preparation or from the graphite substrate during the experiments. After increasing sulfur content in SiMn to 0.62 wt pct, the sulfur distribution shifts towards the slag phase and sulfur mainly concentrates in the bulk of slag (Figure 14). The similar distribution of sulfur has been observed for the FeMn-slag-S system, in which sulfur is predominately found in the slag phase as illustrated in Figure 15. This was confirmed further by calculating the sulfur distribution in FactSage[32] (Figure 16), from which it is evident that sulfur tends to be distributed in slag, whether added to FeMn or SiMn.

## D. *Effect of Temperature*

The effect of temperatures from 1823 to 1923 K on average apparent contact angle between SiMn and slag for $S_{SiMn}$ of 0.02 and 0.62 wt pct at holding time of 5 minutes is shown in Figure 17. From this figure, one can notice that temperature has almost no effect on the apparent contact angle for $S_{SiMn}$ of 0.02 wt pct, slightly decreasing it from 37.3° at 1823 K and 37.8° at 1873 K

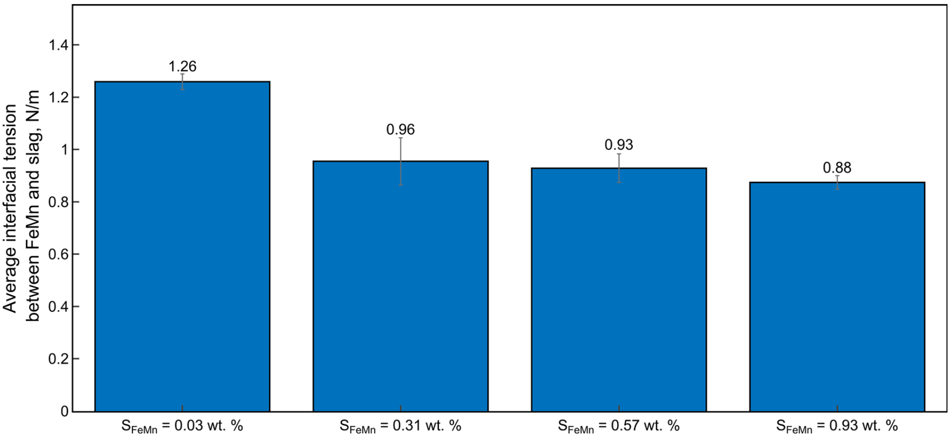

Fig. 11—Effect of sulfur content in FeMn on average interfacial tension between FeMn and slag at temperature of 1673 K and holding time of 5 min. Grey lines on top of bars represent the 95 pct confidence interval for the sample mean.

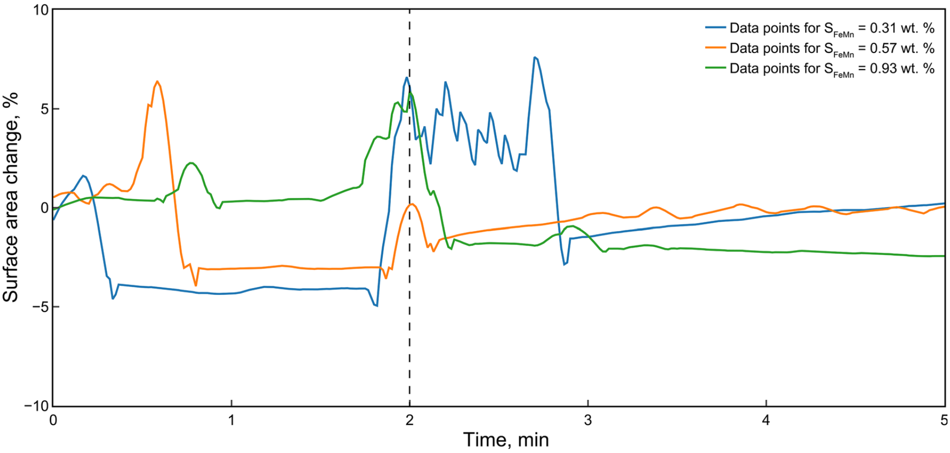

Fig. 12—Temporal change in visible surface area for experiments 2 to 4 during holding.

to 35.6° at 1923 K, $\Delta_{1823\rightarrow1923\,K} = -1.7°$, $\Delta_{1873\rightarrow1923\,K} = -2.2°$. However, for $S_{SiMn}$ of 0.62 wt pct, the temperature influence is more evident, resulting in almost complete covering of SiMn by slag (Figure 18) and in a sharp decrease of apparent contact angle from 30.0 to 5.0° with increase of temperature from 1873 to 1923 K, $\Delta_{1873\rightarrow1923\,K} = -25.0°$. Please note that the contact angle is challenging to determine from images as shown in Figure 18; however, the full dynamics observed in the recorded videos from the experiments allowed the contact angle to be determined based on the initial position of both droplets.

Similarly to the SiMn-slag-S system, temperature affects interfacial behaviour between FeMn and slag both with and without sulfur. As shown in Figure 19, average interfacial tension decreases considerably with temperature in the FeMn-slag-S system with 0.57 wt pct S, $\Delta_{1623\rightarrow1723\,K} = -0.36$ N/m, compared to the system without sulfur addition, $\Delta_{1623\rightarrow1723\,K} = -0.21$ N/m.

As it was found in other studies,[31,33] the mass transfer rate of sulfur tends to increase with temperature, resulting in more intensive reactions and therefore lower values of interfacial tension between metal and slag.

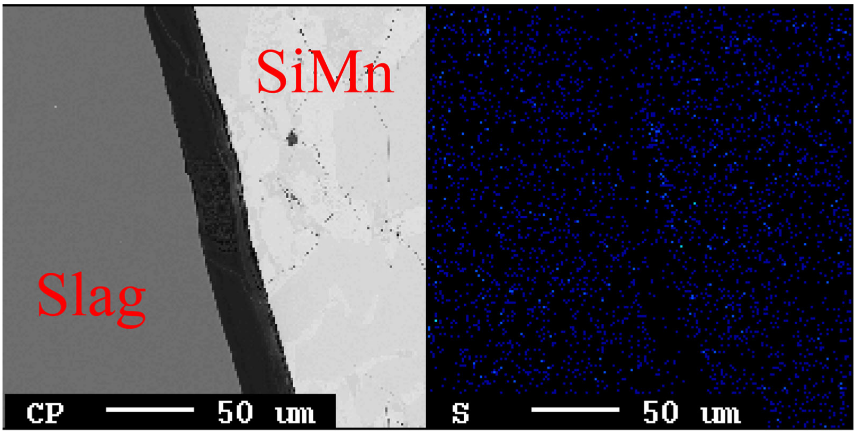

**(a)** BSE image **(b)** S distribution

Fig. 13—EPMA results of the sample from experiment 13 (0.02 wt pct $S_{SiMn}$, 1873 K, 5 min holding time). (*a*) SiMn and slag on the BSE image, (*b*) EPMA elemental mapping showing sulfur distribution between SiMn and slag.

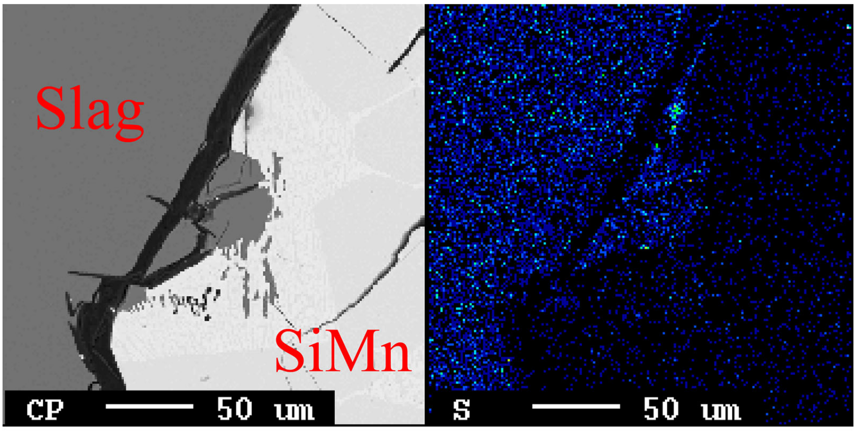

**(a)** BSE image **(b)** S distribution

Fig. 14—EPMA results of the sample from experiment 15 (0.62 wt pct $S_{SiMn}$, 1873 K, 5 min holding time). (*a*) SiMn and slag on the BSE image, (*b*) EPMA elemental mapping showing sulfur distribution between SiMn and slag.

Due to the higher temperatures in experiments with the SiMn system, slag could be reduced by solid carbon, changing the initial slag composition and hence affecting the results. As found by EPMA and shown in Table X, slag composition changes after reaction with the SiMn alloy at different temperatures and, at lower temperatures, MnO reduces first.

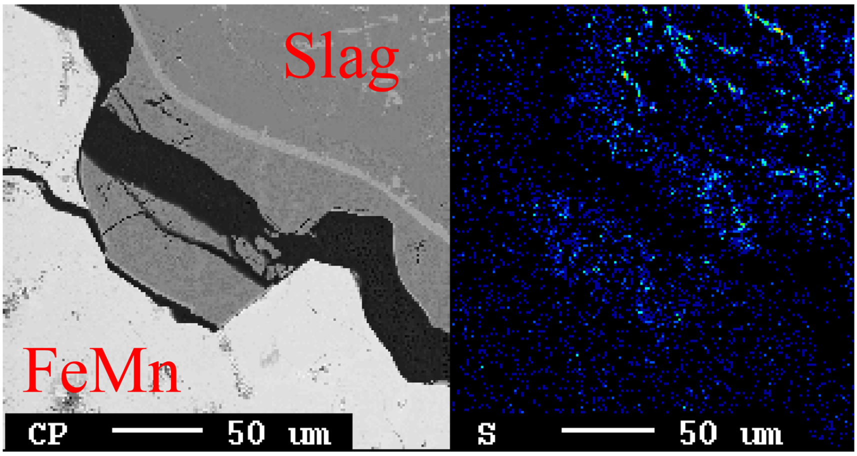

**(a)** BSE image **(b)** S distribution

Fig. 15—EPMA results of the sample from experiment 2 (0.31 wt pct $S_{FeMn}$, 1673 K, 5 min holding time). (*a*) FeMn and slag on the BSE image, (*b*) EPMA elemental mapping showing sulfur distribution between FeMn and slag.

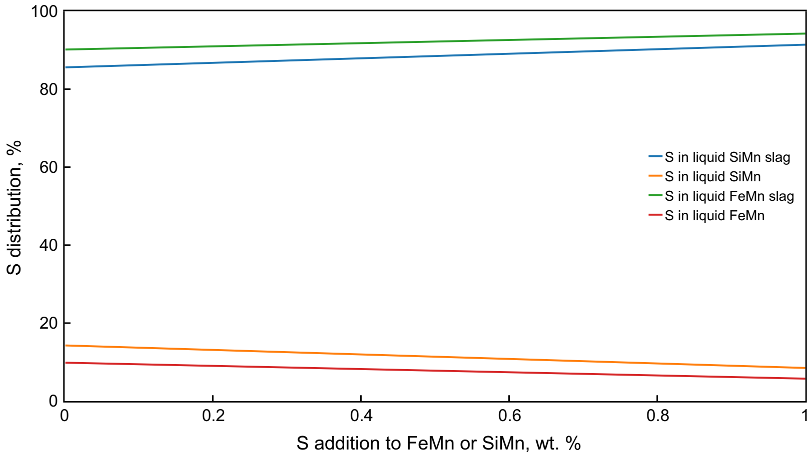

Fig. 16—Sulfur distribution between phases in the FeMn-slag-S-Ar and SiMn-slag-S-Ar systems at 1673 and 1873 K, respectively. Calculated using FactSage 7.3.

**Table X. Slag Composition (In Wt Pct) After Reaction With the SiMn Alloy at Different Temperatures in the Sessile Drop Furnace**

| Temperature (K) | MnO | CaO | MgO | $SiO_2$ | $Al_2O_3$ | FeO | Total |
|---|---|---|---|---|---|---|---|
| 1823 | 7.28 | 24.37 | 5.97 | 45.92 | 17.90 | 0.02 | 101.46 |
| 1873 | 6.38 | 25.14 | 6.17 | 44.71 | 18.65 | 0.01 | 101.06 |
| 1923 | 5.40 | 26.65 | 6.30 | 43.09 | 19.71 | 0.01 | 101.16 |

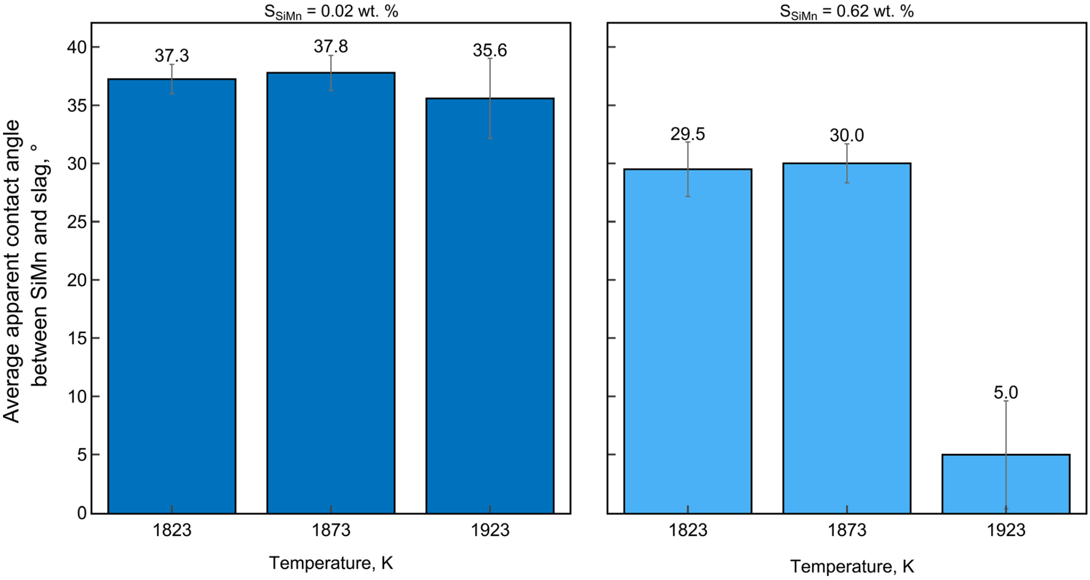

Fig. 17—Effect of temperature on average apparent contact angle between SiMn and slag at holding time of 5 min and different sulfur addition to SiMn. Grey lines on top of bars represent the 95 pct confidence interval for the sample mean.

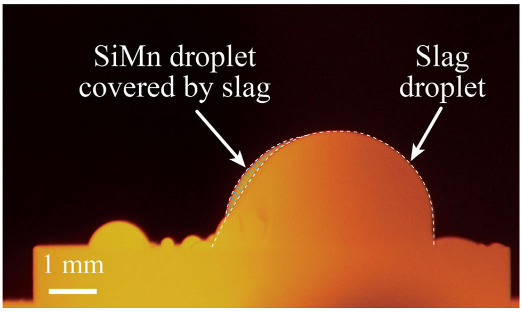

Fig. 18—SiMn and slag droplets at temperature of 1923 K. The hatched area represents the visible part of the SiMn droplet.

### E. *Effect of Holding Time*

Figure 20 shows the influence of holding time of 5, 10 and 15 minutes on average apparent contact angle between SiMn and slag for $S_{SiMn}$ of 0.02 and 0.62 wt pct at 1873 K. Similarly to temperature, holding time seems to have no effect on average apparent contact angle for $S_{SiMn}$ of 0.02 wt pct, $\Delta_{5\rightarrow15\,min} = -1.0°$. Increasing holding time from 5 to 15 minutes for $S_{SiMn}$ of 0.62 wt pct decreases average apparent contact angle between SiMn and slag from 30.0 to 20.1°. However, the largest change is observed with increasing holding time from 5 to 10 min, $\Delta_{5\rightarrow10\,min} = -9.4°$, while the change of holding time from 10 to 15 minutes has no significant effect on apparent contact angle, $\Delta_{10\rightarrow15\,min} = -0.5°$.

The effect of holding time on average interfacial tension between FeMn and slag is presented in Figure 21. For the FeMn system, varying holding time from 5 to 15 minutes seem to have no to little effect on interfacial tension, only insignificantly decreasing in experiments without sulfur and increasing when sulfur has been added to FeMn. Nevertheless, it should be noted that the confidence intervals for all holding experiments overlap, therefore, it is not possible to conclude about the negative or positive effect of holding time on interfacial tension.

Constant interfacial tension for the FeMn system and apparent contact angle for the SiMn system may indicate that the equilibrium in these systems has been reached and further holding does not affect the interfacial interaction. This also accords with previous observations,[30,34–36] where it was concluded that apparent contact angle between metal and slag dynamically changes with holding time, decreasing down to a certain minimum during the absorption of sulfur at the metal–slag interface. Subsequently, apparent contact angle stabilizes after increasing to a certain constant value, when sulfur is desorbed from the interface into the bulk of the molten metal and slag.

The sulfur distribution has been measured after the experiment with $S_{FeMn}$ of 0.57 wt pct and holding time of 10 minutes (Figure 22). It can seen by comparison with Figure 15, that the distribution of sulfur to the slag phase does not change significantly as holding time increases from 5 to 10 min, further indicating that the equilibrium has already been achieved at holding time of 5 min.

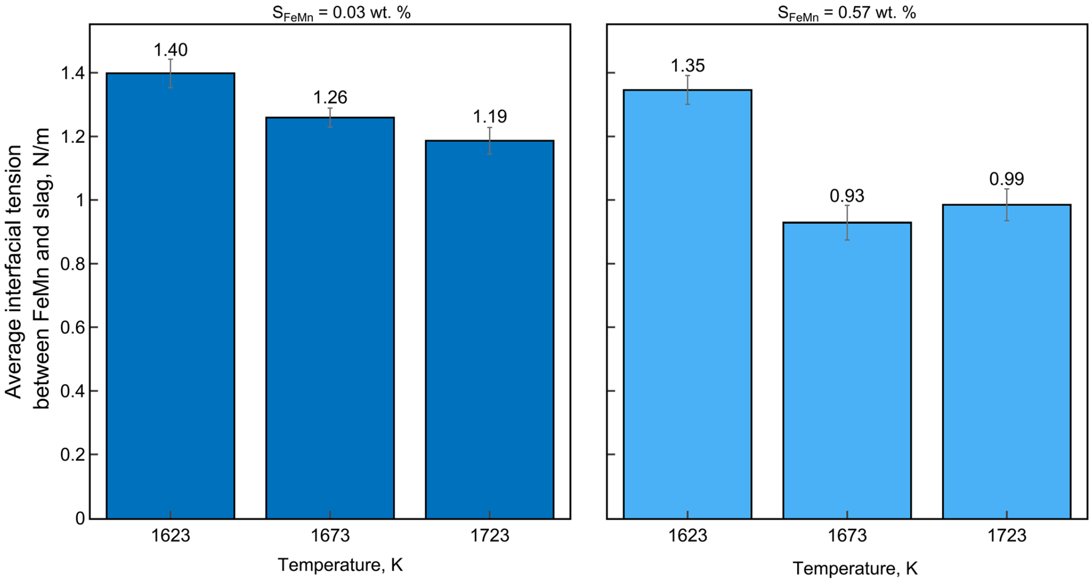

Fig. 19—Effect of temperature on average interfacial tension between FeMn and slag at holding time of 5 min and different sulfur addition to FeMn. Grey lines on top of bars represent the 95 pct confidence interval for the sample mean.

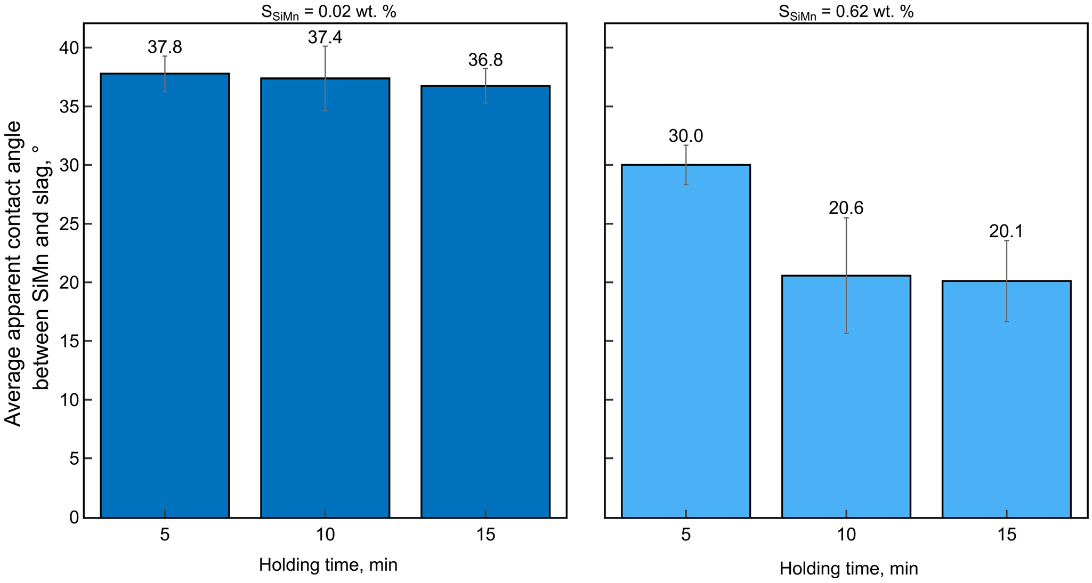

Fig. 20—Effect of holding time on average apparent contact angle between SiMn and slag at temperature of 1873 K and different sulfur addition to SiMn. Grey lines on top of bars represent the 95 pct confidence interval for the sample mean.

The data described statistically for experiments with the FeMn-slag-S and SiMn-slag-S systems is shown in Appendix A. Dynamic evolution towards the steady state for both systems is illustrated in Appendix B, where it is clear that there is a strong indication of reactions between slag and metal during the experiments, which partially explains uncertainties in the measured values.

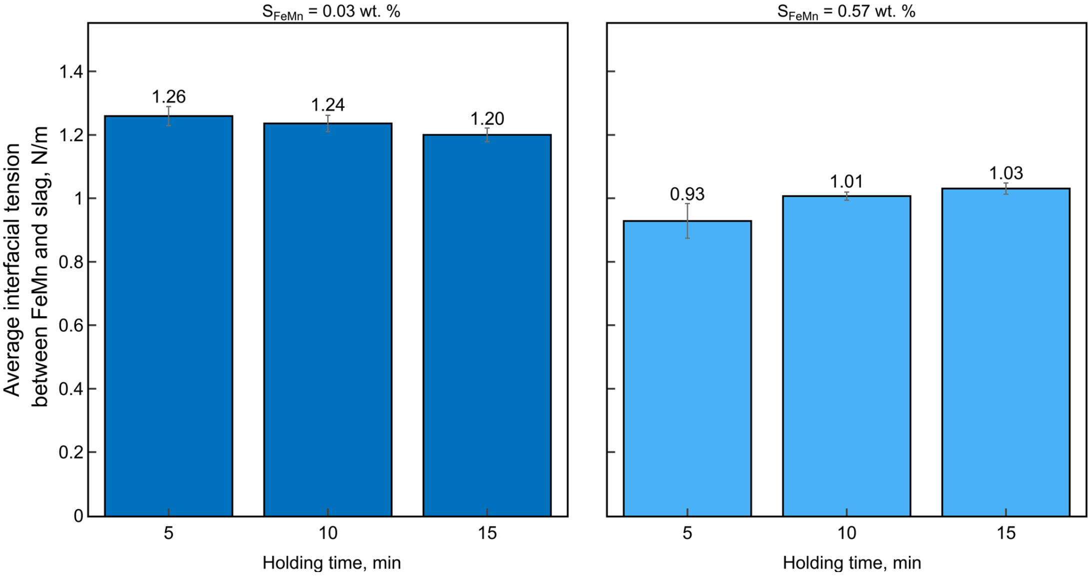

Fig. 21—Effect of holding time on average interfacial tension between FeMn and slag at temperature of 1673 K and different sulfur addition to FeMn. Grey lines on top of bars represent the 95 pct confidence interval for the sample mean.

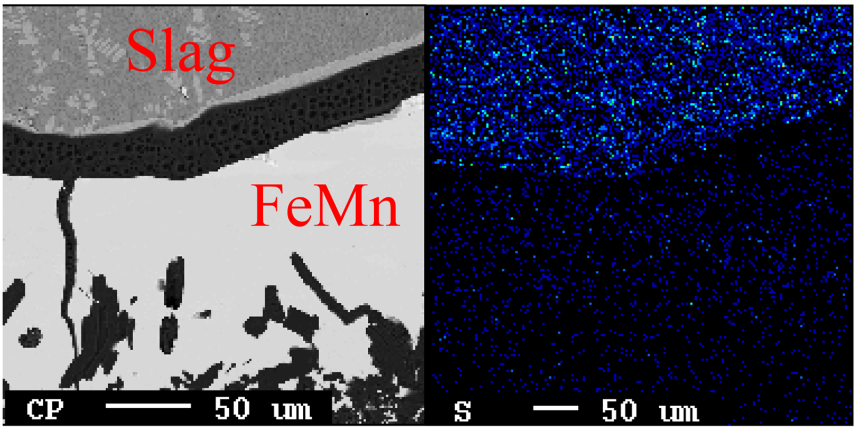

**(a)** BSE image **(b)** S distribution

Fig. 22—EPMA results of the sample from experiment 11 (0.57 wt pct $S_{FeMn}$, 1673 K, 10 min holding time). (*a*) FeMn and slag on the BSE image, (*b*) EPMA elemental mapping showing sulfur distribution between FeMn and slag. Note that the images were taken from the same region at different magnifications.

## IV. CONCLUSIONS

Sulfur plays a major role in the separation of metal and slag in ferroalloy production due to its ability to change the interfacial energy at the metal-slag interface, which leads to the formation of metal-slag emulsion and therefore additional metal losses with slag. In this study, the influence of sulfur added to FeMn or SiMn on the interfacial interaction between ferroalloy and slag has been investigated in a sessile drop furnace by applying different methodologies for FeMn and SiMn systems and comparing statistical data calculated from experimental results.

One of the more significant findings to emerge from this study is that there is a maximum of the extent to which sulfur can change interfacial tension and apparent contact angle between ferroalloy and slag—the maximum change was found at 0.25 wt pct sulfur in the SiMn alloy and 0.31 wt pct sulfur in the FeMn alloy. For all sulfur additions to ferroalloys, it is observed that sulfur distributes mainly to slag after reaching equilibrium and the amount of sulfur remaining in the metal phase is less than 15 pct.

It has been also noted that the effect of temperature on interfacial tension and apparent contact angle is more noticeable in ferroalloy-slag systems with sulfur addition, which can be explained by a higher mass transfer rate and a larger interfacial area in such systems.

The holding time seems to have a limited effect on both interfacial tension and apparent contact angle. Despite small changes observed for both systems, these results must be interpreted with caution, since the confidence intervals in all holding time experiments overlap greatly. These small changes in interfacial properties may indicate that equilibrium in the SiMn-slag system and FeMn-slag system with and without sulfur is achieved before 5 minutes of holding time, while for the SiMn-slag-S system equilibrium is reached at 10 minutes of holding.

Solid carbon particles have been found on top of the FeMn layer and thereby the improvement of the materials preparation methodology might be necessary to reduce the uncertainty in measurements—for example, using crucibles made of other materials than graphite or chemical reagents of a higher purity. However, this might also introduce additional experimental difficulties in saturating the required amount of carbon, since in this case it has be added as a raw material. Besides, interfacial tension has not been measured for the SiMn system due to the fact that only graphite cups were used in the sessile drop furnace and a limited wettability of SiMn towards graphite. Therefore, experiments with cups made of different materials can be a further development of the current methodology.

## ACKNOWLEDGMENTS

This publication has been funded by the Research Council of Norway (KPN Project, 267621). The authors gratefully acknowledge the financial support from the Research Council of Norway and the Norwegian Ferroalloy Producers Research Association (FFF).

## FUNDING

Open access funding provided by NTNU Norwegian University of Science and Technology (incl St. Olavs Hospital - Trondheim University Hospital).

## OPEN ACCESS

This article is licensed under a Creative Commons Attribution 4.0 International License, which permits use, sharing, adaptation, distribution and reproduction in any medium or format, as long as you give appropriate credit to the original author(s) and the source, provide a link to the Creative Commons licence, and indicate if changes were made. The images or other third party material in this article are included in the article's Creative Commons licence, unless indicated otherwise in a credit line to the material. If material is not included in the article's Creative Commons licence and your intended use is not permitted by statutory regulation or exceeds the permitted use, you will need to obtain permission directly from the copyright holder. To view a copy of this licence, visit http://creativecommons.org/licenses/by/4.0/.

## APPENDIX A

See Appendix Tables XI and XII.

**Table XI. Statistical Data for the Experiments With FeMn and Slag**

| | Interfacial Tension Between FeMn and Slag (N/m) | | | |
|---|---|---|---|---|
| Experiment | Mean | Standard Deviation | Standard Error | 95 Pct Margin of Error |
| 1 | 1.26 | 0.04 | 0.02 | 0.04 |
| 2 | 0.96 | 0.12 | 0.05 | 0.11 |
| 3 | 0.93 | 0.07 | 0.03 | 0.07 |
| 4 | 0.88 | 0.04 | 0.01 | 0.03 |
| 5 | 1.40 | 0.06 | 0.02 | 0.05 |
| 6 | 1.19 | 0.06 | 0.02 | 0.05 |
| 7 | 1.35 | 0.06 | 0.02 | 0.06 |
| 8 | 0.99 | 0.07 | 0.03 | 0.06 |
| 9 | 1.24 | 0.05 | 0.01 | 0.03 |
| 10 | 1.20 | 0.06 | 0.01 | 0.02 |
| 11 | 1.01 | 0.02 | 0.01 | 0.01 |
| 12 | 1.03 | 0.05 | 0.01 | 0.02 |

Table XII. **Statistical Data for the Experiments With SiMn and Slag**

| Experiment | Apparent Contact Angle Between SiMn and Slag (°) | | | |
|---|---|---|---|---|
| | Mean | Standard Deviation | Standard Error | 95 Pct Margin of Error |
| 13 | 37.8 | 2.4 | 0.8 | 1.73 |
| 14 | 31.1 | 7.6 | 2.4 | 5.5 |
| 15 | 30.0 | 2.7 | 0.9 | 1.9 |
| 16 | 29.6 | 1.9 | 0.6 | 1.4 |
| 17 | 37.3 | 2.0 | 0.6 | 3.1 |
| 18 | 35.6 | 5.8 | 1.7 | 3.9 |
| 19 | 29.5 | 4.0 | 1.2 | 2.7 |
| 20 | 5.0 | 7.8 | 2.4 | 5.3 |
| 21 | 37.4 | 4.8 | 1.4 | 3.1 |
| 22 | 36.8 | 3.0 | 0.7 | 1.6 |
| 23 | 20.6 | 11.5 | 2.5 | 5.2 |
| 24 | 20.1 | 9.8 | 1.8 | 3.6 |

## APPENDIX B

See Appendix Figs. 23, 24, 25, 26, 27, 28.

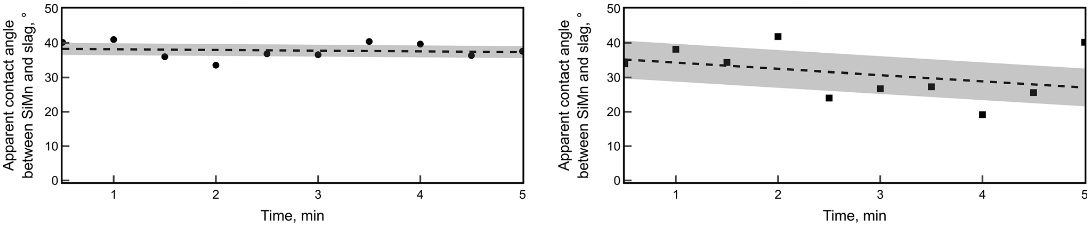

**(a)** S = 0.02 wt. %

**(b)** S = 0.25 wt. %

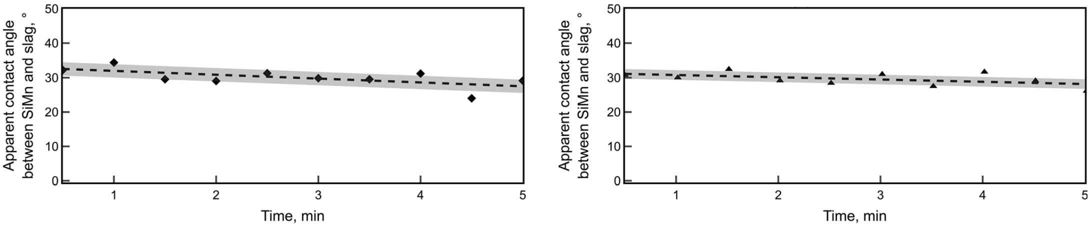

**(c)** S = 0.62 wt. %

**(d)** S = 0.90 wt. %

Fig. 23—Effect of sulfur on dynamic evolution of apparent contact angle between SiMn and slag at temperature of 1873 K and holding time of 5 min. The grey shaded area and the black dashed line represent the 95 pct confidence interval and the linear regression, respectively. Images (*a*) through (*d*) represent sulfur content in SiMn from 0.02 to 0.90 wt pct.

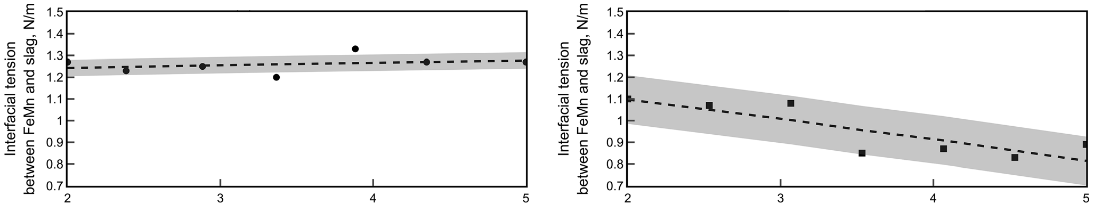

**(a)** S = 0.03 wt. %

**(b)** S = 0.31 wt. %

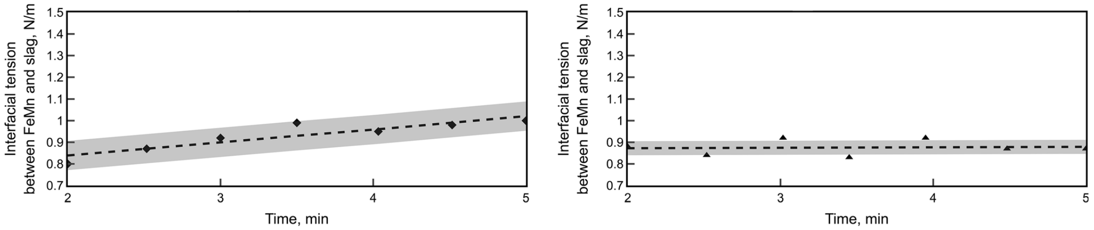

**(c)** S = 0.57 wt. %

**(d)** S = 0.93 wt. %

Fig. 24—Effect of sulfur on dynamic evolution of interfacial tension between FeMn and slag at temperature of 1673 K and holding time of 5 min. The grey shaded area and the black dashed line represent the 95 pct confidence interval and the linear regression, respectively. Images (*a*) through (*d*) represent sulfur content in FeMn from 0.03 to 0.93 wt pct.

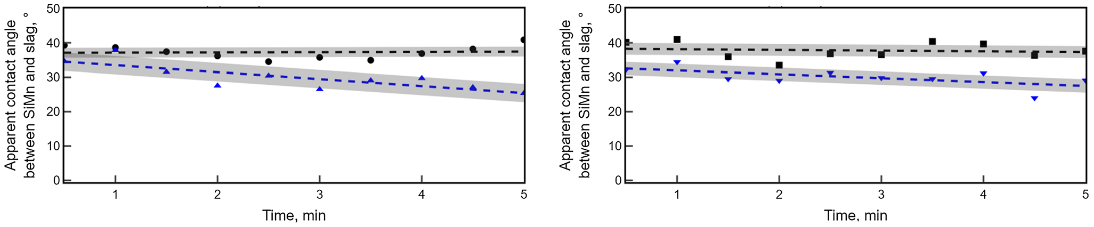

**(a)** Temperature = 1823 K

**(b)** Temperature = 1873 K

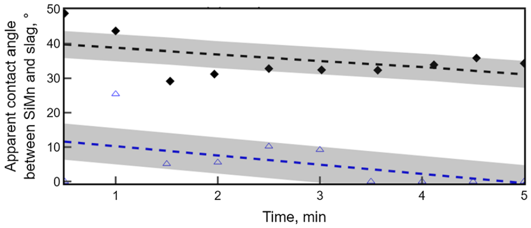

**(c)** Temperature = 1923 K

Fig. 25—Effect of temperature on dynamic evolution of apparent contact angle between SiMn and slag at holding time of 5 min. Black markers and lines refer to 0.02 wt pct $S_{\mathrm{SiMn}}$, while blue markers and lines refer to 0.62 wt pct $S_{\mathrm{SiMn}}$. The grey shaded area and dashed lines represent the 95 pct confidence interval and the linear regression, respectively. Images (*a*) through (*c*) represent temperature from 1823 to 1923 K.

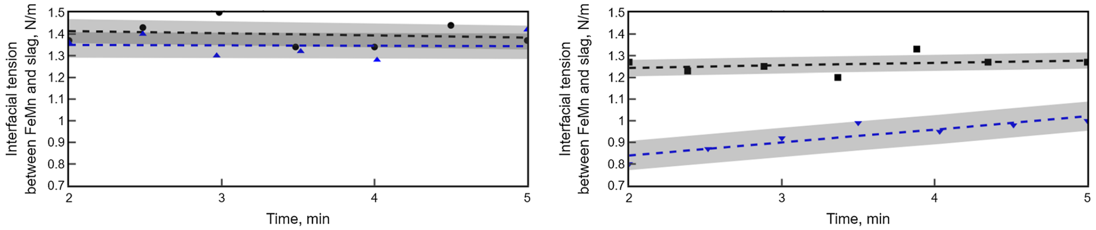

**(a)** Temperature = 1623 K

**(b)** Temperature = 1673 K

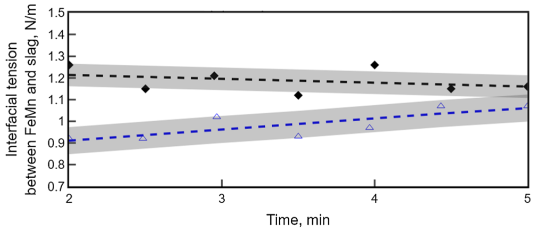

**(c)** Temperature = 1723 K

Fig. 26—Effect of temperature on dynamic evolution of interfacial tension between FeMn and slag at holding time of 5 min. Black markers and lines refer to 0.03 wt pct $S_{\mathrm{FeMn}}$, while blue markers and lines refer to 0.62 wt pct $S_{\mathrm{FeMn}}$. The grey shaded area and dashed lines represent the 95 pct confidence interval and the linear regression, respectively. Images (*a*) through (*c*) represent temperature from 1623 to 1723 K.

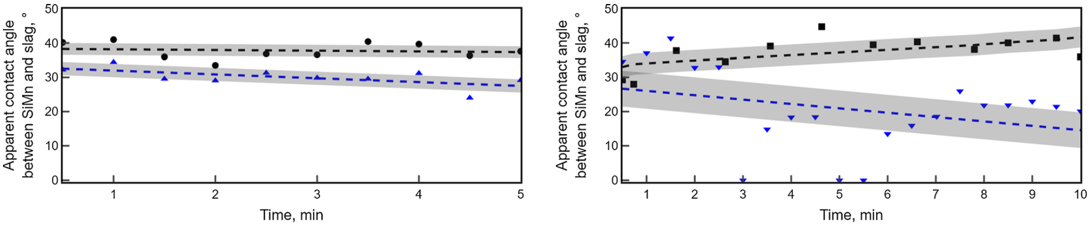

**(a)** Holding time = 5 min

**(b)** Holding time = 10 min

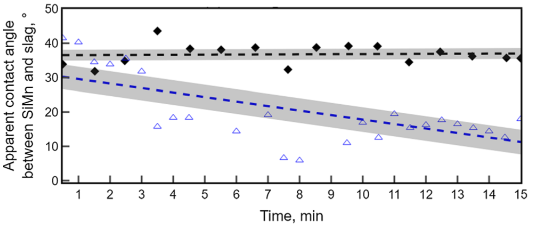

**(c)** Holding time = 15 min

Fig. 27—Effect of holding time on dynamic evolution of apparent contact angle between SiMn and slag at temperature of 1873 K. Black markers and lines refer to 0.02 wt pct $S_{\mathrm{SiMn}}$, while blue markers and lines refer to 0.57 wt pct $S_{\mathrm{SiMn}}$. The grey shaded area and dashed lines represent the 95 pct confidence interval and the linear regression, respectively. Images (*a*) through (*c*) represent holding time from 5 to 15 min.

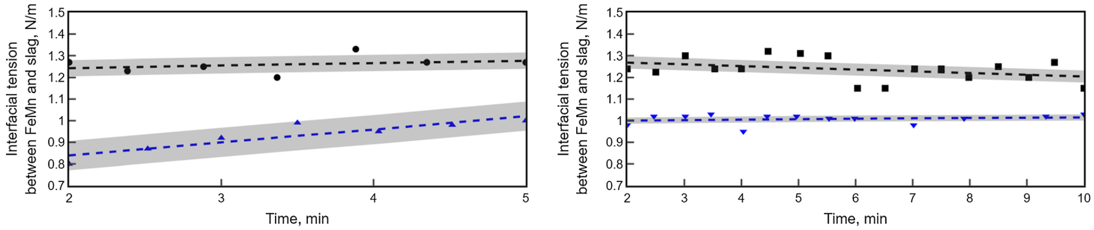

**(a)** Holding time = 5 min

**(b)** Holding time = 10 min

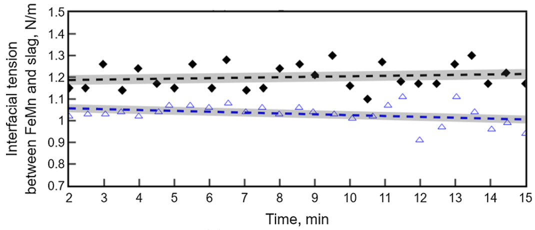

**(c)** Holding time = 15 min

Fig. 28—Effect of holding time on dynamic evolution of interfacial tension between FeMn and slag at temperature of 1673 K. Black markers and lines refer to 0.03 wt pct $S_{\mathrm{FeMn}}$, while blue markers and lines refer to 0.57 wt pct $S_{\mathrm{FeMn}}$. The grey shaded area and dashed lines represent the 95 pct confidence interval and the linear regression, respectively. Images (*a*) through (*c*) represent holding time from 5 to 15 min.

## REFERENCES

1. PR. Scheller, J. Lee, and T. Tanaka: *Treatise on Process Metallurgy: Chapter 1.8—Stability of Interface Between Liquid Steel and Molten Slag*, Elsevier, Boston, 2014, pp. 111–18.
2. M. Tangstad: *Handbook of Ferroalloys: Chapter 7—Manganese Ferroalloys Technology*, Butterworth-Heinemann, Oxford, 2013.
3. RH. Eric: *Treatise on Process Metallurgy: Chapter 1.10—Production of Ferroalloys*, Elsevier, Boston, 2014, pp. 477–32.
4. H. Ooi, T. Nozaki, and H. Yoshii: *Trans. Iron Steel Inst. Jpn.*, 1974, vol. 14, pp. 9–16.
5. AW. Cramb and I. Jimbo: *Steel Res.*, 1989, vol. 60, pp. 157–65.
6. H. Saridikmen, CS. Kucukkaragoz, and RH. Eric: *Sulphur Behaviour in Ferromanganese Smelting*, INFACON XI, New Delhi, 2007, pp. 311–20.
7. A. Jakobsson, D. Sichen, S. Seetharaman, and NN. Viswanathan: *Metall. Mater. Trans. B*, 2000, vol. 31, pp. 973–80.
8. E-J. Jung, W. Kim, I. Sohn, and D-J. Min: *J. Mater. Sci.*, 2010, vol. 45, pp. 2023–29.
9. E. Yakhshi-Tafti, R. Kumar, and HJ. Cho: *Int. J. Optomech.*, 2011, vol. 5, pp. 393–403.
10. S. Bublik, S. Bao, M. Tangstad, and K. E. Einarsrud: Slag-Metal Interactions in the FeMn Tapping Process: Interfacial Properties andWetting, Proceedings of the Liquid Metal Processing & Casting Conference 2019, Birmingham, UK, 2019, pp. 375–84.
11. S. Bublik and K. E. Einarsrud: Inverse Modelling of Interfacial Tension be436 n Ferroalloy and Slag Using OpenFOAM, 14th International Conference on CFD in Oil & Gas, Metallurgical and Process Industries, Trondheim, Nor438 SINTEF Academic Press, 2020, pp. 28–38.
12. HG. Weller, G. Tabor, H. Jasak, and C. Fureby: *Comput. Phys.*, 1998, vol. 12, pp. 620–31.
13. S. Bao, K. Tang, A. Kvithyld, M. Tangstad, and TA. Engh: *Metall. Mater. Trans. B*, 2011, vol. 42, pp. 1358–66.
14. E. Hernańdez-Baltazar and J. Gracia-Fadrique: *J. Colloid Interface Sci.*, 2005, vol. 287, pp. 213–16.
15. J. Muller, JH. Zietsman, and PC. Pistorius: *Metall. Mater. Trans. B*, 2015, vol. 46, pp. 2639–51.
16. AF. Stalder, T. Melchior, M. Müller, D. Sage, T. Blu, and M. Unser: *Colloids Surf. A*, 2010, vol. 364, pp. 72–81.
17. J. Lee, A. Kiyose, S. Nakatsuka, M. Nakamoto, and T. Tanaka: *ISIJ Int.*, 2004, vol. 44, pp. 1793–99.
18. CA. Schneider, WS. Rasband, and KW. Eliceiri: *Nat. Methods*, 2012, vol. 9, pp. 671–75.
19. DC. Montgomery: *Design and Analysis of Experiments*, 8th ed., Wiley, Hoboken, NJ, 2013.
20. E. G. Hoel: Phase Relations of Mn-Fe-Si-C Systems, INFACON 7, Trondheim, Norway, The Norwegian Ferroalloy Research Organization (FFF), 1995, pp. 601–10.
21. SK. Soni, PK. Kirar, P. Kolhe, and KC. Sahu: *Int. J. Multiph. Flow*, 2020, vol. 122, p. 103141.
22. J. Berthier: *Micro-Drops and Digital Microfluidics: Chapter 3–The Physics of Droplets*, 2nd ed., William Andrew Publishing, Burlington, 2013, pp. 75–160.
23. J. Lee, L. Thu Hoai, and M. Shin: *Metall. Mater. Trans. B*, 2011, vol. 42, pp. 546–49.
24. LT. Hoai and J. Lee: *J. Mater. Sci.*, 2012, vol. 47, pp. 8303–307.
25. BJ. Keene: *Int. Mater. Rev.*, 1988, vol. 33, pp. 1–37.
26. K. Mukai, T. Matsushita, KC. Mills, S. Seetharaman, and T. Furuzono: *Metall. Mater. Trans. B*, 2008, vol. 39, pp. 561–69.
27. J. Lee and K. Morita: *Steel Res.*, 2002, vol. 73, pp. 367–72.
28. J. Xin, N. Wang, M. Chen, and L. Gan: *ISIJ Int.*, 2019, vol. 59, pp. 759–67.
29. M. Hanao, T. Tanaka, M. Kawamoto, and K. Takatani: *ISIJ Int.*, 2007, vol. 47, pp. 935–39.
30. M. Suzuki, M. Nakamoto, T. Tanaka, Y. Tsukaguchi, K. Mishima, and M. Hanao: *ISIJ Int.*, 2020, vol. 60, pp. 2332–38.
31. PP. Kim and M. Tangstad: *Metall. Mater. Trans. B*, 2018, vol. 49, pp. 1185–96.
32. CW. Bale, E. Bélisle, P. Chartrand, SA. Decterov, G. Eriksson, AE. Gheribi, K. Hack, IH. Jung, YB. Kang, J. Melançon, AD. Pelton, S. Petersen, C. Robelin, J. Sangster, P. Spencer, and M-A. Van Ende: *CALPHAD: Comput. Coupling Phase Diagr. Thermochem.*, 2016, vol. 54, pp. 35–53.
33. Q. Wang, Y. Liu, F. Wang, Y. Cao, and G. Li: *Metals*, 2019, vol. 9, p. 751.

34. T. Tanaka, H. Goto, M. Nakamoto, M. Suzuki, M. Hanao, M. Zeze, H. Yamamura, and T. Yoshikawa: *ISIJ Int*., 2016, vol. 56, pp. 944–52.
35. P. Ni, T. Tanaka, M. Suzuki, M. Nakamoto, and PG. Jönsson: *ISIJ Int*., 2019, vol. 59, pp. 737–48.
36. P. Ni, T. Tanaka, M. Suzuki, M. Nakamoto, and PG. Jönsson: *ISIJ Int*., 2018, vol. 58, pp. 1979–88.

**Publisher's Note** Springer Nature remains neutral with regard to jurisdictional claims in published maps and institutional affiliations.

# Paper V

ORIGINAL RESEARCH ARTICLE

# Interfacial Behaviour in Ferroalloys: The Influence of FeMn Slag Composition

SERGEY BUBLIK, MERETE TANGSTAD, and KRISTIAN ETIENNE EINARSRUD

The present study investigated the interfacial interaction between FeMn alloy and slags of different compositions and basicity from 0.4 to 1.2 in a sessile drop furnace. Interfacial tension between the FeMn alloy and the slags was measured, and the results were analyzed to assess the sensitivity of the applied methodology. The measurement of the interfacial tension was based on combining the results from experiments, multiphase flow simulations in OpenFOAM, equilibrium calculations in FactSage, and calculation of slag density and surface tension based on numerical models. The results demonstrate that the interfacial tension between the FeMn alloy and slag increases with the slag basicity. It was found that the addition of $Al_2O_3$ to the slag with basicity of 0.8 and 1.2 increases the interfacial tension, while increasing MnO content from 30.0 to 45.0 wt pct does not have any statistically significant influence on the interfacial tension. EPMA analysis of slag and FeMn phases showed that slags at lower basicities and the FeMn alloy form a metal–slag emulsion due to the destabilization of the interface induced by chemical reactions, partial reduction of $SiO_2$ in the slag and the mass transfer of Si across the metal–slag interface.

https://doi.org/10.1007/s11663-022-02605-3
© The Author(s) 2022

## I. INTRODUCTION

THE carbothermic reduction of manganese ores for producing FeMn alloy in submerged arc furnaces is related to the formation of a significant amount of molten slag, which is then tapped simultaneously with FeMn to ladles, where a metal–slag emulsion is formed. Small FeMn droplets are entrained in the slag phase due to the intensive mixing of FeMn and slag. This decreases efficiency of the ferroalloy production process because further removal of metal from slag may cause logistics difficulties and is heavily time- and energy-consuming.[1,2] Interfacial tension between molten metal and slag characterizes the metal-slag separation[3] and thus it is important for ferroalloy production. High interfacial tension promotes a high degree of separation of metal and slag, while a low interfacial tension will promote formation of metal–slag emulsion and small metal droplets in slag.[4] Several studies have shown that the interfacial tension is greatly dependent upon the slag composition due to chemical reactions at the metal–slag interface and the mass transfer across the interface.[5–12]

In FeMn production, the FeMn alloy is highly saturated with carbon, which results in reduction of oxides such as MnO, FeO or $SiO_2$ at the interface between FeMn and slag, and subsequently in the mass transfer of Mn, Fe and Si to the FeMn alloy. The thermodynamic equilibrium between ferroalloy and slag can be described by several reduction reactions:[13]

$$(\mathrm{MnO}) + [\mathrm{C}] = [\mathrm{Mn}] + \mathrm{CO}_{(g)}, \qquad [1]$$

$$(\mathrm{SiO_2}) + 2[\mathrm{C}] = [\mathrm{Si}] + 2\mathrm{CO}_{(g)}, \qquad [2]$$

$$(\mathrm{FeO}) + [\mathrm{C}] = [\mathrm{Fe}] + \mathrm{CO}_{(g)}, \qquad [3]$$

$$(\mathrm{MnO}) + [\mathrm{Fe}] = [\mathrm{Mn}] + (\mathrm{FeO}), \qquad [4]$$

$$(\mathrm{SiO_2}) + 2[\mathrm{Mn}] = [\mathrm{Si}] + 2(\mathrm{MnO}), \qquad [5]$$

where [] and () denote chemical constituents in the FeMn alloy and the slag, respectively.

The determination of the metal–slag interfacial tension is challenging as it requires applying high temperatures and recording metal–slag interaction with X-ray imaging[14] or a digital camera.[6] Generally, these methods may have significant experimental uncertainty

---

SERGEY BUBLIK, MERETE TANGSTAD, and KRISTIAN ETIENNE EINARSRUD are with the Department of Materials Science and Engineering, Norwegian University of Science and Technology (NTNU), 7491 Trondheim, Norway. Contact e-mail: sergey.bublik@ntnu.no

Manuscript submitted December 6, 2021; accepted July 13, 2022.
Article published online August 19, 2022.

due to sensitivity to impurities present in raw materials and crucibles, or the resolution of X-ray images.[15] Therefore, the use of advanced analysis and modelling tools can be of great help in understanding the interfacial phenomena and in improving and simplifying the experimental setup for measuring interfacial tension.

In the current study, the interfacial interaction between FeMn alloy and slags of different compositions was investigated in a sessile drop furnace using the methodology developed by the authors previously,[16,17] which was improved in this study to improve reproducibility and reduce uncertainty due to the precipitation of solid carbon during melting of FeMn alloy and slag. The improved methodology combines analysis of images from experiments in the sessile drop furnace, numerical data obtained in multiphase flow simulations in OpenFOAM v8,[18] the numerical models for calculation of density and surface tension of slag developed by Mills *et al*.[19,20] and results of equilibrium calculations in FactSage 7.3.[21] In addition, the sensitivity of the results was assessed by comparing different experiments.

## II. EXPERIMENTAL

### A. *Material Preparation*

Synthetic FeMn alloy and slags have been prepared from pure powders for studying interfacial tension in the sessile drop furnace. Compositions of the FeMn alloy and the slags have been selected based on the composition of industrial materials and, in addition, the synthetic slags have been selected to cover the most relevant slags for FeMn production. The calculated composition of the synthetic raw materials and the purity of powders used for material preparation are specified in Tables IV and V in "Appendix A", respectively. The composition of FeMn alloy and slag measured by the X-ray fluorescence (XRF) and the combustion infrared detection (combustion-IR) techniques is shown in Table I. The corresponding normalized data is given in Table VI in "Appendix A".

The powders were mixed and melted separately in graphite crucibles in an induction furnace in Ar atmosphere at temperature of 1773 K and holding time of 60 minutes for the FeMn alloy and 5 minutes for master slags. After the first melting, the FeMn alloy and the master slags were cooled down in the crucibles and ground in a ball mill. Thereafter, the master slags were divided into batches of 20 g and an additional amount of the oxide powders has been added according to the composition of the final slags. Both the FeMn alloy and the master slags were then remelted using the same operational parameters in the induction furnace. The amount of the powders required to produce the synthetic materials has been calculated taking into account the purity of the powders and the composition of the industrial materials[1] and is presented in Table VII in "Appendix A". Note that carbon has not been added as a raw material for melting of the FeMn alloy as it is contained in the graphite crucible—this allows to saturate the required amount of carbon, $\approx 7$ wt pct for the FeMn alloy.

### B. *Experimental Setup*

A sessile drop furnace (Figure 1) has been applied for investigating the interfacial interaction between the FeMn alloy and the slags as shown in Figure 2. The sessile drop furnace was equipped with a pyrometer and a C-type thermocouple for measuring temperature, and with a digital video camera (Allied Vision Prosilica GT2000, Edmund Optics, Inc., Barrington) with a telecentric lens (Navitar 1-50993D) for recording images of molten samples with the resolution of 2048 × 1088 pixels at one frame per second after reaching melting temperature of the FeMn alloy and the slags. Every 10 to 15 experiments, the thermocouple was calibrated by melting pure Fe in Ar and assessing its melting temperature from recorded images. The experiments were performed using graphite cups in Ar atmosphere (6N grade) at temperature of 1673 K and holding time of 5 minutes in sets, where three parallels were performed for each slag composition. The heating rate was 300 K/min up to 1473 K and approximately 25 K/min from 1473 K to 1673 K. The graphite cups were cleaned before the experiments with a paper towel dipped in ethanol or acetone and then dried using compressed air. A schematic representation of the slag and the FeMn alloy in the graphite cup before and during the experiments is shown in Figure 3.

After the experiments, the FeMn alloy and the slags were cast in epoxy, sectioned in the centre of the slag droplet, re-cast into epoxy, polished and coated with carbon prior to analysis in EOL JXA-8500F Electron Probe Micro Analyzer (EPMA). The composition of FeMn and slag phases were measured in several points, and the average composition of each phase was calculated based on this. Additionally, the chemical composition of the synthetic FeMn alloy and the slags before the experiments was determined by XRF and combustion-IR. The FeMn alloy was analyzed for Mn, Fe, Si and C, and the slags were analyzed for MnO, CaO, MgO, $SiO_2$, $Al_2O_3$ and FeO.

### C. *Methodology for Determination of Interfacial Tension*

The methodology for determination of the interfacial tension is based on a comparison of geometrical features obtained from multiphase CFD simulations and the experiments in the sessile drop furnace[17] as illustrated in Figure 4. This methodology was developed by the authors previously[16,17] and has been modified in this paper to improve reproducibility and reduce uncertainty due to the precipitation of solid carbon on the surface of FeMn and slag during the experiments in the sessile drop furnace.

The experimental step is performed to obtain images of slag and metal interaction in the molten state. Here, a set of three individual experiments with the slag droplet placed on top of the FeMn layer in the graphite cup are conducted for each slag composition.

Table I. The Measured Chemical Composition of the Synthetic FeMn Alloy and Slags

| | Chemical Composition (Wt Pct) | | | | | | | | | | | |
|---|---|---|---|---|---|---|---|---|---|---|---|---|
| Material | Mn | Fe | Si | C | MnO | CaO | MgO | $SiO_2$ | $Al_2O_3$ | FeO | Total | Basicity* |
| FeMn Alloy | 77.30 | 14.50 | 0.11 | 7.52 | — | — | — | — | — | — | 99.43 | — |
| Slags with $Al_2O_3$ Addition | | | | | | | | | | | | |
| Slag A1 | — | — | — | — | 30.62 | 14.23 | 6.77 | 39.52 | 10.23 | 0.89 | 102.26 | 0.42 |
| Slag A2 | — | — | — | — | 29.30 | 25.50 | 6.75 | 29.18 | 10.17 | 0.79 | 101.69 | 0.82 |
| Slag A3 | — | — | — | — | 28.91 | 32.00 | 6.64 | 22.14 | 10.19 | 0.79 | 100.67 | 1.20 |
| Slag B1 | — | — | — | — | 37.90 | 12.87 | 6.72 | 34.15 | 10.18 | 0.77 | 102.59 | 0.44 |
| Slag B2 | — | — | — | — | 36.77 | 22.50 | 6.58 | 25.21 | 10.08 | 0.74 | 101.88 | 0.82 |
| Slag B3 | — | — | — | — | 37.53 | 27.87 | 6.83 | 18.33 | 10.01 | 0.74 | 101.31 | 1.22 |
| Slag C1 | — | — | — | — | 45.43 | 10.76 | 6.61 | 28.84 | 10.23 | 0.73 | 102.60 | 0.44 |
| Slag C2 | — | — | — | — | 44.65 | 19.04 | 6.83 | 20.80 | 10.19 | 0.73 | 102.24 | 0.83 |
| Slag C3 | — | — | — | — | 45.39 | 23.92 | 6.70 | 15.04 | 10.01 | 0.72 | 101.78 | 1.22 |
| Slags Without $Al_2O_3$ Addition | | | | | | | | | | | | |
| Slag D1 | — | — | — | — | 30.67 | 14.76 | 6.10 | 48.83 | 0.67 | 0.89 | 101.92 | 0.42 |
| Slag D2 | — | — | — | — | 29.83 | 25.30 | 6.31 | 38.32 | 0.77 | 0.85 | 101.38 | 0.81 |
| Slag D3 | — | — | — | — | 29.27 | 31.91 | 6.18 | 32.23 | 0.61 | 0.80 | 101.00 | 1.16 |
| Slag E1 | — | — | — | — | 38.68 | 12.93 | 6.09 | 43.32 | 0.58 | 0.77 | 102.37 | 0.43 |
| Slag E2 | — | — | — | — | 37.01 | 22.69 | 6.16 | 34.40 | 0.69 | 0.75 | 101.70 | 0.82 |
| Slag E3 | — | — | — | — | 37.24 | 28.17 | 6.10 | 28.36 | 0.68 | 0.61 | 101.16 | 1.18 |
| Slag F1 | — | — | — | — | 46.00 | 10.58 | 6.23 | 38.14 | 0.69 | 0.71 | 102.35 | 0.43 |
| Slag F2 | — | — | — | — | 44.33 | 19.64 | 6.10 | 30.53 | 0.56 | 0.68 | 101.84 | 0.83 |
| Slag F3 | — | — | — | — | 45.33 | 24.53 | 6.01 | 25.02 | 0.47 | 0.70 | 102.06 | 1.20 |

*Basicity ($B$) = $\frac{CaO+MgO}{SiO_2+Al_2O_3}$, calculated on mass basis.

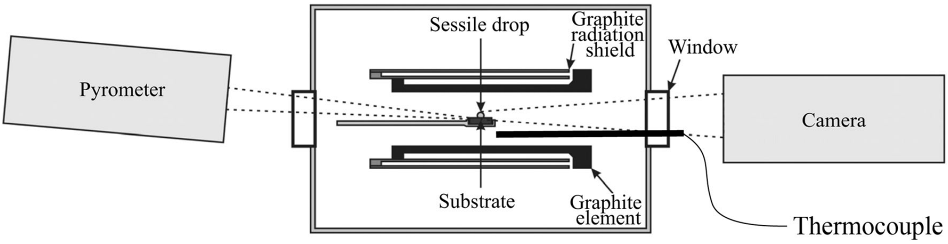

Fig. 1—Schematic of the sessile drop furnace. Reprinted from Ref. [22] under the terms of the Creative Commons CC BY license.

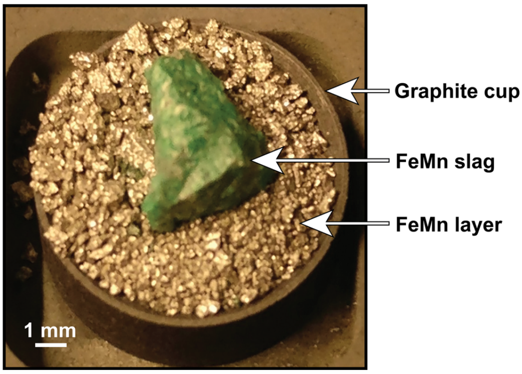

Fig. 2—FeMn alloy and slag in the graphite cup before the experiments in the sessile drop furnace. Reprinted from Ref. [17].

The composition of the slag and metal changes during the experiments, and therefore the composition of the liquid slag and the formed solid monoxide phase must be taken into account to address the change in composition. The amount and composition of liquid slag phase is determined at the adjustment step, which is then used to estimate surface tension and density of the slag droplet at the equilibrium using numerical models developed by Mills *et al.* [19,20] The adjustment step is performed as follows:

(a) Calculate amount and composition of the liquid slag and solid phases after interaction with the FeMn alloy at 1673 K in FactSage in the equilibrium module using FactPS, FToxid and FTmisc databases.

(b) Calculate the surface tension and the density of the slag droplet and its liquid slag phase using the numerical models developed by Mills *et al.*

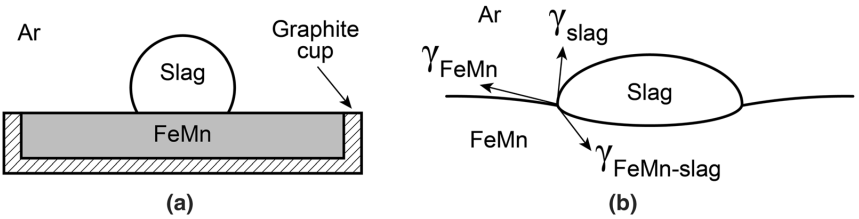

Fig. 3—(*a*) Schematic cross section of the slag droplet on top of the FeMn alloy in the graphite cup before the experiments. (*b*) The force balance at the contact point of Ar, slag and FeMn during the experiments. $\gamma_{\text{FeMn}}$ is surface tension of FeMn, $\gamma_{\text{slag}}$ is surface tension of slag, $\gamma_{\text{FeMn-slag}}$ is interfacial tension between FeMn and slag. It should be observed that the slag droplet is small compared to the surface of FeMn, ensuring that it does not come in contact with the graphite cup.

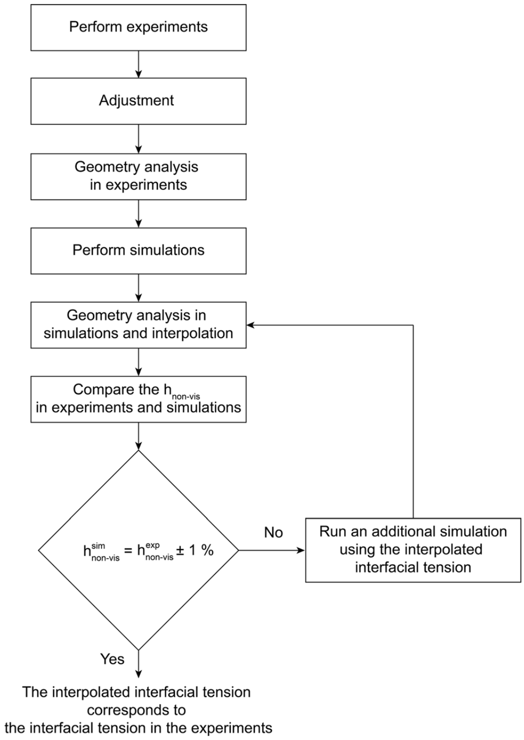

Fig. 4—Schematic describing steps for the determination of interfacial tension in the experiments based on the geometrical parameters of the slag droplet.

(c) Calculate the average surface tension and the average density which can be found as the average between the slag droplet and its liquid phase.

Then, a geometric analysis of the slag droplet in the experiments is carried out to characterize the interfacial interaction between the FeMn alloy and the slags and measure geometrical parameters of the slag droplet. These are assessed after 2 minutes of holding time at the minimum volume expansion of the slag droplet to minimize the influence of volume fluctuations due to chemical reactions and gas evolution on experimental results. In addition, the surface roughness due to the formation of solid carbon and the amount of FeMn layer filling the graphite cup are addressed. The following substeps are conducted at this step:

(a) Determine the surface correction coefficient for each experiment, $k_{\text{R}}$, by direct measurement and averaging of the size of particles at the interfaces. In this study, $k_{\text{R}}$ was up to 0.7 mm, depending on the surface roughness, which corresponds to 25 pct of the typical droplet size.

(b) Calculate total volume of the slag droplet, $V_{\text{total}}$, using slag density in the molten state and weight of the slag droplet measured before the experiments:

$$V_{\text{total}} = \frac{m_{\text{slag}}}{\rho_{\text{slag}}}, \qquad [6]$$

where $m_{\text{slag}}$ is the weight of the slag droplet.

(c) Calculate visible volume of the slag droplet in the experiments, $V^{\text{exp}}_{\text{vis}}$, assuming that the slag droplet forms a spherical cap both above and below the FeMn–gas interface and subtracting $k_{\text{R}}$ from visible height and radius of the slag droplet:

$$V^{\text{exp}}_{\text{vis}} = \frac{1}{6}\pi\left(h^{\text{exp}}_{\text{vis}} - k_{\text{R}}\right)\left(3\left(a^{\text{exp}} - k_{\text{R}}\right)^2 + \left(h^{\text{exp}}_{\text{vis}} - k_{\text{R}}\right)^2\right), \qquad [7]$$

where $h^{\text{exp}}_{\text{vis}}$ is the visible height of the slag droplet and $a^{\text{exp}}$ is the measured radius of the slag droplet.

(d) Calculate non-visible volume of the slag droplet in the experiments, $V^{\text{exp}}_{\text{non-vis}}$:

$$V^{\text{exp}}_{\text{non-vis}} = V^{\text{exp}}_{\text{total}} - V^{\text{exp}}_{\text{vis}}. \qquad [8]$$

(e) Calculate non-visible height of the slag droplet in the experiments, $h^{\text{exp}}_{\text{non-vis}}$, by expressing it from the equation:

$$V^{\text{exp}}_{\text{non-vis}} = \frac{1}{6}\pi h^{\text{exp}}_{\text{non-vis}}\left(3\left(a^{\text{exp}} - k_{\text{R}}\right)^2 + \left(h^{\text{exp}}_{\text{non-vis}}\right)^2\right). \qquad [9]$$

(f) The FeMn layer does not completely fill the graphite cup, therefore, distance from the FeMn–gas interface to the edge of the graphite cup has to be taken into account as well. It can be calculated using volume of the cup, density of the FeMn alloy in the molten state and weight of the FeMn layer:

$$V_{\mathrm{cup}} = \pi r_{\mathrm{cup}}^2 h_{\mathrm{cup}}, \qquad [10]$$

$$V_{\mathrm{FeMn}} = \frac{m_{\mathrm{FeMn}}}{\rho_{\mathrm{FeMn}}}, \qquad [11]$$

$$h_{\mathrm{add}} = \frac{V_{\mathrm{cup}} - V_{\mathrm{FeMn}}}{\pi r_{\mathrm{cup}}^2}, \qquad [12]$$

where $V_{\mathrm{cup}}$ is the volume of the cup, $r_{\mathrm{cup}}$ is the inner radius of the cup (4 mm), $h_{\mathrm{cup}}$ is the inner height of the cup (3 mm), $V_{\mathrm{FeMn}}$ is the volume of the FeMn layer, $m_{\mathrm{FeMn}}$ is the weight of the FeMn layer, $\rho_{\mathrm{FeMn}}$ is the density of FeMn in the molten state (5612 kg/m$^3$[23]), $h_{\mathrm{add}}$ is the distance from the FeMn–gas interface to the edge of the graphite cup, correcting for the cup not being 100 pct filled. A visual explanation of all geometrical parameters is shown in Figure 5.

(g) Considering $h_{\mathrm{add}}$, calculate the non-visible height of the slag droplet in the experiments (in pct):

$$h_{\mathrm{non-vis}}^{\mathrm{exp}}\,(\mathrm{pct}) = \frac{h_{\mathrm{non-vis}}^{\mathrm{exp}} - h_{\mathrm{add}}}{h_{\mathrm{non-vis}}^{\mathrm{exp}} + h_{\mathrm{vis}}^{\mathrm{exp}}} \cdot 100. \qquad [13]$$

(h) Calculate the average non-visible height for each experiment:

$$\bar{h}_{\mathrm{non-vis}}^{\mathrm{exp}}\,(\mathrm{pct}) = \frac{\sum h_{\mathrm{non-vis}}^{\mathrm{exp}}(\mathrm{pct})}{n}, \qquad [14]$$

where $n$ is the number of observations, considering the minimum volume expansion of the slag droplet.

Furthermore, at the modelling step, simulations are performed using the physical properties and parameters from the experiments: surface tension (assumed to be a constant value of 1.50 N/m as was calculated previously[24] by the authors for the FeMn alloy composition considered in this study) and the density of the FeMn alloy in the molten state; the average surface tension and the average density of slag in the molten state; the weight of the slag droplet and the FeMn layer. As shown in Figure 6, the interfacial interaction between the FeMn alloy and the slag droplet is simulated without walls of the graphite cup. However, the geometrical features of the slag droplet have to be calculated considering that a part of the slag droplet cannot be seen due to the walls. The non-visible height in the simulation is then compared to the non-visible height in the experiment, and if they differ significantly, a new simulation is started. Here, the following substeps are performed:

(a) Perform three parallel simulations using the interfacial tension between the FeMn alloy and the slag droplet of 0.30, 1.15 and 2.00 N/m.

(b) Knowing the apex position of the slag droplet on $Y$-axis ($Y_{\mathrm{slag\,apex}}$) and the edge position of the graphite cup on $Y$-axis ($Y_{\mathrm{edge}}$), visible height of the slag droplet in simulations can be obtained:

$$h_{\mathrm{vis}}^{\mathrm{sim}} = Y_{\mathrm{slag\,apex}} - Y_{\mathrm{edge}}, \qquad [15]$$

$$h_{\mathrm{vis}}^{\mathrm{sim}}\,(\mathrm{pct}) = \frac{h_{\mathrm{vis}}^{\mathrm{sim}}}{h_{\mathrm{droplet}}^{\mathrm{sim}}} \cdot 100. \qquad [16]$$

(c) Non-visible height is then expressed as:

$$h_{\mathrm{non-vis}}^{\mathrm{sim}}\,(\mathrm{pct}) = 100 - h_{\mathrm{vis}}^{\mathrm{sim}}\,(\mathrm{pct}). \qquad [17]$$

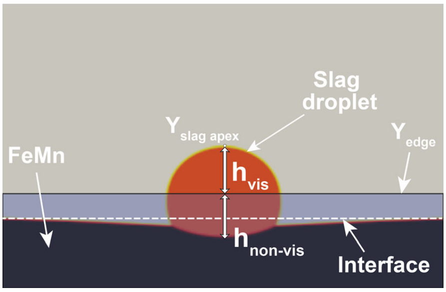

Fig. 6—The slag droplet at the FeMn–Ar interface in the steady state in the simulations. The semi-transparent blue filled area represents the walls of the graphite cup with $r_{\mathrm{cup}}$ of 4 mm and $h_{\mathrm{cup}}$ of 3 mm (Color figure online).

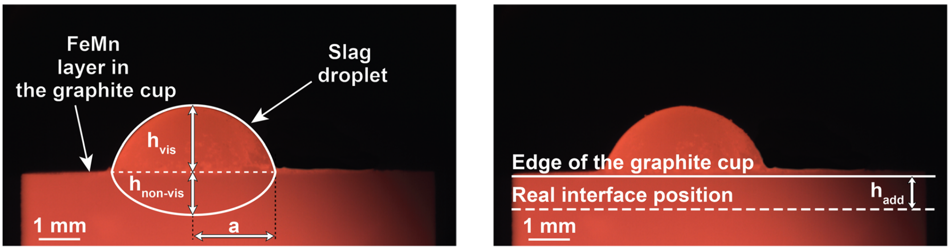

(a)

(b)

Fig. 5—Geometrical parameters of the slag droplet (*a*) and the real position of the interface (*b*) used in the calculations. Note that the lines shown in the figures are schematic only and may not represent actual measured geometrical parameters.

Consequently, the average non-visible height of the slag droplet in a steady state is calculated (in pct):

$$\overline{h}^{\text{sim}}_{\text{non-vis}}\,(\text{pct}) = \frac{\sum h^{\text{sim}}_{\text{non-vis}}\,(\text{pct})}{n_t}, \qquad [18]$$

where $n_t$ is the number of time steps in the steady state corresponding to the last 0.4 seconds of the simulation. $h^{\text{sim}}_{\text{non-vis}}$ is calculated for each time step and the simulation is stopped when two conditions are met: simulation time is higher than 0.8 seconds and $\overline{h}^{\text{sim}}_{\text{non-vis}}\,(\text{pct})$ is almost constant ($\pm 2$ pct) during the last 0.4 seconds of the simulation, *i.e.*, when the steady state is reached.

(d) Linearly interpolate $\overline{h}^{\text{sim}}_{\text{non-vis}}\,(\text{pct})$ from the current set of simulations as a function of the interfacial tension and determine the corresponding value of the interfacial tension to $\overline{h}^{\text{exp}}_{\text{non-vis}}$.

(e) Perform a simulation using the interpolated interfacial tension and calculate $\overline{h}^{\text{sim}}_{\text{non-vis}}\,(\text{pct})$ as described in step (c).

(f) Repeat steps from (c) to (e) until $\overline{h}^{\text{sim}}_{\text{non-vis}}\,(\text{pct})$ is ±1 pct from the experimental value ($\overline{h}^{\text{exp}}_{\text{non-vis}}$).

The 80 pct confidence interval was calculated for each set of three experiments based on the Student's *t*-distribution[25]:

$$\text{CI} = \overline{y} \pm t\frac{s}{\sqrt{n}}, \qquad [19]$$

where $\overline{y}$ is the sample mean, $t$ is the critical value found from the confidence level and degrees of freedom of the sample (1.886 for a two-tailed test with a statistical significance of 0.2 and two degrees of freedom), $s$ is the sample standard deviation and $n$ is the number of experiments in a set. Here, $s$ is expressed as:

$$s = \sqrt{\frac{\sum_{i=1}^{n}\left(y_i - \overline{y}\right)^2}{n-1}}, \qquad [20]$$

where $y_i$ $\{y_1, y_2, \ldots, y_n\}$ represents one measured value of the sample (*i.e.*, interfacial tension in a single experiment).

## III. RESULTS AND DISCUSSION

### A. *Surface Tension and Density of Slags*

The composition of liquid slag phase of the slags after interaction with the FeMn alloy at 1673 K was calculated in FactSage and is shown in Table II. As can be seen from this table, the composition of the liquid slag changes after reacting with FeMn, which can be partially attributed to the reduction of MnO to Mn by Reaction (1) and mainly due to the formation of solid MnO–MgO–CaO phase resulting in a lower MnO and MgO content in the liquid slag when the basicity increases. In addition, there is no solid slag phase at low slag basicity of 0.4 and $SiO_2$ in the slag is partially reduced to the metal phase by Reaction (2). Note that $Al_2O_3$ remains in the liquid slag phase and FeO introduced into the slag by impurities in the raw materials is completely reduced to the metal phase through Reaction (3).

The surface tension and density of the slags, as given in Table III, were calculated considering the composition of the initial slag (Table I) and the liquid slag phase calculated in FactSage. The surface tension does not vary significantly between the initial slag and the liquid slag phase; the maximum variation of 0.025 N/m (5.5 pct) was observed for slag D1. Higher values of the surface tension at higher basicities are related to the composition change, thereby the content of CaO increases while $SiO_2$ decreases. CaO has a high surface tension of 0.625 N/m in its pure form, whereas surface tension of pure $SiO_2$ (0.260 N/m) is substantially lower.[20] In addition, slags without $Al_2O_3$ addition have lower surface tension due to the low content of $Al_2O_3$ which has a high surface tension of 0.655 N/m. However, the variation in the density between the initial slag and the liquid slag phase is higher and reaches 301 kg/m$^3$ or 9.6 pct for slag C3. The density for the initial slags is almost constant regardless of the slag basicity, but it increases when MnO and $Al_2O_3$ content in the slags increases as they have a higher density of 5370 and 3965 kg/m$^3$, respectively, in their pure form compared with CaO (3340 kg/m$^3$), MgO (3580 kg/m$^3$) and $SiO_2$ (2650 kg/m$^3$).[26] For the liquid slag phase, the density decreases with the slag basicity due to the significant change in the composition of the liquid phase after interacting with the FeMn alloy, which leads to a lower MnO content.

### B. *Effect of Slag Composition on Interfacial Tension*

The interfacial tension between the FeMn alloy and the slags with and without $Al_2O_3$ addition is shown in Figures 7 and 8, respectively. It can be seen from the figures that the interfacial tension sharply increases with the slag basicity for both groups of slags. Moreover, for slags with $Al_2O_3$, the increase in interfacial tension is more pronounceable at higher basicities. As such, the average interfacial tension for the slags with $Al_2O_3$ addition is 0.21 to 0.40 N/m higher at the basicity of 0.8, and 0.05 to 0.36 N/m higher for the basicity of 1.2. In addition, the 80 pct confidence intervals overlap greatly in each group of basicities due to the low number of experiments in parallels; however, the measured values of the interfacial tension fall within the proposed ranges of the confidence intervals. Increasing MnO content in slag from 30.0 to 45.0 wt pct does not show statistically significant differences in the interfacial tension for all slags. Here, it is important to note that due to the fluctuations of the slag droplet during reaction with the FeMn alloy, which can influence the experimental results, the non-visible height and, accordingly, the interfacial tension were measured only at local minimum expansion of the slag droplet as shown in Figure 9.

Table II. The Chemical Composition of the Liquid Slag Phase After Interaction with the FeMn Alloy Calculated in FactSage

| | Chemical Composition (Wt Pct) | | | | |
|---|---|---|---|---|---|
| Liquid Phase Corresponding to | MnO | CaO | MgO | $SiO_2$ | $Al_2O_3$ |
| Slags with $Al_2O_3$ Addition | | | | | |
| Slag A1 | 34.76 | 14.05 | 6.68 | 34.41 | 10.10 |
| Slag A2 | 26.60 | 26.22 | 6.95 | 29.72 | 10.46 |
| Slag A3 | 21.15 | 36.27 | 4.92 | 25.57 | 12.11 |
| Slag B1 | 38.15 | 12.96 | 6.77 | 31.87 | 10.25 |
| Slag B2 | 31.42 | 24.09 | 6.68 | 27.02 | 10.79 |
| Slag B3 | 22.82 | 35.91 | 3.92 | 24.26 | 13.09 |
| Slag C1 | 42.75 | 11.11 | 6.82 | 28.75 | 10.56 |
| Slag C2 | 33.28 | 23.20 | 5.52 | 25.53 | 12.46 |
| Slag C3 | 24.77 | 34.36 | 3.33 | 22.70 | 14.83 |
| Slags Without $Al_2O_3$ Addition | | | | | |
| Slag D1 | 42.66 | 13.56 | 5.60 | 37.55 | 0.62 |
| Slag D2 | 31.69 | 25.55 | 6.37 | 35.61 | 0.78 |
| Slag D3 | 26.18 | 33.26 | 6.51 | 33.39 | 0.65 |
| Slag E1 | 44.43 | 12.76 | 6.01 | 36.22 | 0.58 |
| Slag E2 | 35.92 | 23.33 | 6.34 | 33.70 | 0.71 |
| Slag E3 | 29.87 | 31.51 | 6.14 | 31.72 | 0.76 |
| Slag F1 | 48.34 | 10.65 | 6.28 | 34.03 | 0.69 |
| Slag F2 | 40.96 | 20.64 | 6.41 | 31.41 | 0.59 |
| Slag F3 | 31.82 | 30.69 | 5.47 | 31.42 | 0.59 |

Table III. The Calculated Surface Tension and Density of the Initial Slag and the Liquid Slag Phase

| | Surface Tension (N/m) | | | Density ($kg/m^3$) | | |
|---|---|---|---|---|---|---|
| Slag | Initial Slag | Liquid Phase | Average | Initial Slag | Liquid Phase | Average |
| Slags with $Al_2O_3$ Addition | | | | | | |
| A1 | 0.460 | 0.472 | 0.466 | 3138 | 3223 | 3181 |
| A2 | 0.502 | 0.501 | 0.502 | 3170 | 3126 | 3148 |
| A3 | 0.529 | 0.521 | 0.525 | 3187 | 3076 | 3132 |
| B1 | 0.474 | 0.485 | 0.479 | 3270 | 3313 | 3292 |
| B2 | 0.510 | 0.506 | 0.508 | 3292 | 3209 | 3251 |
| B3 | 0.536 | 0.524 | 0.530 | 3318 | 3108 | 3213 |
| C1 | 0.486 | 0.486 | 0.486 | 3414 | 3376 | 3395 |
| C2 | 0.519 | 0.508 | 0.514 | 3426 | 3247 | 3337 |
| C3 | 0.541 | 0.527 | 0.534 | 3446 | 3145 | 3296 |
| Slags Without $Al_2O_3$ Addition | | | | | | |
| D1 | 0.429 | 0.454 | 0.442 | 3025 | 3266 | 3146 |
| D2 | 0.470 | 0.476 | 0.473 | 3083 | 3115 | 3099 |
| D3 | 0.493 | 0.491 | 0.492 | 3103 | 3050 | 3077 |
| E1 | 0.441 | 0.458 | 0.450 | 3169 | 3298 | 3234 |
| E2 | 0.477 | 0.478 | 0.478 | 3201 | 3185 | 3193 |
| E3 | 0.499 | 0.493 | 0.496 | 3229 | 3110 | 3170 |
| F1 | 0.453 | 0.462 | 0.458 | 3311 | 3375 | 3343 |
| F2 | 0.484 | 0.482 | 0.483 | 3327 | 3270 | 3299 |
| F3 | 0.505 | 0.492 | 0.499 | 3360 | 3139 | 3250 |

Previous studies[5,8,27] investigated the mechanisms of the interfacial interaction between molten Fe and $CaO–SiO_2–Al_2O_3$ slag, where it was suggested that the interfacial tension between slag and metal changes due to reduction or oxidation reactions in molten Fe containing Al (Eq. [21]) or decomposition and dissolution of $SiO_2$ into molten Fe without Al (Eq. [22]). The interfacial tension rapidly decreases due to the proposed reactions, and then gradually increases before reaching a constant value at the equilibrium between slag and metal. As shown in Figure 9, the similar behaviour can be observed in the current study, when the visible surface area of slag B1 and B2 sharply changes in the beginning of the holding period (0 to 1.5 minutes) and then remains practically constant. This may indicate that the dynamic interfacial oxygen potential and the

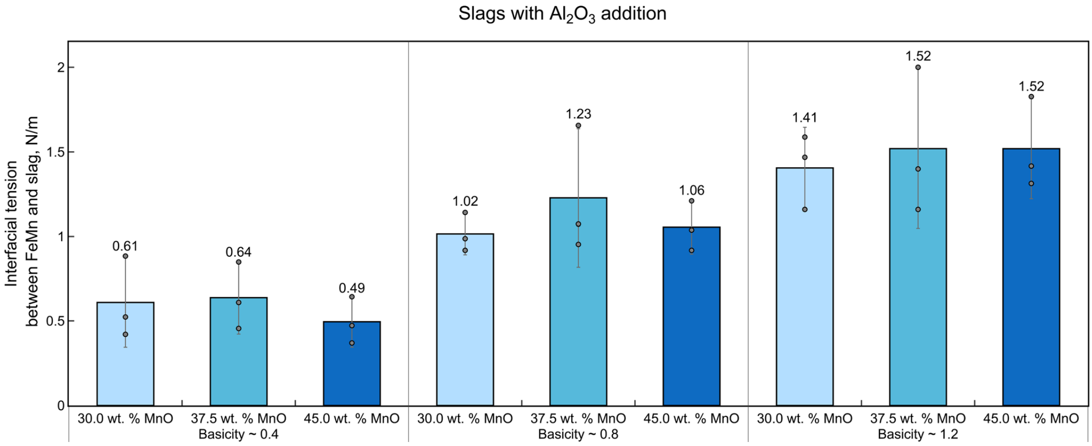

Fig. 7—The interfacial tension between the FeMn alloy and the slag with the addition of $Al_2O_3$ at different slag basicities and MnO content at 1673 K. The top part of the bars corresponds to the average interfacial tension between the FeMn alloy and the slag. The grey lines on top of bars represent the 80 pct confidence interval, and the circle markers represent the experimental measurements.

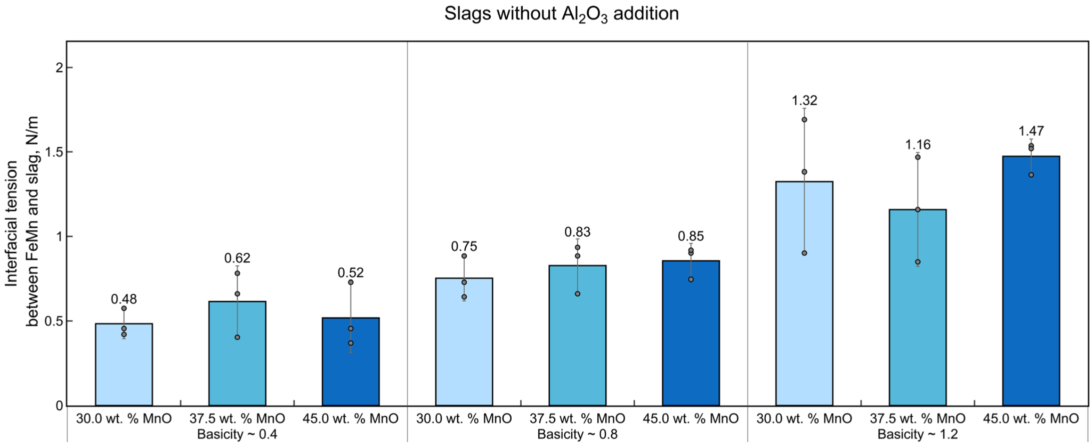

Fig. 8—The interfacial tension between the FeMn alloy and the slag without the addition of $Al_2O_3$ at different slag basicities and MnO content at 1673 K. The top part of the bars corresponds to the average interfacial tension between the FeMn alloy and the slag. The grey lines on top of bars represent the 80 pct confidence interval, and the circle markers represent the experimental measurements.

mass transfer rate across the interface decrease as reactions between slag and metal proceed as previously was found by Gu *et al.*[28]

$$4[\mathrm{Al}] + 3(\mathrm{SiO_2}) \rightarrow 2(\mathrm{Al_2O_3}) + 3[\mathrm{Si}], \quad [21]$$

$$(\mathrm{SiO_2}) \rightarrow [\mathrm{Si}] + 2[\mathrm{O}]. \quad [22]$$

Nakashima and Mori[11] studied interfacial interaction between molten Fe and $CaO–SiO_2–Al_2O_3$, and $CaO–MgO–Al_2O_3$ slags, where it was concluded that the interfacial tension can be greatly modified due to the change of slag composition. Several researchers[10,29–31] have shown that a decrease of $SiO_2$ in slag with increasing $CaO/SiO_2$ ratio decreases oxygen content and therefore oxygen activity in molten Fe, which causes an increase of the interfacial tension.[6,7] As such, the addition of CaO and $Al_2O_3$ to the slag slightly increases the interfacial tension, while the addition of MnO and FeO substantially decreases it. However, it was pointed out that the interfacial tension, depending on MnO content, decreases exponentially, reaching a steady value at high MnO content (after adding 20 mol pct MnO). As it is shown in the present results, the interfacial tension does not change with the MnO content, meaning that a steady value has been reached, after which the interfacial tension does not change after the addition of MnO. The $Al_2O_3$ addition and the slag basicity also show a similar effect on the interfacial tension, similar to what was reported in the literature.

Interfacial interaction of the slag droplet with the FeMn alloy in the graphite cup depending on different slag composition is shown in Figures 10, 11 and 12. The non-visible height of the slag droplet with MnO content of 30 wt pct decreases with the basicity (Figure 10), which means that the droplet tends to stay at the interface and leads to better separation of slag and metal. Furthermore, the angle between the tangent of the droplet and the top of the crucible $\theta_{s-cr}$ increases from 73.8 to 90.4 deg, indicating a reduced contact area between slag and metal owing to increased interfacial tension between these phases.

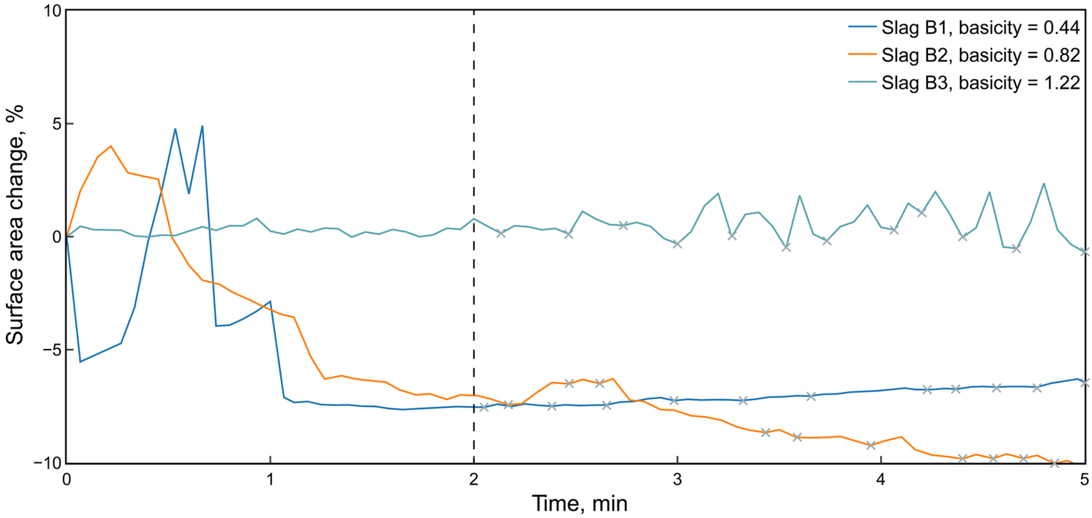

Fig. 9—Temporal change in visible surface area for slags B1–B3 during holding at 1673 K. The grey cross markers correspond to the local minimum expansion of the slag droplet in the experiments. Note that interfacial tension was measured only after 2 minutes of holding time as indicated with the vertical dashed line.

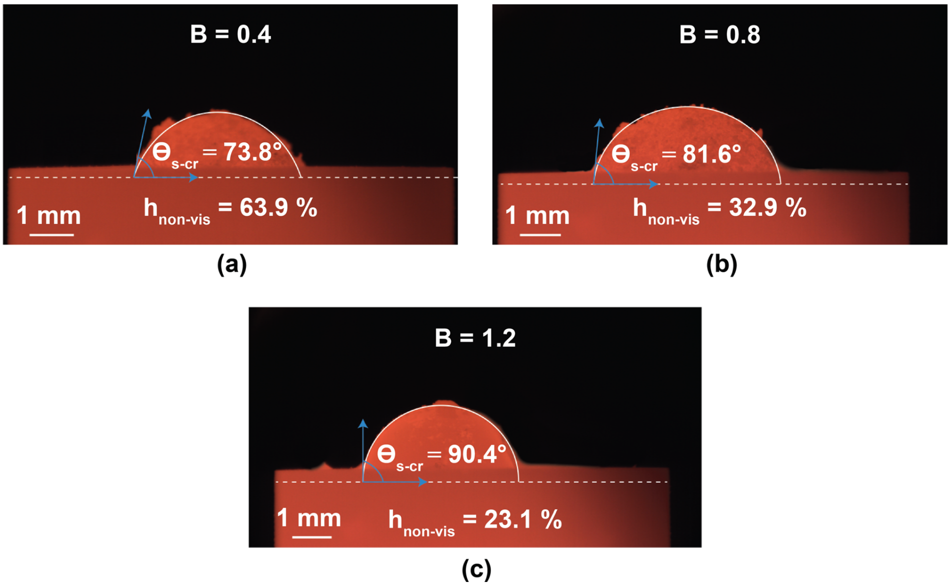

Fig. 10—Slag droplets with various basicity and constant MnO content of 30 wt pct during interaction with the FeMn alloy at 1673 K: (*a*) slag A1, (*b*) slag A2, and (*c*) slag A3. The droplet contour and the real position of the interface are shown by the solid and the dashed line, respectively.

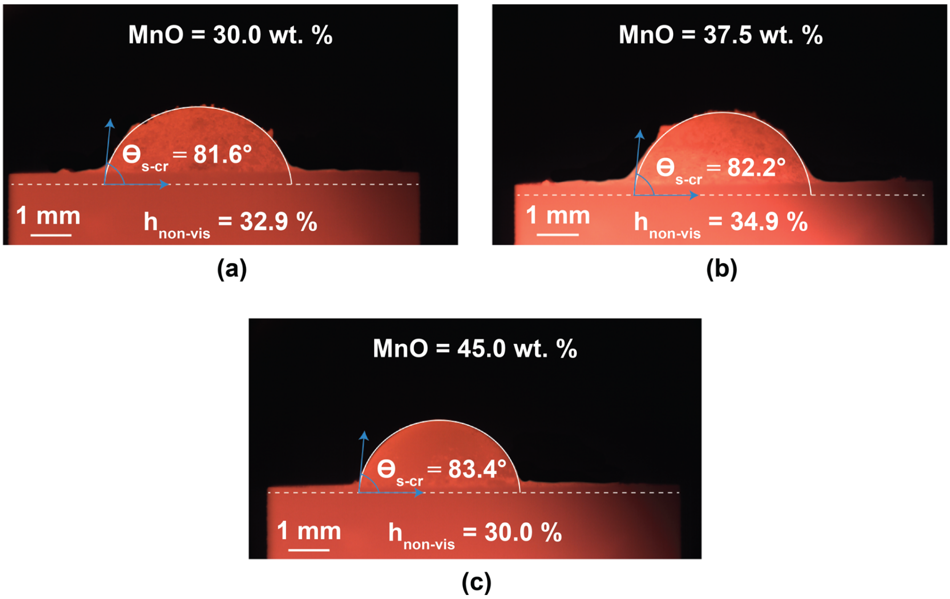

Fig. 11—Slag droplets with constant basicity of 0.8 and various MnO content during interaction with the FeMn alloy at 1673 K: (*a*) slag A2, (*b*) slag B2, and (*c*) slag C2. The droplet contour and the real position of the interface are shown by the solid and the dashed line, respectively.

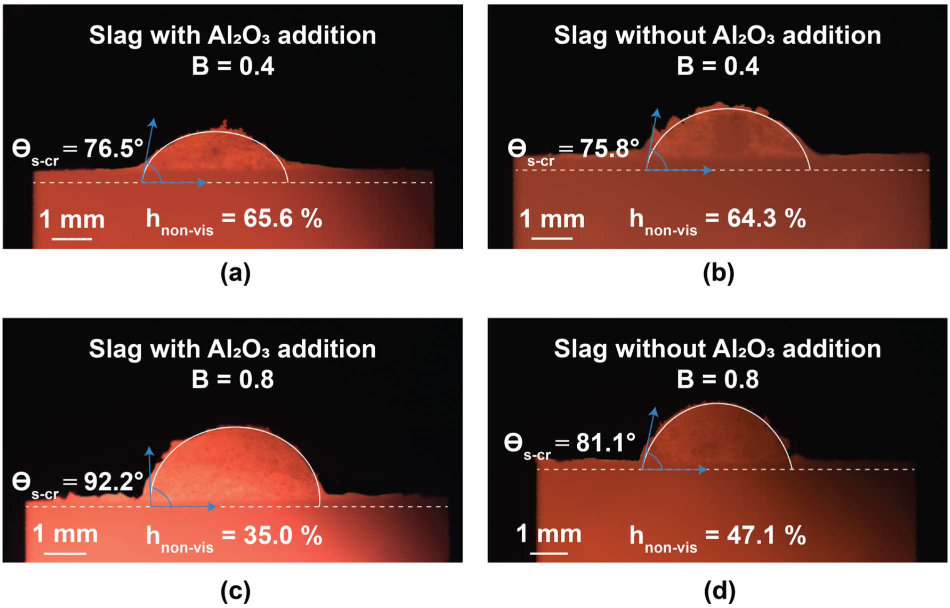

Fig. 12—Slag droplets with various basicity and constant MnO content of 37.5 wt pct during interaction with the FeMn alloy at 1673 K. Images (*a*) and (*c*) correspond to slags B1 and B2 (with $Al_2O_3$ addition); images (*b*) and (*d*) show slags E1 and E2 (without $Al_2O_3$ addition). The droplet contour and the real position of the interface are shown by the solid and the dashed line, respectively.

As illustrated in Figure 11, the variation in MnO content in the slag from 30.0 to 45.0 wt pct at basicity of 0.8 shows that both the non-visible height of the slag droplet and the angle between slag and the top of the crucible are nearly constant which results in comparable values of the interfacial tension for all MnO contents. Similarly, the addition of $Al_2O_3$ to the low basicity slag (Figures 12(a) and (b)) does not show any influence on the non-visible height and the angle $\theta_{s-cr}$, while the effect of alumina addition is more obvious at a higher slag basicity of 0.8 (Figures 12(c) and (d)) as the angle $\theta_{s-cr}$ decreases and the non-visible height increases which leads to lower values of the interfacial tension and therefore worse separation of slag and metal.

## C. *EPMA Results*

A general view of the FeMn alloy and slags with and without $Al_2O_3$ addition after the experiments in the sessile drop furnace is shown in Figures 13 and 14, respectively. As observed for the slags with low basicities (0.4 and 0.8), the slag penetrates the FeMn phase, indicating that the interface is disturbed and the interfacial area increases due to the chemical reactions between the slag and metal. The chemical composition of slag and metal phases (Tables VIII and IX in "Appendix B") confirms that interfacial tension decreases at low slag basicity due to chemical reactions between slag and FeMn alloy and mass transfer of Si to the metal phase. As such, Si can be found in the metal phases after interaction with the low basicity slags at high temperatures, despite the fact that Si was not originally added to the FeMn alloy, which indicates that $SiO_2$ in the slag is reduced through Reaction (2). In addition, FeMn droplets were observed on top of the slag phase (Figures 13(a) and 14(a)), specifying that the slag of low basicity and the FeMn alloy form a metal–slag emulsion during the reactions, resulting in their poor separation.

Chung and Cramb[12] suggested that the emulsification phenomena are closely related to the interaction of fluids at the interface and that the driving force for fluid flow across the interface depends on reactions in the system under isothermal conditions due to the concentration gradient at the interface. In case of the concentration gradient and the fluid flow driven by the

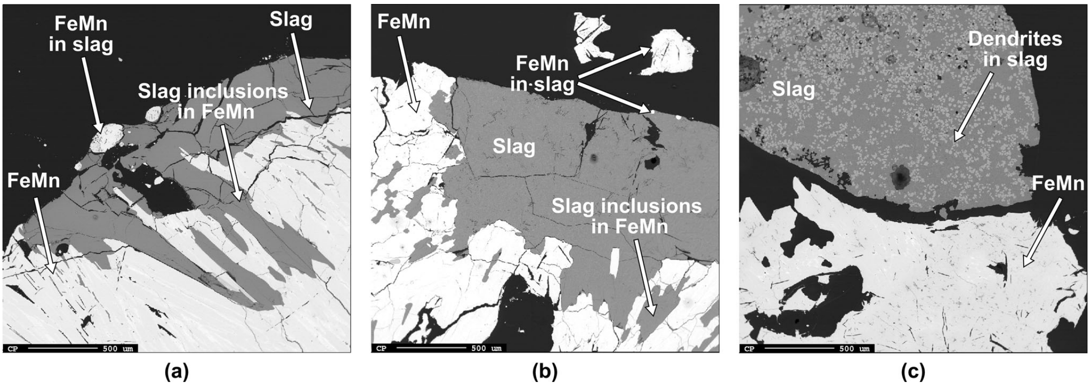

Fig. 13—BSE images of the FeMn alloy and slags with $Al_2O_3$ addition after the experiments: (*a*) slag B1 (basicity = 0.4), (*b*) slag B2 (basicity = 0.8), and (*c*) slag B3 (basicity = 1.2).

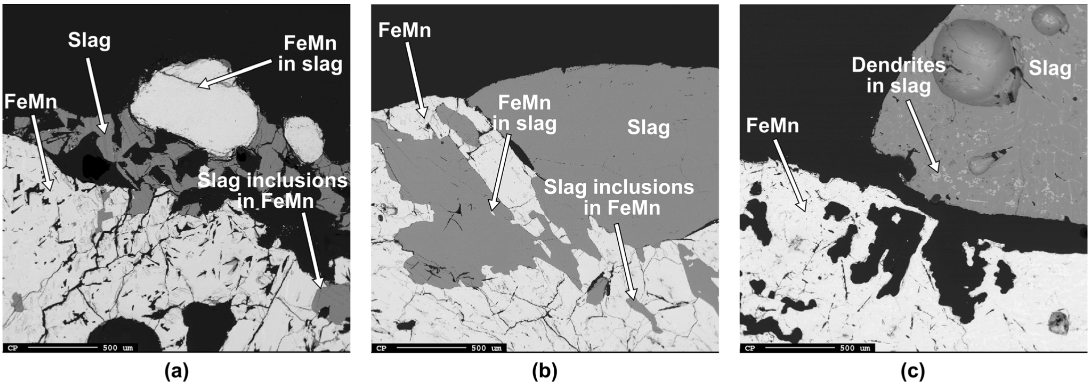

Fig. 14—BSE images of the FeMn alloy and slags without $Al_2O_3$ addition after the experiments: (*a*) slag E1 (basicity = 0.4), (*b*) slag E2 (basicity = 0.8), and (*c*) slag E3 (basicity = 1.2).

interfacial reaction, the interface eventually becomes unstable and the metal–slag interfacial area increases (the Kelvin–Helmholtz interfacial instability). Based on the Kelvin–Helmholtz model, Gopal[3] discussed the mechanism of small droplet formation and emulsification of slag and metal during reactions between them. If the mass transfer rate of elements or compounds across the interface is low, it results in a slight destabilization of the interface (Figure 15(a)), corresponding to the high slag basicity of 1.2 in this study. At higher mass transfer rates, the destabilization of the interface is more severe as shown in Figures 15(b) and (c), which results in the formation of the metal–slag emulsion and droplets of one phase into another as it was observed for the low slag basicities from 0.4 to 0.8.

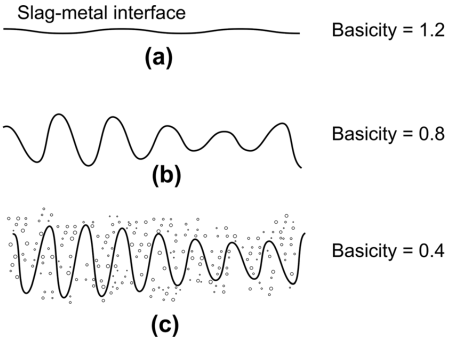

Fig. 15—Emulsification of slag and metal and formation of small droplets due to the Kelvin–Helmholtz instability. Images (*a*) through (*c*) represent disturbances of the interface between slag and metal at different slag basicities.

Solid carbon particles in the form of graphite whiskers have been observed on top of FeMn layer and along the walls of the graphite cup in all experiments as illustrated in Figure 16. The formation of the solid carbon particles may be attributed to different temperatures used for the materials preparation and the experiments.[24] Bao *et al.*[32] also confirmed this finding and showed that solid carbon particles can form extensively when non-carbon saturated FeMn alloy reacts with slag and a graphite substrate, especially if CO is present in the system. In addition, carbon is consumed from the FeMn alloy due to the partial reduction of MnO, $SiO_2$ and FeO by Reactions (1), (2) and (3), therefore this creates an additional driving force for the FeMn alloy to dissolve carbon from the graphite cup, which causes the molten FeMn alloy to penetrate the walls of the graphite cup.

## IV. CONCLUSIONS

In the present study, the interaction between FeMn alloy and slags of different compositions has been studied by comparing experimental results from a sessile drop furnace and modelling results from multiphase flow simulations in OpenFOAM.

The current results show that the interfacial tension between FeMn alloy and slag increases when the slag basicity changes from 0.4 to 1.2. It was also found that the addition of $Al_2O_3$ to the slag with basicity of 0.8 and

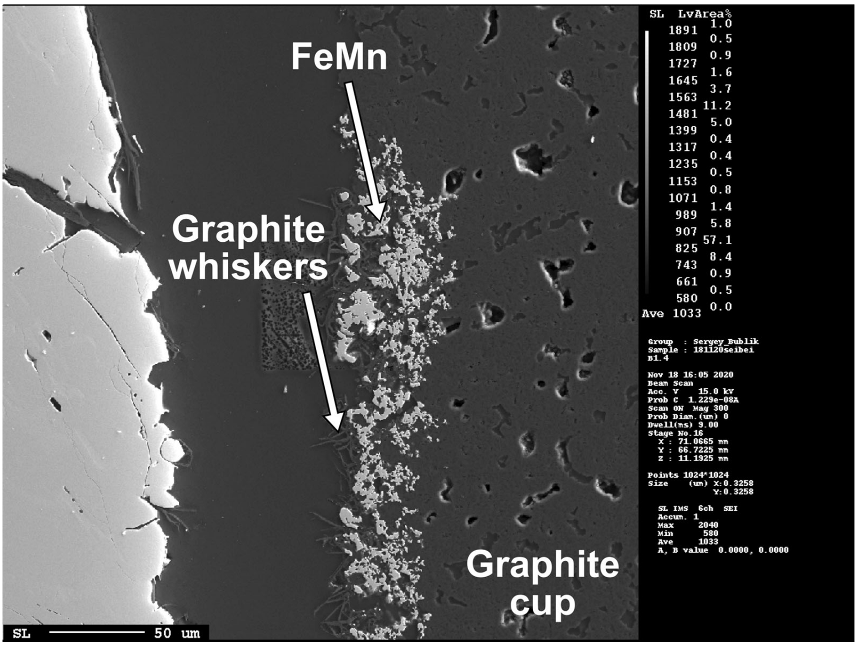

Fig. 16—FeMn alloy inclusions in the graphite cup and graphite whiskers formed along the walls of the graphite cup.

1.2 increases the interfacial tension, while increasing MnO content from 30.0 to 45.0 wt pct does not have any statistically significant influence on the interfacial tension.

EPMA analysis demonstrates an important phenomenon which contributes to the understanding of interfacial tension drop at low slag basicity. $SiO_2$ in the slag is reduced by the saturated carbon from the FeMn alloy at the interface and afterwards Si distributes to the metal phase. The mass transfer of Si across the interface creates the interface instability due to the growing interfacial area between slag and FeMn, which leads to the formation of a metal–slag emulsion and small droplets and, thus, to an increase in losses of the FeMn alloy with the slag.

Since the study was limited to using only graphite crucibles for the materials preparation and graphite cups for the melting experiments in the sessile drop furnace, solid carbon particles were observed on the surface of the slag and the FeMn alloy in the experiments, which may introduce additional uncertainty to the experimental results. However, the surface roughness correction coefficient has been used in this study to address this issue.

Further experiments, using a broader range of MnO content in the slag, could provide more data on the effect of MnO influence on the interfacial tension between slag and metal, which might be crucial for the ferroalloy industry. In addition, experiments in the sessile drop furnace with cups made of different materials can be a further development of the current methodology.

## ACKNOWLEDGMENTS

This publication has been funded by the Research Council of Norway (KPN Project, 267621). The authors gratefully acknowledge the financial support from the Research Council of Norway and the Norwegian Ferroalloy Producers Research Association (FFF).

## CONFLICT OF INTEREST

On behalf of all authors, the corresponding author states that there is no conflict of interest.

## OPEN ACCESS

This article is licensed under a Creative Commons Attribution 4.0 International License, which permits use, sharing, adaptation, distribution and reproduction in any medium or format, as long as you give appropriate credit to the original author(s) and the source, provide a link to the Creative Commons licence, and indicate if changes were made. The images or other third party material in this article are included in the article's Creative Commons licence, unless indicated otherwise in a credit line to the material. If material is not included in the article's Creative Commons licence and your intended use is not permitted by statutory regulation or exceeds the permitted use, you will need to obtain permission directly from the copyright holder. To view a copy of this licence, visit http://creativecommons.org/licenses/by/4.0/.

## APPENDIX A

See Tables IV, V, VI and VII.

**Table IV. The Calculated Chemical Composition of the Synthetic FeMn Alloy and Slags**

| | Chemical Composition (Wt Pct) | | | | | | | | |
|---|---|---|---|---|---|---|---|---|---|
| Material | Mn | Fe | C | MnO | CaO | MgO | $SiO_2$ | $Al_2O_3$ | Basicity |
| FeMn Alloy | 78.00 | 15.00 | 7.00 | — | — | — | — | — | — |
| Slags with $Al_2O_3$ Addition | | | | | | | | | |
| Master Slag #1 | — | — | — | 38.00 | 23.00 | 6.00 | 23.00 | 10.00 | 0.9 |
| Slag A1 | — | — | — | 30.00 | 14.00 | 6.00 | 40.00 | 10.00 | 0.4 |
| Slag A2 | — | — | — | 30.00 | 25.11 | 6.00 | 28.89 | 10.00 | 0.8 |
| Slag A3 | — | — | — | 30.00 | 32.18 | 6.00 | 21.82 | 10.00 | 1.2 |
| Slag B1 | — | — | — | 37.50 | 11.86 | 6.00 | 34.64 | 10.00 | 0.4 |
| Slag B2 | — | — | — | 37.50 | 21.78 | 6.00 | 24.72 | 10.00 | 0.8 |
| Slag B3 | — | — | — | 37.50 | 28.09 | 6.00 | 18.41 | 10.00 | 1.2 |
| Slag C1 | — | — | — | 45.00 | 9.71 | 6.00 | 29.29 | 10.00 | 0.4 |
| Slag C2 | — | — | — | 45.00 | 18.44 | 6.00 | 20.56 | 10.00 | 0.8 |
| Slag C3 | — | — | — | 45.00 | 24.00 | 6.00 | 15.00 | 10.00 | 1.2 |
| Slags Without $Al_2O_3$ Addition | | | | | | | | | |
| Master Slag #2 | — | — | — | 42.52 | 25.74 | 6.00 | 25.74 | — | 1.2 |
| Slag D1 | — | — | — | 30.00 | 14.00 | 6.00 | 50.00 | — | 0.4 |
| Slag D2 | — | — | — | 30.00 | 25.11 | 6.00 | 38.89 | — | 0.8 |
| Slag D3 | — | — | — | 30.00 | 32.18 | 6.00 | 31.82 | — | 1.2 |
| Slag E1 | — | — | — | 37.50 | 11.86 | 6.00 | 44.64 | — | 0.4 |
| Slag E2 | — | — | — | 37.50 | 21.78 | 6.00 | 34.72 | — | 0.8 |
| Slag E3 | — | — | — | 37.50 | 28.09 | 6.00 | 28.41 | — | 1.2 |
| Slag F1 | — | — | — | 45.00 | 9.71 | 6.00 | 39.29 | — | 0.4 |
| Slag F2 | — | — | — | 45.00 | 18.44 | 6.00 | 30.56 | — | 0.8 |
| Slag F3 | — | — | — | 45.00 | 24.00 | 6.00 | 25.00 | — | 1.2 |

Table V. The Purity of the Powders Used for the Preparation of the Synthetic Raw Materials

| Purity of Corresponding Powders (Pct) | | | | | | |
|---|---|---|---|---|---|---|
| Mn | Fe | MnO | CaO | MgO | $SiO_2$ | $Al_2O_3$ |
| 99.30 | 99.00 | 99.00 | 95.00 | 99.00 | 99.50 | 99.00 |

Table VI. Normalized Values of the Measured Chemical Composition of the Synthetic FeMn Alloy and Slags

| | Chemical Composition (Wt Pct) | | | | | | | | | | | |
|---|---|---|---|---|---|---|---|---|---|---|---|---|
| Material | Mn | Fe | Si | C | MnO | CaO | MgO | $SiO_2$ | $Al_2O_3$ | FeO | Total | Basicity |
| FeMn Alloy | 77.75 | 14.58 | 0.11 | 7.56 | — | — | — | — | — | — | 100.00 | — |
| Slags with $Al_2O_3$ Addition | | | | | | | | | | | | |
| Slag A1 | — | — | — | — | 29.94 | 13.92 | 6.62 | 38.65 | 10.00 | 0.87 | 100.00 | 0.42 |
| Slag A2 | — | — | — | — | 28.81 | 25.08 | 6.64 | 28.70 | 10.00 | 0.78 | 100.00 | 0.82 |
| Slag A3 | — | — | — | — | 28.72 | 31.79 | 6.60 | 21.99 | 10.12 | 0.78 | 100.00 | 1.20 |
| Slag B1 | — | — | — | — | 36.94 | 12.55 | 6.55 | 33.29 | 9.92 | 0.75 | 100.00 | 0.44 |
| Slag B2 | — | — | — | — | 36.09 | 22.08 | 6.46 | 24.74 | 9.89 | 0.73 | 100.00 | 0.82 |
| Slag B3 | — | — | — | — | 37.04 | 27.51 | 6.74 | 18.09 | 9.88 | 0.73 | 100.00 | 1.22 |
| Slag C1 | — | — | — | — | 44.28 | 10.49 | 6.44 | 28.11 | 9.97 | 0.71 | 100.00 | 0.44 |
| Slag C2 | — | — | — | — | 43.67 | 18.62 | 6.68 | 20.34 | 9.97 | 0.71 | 100.00 | 0.83 |
| Slag C3 | — | — | — | — | 44.60 | 23.50 | 6.58 | 14.78 | 9.83 | 0.71 | 100.00 | 1.22 |
| Slags Without $Al_2O_3$ Addition | | | | | | | | | | | | |
| Slag D1 | — | — | — | — | 30.09 | 14.48 | 5.99 | 47.91 | 0.66 | 0.87 | 100.00 | 0.42 |
| Slag D2 | — | — | — | — | 29.42 | 24.96 | 6.22 | 37.80 | 0.76 | 0.84 | 100.00 | 0.81 |
| Slag D3 | — | — | — | — | 28.98 | 31.59 | 6.12 | 31.91 | 0.60 | 0.79 | 100.00 | 1.16 |
| Slag E1 | — | — | — | — | 37.78 | 12.63 | 5.95 | 42.32 | 0.57 | 0.75 | 100.00 | 0.43 |
| Slag E2 | — | — | — | — | 36.39 | 22.31 | 6.06 | 33.82 | 0.68 | 0.74 | 100.00 | 0.82 |
| Slag E3 | — | — | — | — | 36.81 | 27.85 | 6.03 | 28.03 | 0.67 | 0.60 | 100.00 | 1.18 |
| Slag F1 | — | — | — | — | 44.94 | 10.34 | 6.09 | 37.26 | 0.67 | 0.69 | 100.00 | 0.43 |
| Slag F2 | — | — | — | — | 43.53 | 19.29 | 5.99 | 29.98 | 0.55 | 0.67 | 100.00 | 0.83 |
| Slag F3 | — | — | — | — | 44.42 | 24.03 | 5.89 | 24.51 | 0.46 | 0.69 | 100.00 | 1.20 |

Table VII. Weight of the Powders Used for the Preparation of the Synthetic Raw Materials

| | Weight of Powders (g) | | | | | | | |
|---|---|---|---|---|---|---|---|---|
| Material | Mn | Fe | MnO | CaO | MgO | $SiO_2$ | $Al_2O_3$ | Total |
| FeMn | 211.16 | 40.73 | — | — | — | — | — | 251.89 |
| Slags with $Al_2O_3$ Addition | | | | | | | | |
| Master Slag #1 | — | — | 95.00 | 57.50 | 15.00 | 57.50 | 25.00 | 250.00 |
| Powders Addition to Master Slag #1, g | | | | | | | | |
| Slag A1 | — | — | 2.28 | — | 0.78 | 8.59 | 1.30 | 12.95 |
| Slag A2 | — | — | — | 1.85 | 0.32 | 2.73 | 0.54 | 5.44 |
| Slag A3 | — | — | — | 3.74 | 0.32 | 0.93 | 0.54 | 5.53 |
| Slag B1 | — | — | 7.02 | — | 1.14 | 8.88 | 1.90 | 18.94 |
| Slag B2 | — | — | 0.32 | — | 0.07 | 0.63 | 0.11 | 1.13 |
| Slag B3 | — | — | 1.79 | 2.55 | 0.30 | — | 0.50 | 5.14 |
| Slag C1 | — | — | 13.85 | — | 1.66 | 9.31 | 2.76 | 27.58 |
| Slag C2 | — | — | 3.66 | — | 0.30 | 0.53 | 0.50 | 4.99 |
| Slag C3 | — | — | 6.26 | 2.91 | 0.65 | — | 1.08 | 10.90 |
| Slags Without $Al_2O_3$ Addition | | | | | | | | |
| Master Slag #2 | — | — | 106 | 64 | 15 | 64 | — | 250.00 |
| Powders Addition to Master Slag #2, g | | | | | | | | |
| Slag D1 | — | — | 3.47 | 0.58 | 1.02 | 13.85 | — | 18.92 |
| Slag D2 | — | — | 0.91 | 2.65 | 0.51 | 6.46 | — | 10.53 |
| Slag D3 | — | — | 0.91 | 4.76 | 0.51 | 4.44 | — | 10.62 |
| Slag E1 | — | — | 8.77 | 0.58 | 1.42 | 14.86 | — | 25.63 |

**Table VII. continued**

| | Weight of Powders (g) | | | | | | | |
|---|---|---|---|---|---|---|---|---|
| Material | Mn | Fe | MnO | CaO | MgO | $SiO_2$ | $Al_2O_3$ | Total |
| Slag E2 | — | — | 1.28 | 0.58 | 0.22 | 3.63 | — | 5.71 |
| Slag E3 | — | — | 0.91 | 1.86 | 0.16 | 1.85 | — | 4.78 |
| Slag F1 | — | — | 16.41 | 0.58 | 2.00 | 16.30 | — | 35.29 |
| Slag F2 | — | — | 5.01 | 0.58 | 0.48 | 3.95 | — | 10.02 |
| Slag F3 | — | — | 2.07 | 0.58 | 0.09 | 0.77 | — | 3.51 |

## APPENDIX B

See Tables VIII and IX.

**Table VIII. Average Chemical Composition (in Wt Pct) of Slag Phases after the Experiments in the Sessile Drop Furnace**

| Slag | Matrix* | Dendrites* | MnO | CaO | MgO | $SiO_2$ | $Al_2O_3$ | FeO | Total |
|---|---|---|---|---|---|---|---|---|---|
| Bulk | | | | | | | | | |
| B1 | 100 | — | 28.85 | 16.23 | 8.01 | 33.35 | 13.35 | 0.09 | 99.89 |
| B2 | 100 | — | 27.30 | 25.78 | 7.36 | 27.01 | 12.72 | 0.06 | 100.21 |
| B3 | 82 | 18 | 30.20 | 30.36 | 6.43 | 19.77 | 13.11 | 0.08 | 99.95 |
| E1 | 70/30** | — | 40.86 | 13.58 | 8.44 | 36.54 | 0.46 | 0.10 | 99.98 |
| E2 | 87/13** | — | 34.79 | 22.51 | 7.15 | 34.36 | 0.54 | 0.10 | 99.45 |
| E3 | 87 | 13 | 33.65 | 28.13 | 7.97 | 29.53 | 0.05 | 0.09 | 99.43 |
| Slag Inclusions in the Metal Phase | | | | | | | | | |
| B1 | 100 | — | 32.41 | 14.88 | 7.59 | 32.87 | 12.21 | 0.15 | 100.11 |
| B2 | 100 | — | 27.94 | 25.38 | 7.24 | 27.02 | 13.02 | 0.40 | 101.00 |
| B3 | — | — | — | — | — | — | — | — | — |
| E1 | 70/30** | — | 37.94 | 13.84 | 9.95 | 37.41 | 0.64 | 0.18 | 99.96 |
| E2 | 87/13** | — | 35.26 | 22.52 | 6.91 | 33.17 | 0.77 | 0.20 | 98.82 |
| E3 | — | — | — | — | — | — | — | — | — |

*Percentage from the total surface area of the slag phase.

**Matrix consists of two distinctive phases: bright and grey.

**Table IX. Average Chemical Composition (in Wt Pct) of the FeMn Alloy After the Experiments in the Sessile Drop Furnace**

| Slag in experiment | Phase | Mn | Fe | Si | C | Total |
|---|---|---|---|---|---|---|
| Bulk | | | | | | |
| B1 | Bright | 75.90 | 19.23 | 0.57 | 5.07 | 100.78 |
| | Grey | 79.23 | 13.61 | 0.00 | 6.12 | 98.96 |
| | Dark | 79.46 | 13.69 | 2.78 | 5.18 | 101.11 |
| B2 | Bright | 75.61 | 19.57 | 0.12 | 4.69 | 99.98 |
| | Dark | 79.39 | 13.53 | 0.00 | 5.87 | 98.79 |
| B3 | Bright | 73.79 | 22.66 | 0.10 | 5.19 | 101.75 |
| | Grey | 75.74 | 19.15 | 0.00 | 6.19 | 101.08 |
| | Dark | 78.78 | 14.30 | 0.00 | 6.96 | 100.04 |
| E1 | Bright | 67.95 | 26.10 | 3.95 | 4.59 | 102.58 |
| | Grey | 72.79 | 21.00 | 1.28 | 5.73 | 100.80 |
| | Dark | 79.08 | 14.66 | 0.00 | 5.80 | 99.55 |
| E2 | Grey | 79.96 | 13.76 | 0.01 | 6.49 | 100.23 |
| E3 | Bright | 72.51 | 27.54 | 0.32 | 4.11 | 104.48 |
| | Grey | 77.66 | 17.54 | 0.00 | 5.62 | 100.82 |
| | Dark | 80.19 | 13.63 | 0.00 | 6.08 | 99.89 |
| Near the Interface | | | | | | |
| B1 | Bright | 72.36 | 22.12 | 2.32 | 4.43 | 101.22 |
| | Dark | 80.25 | 13.35 | 0.01 | 6.22 | 99.83 |

Table IX. continued

| Slag in experiment | Phase | Mn | Fe | Si | C | Total |
|---|---|---|---|---|---|---|
| B2 | Bright | 75.57 | 23.56 | 0.13 | 2.98 | 102.24 |
| | Grey | 79.59 | 15.31 | 0.00 | 5.16 | 100.06 |
| | Dark | 79.74 | 13.81 | 0.00 | 5.75 | 99.30 |
| B3 | Bright | 74.52 | 23.03 | 0.03 | 4.64 | 102.22 |
| | Grey | 76.77 | 17.88 | 0.00 | 6.22 | 100.87 |
| | Dark | 79.40 | 13.85 | 0.00 | 6.83 | 100.08 |
| E1 | Bright | 73.13 | 20.09 | 4.50 | 4.87 | 102.58 |
| | Dark | 81.68 | 11.76 | 0.03 | 5.92 | 99.39 |
| E2 | Bright | 77.25 | 17.81 | 0.01 | 6.00 | 101.07 |
| | Grey | 79.71 | 14.15 | 0.00 | 6.63 | 100.50 |
| E3 | Bright | 74.56 | 23.87 | 0.19 | 3.80 | 102.42 |
| | Grey | 76.59 | 19.20 | 0.02 | 5.76 | 101.56 |
| | Dark | 79.89 | 13.41 | 0.00 | 6.42 | 99.72 |
| FeMn Inclusions in the Graphite Cup | | | | | | |
| B1 | Bright | 77.17 | 14.82 | 0.02 | 8.08 | 100.08 |
| B2 | Bright | 75.93 | 14.81 | 0.00 | 7.67 | 98.42 |
| B3 | Bright | 76.42 | 14.18 | 0.00 | 8.99 | 99.60 |
| E1 | Bright | 77.32 | 13.83 | 0.00 | 7.32 | 98.48 |
| E2 | Bright | 76.79 | 14.89 | 0.00 | 8.10 | 99.79 |
| E3 | Bright | 73.84 | 14.60 | 0.03 | 9.48 | 97.94 |

## REFERENCES

1. M. Tangstad: *Handbook of Ferroalloys*, Butterworth-Heinemann, Oxford, 2013.
2. R.H. Eric: *Treatise on Process Metallurgy*, Elsevier, Boston, 2014, pp. 477–532.
3. E.S.R. Gopal: *Principles of Emulsion Formation*, Academic, London, 1968, pp. 1–75.
4. P.R. Scheller, J. Lee, and T. Tanaka: *Treatise on Process Metallurgy*, Elsevier, Boston, 2014, pp. 111–18.
5. P. Ni, T. Tanaka, M. Suzuki, M. Nakamoto, and P.G. Jönsson: *ISIJ Int*., 2019, vol. 59, pp. 737–48.
6. E.-J. Jung, W. Kim, I. Sohn, and D.-J. Min: *J. Mater. Sci*., 2010, vol. 45, pp. 2023–29.
7. S.-C. Park, H. Gaye, and H.-G. Lee: *Ironmak. Steelmak*., 2009, vol. 36, pp. 3–11 .
8. T. Tanaka, H. Goto, M. Nakamoto, M. Suzuki, M. Hanao, M. Zeze, H. Yamamura, and T. Yoshikawa: *ISIJ Int*., 2016, vol. 56, pp. 944–52.
9. L. Muhmood, N.N. Viswanathan, and S. Seetharaman: *Metall. Mater. Trans. B*, 2011, vol. 42B, pp. 460–70.
10. H. Sun, K. Nakashima, and K. Mori: *ISIJ Int*., 2006, vol. 46, pp. 407–12.
11. K. Nakashima and K. Mori: *ISIJ Int*., 1992, vol. 32, pp. 11–18.
12. Y. Chung and A.W. Cramb: *Metall. Mater. Trans. B*, 2000, vol. 31B, pp. 957–71.
13. Y.E. Lee and L. Kolbeinsen: *Metall. Mater. Trans. B*, 2021, vol. 52, pp. 3142–3150.
14. A. Jakobsson, D. Sichen, S. Seetharaman, and N.N. Viswanathan: *Metall. Mater. Trans. B*, 2000, vol. 31B, pp. 973–80.
15. H. Terasaki, S. Urakawa, K. Funakoshi, N. Nishiyama, Y. Wang, K. Nishida, T. Sakamaki, A. Suzuki, and E. Ohtani: *Phys. Earth Planet. Inter*., 2009, vol. 174, pp. 220–26.
16. S. Bublik, S. Bao, M. Tangstad, and K.E. Einarsrud: *Proc. Liq. Met. Process. Cast. Conf. (2019)*, Birmingham, UK, 2019, pp. 375–84.
17. S. Bublik and K.E. Einarsrud: *14th International Conference on CFD in Oil and Gas, Metallurgical and Process Industries*, Trondheim, Norway, SINTEF Academic Press, 2020, pp. 28–38.
18. H.G. Weller, G. Tabor, H. Jasak, and C. Fureby: *Comput. Phys*., 1998, vol. 12, pp. 620–31.
19. K.C. Mills, Y. Lang, and R.T. Jones: *J. S. Afr. Inst. Min. Metall*., 2011, vol. 111, pp. 649–58.
20. K.C. Mills, S. Karagadde, P.D. Lee, L. Yuan, and F. Shahbazian: *ISIJ Int*., 2016, vol. 56, pp. 264–73.
21. C.W. Bale, E. Bélisle, P. Chartrand, S.A. Decterov, G. Eriksson, A.E. Gheribi, K. Hack, I.H. Jung, Y.B. Kang, J. Melançon, A.D. Pelton, S. Petersen, C. Robelin, J. Sangster, P. Spencer, and M.-A. Van Ende: *CALPHAD: Comput. Coupling Phase Diagr. Thermochem*., 2016, vol. 54, pp. 35–53.
22. S. Bao, K. Tang, A. Kvithyld, M. Tangstad, and T.A. Engh: *Metall. Mater. Trans. B*, 2011, vol. 42B, pp. 1358–66.
23. J. Muller, J.H. Zietsman, and P.C. Pistorius: *Metall. Mater. Trans. B*, 2015, vol. 46B, pp. 2639–51.
24. S. Bublik, S. Bao, M. Tangstad, and K.E. Einarsrud: *Metall. Mater. Trans. B*, 2021, vol. 52B, pp. 3624–45.
25. D.C. Montgomery: *Design and Analysis of Experiments*, 8th ed., Wiley, Hoboken, NJ, 2013.
26. P. Patnaik: *Handbook of Inorganic Chemicals*, McGraw-Hill, New York, 2003.
27. P. Ni, T. Tanaka, M. Suzuki, M. Nakamoto, and P.G. Jönsson: *ISIJ Int*., 2018, vol. 58, pp. 1979–88.
28. K. Gu, N. Dogan, and K.S. Coley: *Metall. Mater. Trans. B*, 2017, vol. 48B, pp. 2595–2606.
29. H. Sun, K. Nakashima, and K. Mori: *ISIJ Int*., 1997, vol. 37, pp. 323–31.
30. S. Rosypalova, R. Dudek, and J. Dobrovska: *Proc. 21st Int. Metall. Mater. Conf*., Ostrava, 2012, pp. 109–14.
31. S. Rosypalova, R. Dudek, J. Dobrovska, L. Dobrovsky, and M. Zaludova: *Mater. Technol*., 2014, vol. 48, pp. 415–18.
32. S. Bao, M. Tangstad, K. Tang, K.E. Einarsrud, M. Syvertsen, M. Onsøien, A. Kudyba, and S. Bublik: *Metall. Mater. Trans. B*, 2021, vol. 52B, pp. 2847–58.

**Publisher's Note** Springer Nature remains neutral with regard to jurisdictional claims in published maps and institutional affiliations.

# Paper VI

INVITED REVIEW ARTICLE

# Slag Properties in the Primary Production Process of Mn-Ferroalloys

MERETE TANGSTAD, SERGEY BUBLIK, SHOKOUH HAGHDANI,
KRISTIAN ETIENNE EINARSRUD, and KAI TANG

The thermodynamic and kinetic properties of the carbothermic reduction of MnO in the five-component slag, $MnO-SiO_2-CaO-MgO-Al_2O_3$, is critical in the production process of Mn-ferroalloys. While the reduction rate is mainly dependent on the presence of a solid MnO phase in the slag for Mn-Fe-alloys, the rate for the Mn-Si-Fe alloys has two distinct steps, a slow step followed by a fast step. The extent of the slow step has been shown to be dependent on the S content in the slag. The thermo-physical properties of viscosity, density, interfacial tension and electrical resistivity is reviewed, and these properties are mainly determined by the total basicity.

https://doi.org/10.1007/s11663-021-02347-8
© The Author(s) 2021

## I. OVERVIEW OF THE MN-ALLOY PRODUCTION PROCESS

MN-FERROALLOYS are alloys containing mostly Mn, Fe, Si and C. Manganese is the main element and typically accounts for between 60 and 80 wt pct of the alloy. Iron will always follow the raw materials and practically all iron in the raw materials will end up in the alloy. Silicon may be less than 1 pct or up to 30 pct. Less than 1 pct Si is usually called FeMn (ferromanganese) and alloys with 16 to 30 pct is called SiMn (silicomanganese). The metal will be saturated with carbon from the furnace and will be 7 pct C for FeMn and for SiMn the carbon content is dependent on the amount of silicon. Typically, for 18 pct Si the carbon content is less than 2 pct C. As for most reduction processes, the metal composition is determined by the slag properties, and the slag in the Mn-ferroalloy will mainly be MnO, $SiO_2$, MgO, CaO and $Al_2O_3$ as all the iron ends up in the metal. There are a number of definitions of slag basicity that can be used to describe the composition of the slag. In this paper, the basicity will be given as $B = \frac{CaO+MgO}{SiO_2+Al_2O_3}$. Trace elements are counted as basic or acid oxides, depending on their nature.

The temperatures in the closed Mn-ferroalloy furnaces can be from 200 °C to 600 °C on the top of the charge to 1500 °C to 1600 °C in the tapped slag. This means that in upper part of the furnace, the low temperature zone, the raw materials will be solid, and when it enters the area on top of the coke-bed, around 1200 °C to 1400 °C, the raw materials will melt into a primary slag. This slag will coexist with the solid carbon materials added to the furnace (Figure 1). This paper will discuss the knowledge we have on MnO-slags related to the primary production of FeMn or SiMn inside the Submerged Arc Furnace. First we will discuss the mechanism of slag formation, the thermodynamics, and the kinetics. Next, a summary of key slag properties is presented. These key properties include the MnO slag structure, viscosity, density, interfacial tension and wetting properties, and electrical conductivity. The pathway of the slag considered in this work will start with the production of a primary slag from the raw materials, followed by the reduction of valuable elements into a Mn-alloy and finally the drainage, or tapping, from the furnace.

Most of the slag will as discussed later, follow the increasing temperature. Some slag may however be circulated into the low temperature area. In Mn-alloy production, slags have been known to be sputtered up to the cold furnace top from the high temperature area as seen in Figure 2.[2,3] This is believed to happen if the permeability of the charge is poor, and the raw materials are not heated gradually, or if too violent foaming of the slag occurs.

---

MERETE TANGSTAD, SERGEY BUBLIK, SHOKOUH HAGHDANI, KRISTIAN ETIENNE EINARSRUD are with the Department of Material Science and Engineering, Norwegian University of Science and Technology, 7491 Trondheim, Norway. Contact e-mail: Merete.Tangstad@ntnu.no KAI TANG is with the SINTEF Industry, SINTEF, 7465 Trondheim, Norway.

Manuscript submitted March 21, 2021; accepted October 2, 2021.
Article published online November 1, 2021.

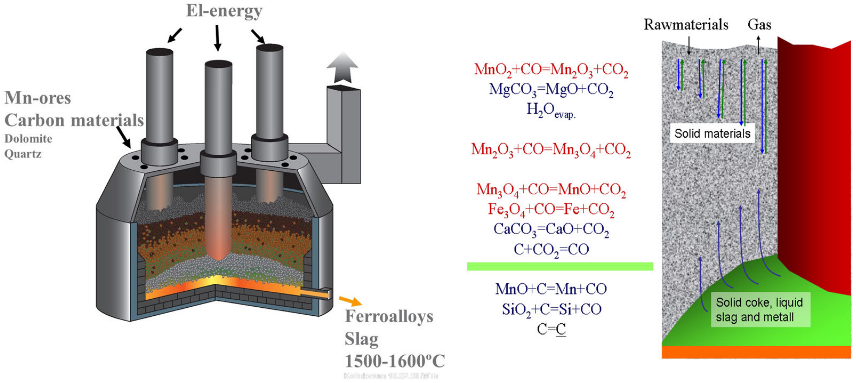

Fig. 1—Overview of a typical closed furnace producing Mn-alloys (left) and an illustration of zones and reactions around one of the electrodes (right).[1] (Figure is reprinted with permission from Ref. 1).

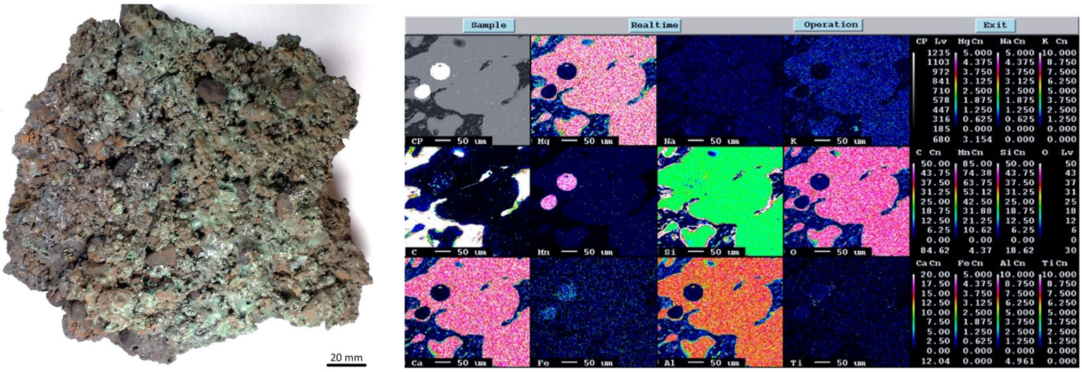

Fig. 2—Slag infiltrated charge sample at top of the furnace charge taken from a FeMn furnace (left picture) showing low alkali binder phase (right)[4].

## II. MELTING OF ORES AND REDUCTION OF PRIMARY SLAGS

The melting of the raw materials to a primary slag and the following reduction to Mn-ferroalloys are closely related. It is hence appropriate to start with the Mn-bearing raw materials and the primary slag it produces at around 1200 °C and up. Table I show some typical ores, where the metallurgical grade ore typically have more than 35 pct Mn. After being heated in solid state in the prereduction zone, all higher manganese ($MnO_2$, $Mn_2O_3$ and $Mn_3O_4$) has been reduced to MnO, the iron oxides are reduced to metallic phase, and all the carbonates ($CaCO_3$, $MgCO_3$, $MnCO_3$) are decomposed to basic oxides (CaO, MgO and MnO). The main elements in the oxide phase will now be the 5 components MnO-$SiO_2$-$Al_2O_3$-CaO-MgO. Table II shows the chemical composition calculated from the chemical analyses of the ore of the primary slag. It can be noted that there will also be a number of trace elements like $TiO_2$, $K_2O$, BaO, however these will not be discussed further here.

The five-component pre-reduced Mn-ores, typically containing around 70 pct MnO, will as it melts down dissolve fluxes. The fluxes can typically be ''pre-reduced'' limestone or dolomite or quartz and reduced MnO-slags if SiMn is produced. In the liquid (or partly liquid) state , the MnO and $SiO_2$ may be reduced to metallic Mn-Fe-Si-$C_{saturated}$ alloy according to reactions [1] and [2], where the parentheses denote a slag phase and underscored denotes metallic phases. The carbon can be solid carbon, *i.e.,* coke particles, or carbon dissolved in the metal. Some of the MnO and $SiO_2$ still will remain in the slag, and the tapped slag will thus be the same 5-component slag containing MnO, $SiO_2$, $Al_2O_3$, CaO and MgO.

$$(\mathrm{MnO}) + \mathrm{C} = \underline{\mathrm{Mn}} + \mathrm{CO_g} \quad [1]$$

$$(\mathrm{SiO_2}) + 2\mathrm{C} = \underline{\mathrm{Si}} + 2\mathrm{CO_g} \quad [2]$$

**Table I. Typical Analyses of Mn-Ores[1,5,6]**

| Manganese Ore | | Mn | Fe | SiO2 | Al2O3 | MgO | CaO | P | CO2 |
|---|---|---|---|---|---|---|---|---|---|
| Comilog MMA | Gabon | 50.5 | 2.7 | 4.0 | 5.5 | 0.3 | 0.2 | 0.11 | 0.1 |
| Comilog Sinter | | 58.5 | 3.5 | 7.0 | 6.5 | 0.0 | 0.1 | 0.12 | 0.0 |
| Mn-Nodules | Mexico | 37.7 | 7.9 | 14.9 | 3.9 | 8.1 | | 0.085 | |
| Asman 48 | South Africa | 51.3 | 10.1 | 5.5 | 0.4 | 0.7 | 4.3 | 0.04 | 0.8 |
| Mamatwan | | 37.8 | 4.6 | 4.0 | 0.5 | 3.5 | 14.7 | 0.02 | 17.0 |
| Gloria | | 39.1 | 5.0 | 5.7 | 0.3 | 3.8 | 12.7 | 0.02 | 15.4 |
| Wessel 38 pct | | 42.3 | 13.2 | 4.9 | 2.5 | 1.0 | 6.0 | 0.04 | 3.6 |
| Wessel 50 pct | | 50.2 | 10.0 | 3.6 | 0.4 | 1.0 | 5.6 | 0.04 | 2.6 |
| Groote Eylandt | Australia | 48.8 | 4.2 | 6.9 | 4.2 | 0.1 | 0.1 | 0.09 | 0.5 |
| Amapa Sinter | Brazil | 49.1 | 9.6 | 7.6 | 7.6 | 0.5 | 0.8 | 0.10 | 0.0 |
| Amapa Miudo 40 | | 41.3 | 12.5 | 5.9 | 8.1 | 0.1 | 0.3 | 0.11 | 3.5 |
| CVRD Sinter | | 54.5 | 4.7 | 5.4 | 8.7 | 0.5 | 1.9 | 0.11 | 0.2 |
| CVRD Lump | | 45.0 | 4.7 | 2.6 | 8.6 | 0.2 | 0.2 | 0.09 | 14.4 |
| Nikopol-Oxide | Ukraine | 29–43 | 1–3 | 11–24 | 1.4–3.3 | 0.8–2 | 4–10 | 0.15–0.3 | |
| Nikopol-Pyrolusite | | 47.5 | 0.65 | 8.6 | 1.6 | 0.6 | 2 | 0.2 | |
| Nikopol-Carbonate | | 22–28 | 1.5–3 | 13–16 | 1.7–2.3 | 1.5–2.2 | 7–13 | 0.3–0.6 | |
| Tchiatura-Oxide | Georgia | 30–44 | 0.7–4 | 6–17 | 1.3–2.6 | 1–2.5 | 3.8–5.5 | 0.1–0.4 | |
| Tchiatura-Pyrolusite | | 28 | 1.3 | 17.6 | 2.9 | 1.5 | 8.2 | 0.2 | |
| Tchiatura-carbonate | | 23–25 | 1.3 | 16–17 | 2 | 2.5 | 10 | 0.15 | |
| Zapadny Kamys | Kazakhstan | 17–19 | 5–6 | 40–42 | 5–6.5 | 1–1.5 | 1.2–1.7 | 0.035 | |

A number of industrial-, and pilot scale- tap-slag composition have been reported. For FeMn slags the MnO content varies from 15 to 40 wt pct depending on the basicity.[1,5,7–12] High basicity charges, that is basicities above 1.1, typically have less than 25 pct MnO. Basicities around 0.7 typically has 35-40 pct MnO, and this is close to the liquidus line at 1500 °C, which is reported to be close to the tapping temperature.[13] Some smaller furnaces, *e.g.,* a 21 MVA furnace,[9] show an MnO content as low as 19 pct MnO with a basicity of 0.9, and it is speculated if smaller furnaces may produce lower MnO contents. Acid slags with a basicity 0.2-0.3 will also tap at about 40 pct MnO.

For SiMn slags a typical Si content is 15-18 pct Si, and to obtain this around 40 pct $SiO_2$ is needed in the slag. Industrially, less than 20 pct MnO is remaining in the slag, and it can be down to 5-10 pct. In pilot scale operation the MnO content in SiMn slags are typically seen to be a bit higher than the industrial slags, that is up to 25 pct MnO.[1,5,14–19]

To sum this up, FeMn charges will be reduced from a primary slag with more than 60 pct MnO to 15 to 40 pct MnO in the tapped slag, while SiMn charge mixes is reduced from a primary slag with more than 35 pct MnO (as the Mn-sources are mixed with both fluxes and quartz) to around 10 pct MnO tapped at 1600 °C.[16]

The slag composition will of course be affected by the temperature. Due to reported tapping temperatures of around 1500 °C for FeMn[13] and 1600 °C for SiMn tappings,[16] one assumes that this can also be the temperatures inside the high temperature zones in the furnaces. As the temperatures are varying both due to the electrode paths in the furnace, given by the coke-bed size and shape, and raw material properties, the temperature in the high temperature zone will vary both in space and in time.

### A. *Phase Composition in Mn-Slags and Melting Behaviour Of Ores.*

The melting behaviour of the above described 5 component system can be simplified to the MnO-$SiO_2$ system where "MnO" in reality represents the basic oxides MnO, CaO, and MgO and "$SiO_2$" represent the acid oxides $SiO_2$ and $Al_2O_3$ as illustrated in Figure 3. Although $Al_2O_3$ is an amphoteric oxide, it will for manganese slags behave as an acidic oxide, though less acid in more acid SiMn slags *vs.* more basic FeMn slags.[16,20]

For FeMn slags, containing a high amount of MnO, the reduction will start when a liquid phase is present in the material that is above the solidus, represented by the 1306 °C horizontal line in Figure 3. The reduction may hence start in the area of 1300 °C according to the equilibrium state. At this point, the reduction starts and hence it is believed that the endothermic reaction (reaction [1]) will consume more energy and hence the heating rate will decrease drastically. The reduction will go through a two-phase area, and the primary slag will consist of a liquid with a solid MnO phase as seen in Figure 4. The presence of a solid MnO phase has two major consequences; first it will have a high impact on the activity of MnO and secondly it will have a large effect on the flow properties (*i.e.,* viscosity) of the slag.

Even if the slag is partly molten, it will not be able to flow into a coke-bed as illustrated by an ore particle being heated and reduced in Figure 5. The partly liquid slag will not flow into the coke bed until it is reduced down to the point where no solid MnO is present, where the slag viscosity will be at its minimum as indicated in Figure 6 (left figure). It must also be mentioned that in addition to slag viscosity being affected by solid MnO particles, the size of the coke particles will also affect the

**Table II. Primary Slag From Various Commercial African, Australian and South-American Ores (Calculated From Ref. 1)**

| | Comilog MMA | Comilog MMD | Comilog MMR | Comilog MMS | Comilog Sinter | Asman 48 | Amapa Sinter | Amapa Miudo 40 | Mamatwan | Gloria | Groote Eylandt | CVRD sinter | Wessel 38 pct | Wessel 50 pct |
|---|---|---|---|---|---|---|---|---|---|---|---|---|---|---|
| MnO | 85 | 78 | 84 | 80 | 86 | 85 | 79 | 79 | 68 | 69 | 84 | 81 | 79 | 86 |
| $SiO_2$ | 7 | 11 | 8 | 11 | 7 | 7 | 10 | 9 | 6 | 8 | 9 | 6 | 7 | 5 |
| $Al_2O_3$ | 7 | 11 | 8 | 9 | 7 | 1 | 9 | 12 | 1 | 0 | 6 | 10 | 4 | 0 |
| MgO | 0 | 0 | 0 | 0 | 0 | 1 | 1 | 0 | 5 | 5 | 0 | 1 | 1 | 1 |
| CaO | 0 | 0 | 0 | 0 | 0 | 6 | 1 | 0 | 21 | 17 | 0 | 2 | 9 | 7 |

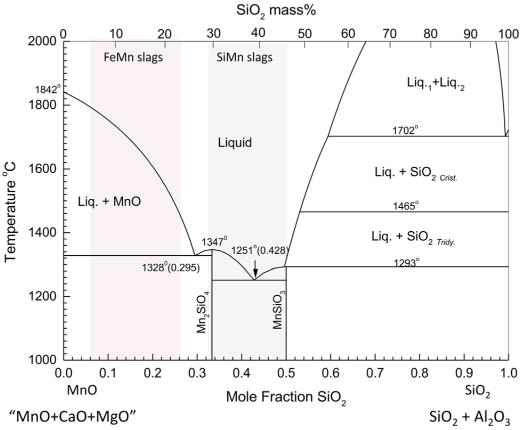

Fig. 3—MnO-$SiO_2$ phase diagram indicating the primary slag in FeMn and SiMn production, where MnO represents the basic oxides of MnO + CaO + MgO and $SiO_2$ represents the acid oxides such as $SiO_2 + Al_2O_3$.

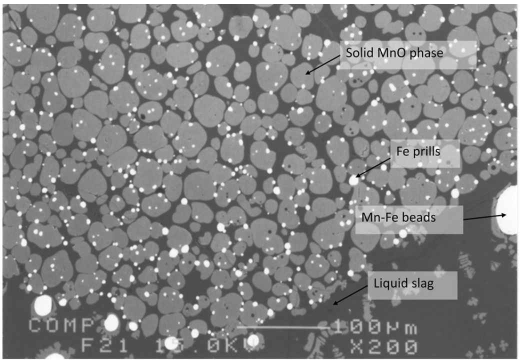

Fig. 4—Partly reduced FeMn slag containing solid MnO spheres in a liquid phase (adapted from Ref. 13).

flow of the slag into the coke bed as seen in Figure 6 (right picture) where the reduced slag is lingering on top of the coke particles.

The phase composition in slags from primary slag composition to tap-slag compositions may be illustrated with the ternary phase diagrams MnO-$SiO_2$-$Al_2O_3$ that represents the Comilog ore, Groote Eyland ore and the South-American ores, and the MnO-$SiO_2$-CaO diagram representing the South-African ores. While experimental work determining the slag phases exists,[22–24] we will in this paper use the FactSage databases to illustrate the reduction path, which equal the basicity line, as shown in Figure 7. There may of course be some deviations between experimental work and FactSage,[23] but the overall correlation is expected to be acceptable. From the Figure 7, the main reduction path seen in the binary MnO-$SiO_2$ phase diagram can be found. The high MnO ores will, when enough liquid phase is formed, start to reduce in a liquid + solid MnO phase area. As the

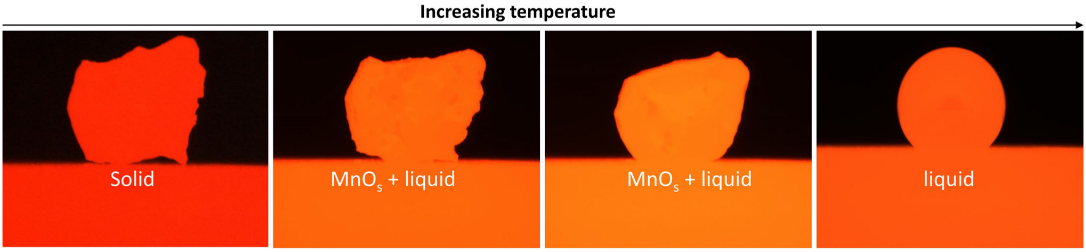

Fig. 5—Mn-ore particle being heated in CO gas on a carbon substrate.

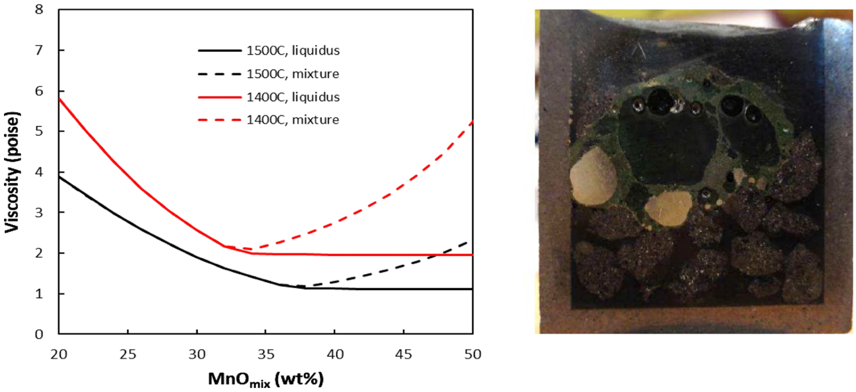

Fig. 6—FeMn-production: Slag viscosity during cooling adapted from Ref. 1 (left) and example of reduced slag from Comilog ore at 1600 °C[21] (right).

reduction proceeds to a lower MnO content, the solid MnO phase will gradually dissolve until the saturation composition is reached. It is also seen that this saturation compostion will be reached at a lower MnO content with higher basicities, which can also be seen in Figure 8. As mentioned above, the tap-slag is quite close to the saturation composition of around 30-40 pct MnO for a basicity of 0.7 and around 20 pct MnO at basicities of 1.1. This is believed to be due to the activity of MnO, and the effect the activity of MnO has on the reaction rate, as will be discussed later.

Depending on the mineralogy and distribution of minerals in the original ores, the raw materials will not always behave close to the equilibrium state given by the phase diagrams. A large effort has hence been done to find the melting behaviour of the ores under a certain heating rate with carbon present, that is when it starts to soften, also called initial melting, when it melts, and when it is completely molten (i.e the liquidus is obtained either due to a high temperature and/or to a low MnO content.[3,6,19,25–31]) These stages represent the steps an ore particle experiences in the Submerged Arc Furnace and are illustrated in Figure 5. While large variation exists in the results, the main trend is that more acid materials will produce a larger amount of liquid phase at a lower temperatures, in agreement with the phase diagrams already discussed. The materials will also produce a larger amount of liquid phase at low temperatures when it has been heat-treated at high temperatures. This can be explained by the basic and acid minerals mixed in an ore has dissolved into silicate phases when heat-treated and will hence melt at lower temperatures. To exemplify this according to Figure 3 for a constant heating rate: if a pre-reduced ore contains the two individual phases MnO, with a melting point above 1800 °C, and $SiO_2$, with a melting point above 1700 °C, it will start to behave as partly liquid material at higher temperatures, than a $Mn_2SiO_4$ phase that has a melting point of 1363 °C due to kinetic restraints. It is of course the time to reach equilibrium state that will increase, however in a furnace with a fixed heating rate, this will then happen at a higher temperature (Figure 9).

When it comes to the primary slag formation for SiMn production, the average composition will be in the green area in Figure 3, as quartz is also added to the charge mix. Many producers are also using tap-slag from the FeMn production as a raw material. Since this slag contains around 30-40 pct MnO, it will be molten already at around 1250 °C, in the same area as the average primary slag composition. Two hypotheses exist for the reduction step in SiMn furnaces:

1. The Mn-sources will dissolve the quartz first, and the reduction will hence be from the average charge composition, that is the average primary slag com-

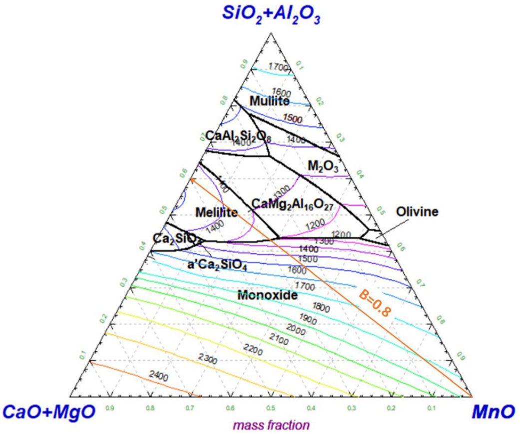

Fig. 7—Liquidus surface of MnO-$SiO_2$-$Al_2O_3$-CaO-MgO (A/S = 0.8, C/M = 7) slags calculated by FactSage software package. The basicity line of 0.8 is indicated.

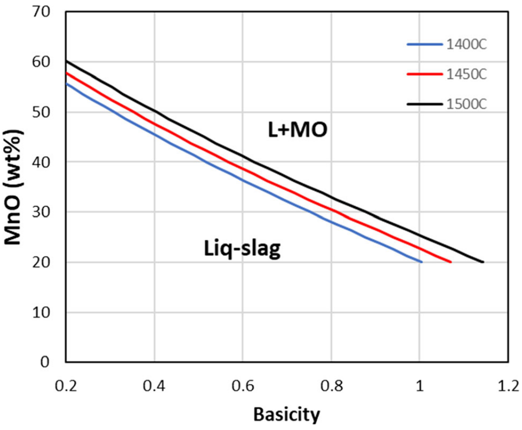

Fig. 8—Liquidus content of MnO *vs.* slag basicity in the MnO-$SiO_2$-CaO-$Al_2O_3$-5 pct MgO ($Al_2O_3$/$SiO_2$ = 0.57).

position. For quartz particles smaller than 2 cm it has been experimentally found that the quartz will dissolve in the Mn-source at temperatures less than 1400 °C, and that the reduction will not occur until around 1500 °C.[32–35] This step thus seems to hold for smaller quartz particles with good contact to the Mn-ore.

2. The reduction of Mn occurs from the partly molten Mn-source due to a slow quartz dissolution. The reduction of Si is thus determined by the quartz dissolution in the Mn-sources. Partly molten quartz has been found in the high temperature area in some industrial excavations, however it is rarely seen in pilot scale excavations. The dissolution of large quartz particles may hence be a larger problem for the electric current paths in the furnace, than for the average slag reduction.

As the effect of dissolution rate of quartz is yet not agreed upon, one can mention that Maroufi *et al.*[36] investigated the quartz dissolution in a SiMn slag and found that the dissolution rate was determined by mass transfer of silica in the slag.

### B. *High Temperature Thermodynamics*

The thermodynamics of the alloy-slag-gas-solid carbon system is investigated by a number of researchers like.[13,37–40] In the following, FactSage will be used to highlight the main issues regarding the thermodynamics in the FeMn and SiMn process.

In the two-phase reaction area in Figure 14, it can also be seen that the higher basicity has a slightly lower reduction rate than the lower basicity slags. As a higher basicity will have more solid MnO phase, and hence a higher viscosity, the mass transport of MnO in the slag may be contributing to the reduced reaction rate. It was however concluded that the chemical reaction was rate determining reaction as no MnO gradients was found in the liquid phase in the slag.[13,44] The effect on the reduction rate on the basicity is not yet fully understood. Both Ngoy[45] and Li[46] investigated Nchwaning and Comilog ores at various basicities from 0.04 to 1.3 by adding either quartz or lime to the ore. In the basicity area of 0.4-1, the effect of basicity was not seen. It was however seen that Comilog was reduced much faster than Nchwaning ore, for all basicities, and hence it is believed that the reduction rate may also be affected by trace elements as seen also for the reduction of SiMn slags.

The metal produced in the FeMn process is typically 78 pct Mn, 7 pct C, less than 1 pct Si and the rest is iron, typically ~ 14 pct (ASTM, grade B[41]). The equilibrium constant for reaction [1] can be expressed by equation.[3]

$$K = \frac{a_{\mathrm{Mn}} \cdot p_{\mathrm{CO}}}{a_{\mathrm{MnO}} \cdot a_{\mathrm{C}}} = \frac{a_{\mathrm{Mn}} \cdot p_{\mathrm{CO}}}{X_{\mathrm{MnO}} \cdot \gamma_{\mathrm{MnO}} \cdot a_{\mathrm{C}}} \quad [3]$$

where $K$ is the equilibrium constant, $a_{\mathrm{Mn}}$ is the activity of Mn in the metal, $p_{\mathrm{CO}}$ is the partial pressure of CO in the gas phase, $a_{\mathrm{MnO}}$ is the activity of MnO in the slag, $a_{\mathrm{C}}$ is the activity of carbon, $X_{\mathrm{MnO}}$ is the mole fraction of MnO in slag and $\gamma_{\mathrm{MnO}}$ is the activity coefficient of MnO in the slag. As there is solid coke present, the activity of carbon is close to 1. The partial pressure of CO in equilibrium with solid carbon above 1200 °C is also close to 1, and as the metal composition is fixed at a fixed temperature, $a_{\mathrm{Mn}}$ is fixed. The amount of MnO in the slag can thus be determined by Eq. [4]. Evidently, the only variables affecting the MnO content in the slag is K and $\gamma_{\mathrm{MnO}}$.

$$X_{\mathrm{MnO}} = \frac{1}{K} \cdot \frac{a_{\mathrm{Mn}}}{\gamma_{\mathrm{MnO}}} \quad [4]$$

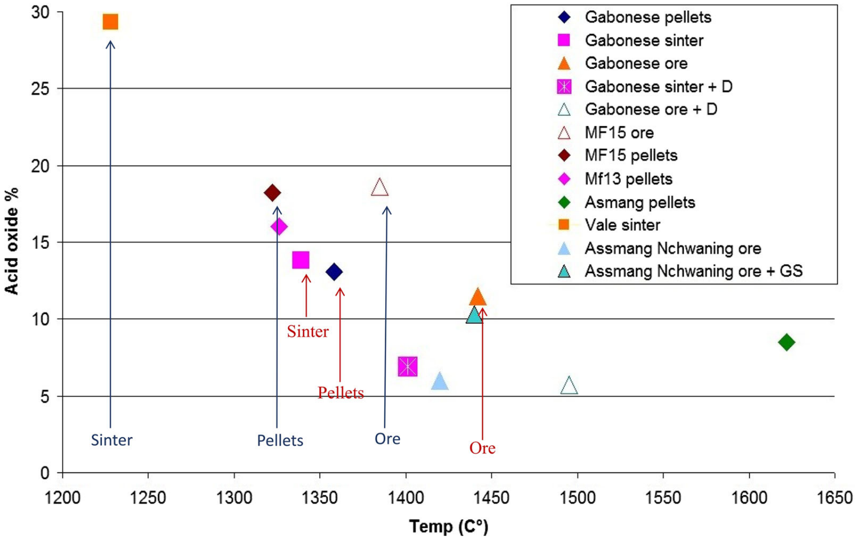

Fig. 9—Initial melting for various raw materials with various basicities and pre-treatment methods. Blue and red notation indicates the same ore with different pre-treatment (Color figure online) (adapted from Brynjulfsen 2013,[26] Ringdalen 2015[28]).

The practical aspects of Eq. [4] is that the MnO content in the slag will be determined by temperature, mainly through the equlibrium constant, and the slag composition, through the activity coefficient. The equlibrium constant is, as seen in Figure 10, strongly dependent on temperature, and hence a lower MnO content will be achieved at higher temperatures. The activity coefficient of MnO will increase with the basic oxides CaO and MgO, and decrease with the acid oxides $SiO_2$ and $Al_2O_3$. According to Gibbs phase rule one can then determine the MnO content as a function of basicity and temperature when two variables are fixed like *e.g.,* the $Al_2O_3$/SiO2 ratio and pct MgO, as shown in Figure 11 for typical FeMn slags.

For SiMn slags, one needs to take into account reaction (2), that is the silicon distribution between the slag and the metal. Doing the same exercise as for the Mn distribution through Eqs. [5] and [6], it is seen that the silicon content in the metal is determined by the amount of $SiO_2$ in the slag, the temperature ($f(T)$, mainly given by the equilibrium constant), the other slag constituents, and the metal composition ($h(mc)$) as shown in Eq. [7]. The metal composition, that is the Mn/Fe ratio is not affecting the silicon content in the same manner as temperature and slag composition.[1] The correlation between the slag composition and temperature is shown in Figure 12. In order to obtain about 18 pct Si in the metal, the slag should be slightly below 40 pct $SiO_2$ at 1600 °C for a $(CaO + MgO)/Al_2O_3$ ratio of 1, which corresponding to most tapped slags. At low $Al_2O_3$ contents, *i.e.,* a high $(CaO + MgO)/Al_2O_3$ ratio, a higher pct $SiO_2$ is needed to compensate for the lack of acid components.

$$K = \frac{a_{\mathrm{Si}} \cdot p_{\mathrm{CO}}^2}{a_{\mathrm{SiO_2}} \cdot a_{\mathrm{C}}^2} = \frac{X_{\mathrm{Si}} \cdot \gamma_{\mathrm{Si}} \cdot p_{\mathrm{CO}}}{X_{\mathrm{SiO_2}} \cdot \gamma_{\mathrm{SiO_2}} \cdot a_{\mathrm{C}}} \qquad [5]$$

$$X_{\mathrm{Si}} = X_{\mathrm{SiO_2}} \cdot K \cdot \gamma_{\mathrm{SiO_2}} \cdot \frac{1}{\gamma_{\mathrm{Si}}} \qquad [6]$$

$$Pct\,\mathrm{Si} = pct\,\mathrm{SiO_2} \cdot f(T) \cdot g\left(\frac{\mathrm{pct\,CaO} + \mathrm{pct\,MgO}}{\mathrm{pct\,Al_2O_3}}\right) \cdot h(\mathrm{mc}) \qquad [7]$$

The function *f*() describes the temperature-dependent part, *g*() the slag composition and *h*() the metal composition. The MnO content in equilibrium with SiMn alloys is relatively low, as seen in Figure 13, typically around 10 pct at 1600 °C. This is quite low compared to what is typically tapped between 10-20 pct as discussed above.

### C. *Reaction Rates and Reduction Mechanism*

The reduction mechanisms for FeMn and SiMn are quite different, and will in this part be discussed separately. For industrial conditions in Submerged Arc Furnaces, Mn has not been seen to be reduced in solid state more than a couple of percentages. This indicates that the major part of the reduction is occurring in liquid state. As discussed above, and illustrated in Figure 3, it means for FeMn primary slags, that the reduction will initiate in the two phase area of liquid phase and a solid MnO-phase. SiMn primary slag will

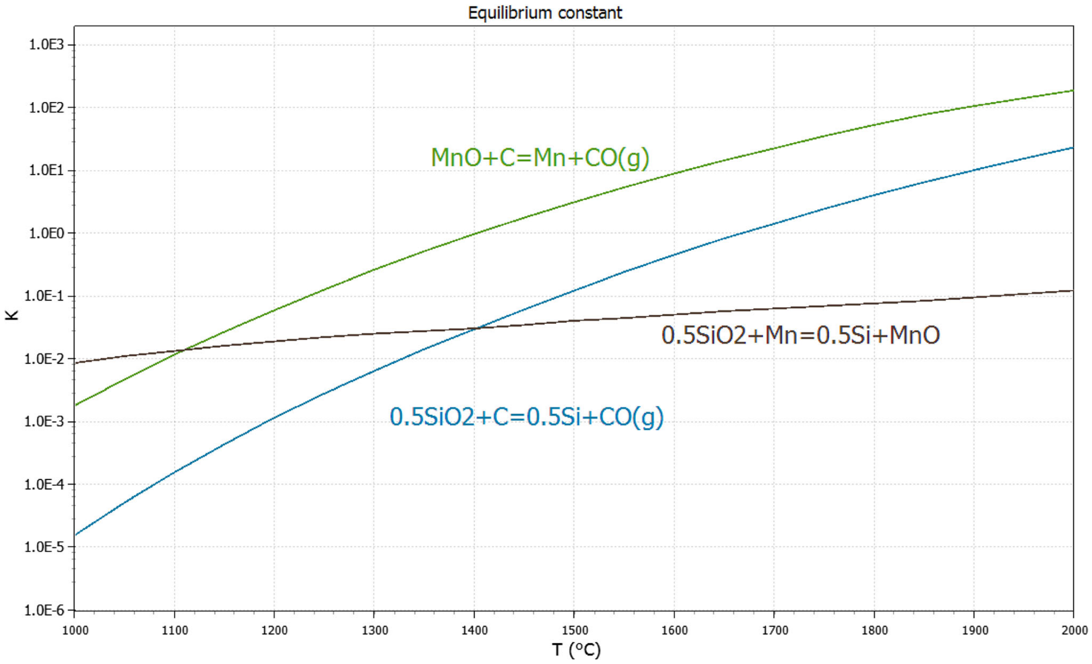

Fig. 10—Equilibrium constant of MnO and $SiO_2$ reduction according to reactions (1) and (2) (calculated from HSC Chemistry v.10).

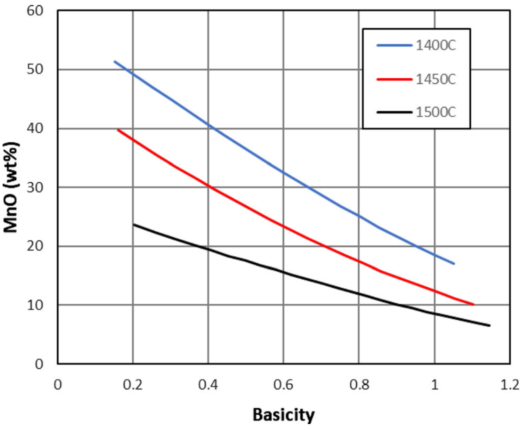

Fig. 11—MnO content *vs.* basicity for a $Al_2O_3/SiO_2$ ratio of 0.57 with 5 pct MgO in equilibrium with a FeMn where the Mn/Fe ratio is 7.8.

probably be all liquid when the reduction starts. The mechanism during reduction will hence be affected by the phases in the primary slag.

The kinetics of a FeMn slag is described by a rapid reaction when the activity of MnO is high and close to 1 (above the liquidus composition) followed by a slow reaction step below the liquidus composition as the activity of MnO is drastically reduced, as shown in Figure 14. This is since the reaction rate will follow the activity of MnO according to reaction (8).

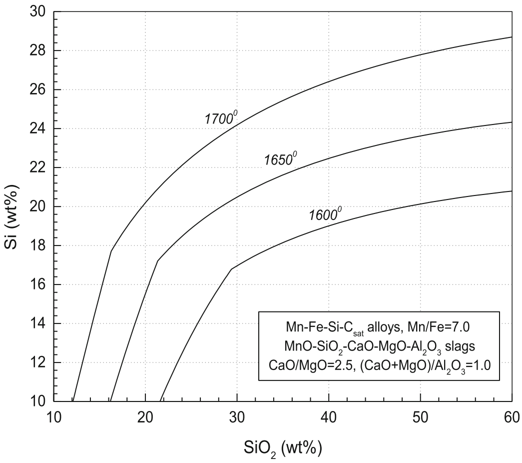

Fig. 12—Pct Si in the metal as a function of pct $SiO_2$ and temperature (for a fixed slag and metal composition)[1]. (Figure is reprinted with permission from Ref. 1).

$$\frac{\mathrm{d\ Pct\ MnO}}{\mathrm{d}t} = A \cdot k \cdot \left(a_{\mathrm{MnO}} - a_{\mathrm{MnO(eq.)}}\right) \qquad [8]$$

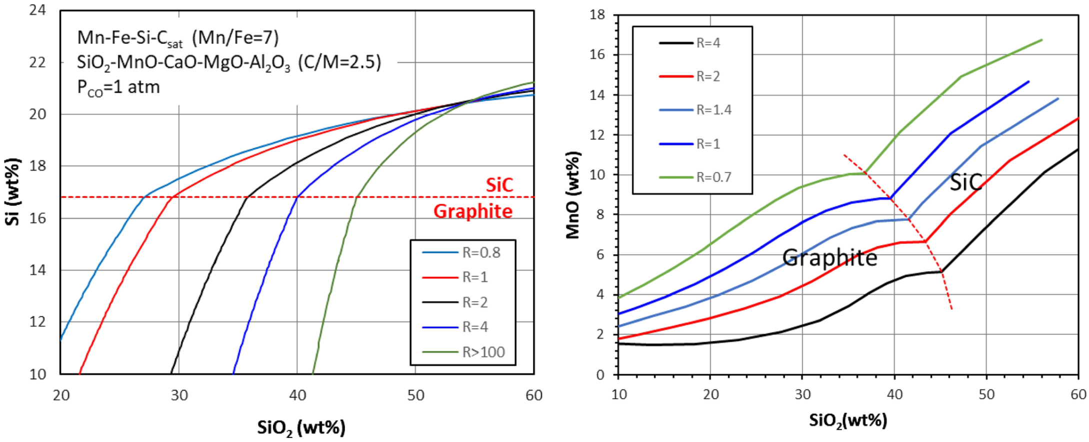

Fig. 13—Pct Si in the metal and wt pct MnO in the slag as a function of slag composition for SiMn slags at 1600 °C. Slag composition is given by R = (CaO + MgO)/Al$_2$O$_3$.

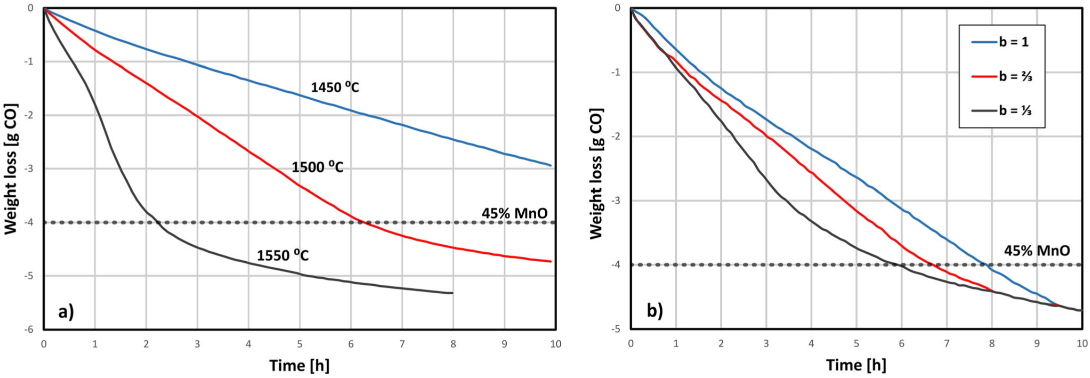

Fig. 14—Weight loss, representing the reaction rate of reaction (1) from 72 to 73 pct MnO with (*a*) Al$_2$O$_3$/SiO$_2$ ratio of 0.25 and basicity of 0.67 and (*b*) at 1500 °C and Al$_2$O$_3$/SiO$_2$ ratio of 0.5 (adapted from Ref. 40).

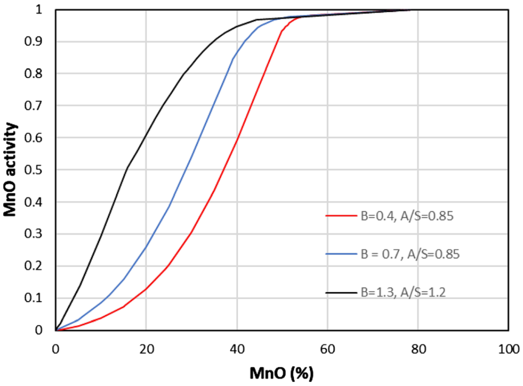

Fig. 15—MnO activity as a function of pct MnO at various basicities and Al$_2$O$_3$/SiO$_2$ ratios at 1500 °C.

where $k$ is rate constant and A is the reaction area between the slag and the carbon material.[13,30,42] When the solid MnO phase is in equilibrium with the liquid slag, the activity of MnO is close to 1. Less than 20 pct MgO has been found to be present in the solid MnO phase[13] and according to Geldenhuis 43, the MnO activity in an MnO-MgO solid solution are ideal in this area. The activity will hence be high in the two-phase area, and when reaching the one phase liquid area, the reduction rate will decrease due to lower MnO activity. The MnO activity in the two and one phase area is shown in Figure 15.

The kinetics for the reduction of SiMn-slag is quite different. The reduction will occur while the slag is in liquid state above 1500 °C, above liquidus composition. It has previously been observed that sulfur in small amounts would increase the reaction rate, corresponding to iron in the metal.[47,48] This was in the later years verified by References 32, 33, 49 through 51. The reaction rate will be very different when sulfur is present, as

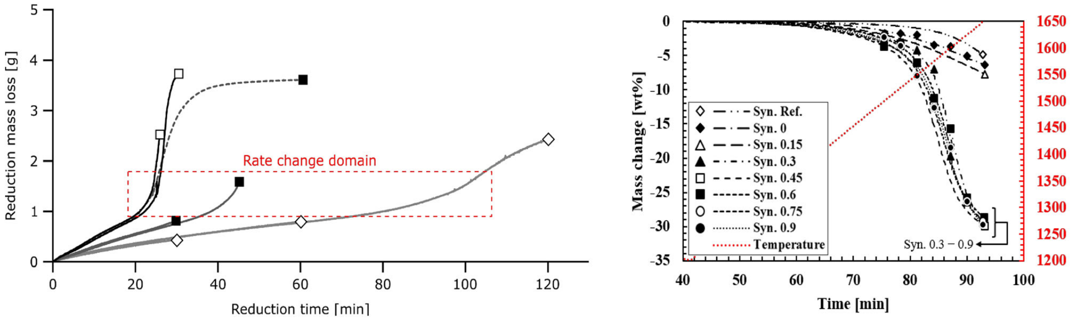

Fig. 16—Reduction rate of primary SiMn slag based on Assmang ore at 1540, 1610 and 1660°C (left figure)[50] and the reduction rate with varying S content (right figure), given as wt pct in the figure, at non-isothermal conditions.[55]

shown in the work from Tranell 52 and Hosum 53, where it was seen that the reaction rate was faster with charcoal compared to coke, when 0.3 pct S was present in the slag. When no slag was present, the coke would give a higher reaction rate, probably because of the high inherent S content in the coke.

In the SiMn reaction, the slag will initially react with a slow reduction step, followed by a fast reduction step as shown in Figure 16. Foaming has been observed in the slag after the initial step[33,50,53,54] and hence both a larger reduction area towards the coke as well as convection in the slag phase may increase the reduction rate. When enough sulfur was present (~ 0.3 pct S) it is seen that the first slow step, would hardly be present, and that the reduction would only go through the fast second step. The reaction rate for both MnO and $SiO_2$ can be calculated based on reaction (8).[50,55]

## III. FUNDAMENTAL SLAG PROPERTIES IN THE FIVE COMPONENT MNO, MGO, CAO, $SIO_2$, $AL_2O_3$ SYSTEM

Numerous slag properties that are important for the Mn-ferroalloy productionare reviewed in this part of the paper. Specifically the slag structure, viscosity, density, surface- and interfacial tension and the electrical conductivity of the five-component slag system will be considered.

### A. *Slag Structure*

The structure of silicate melts is of fundamental importance in metallurgical processes because the melt structure is closely linked to transport properties such as viscosity, density, and electrical conductivity.[56,57] The degree of polymerization (DOP) of silicate networks has been introduced as the most influential parameter for linking these properties and slag structure. DOP and viscosity are proportional, while density and electrical conductivities are inversely proportional to DOP.[58,59] In silicate slags, the presence of network-former and network-modifier elements determines the DOP of the silicate structure. $SiO_2$ is among the network-former oxides, while alkali and alkali-earth oxides, such as $Na_2O$ and CaO(basic oxides), contribute to depolymerization of the silicate network as network-modifying components. Amphoteric oxides, such as $Al_2O_3$, can act as either network-former or network-modifier oxide based on the availability of basic oxides in the silicate network.[60]

Other important parameters are oxygens species, namely bridging oxygen ($O^0$), non-bridging oxygen ($O^-$), and free oxygen ($O^{2-}$). In silicate networks, $O^0$ is connected to two network-former cations ($Si-O^0-Si$ or $Si-O^0-Al$), $O^-$ is bounded to only one network-former cations ($Ca-O^--Si$), while $O^{2-}$ is connected to only network-modifier cations ($Ca-O^{2-}-Ca$). By increasing $O^{2-}$ through dissociation of basic oxides, the DOP of silicate networks decrease because $O^{2-}$ reacts with $O^0$ in the silicates to split the highly complex structures of Si–O into low polymerized units. There are various types of Si–O units called $Q^n$ species where n is the number of $O^0$ in the unit and can be 0 to 4. These units are monomer structure ($Q^0$), dimer structure ($Q^1$), chain structure ($Q^2$), sheet structure ($Q^3$), and 3-dimensional structure ($Q^4$).[61] The DOP parameter can be found both experimentally and theoretically through $Q^n$ species obtained by Raman analysis and slag compositions, respectively. Oxygens species are also given experimentally using X-ray photoelectron spectroscopy (XPS) and theoretically using slag compositions.[62]

Raman spectroscopy has been employed to obtain information on the structural properties of various slags. So far, extensive research has been conducted on the silicate systems using Raman spectroscopy technique including the influence of basic and amphoteric oxides on the silicate structures.[61]

Although the five-component slag system MnO-$SiO_2$-CaO-MgO-$Al_2O_3$ has not been studied through Raman spectroscopic yet, there are several studies that have investigated slags containing MnO using Raman analysis.[58,59,63–66] Slag structure has been reported for the ternary systems of CaO-$SiO_2$-MnO[58,59,63] and MnO-$SiO_2$-$Al_2O_3$[66] as well as the quaternary systems of CaO-$SiO_2$-MnO-$x$CaF$_2$ [$x$ = 0.0 to 14.5 wt pct],[63]

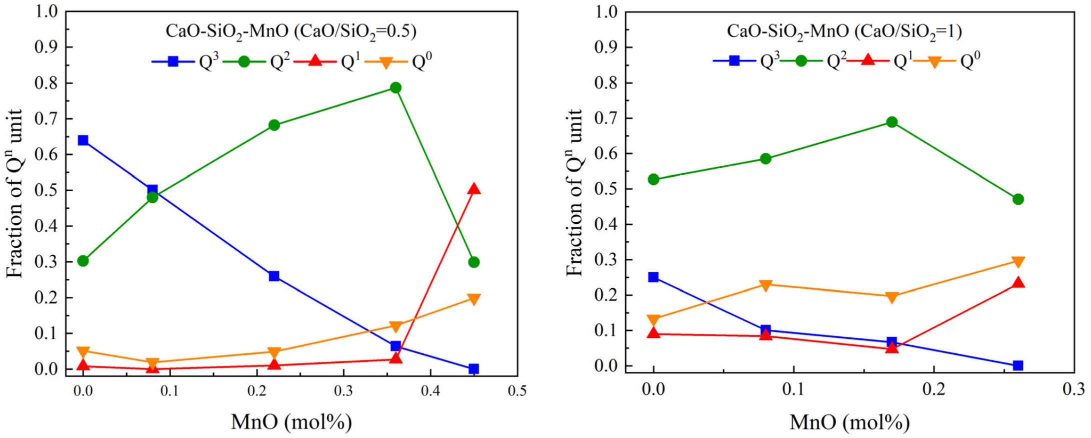

**(a)** **(b)**

Fig. 17—Fraction of Q$^n$ units *vs.* the MnO (mol pct) content. (*a*) the CaO-SiO$_2$-MnO (CaO/SiO$_2$ = 0.5) system and (*b*) the CaO-SiO$_2$-MnO (CaO/SiO$_2$ = 1) system (data from Ref. 58).

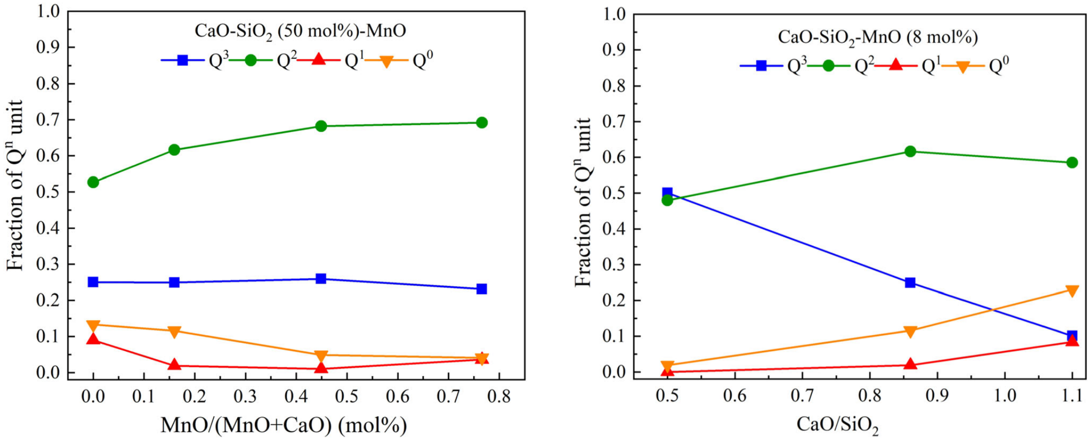

**(a)** **(b)**

Fig. 18—(*a*) Fraction of Q$^n$ units *vs.* the MnO/(MnO + CaO) (mol pct) content in the CaO-SiO$_2$ (50 mol pct)-MnO. (*b*) Fraction of Q$^n$ units *vs.* the CaO/SiO$_2$ (mol pct) content in the CaO-SiO2-MnO (8 mol pct) (data from Ref. 58).

TiO$_2$-MnO (30 wt pct)-SiO$_2$-Al$_2$O$_3$,[64] MO-SiO$_2$-MnO-$y$CaF$_2$ [M(= Ca or Ba)O, $y$ = 0 to 15 mol pct],[65] and MnO-SiO$_2$-Al$_2$O$_3$-zCe$_2$O$_3$ [$z$ = 0.0 to 5.6 mol pct].[66]

Park[58] studied the structure of the CaO-SiO$_2$-MnO system using micro-Raman spectroscopic analysis quantitively. In this slag system, CaO, SiO$_2$, and MnO were varied from 0 to 52 mol pct, 36 to 63 mol pct, and 0 to 58 mol pct, respectively. The compositions containing around 10 to 20 and 40 to 50 mol pct MnO can be considered as simpler representatives of SiMn and FeMn slags, respectively. The variations of $Q^n$ ($Q^0$ to $Q^3$) species were investigated with respect to MnO content, the substitution of CaO with MnO, and the ratio of CaO to SiO$_2$.

The influence of MnO addition was investigated for the CaO-SiO$_2$-MnO system at CaO/SiO$_2$ equal to 0.5 and 1.1 as shown in Figures 17(a) and (b), respectively. For both ratios of CaO/SiO$_2$, the variations of $Q^0$ to $Q^3$ showed similar behavior of increasing MnO. The $Q^3$ unit reduced and the fractions of $Q^1$ and $Q^0$ units increased continuously, while the fraction of $Q^2$ illustrated a maximum at around SiO$_2$ 40 mol pct.

Figure 18(a) presents the fractions of $Q^n$ units with respect to the MnO/(MnO + CaO) changes in the CaO-SiO$_2$ (~ 50 mol pct)-MnO system. By the substitution of CaO by MnO, the Raman analysis found that the $Q^3$ unit slightly decreased while the $Q^2$ unit increased. The fractions of $Q^1$ and $Q^0$ units were slightly reduced by increasing MnO/(MnO + CaO). The effect of

$CaO/SiO_2$ changes on the slag structure was studied in the $CaO-SiO_2-MnO$ (8 mol pct) system. Figure 18(b) displays the fractions of $Q^n$ units *vs.* increasing $CaO/SiO_2$. The fraction of $Q^3$ unit was reduced while the fractions of $Q^1$ and $Q^0$ units were increased by increasing $CaO/SiO_2$ from 0.5 to 1.1, demonstrating that the depolymerization of the silicate network (or reducing DOP of the silicate structure) as the ratio of CaO to $SiO_2$ was increased at a fixed MnO content.

In this study, the $Q^3/Q^2$ ratio was proposed for determining DOP of the silicate network. The results shown in Figures 17 and 18 indicate that MnO is a network-modifier element in the silicate systems similarly to CaO, because the $Q^3/Q^2$ ratio reduced by increasing the MnO content, thereby the silicate network was depolymerized. Also, a linear correlation between ln $(Q^3/Q^2)$ and viscosity, density, and electrical conductivity were explored, demonstrating the influence of slag structure (DOP of the slag network) on these slag properties. It was found that log viscosity increases linearly by increasing ln $(Q^3/Q^2)$ while log density and log electrical conductivity reduce with increasing ln $(Q^3/Q^2)$ linearly.[58]

## B. *Slag Viscosity*

The viscosity of slag contributes to the metal-slag separation efficiency and tapping process, and is thus closely related to operation efficiency and minimizing the energy usage.[67] Slag viscosity depends on temperature and slag composition as the viscosity decreases with increasing temperature and basic oxide contents.

Viscosity measurements for the slag system $MnO-SiO_2-CaO-MgO-Al_2O_3$ have been carried out for various industrial applications.[68–71] A wide variation of slag compositions has been investigated which were close to slags in Mn-ferroalloy production in the submerged arc furnace. In addition to $MnO-SiO_2-CaO-MgO-Al_2O_3$, viscosity has been measured for its various subsystems such as the binary $MnO-SiO_2$ system,[72,73] the ternary systems of $MnO-SiO_2-CaO$[72,74,75] and $MnO-SiO_2-Al_2O_3$[73] as well as the quaternary systems of $MnO-SiO_2-CaO-MgO$[76] and $MnO-SiO_2-CaO-Al_2O_3$.[68,77] In general, the results of these investigations have revealed the effect of both temperature and MnO content. These findings suggest that slag viscosity decreases by increasing temperature and reduces by increasing the MnO content. The latter can be understood by considering the fact that MnO is a basic oxide and acts as a network breaker in the silicate network. In the following, some of the results and observations will be reviewed in more detail.

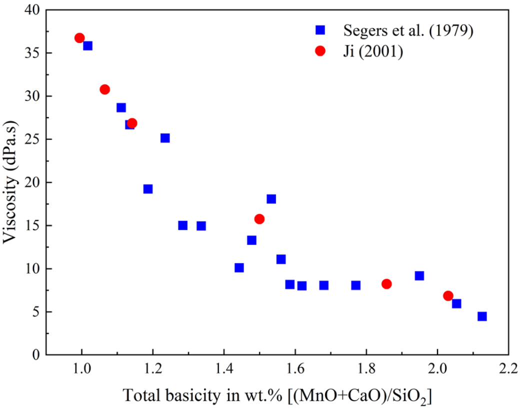

Fig. 19—Experimental viscosities (dPa.s) with respect to total basicity (wt pct) for the $MnO-SiO_2-CaO$ system. Comparing results from Segers *et al.*[72] at 1500 °C and Ji[75] at 1480 °C.

Viscosity measurements for $MnO-SiO_2-CaO$ have been performed for a wide variety of compositions. In Segers *et al.* study,[72] the $SiO_2$ content was given as 32 to 50 wt pct while the contents of MnO and CaO were varied from 10 to 64 and 0 to 45 wt pct, respectively. The measurements were carried out at 1500 °C and illustrated the effect of $SiO_2$ and the substitution of CaO by MnO. In Ji's (2001) work,[75] $SiO_2$, MnO, and CaO were changed from 33 to 50 wt pct, 15 to 56 wt pct, and 8 to 45 wt pct. The viscosity measurements were reported for the temperature range from 1300 °C to 1480 °C. In Figure 19, the viscosity (dPa.s) is plotted as a function of the slag basicity (wt pct) introduced as $(MnO + CaO)/SiO_2$ for the $MnO-SiO_2-CaO$ system to compare the results found by Segers *et al.*[72] at 1500 °C and Ji[75] at 1480 °C. As seen, the viscosity results of these two studies display the same trend, revealing that the viscosity reduces with increasing the basicity through increasing the basic oxides, namely MnO and CaO.

Woollacott *et al.*[69] reported the experimental viscosities at 1500 °C for a group of $MnO-SiO_2-CaO-MgO-Al_2O_3$ compositions related to slags in the production of high-carbon ferromanganese alloys. The MnO and $SiO_2$ contents were changed from 7 to 35 and 27 to 37 mol pct, respectively. $Al_2O_3$ was fixed at 10 mol pct, CaO and MgO were varied from 13 to 45 mol pct and 6 to 21 mol pct, respectively. It was found that $SiO_2$ content induces the major effect on viscosity. While an increase in the $SiO_2$ content increased the viscosity, MnO proved the strongest ability for reducing the viscosity among the involved basic oxides in the slag systems.

In another study published by Persson,[70] for slags associated with Mn-ferroalloy production in the submerged arc furnace, viscosity measurements were carried out within four groups of synthetic slags (called Slag A, B, C, and D) over wide composition ranges as presented in Table III. Each group includes compositions containing 30, 40, and 50 wt pct MnO, while $SiO_2$ and $Al_2O_3$ were varied from 14 to 33 and 8 to 33 wt pct respectively. CaO and MgO as basic oxides in the slag systems were changed from 4 to 29 and 0.3 to 7 wt pct, respectively. Table III displays the lower and higher measured temperatures which were limited by the presence of MnO precipitates and the use of alumina tube in the viscometer apparatus, respectively. The viscosities were measured over the temperature range from 1265 °C to 1712 °C where this range was varied based on the compositions.

Table III. **Compositions (Wt Pct), Viscosity Measurements (dPa.s), and Temperature Ranges (°C) for Four Groups of Slags Associated With Mn-Ferroalloy Production (Data from Ref. 70)**

| Slag name | MnO | $SiO_2$ | CaO | $Al_2O_3$ | MgO | Viscosity (dPa.s) | Temperature (°C) |
|---|---|---|---|---|---|---|---|
| A50 | 51.08 | 20.8 | 15.04 | 9.49 | 4.39 | 0.29–2.50 | 1321–1703 |
| A40 | 40.8 | 25.29 | 18.21 | 11.34 | 5.25 | 0.38–2.86 | 1277–1706 |
| A30 | 30.61 | 29.58 | 21.36 | 13.14 | 6.12 | 0.50–7.46 | 1265–1698 |
| B50 | 50.69 | 14.38 | 10.63 | 24.65 | 0.35 | 0.34–4.48 | 1275–1696 |
| B40 | 40.49 | 17.34 | 12.76 | 29.84 | 0.36 | 0.42–3.10 | 1355–1703 |
| B30 | 31.47 | 20.19 | 14.99 | 33.15 | 0.62 | 0.66–4.55 | 1430–1712 |
| C50 | 49.44 | 22.02 | 3.69 | 23.82 | 1.51 | 0.41–7.51 | 1284–1710 |
| C40 | 39.96 | 27.2 | 4.49 | 27.33 | 1.83 | 0.77–6.47 | 1333–1703 |
| C30 | 31.96 | 32.65 | 4.87 | 28.86 | 2.15 | 1.02–10.90 | 1368–1699 |
| D50 | 50.84 | 15.62 | 21.13 | 8.09 | 4.94 | 0.23–0.56 | 1617–1695 |
| D40 | 40.62 | 19.44 | 25.43 | 9.66 | 6 | 0.22–0.44 | 1449–1704 |
| D30 | 32.14 | 22.07 | 28.69 | 11.44 | 6.65 | 0.31–0.65 | 1486–1694 |

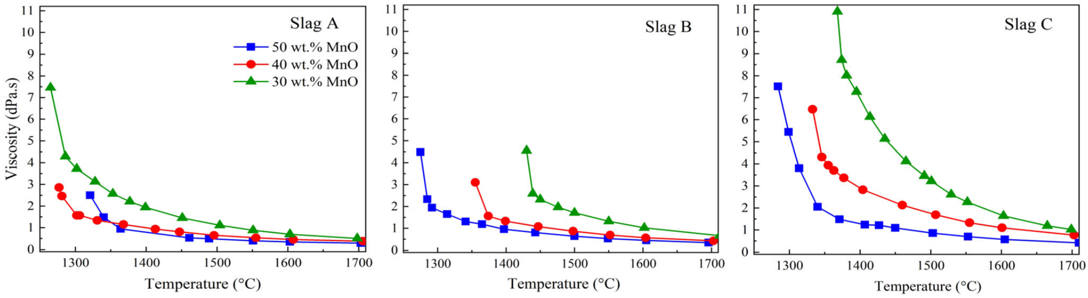

Fig. 20—Viscosity measurements (dPa.s) *vs.* temperature (°C) for Slag A, B, C, presented in Persson.[70]

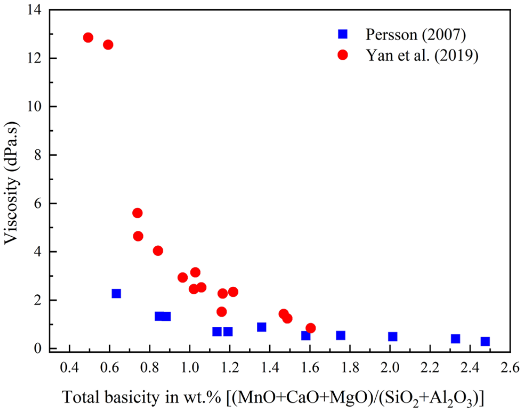

Fig. 21—Experimental viscosities (dPa.s) with respect to total basicity (wt pct) for the $MnO-SiO_2-CaO-MgO-Al_2O_3$ system. Comparing results from Persson 70 at 1550 °C to 1555 °C and Yan *et al.*[71] at 1550 °C.

Figure 20 shows the viscosity measurements (dPa s) with respect to the temperature (°C) for Slag A, B, and C. As expected, viscosities were decreased by increasing MnO from 30 to 50 wt pct for all slag groups.

Comparing the viscosities for slags containing the same amount of MnO suggested that slags with the highest amount of CaO possess the lowest viscosities, namely Slag D, while the highest viscosity values were reported for slags containing the highest amounts of $SiO_2$ and $Al_2O_3$, namely Slag C. It was also noted that the viscosity increases significantly below liquidus temperature because of the presence of solid particles. It is worth noting that MnO content further enhances the viscosity, due to higher amount of solid particles, compared to counterparts with a low amount of MnO, with smaller amount of solid particles.

Yan *et al.*[71] studied viscosity both experimentally and theoretically for the MnO (0 to 55 wt pct)-$SiO_2$-CaO-MgO (5 wt pct)-$Al_2O_3$ (20 wt pct) system in the temperature range from 1300 °C to 1600 °C. The $SiO_2$ and CaO contents were varied from 11 to 48 and 7 to 45 wt pct, respectively. The studied compositions were similar to the slags in FeMn- and SiMn-production. The results showed that the viscosity goes down by increasing MnO, specifically in melts with higher ratio of CaO to $SiO_2$.[71] The addition of 5 wt pct MnO increased the viscosities considerably for melts with the ratio of CaO to $SiO_2$ equal to 1.0 and 1.5, while the viscosity was only slightly reduced for the slag system with the ratio of CaO to $SiO_2$ equal to 0.6.

**Table IV. Chemical Composition of Slags in FeMn and SiMn Production**

| | Chemical Composition (Wt Pct) | | | | | |
|---|---|---|---|---|---|---|
| Slag | MnO | CaO | MgO | $SiO_2$ | $Al_2O_3$ | Other |
| High MnO-FeMn production[94] | 28.0 to 30.0 | 28.0 to 30.0 | 6.0 to 6.5 | 28.0 to 30.0 | 5.0 to 5.5 | 1.0 to 1.3 |
| Low MnO-SiMn production[95] | 10.9 | 28.1 | 7.3 | 32.5 | 21.1 | 0.1 |

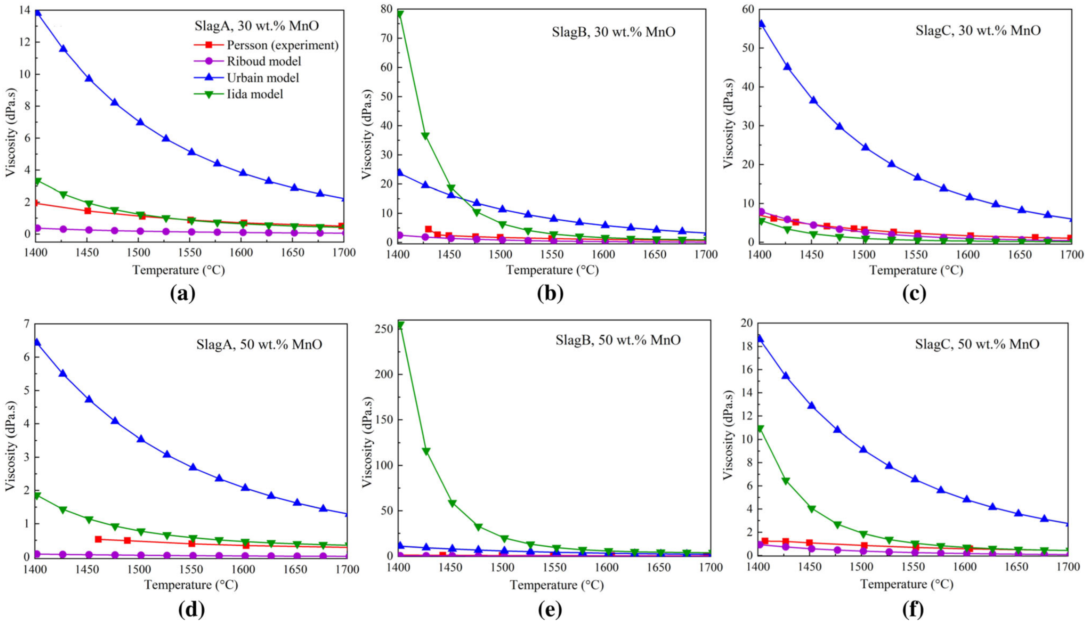

Fig. 22—Viscosity variations (dPa.s) *vs.* temperature (°C). Comparison of viscosities reported by Persson[70] with models from Riboud[84], Urbain[85], and Iida[86] for Slags A to C containing 30 and 50 wt pct MnO. (*a*) to (*f*) represents slag composition from Table III. (*a*) Slag A30, (*b*) Slag B30 (*c*) Slag C30, (*d*) Slag A50, (*e*) SlagB50 and (*f*) Slag C50.

Figure 21 exhibits the viscosity variations with respect to the total basicity (wt pct) defined as $[(MnO + CaO + MgO)/(SiO_2 + Al_2O_3)]$ for data reported by Persson (2007)[70] at 1550 °C to 1555 °C and Yan *et al.* [71] at 1550 °C. As expected, the viscosity reduces by increasing the basicity in both studies, while the measured viscosity magnitudes by Yan *et al.* is larger than those viscosity values by Persson, specifically in lower basicities.

Although viscosity measurements have been performed on various slag systems, it is extremely challenging to produce experimental data for the entire range of compositions and temperatures. Furthermore, the high-temperature viscosity measurement is practically both time-consuming and high-cost. Accordingly, several models have been developed to predict slag viscosity for systems containing MnO.[71,74,76,78–83] The viscosity has been estimated for various binary, ternary, quaternary, and multicomponent systems. Comparing predicted viscosity values with experimental data has demonstrated that the models can provide reliable estimations of viscosity behavior with respect to both temperature and slag compositions.

In Figure 22, experimental viscosity results from Persson 70 are compared to the models proposed by Riboud 84, Urbain 85, and Iida 86 which depend only on slag compositions and temperature. It can be found that while the Urbain model overestimates the experimental data for all compositions presented, two other models predict better values especially the Iida model for the temperatures above 1550 °C. For slags in group B containing the lowest content of $SiO_2$ and highest content of $Al_2O_3$, the Iida model shows large variations with respect to temperatures lower than 1500 °C.

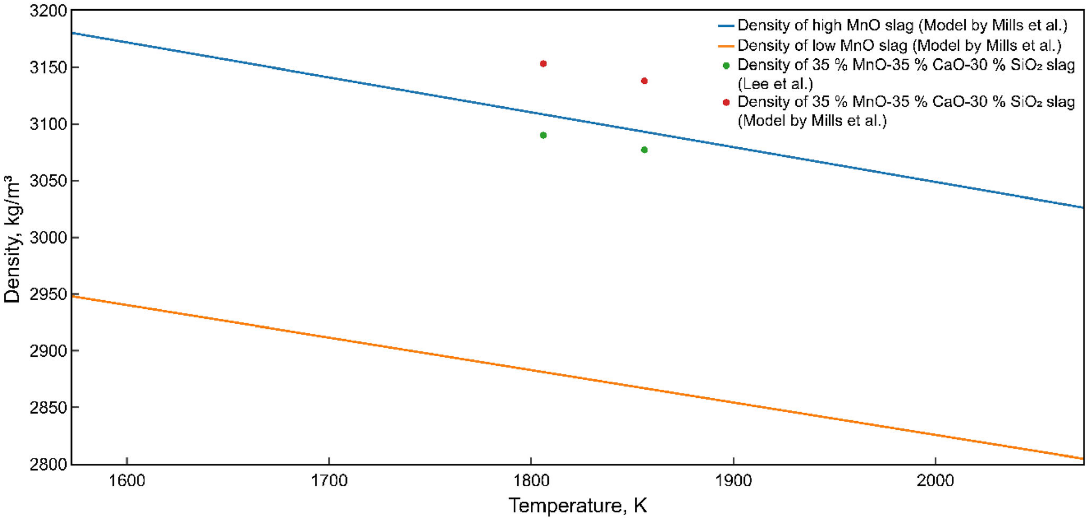

Fig. 23—Density of multicomponent MnO-containing slags. Composition of low and high MnO slags is shown in Table IV.

## C. *Density*

There is a lack of density data on slags in Mn-ferroalloy production, but some insight may be gained by considering slags in steel production. Particularly, so-called mould slags in steel production consist of similar components as slags in Mn-ferroalloy production, MnO, CaO, MgO, $SiO_2$, $Al_2O_3$, while the main difference is the content of these components in both types of slags.[87]

In general, slag density can be determined by (a) numerical calculations based on previously established models[88] and (b) experimental methods, such as the sessile drop technique,[89] the Archimedes principle[90] or electrostatic levitation method.[91]

One of the most well-known numerical methods for calculating density of a multicomponent slag in liquid state is based on calculation of partial molar volumes,[88] which are expressed as:

$$V_{1773} = \sum_{i=1}^{N} X_i V_i \qquad [9]$$

$$V_T = V_{1773} + 0.01(T - 1773\ \mathrm{K})$$

where $V_{1773}$ is slag partial molar volume of at 1773 K,[88,92] $X_i$ is molar fraction of a component, $V_i$ is partial molar volume of a component at 1773 K, $V_T$ is slag partial molar volume at a certain temperature in liquid state and $T$ is the certain temperature in liquid state.

Subsequently, density is defined as:

$$\rho_T = \frac{M}{V_T} \qquad [10]$$

where $\rho_T$ is density liquid state, $M$ is mean molecular weight of all components in slag.

Figure 23 illustrates a comparison of the experimentally measured densities by Lee at al.93 and the calculated densities by the model from Mills *et al.*[2] for $MnO\text{-}CaO\text{-}SiO_2\text{-}MgO\text{-}Al_2O_3$ and $MnO\text{-}CaO\text{-}SiO_2$ slags. The density of $MnO\text{-}CaO\text{-}SiO_2$ slag estimated using the model shows fairly close values to those determined by Lee *et al.*, and in addition, the calculated densities show the expected increase when MnO content is increased, which may indicate that the model of Mills *et al.* can be applied for slags in ferroalloy production with high reproducibility.

## D. *Surface and Interfacial Tension*

Surface and interfacial tensions govern important phenomena such as wetting, foaming, refractory infiltration and slag-metal separation.[96–98] Interfacial behaviour depends upon the content of chemical elements and components interacting at the slag-metal interface, and thus interfacial tension changes as a function of slag composition. As with other properties of slags in ferroalloy production, there are few published data on surface tension of multicomponent slags and interfacial tension between slag and ferroalloys. However, studies on slags in steel production have shown that surface tension of most multicomponent slags lies in the range from 0.30 to 0.70 N/m.[99–101] Bublik *et al.*[102] have found that surface tension of slags corresponding to FeMn and SiMn production are 0.65 and 0.50 N/m, respectively.

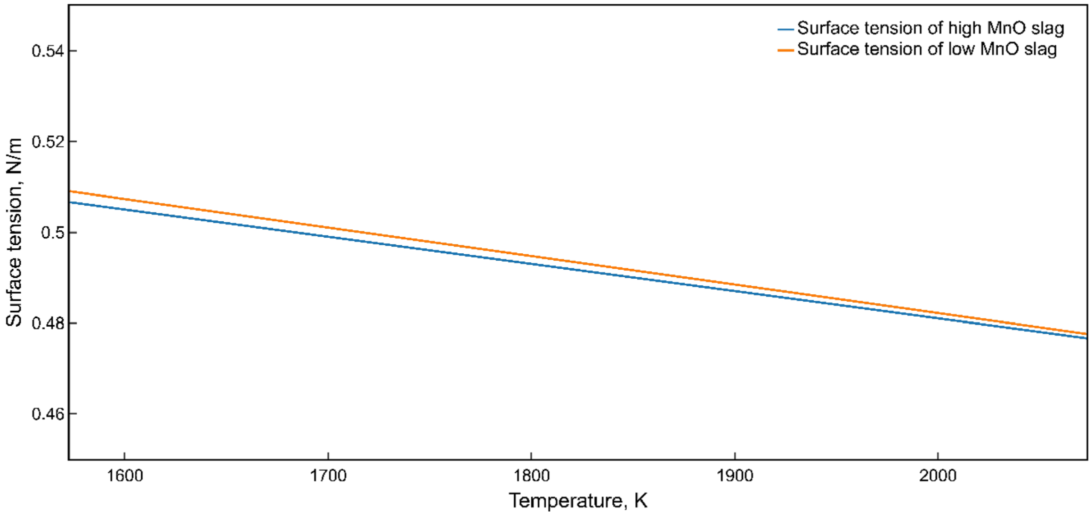

Fig. 24—Surface tension of high and low MnO slags. Composition of low- and high-MnO slags is shown in Table IV.

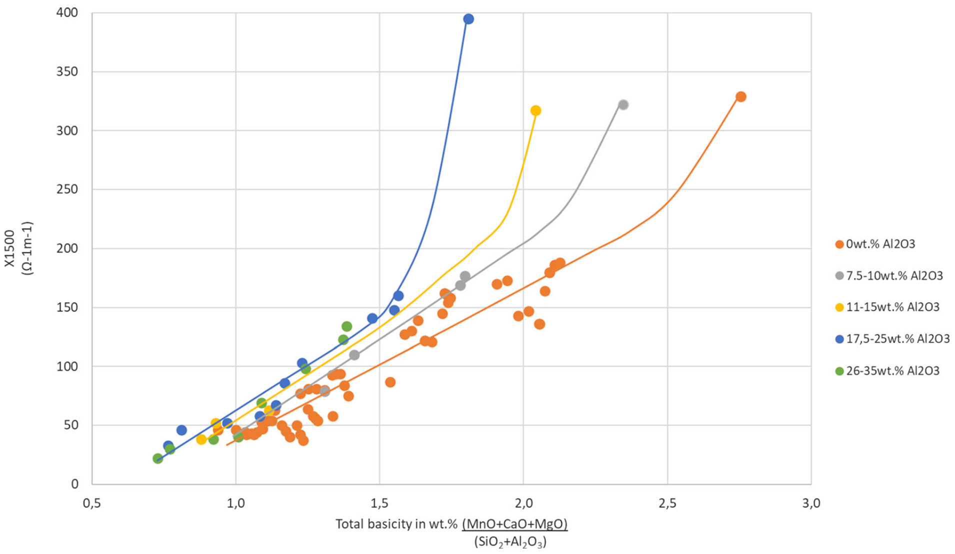

Fig. 25—Electrical conductivity *vs.* total basicity in wt pct for slags with various $Al_2O_3$ contents. The 4 non-linear points giving the electrical resistivity 250 S/m, are the slags with an MnO content above 65 wt pct [data used[108]].

Mills *et al.*[88] have reported that surface tension of multicomponent slags can be calculated assuming that surface tension is temperature-dependent and that all slag components modify surface tension depending on the mole fraction and their content in the bulk or at the surface. As such, $Na_2O$, $K_2O$, $CaF_2$ and $B_2O_3$ are treated as surfactants, while others as bulk components. Surface tension is then calculated using a system of equations:

$$\begin{aligned} \gamma_T &= \gamma_{1773} + \frac{\mathrm{d}\gamma}{\mathrm{d}T}(T - 1773\ \mathrm{K}) \\ \gamma_{1773} &= \left(\sum_{i=1}^{N} X_i\gamma_i\right)_{\mathrm{bulk}} + \left(\sum_{i=1}^{N} X_i\gamma_i\right)_{\mathrm{surf}} \\ \frac{\mathrm{d}\gamma}{\mathrm{d}T} &= \sum_{i=1}^{N} X_i\frac{\mathrm{d}\gamma_i}{\mathrm{d}T} \end{aligned} \qquad [11]$$

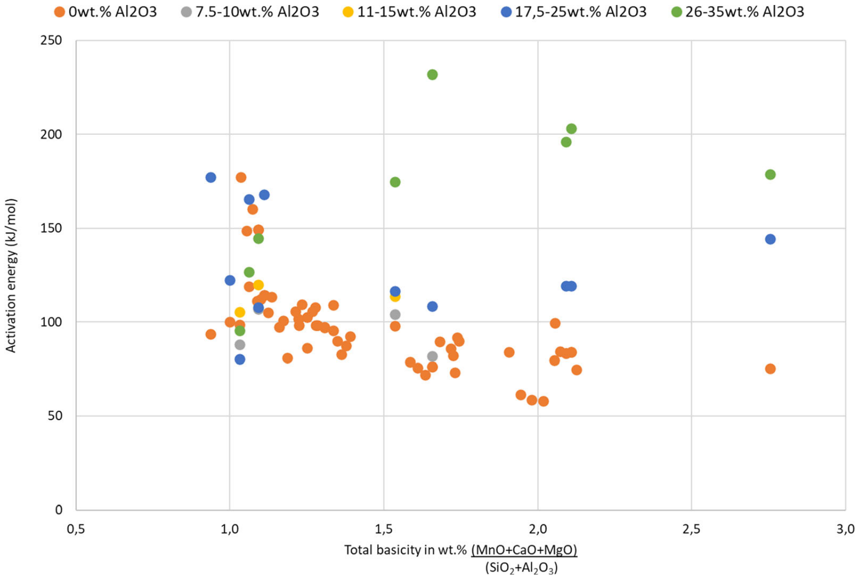

Fig. 26—Activation energy of the conductivity of slags *vs*. total basicity in wt pct for slags with various $Al_2O_3$ content (data from Ref. 108).

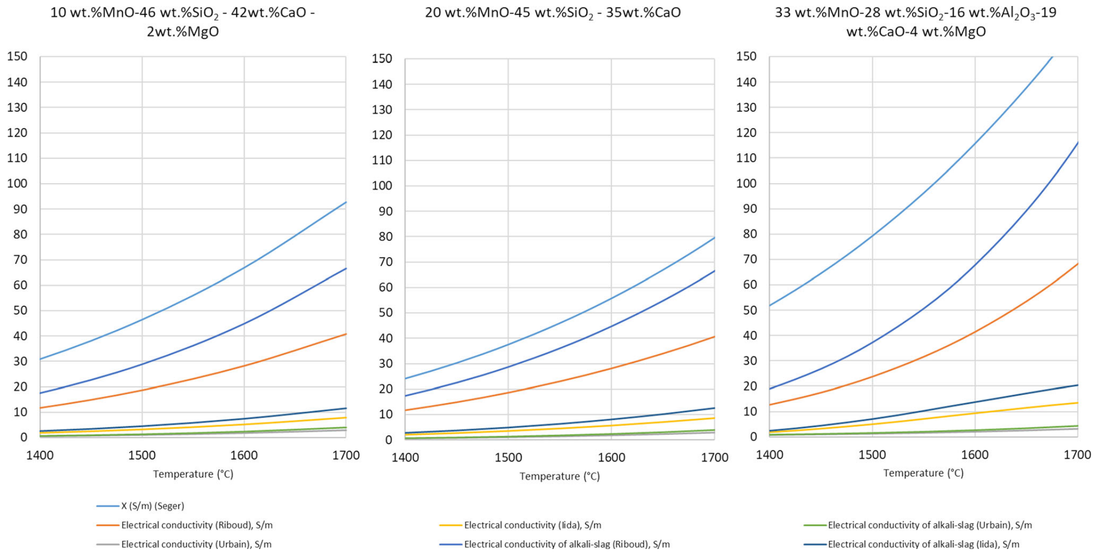

Fig. 27—Comparison of electrical conductivity (S/m) measured by Segers *et al.* with models from Riboud, Urbain and Iida of close to two SiMn slags and one FeMn slag. Though there are some differences, it is the alkali Riboud model that has the smallest deviation from the experimental data, followed by the Riboud model.

where $\gamma_T$ and $\gamma_{1773}$ are surface tension at a certain temperature and 1773 K, respectively.

Values of surface tension calculated using this model for slags as shown in Table IV is illustrated in Figure 24.

Sulfur and other surface-active elements have a significant influence on interfacial tension in liquid systems because they can affect the interfacial interaction at the slag-metal interface.[103–105] As a result, low interfacial tension leads to the formation of a slag-metal emulsion, metal droplet entrainment during tapping, and therefore poor slag-metal separation. Cramb *et al.*[106] have shown that interfacial tension between steel and slag sharply decreases with an increase of sulfur or oxygen activity. Bublik *et al.*[102] have suggested that higher sulfur content in ferroalloy-slag systems results in a higher mass transfer rate at the slag-metal interface, which again decreases both interfacial tension and apparent contact angle between slag and ferroalloys.

### E. *Electrical Conductivity*

The electrical conductivity of slags in the steelmaking area, that is MgO, CaO, $SiO_2$ and $Al_2O_3$ has been investigated by several researchers and to mention one recent review on this system Wang *et al.*[107] can be mentioned. In the five component system including MnO, there is one main reference and that is Seger *et al.*[108]. Seger and his group experimentally determined the slag from a basicity [$= (CaO + MgO)/(SiO_2 + Al_2O_3)$] from 0 to 0.93 and from 10 to 73 pct MnO, that is within the area of FeMn and SiMn production. The electrical conductivity at 1500 °C are shown in Figure 25. The tapping slags for FeMn and SiMn will typically be above 150 S/m and 40-120 S/m respectively. Overall, the electrical conductivity increases with basicity, and as the conductivity is shown as a function of the total basicity, including all 5 components, the conductivity of slags with higher alumina contents will be slightly higher, as alumina is less acid compared to silica. Most of the slags have a linear relationship between the total basicity and the conductivity, and the only exemption is the 4 points with higher than 65 wt pct MnO and no CaO and MgO, which shows conductivities higher than 300 S/m. It can however be mentioned that the MnO/(CaO + MgO) ratio has no significant effect on the rest of the data.

The electrical conductivity is dependent on temperature and can be given by the Arrhenius equation where $X$ (S/m) is conductivity, $A$ is pre-exponential factor (S/m), $E$ is activation energy in kJ/mol, $R$ is gas constant (8.314 J/mol/K) and $T$ is temperature (K):

$$X = A \cdot \exp\left(\frac{-E}{RT}\right) \qquad [12]$$

The activation energy, representing the temperature dependence of the conductivity of the slag, varies between 50-350 kJ/mol as can be seen in Figure 26. There is an indication that the activation energy of the low alumina slags decreases with basicity, while it increases for the high alumina slags.

As both the viscosity and the electrical conductivity is dependent on the slag structure, a correlation between the electrical conductivity and the viscosity has been proposed.[109] Based on the viscosity models of Riboud 110, Urbain 85 and Iida 86 one can hence calculate the electrical conductivity from slag composition and temperature, and in Figure 27 the experimental data from Segers *et al.* has been compared to the models. It can be seen that the experimental data are much higher compared to the models, however the Riboud alkali-model[109,110] gives the best fit.

## ACKNOWLEDGMENTS

This publication has been partly funded by the SFI Metal Production, (Centre for Research-based Innovation, 237738) and Controlled Tapping (267621). The authors gratefully acknowledge the financial support from the Research Council of Norway and the partners of the SFI Metal Production and Controlled Tapping.

## CONFLICT OF INTEREST

On behalf of all authors, the corresponding author states that there is no conflict of interest.

## FUNDING

Open access funding provided by NTNU Norwegian University of Science and Technology (incl St. Olavs Hospital - Trondheim University Hospital).

## OPEN ACCESS

This article is licensed under a Creative Commons Attribution 4.0 International License, which permits use, sharing, adaptation, distribution and reproduction in any medium or format, as long as you give appropriate credit to the original author(s) and the source, provide a link to the Creative Commons licence, and indicate if changes were made. The images or other third party material in this article are included in the article's Creative Commons licence, unless indicated otherwise in a credit line to the material. If material is not included in the article's Creative Commons licence and your intended use is not permitted by statutory regulation or exceeds the permitted use, you will need to obtain permission directly from the copyright holder. To view a copy of this licence, visit http://creativecommons.org/licenses/by/4.0/.

## REFERENCES

1. S. Olsen, M. Tangstad, and T. Lindstad: *Production of Manganese Ferroalloys*, Tapir, Trondheim, 2007.

2. D. Slizovskiy and M. Tangstad: Infacon, Helsinki, 2010.
3. D. Slizovskiy and M. Tangstad: Infacon, Almaty, Kazakhstan, 2013, pp. 185–94.
4. D. Slizovskiy: Doctoral Thesis, NTNU, Norway 2012.
5. M. Tangstad: *Handbook of Ferroalloys*, Elsevier, Amsterdam, 2013, pp. 221–66.
6. M. Tangstad, E. Ringdalen, E. Manilla, and D. Davila: in *7th International Symposium on High-Temperature Metallurgical Processing*, J.-Y. Hwang, T. Jiang, P.C. Pistorius, G.R.F. Alvear F., O. Yücel, L. Cai, B. Zhao, D. Gregurek, and V. Seshadri, eds., Springer, Cham, 2016, pp. 181–88.
7. M. Tangstad, P. Calvert, H. Brun, and A.G. Lindseth: Infacon, Cape Town, 2004, pp. 213–22.
8. H. Lagendijk, B. Xakalashe, T. Ligege, P. Ntikang, and K. Bisaka: Infacon, Helsinki, 2010, pp. 497–508.
9. M. Eissa, H. El-Faramawy, A. Ahmed, S. Nabil, and H. Halfa: *J. Miner. Mater. Charact. Eng.*, 2012, vol. 11, pp. 1–20.
10. T. Coetsee, C. Reinke, J. Nell, and P.C. Pistorius: *Metall. Mater. Trans. B*, 2015, vol. 46, pp. 2534–52.
11. M. Tangstad, E. Ringdalen, E. Manilla, and D. Davila: *JOM*, 2017, vol. 69, pp. 358–64.
12. N.A. Barcza, A. Koursaris, J.B. See, and W.A. Gericke: vol. 37, Iron & Steel Society of AIME, Detroit, 1979, pp. 19–33.
13. M. Tangstad: *PhD-thesis*, NTH, Norway, 1996.
14. M. Tangstad, B.Heiland, S.E.Olsen,R.Tronstad: INFACON, Canada, 2001, p. 6.
15. B. Monsen, M. Tangstad, and H. Midtgaard: Infacon,Cape Town, South Africa, 2004, pp. 392–404.
16. S.E. Olsen and M. Tangstad: Infacon, vol. 10, Cape Town, South Africa, 2004, pp. 231–38.
17. B. Monsen, M. Tangstad, I. Solheim, M. Syvertsen, R. Ishak, and H. Midtgaard: Infacon, vol. 11, The Indian Ferro Alloy Producers' Association, New Delhi, 2007, pp. 297–10.
18. E. Ringdalen and I. Solheim: *Infacon*, Southern African Institute of Mining and Metallurgy, Cape Town, 2018.
19. E. Ringdalen and M. Tangstad: Infacon, Almaty, Kazakhstan, 2013, pp. 195–206.
20. K. Tang and S.E. Olsen: *Infacon*, The Southern African Institute of Mining and Metallurgy, Cape Town, 2004.
21. D. Leroy: Master thesis, NTNU, Norway, 2007.
22. R. Rait and S.E. Olsen: Infacon, Helsinki, 2000.
23. E. Haccuria, P.C. Hayes, and E. Jak: *Int. J. Mater. Res.*, 2015, vol. 106, pp. 225–36.
24. B. Zhao, E. Jak, and P.C. Hayes: *ISIJ Int.*, 2006, vol. 46, pp. 1594–1602.
25. E. Ringdalen, M. Tangstad, and S. Gaal: in *Proceedings of the VIII International Conference on Molten Slags, Fluxes and Salts: 18 - 21 January 2009, Santiago, Chile*, M. Sanchez and Universidad de Concepción, eds., 1. ed., GECAMIN, Santiago, 2009.
26. T. Brynjulfsen and M. Tangstad: Infacon, Almaty, Kazakhstan, 2013, pp. 137–48.
27. M. Visser, H. Smith, E. Ringdalen, and M. Tangstad: Infacon in *MANGANESE FUNDAMENTALS*, Almaty, Kazakhstan, 2013, pp. 553–66.
28. E. Ringdalen, M. Tangstad, and T. Brynjulfsen: Infacon in *FUNDAMENTALS, THEORY*, Kiev, Ukraine, 2015.
29. B. Sorensen, S. Gaal, E. Ringdalen, M. Tangstad, R. Kononov, and O. Ostrovski: in *INFACON XII*, Helsinki, 2010, pp. 439–48.
30. T. Brynjulfsen and M. Tangstad: in *Characterization of Minerals, Metals, and Materials*, J.-Y. Hwang, S.N. Monteiro, C.-G. Bai, J. Carpenter, M. Cai, D. Firrao, and B.-G. Kim, eds., Wiley, Hoboken, NJ, 2012, pp. 147–54.
31. D. Slizovskiy, M. Tangstad, and S. Wasbø: unpublished research 2021.
32. P.P. Kim, J. Holtan, and M. Tangstad: in *Advances in Molten Slags, Fluxes, and Salts: Proceedings of the 10th International Conference on Molten Slags, Fluxes and Salts 2016*, R.G. Reddy, P. Chaubal, P.C. Pistorius, and U. Pal, eds., Springer, Cham, 2016, pp. 1285–92.
33. P.P. Kim and M. Tangstad: *Metall. Mater. Trans. B*, 2018, vol. 49B, pp. 1185–96.
34. J. Holtan: Master thesis, NTNU, Norway, 2016.
35. T.A. Larssen: Master thesis, NTNU, Norway, 2017.
36. S. Maroufi, G. Ciezki, S. Jahanshahi, S. Sun, and O. Ostrovski: *Metall. Mater. Trans. B*, 2015, vol. 46B, pp. 101–108.
37. D. Swinbourne, W.J. Rankin, and R.H. Eric: *Metall. Mater. Trans. B*, 1995, vol. 26B, pp. 59–65.
38. H. Cengizler and R.H. Eric: vol. 1, Southern African Institute of Mining and Metallurgy, Cape Town, South Africa, 1992, pp. 167–74.
39. A.L. Oklei, T.A. Chubnidize, and G.G. Arevadze: *J. Appl. Chem. USSR*, 1991, pp. 1565–68.
40. V. Olsø, M. Tangstad, and S.E. Olsen: Infacon, Beijing, China, 1998, pp. 279–83.
41. Y.E. Lee: *Encyclopedia of Materials: Science and Technology*, Elsevier, Amsterdam, 2001, pp. 3039–44.
42. O. Ostrovski, S.E. Olsen, M. Tangstad, and M. Yastreboff: *Can. Metall. Q.*, 2002, vol. 41, pp. 309–18.
43. J.M.A. Geldenhuis, E.B. Pretorius, and R.J. Dippenaar: The South African Institute of Mining and Metallurgy, Cape Town, 1992.
44. T. Brynjulfsen: Doctoral Thesis, NTNU, Norway 2013.
45. D. Mwana Bute Ngoy, M. Kalenga wa Kalenga, and M. Tangstad: *Metallurgist*, 2018, vol. 62, pp. 658–66.
46. X. Li, K. Tang, and M. Tangstad: *Minerals*, 2020, vol. 10, p. 97.
47. T.-A. Skjervheim: PhD, NTH, Norway, 1994.
48. B. Nadir: Master thesis, NTNU, Norway, 2015.
49. X. Li and M. Tangstad: *Metall. Mater. Trans. B*, 2019, vol. 50B, pp. 136–49.
50. V. Canaguier and M. Tangstad: *Metall. Mater. Trans. B*, 2020, vol. 51B, pp. 953–62.
51. P. Kim, T. Larssen, M. Tangstad, and R. Kawamoto: in *Applications of Process Engineering Principles in Materials Processing, Energy and Environmental Technologies*, S. Wang, M.L. Free, S. Alam, M. Zhang, and P.R. Taylor, eds., Springer, Cham, 2017, pp. 475–83.
52. G. Tranell, S. Gaal, D. Lu, M. Tangstad, and J. Safarian: Infacon,The Indian Ferro Alloy Producers' Association, New Delhi, 2007, pp. 231–40.
53. B.D. Hosum: Master thesis, NTNU, Norway, 2020.
54. V. Canaguier and M. Tangstad: *Metall. Mater. Trans. B*, 2020, vol. 51 (3), pp. 952–63.
55. P.P. Kim: Doctoral Thesis, NTNU, Norway, 2018.
56. B.O. Mysen, D. Virgo, and F.A. Seifert: *Rev. Geophys.*, 1982, vol. 20, p. 353.
57. K.C. Mills: *ISIJ Int.*, 1993, vol. 33, pp. 148–55.
58. J.H. Park: *ISIJ Int.*, 2012, vol. 52, pp. 1627–36.
59. J.H. Park: *J. Non-Cryst. Solids*, 2012, vol. 358, pp. 3096–102.
60. K.C. Mills, L. Yuan, Z. Li, G. Zhang, and K. Chou: *High Temp. Mater. Process.*, 2012, vol. 31, pp. 301–21.
61. B. Mysen and P. Richet: *Silicate Glasses and Melts*, Elsevier, Amsterdam, 2019, pp. 223–62.
62. I. Sohn and D.J. Min: *Steel Res. Int.*, 2012, vol. 83, pp. 611–630.
63. J.H. Park, K.Y. Ko, and T.S. Kim: *Metall. Mater. Trans. B*, 2015, vol. 46B, pp. 741–48.
64. J.B. Kim and I. Sohn: *ISIJ Int.*, 2014, vol. 54, pp. 2050–58.
65. T.S. Kim and J.H. Park: *J. Am. Ceram. Soc.*, 2019, vol. 102, pp. 4943–55.
66. T.S. Kim, S.J. Jeong, and J.H. Park: *Met. Mater. Int.*, 2020, vol. 26, pp. 1872–80.
67. C. Han: PhD Thesis, The University of Queensland, Australia, 2017.
68. I. Tanabe, K. Oku, and T. Honda: *J. Electrochem. Soc. Jpn.*, 1960, vol. 28, pp. E262–66.
69. L.C. Woolacott, D.D. Howat, and P.R. Jochens: South African Institute of Mining and Metallurgy, Johannesburg, South Africa, 1974, pp. 227–32.
70. M. Persson: PhD Thesis, Royal Institute of Technology, Sweden, 2007.
71. B. Yan, Y. Liu, Q. Shu, T. Deng, and B. Glaser: *Metall. Mater. Trans. B*, 2019, vol. 50B, pp. 376–84.
72. L. Segers, A. Fontana, and R. Winand: *Electrochim. Acta*, 1979, vol. 24, pp. 213–18.
73. G. Urbain, Y. Bottinga, and P. Richet: *Geochim. Cosmochim. Acta*, 1982, vol. 46, pp. 1061–72.
74. S. Sridhar, D. Sichen, S. Seetharaman, and K.C. Mills: *Steel Res.*, 2001, vol. 72, pp. 3–10.
75. F-.Z. Ji: *Metall. Mater. Trans. B*, 2001, vol. 32B, p. 181.
76. F-.Z. Ji, D. Sichen, and S. Seetharaman: *Int. J. Thermophys.*, 1999, vol. 20, pp. 309–23.

77. M. Kato and S. Minowa: *Trans. Iron Steel Inst. Jpn.*, 1969, vol. 9, pp. 31–38.
78. L. Zhang and S. Jahanshahi: *Metall. Mater. Trans. B*, 1998, vol. 29B, pp. 177–86.
79. S. Vargas, F.J. Frandsen, and K. Dam-Johansen: *Prog. Energy Combust. Sci.*, 2001, vol. 27, pp. 237–29.
80. K. Tang and M. Tangstad: vol. 11, Infacon, The Indian Ferro Alloy Producers' Association, New Delhi, 2007, pp. 345–57.
81. G-.H. Zhang, K-.C. Chou, Q-.G. Xue, and K.C. Mills: *Metall. Mater. Trans. B*, 2012, vol. 43B, pp. 64–72.
82. M.A. Duchesne, A.M. Bronsch, R.W. Hughes, and P.J. Masset: *Adv. Coal Sci. Technol. ICCST 2011*, 2013, vol. 114, pp. 38–43.
83. W-.Y. Kim, A. Pelton, C. Bale, E. Bélisle, and S. Decterov: *J. Miner. Metall. Sect. B*, 2013, vol. 49, pp. 323–37.
84. P.V. Riboud, Y. Roux, L.D. Lucas, and H. Gaye: *Fachber Huttenprax Met.*, 1981, vol. 19, pp. 859–69.
85. G. Urbain: *Steel Res.*, 1987, vol. 58, pp. 111–16.
86. T. Iida, H. Sakai, Y. Kita, and K. Shigeno: *ISIJ Int.*, 2000, vol. 40, pp. S110–14.
87. K.C. Mills and C-.Å. Däcker: *The Casting Powders Book*, Springer, Cham, 2017.
88. K.C. Mills, S. Karagadde, P.D. Lee, L. Yuan, and F. Shahbazian: *ISIJ Int.*, 2016, vol. 56, pp. 264–73.
89. M.A. Duchesne and R.W. Hughes: *Fuel*, 2017, vol. 188, pp. 173–81.
90. L. Muhmood and S. Seetharaman: *Metall. Mater. Trans. B*, 2010, vol. 41B, pp. 833–40.
91. T. Matsushita, T. Ishikawa, P-.F. Paradis, K. Mukai, and S. Seetharaman: *ISIJ Int.*, 2006, vol. 46, pp. 606–10.
92. K.C. Mills and B.J. Keene: *Int. Mater. Rev.*, 1987, vol. 32, pp. 1–120.
93. J. Lee, L.T. Hoai, J. Choe, and J.H. Park: *ISIJ Int.*, 2012, vol. 52, pp. 2145–48.
94. D. Groot, D. Kazadi, H. Pollman, J. Villiers, T. Redtmann, and J.D. Steenkamp: Infacon13, Almaty, Kazakstan, 2013.
95. E. Ringdalen, S. Gaal, M. Tangstad, and O. Ostrovski: *Metall. Mater. Trans. B*, 2010, vol. 41B, pp. 1220–29.
96. Y. Wanibe, H. Tsuchida, T. Fujisawa, and H. Sakao: *Trans. Iron Steel Inst. Jpn.*, 1983, vol. 23, pp. 322–30.
97. J. Wikström: PhD thesis, Royal Institute of Technology, Sweden, 2007.
98. R.A.M. de Almeida, D. Vieira, W.V. Bielefeldt, A.C.F. Vilela, R.A.M. de Almeida, D. Vieira, W.V. Bielefeldt, and A.C.F. Vilela: *Mater. Res.*, 2017, vol. 20, pp. 474–80.
99. J. Xin, N. Wang, M. Chen, and L. Gan: *ISIJ Int.*, 2019, vol. 59, pp. 759–67.
100. M. Hanao, T. Tanaka, M. Kawamoto, and K. Takatani: *ISIJ Int.*, 2007, vol. 47, pp. 935–39.
101. M. Wegener, L. Muhmood, S. Sun, and A.V. Deev: *Metall. Mater. Trans. B*, 2015, vol. 46B, pp. 316–27.
102. S. Bublik, S. Bao, M. Tangstad, and K.E. Einarsrud: *Metall. Mater. Trans. B*, 2021, vol. 52, pp. 2847–58.
103. L. Muhmood, N.N. Viswanathan, and S. Seetharaman: *Metall. Mater. Trans. B*, 2011, vol. 42B, pp. 460–70.
104. M. Suzuki, M. Nakamoto, T. Tanaka, Y. Tsukaguchi, K. Mishima, and M. Hanao: *ISIJ Int.*, 2020, vol. 60, pp. 2332–38.
105. T. Tanaka, H. Goto, M. Nakamoto, M. Suzuki, M. Hanao, M. Zeze, H. Yamamura, and T. Yoshikawa: *ISIJ Int.*, 2016, vol. 56, pp. 944–52.
106. A.W. Cramb and I. Jimbo: *Steel Res.*, 1989, vol. 60, pp. 157–65.
107. Y. Wang, L. Wang, and K-.C. Chou: *High Temp. Mater. Process.*, 2016, vol. 35, pp. 253–59.
108. L. Segers, A. Fontana, and R. Winand: *Can. Metall. Q.*, 1983, vol. 22, pp. 429–35.
109. K. Mills: Southern African Pyro Metallurgy, The Southern African Institute of Mining and Metallurgy, Johannesburg, 2011.
110. D. Kalisz: *Arch. Mater. Sci. Eng.*, 2012, vol. 58, pp. 164–70.

**Publisher's Note** Springer Nature remains neutral with regard to jurisdictional claims in published maps and institutional affiliations.

# Paper VII

*Infacon XVI: International Ferro-Alloys Congress,*
Edited by A.N. Wærnes, G. Tranell, M. Tangstad, E. Ringdalen, and C. van der Eijk
SINTEF/NTNU/FFF, Trondheim, 27-29 September 2021

# SlagCalculator:
# a framework for slag and metallurgical properties

**S. Bublik[1], S. Gouttebroze[2], T. Coudert[2], M. Tangstad[1] and K. E. Einarsrud[1]**
[1]Norwegian University of Science and Technology (NTNU), Norway,
e-mail: kristian.e.einarsrud@ntnu.no
[2]SINTEF Industry, Norway, e-mail: sylvain.gouttebroze@sintef.no

*Keywords:* Slag properties, slag, modelling, process metallurgy, web application, REST API, SlagCalculator

**Abstract** – Physical properties of multi-component slag systems are of great importance for metallurgical processes, thereby many studies have shown that properties such as density, surface tension or viscosity can be predicted using previously developed models. However, nowadays there is no such framework integrating published models for calculation of slag properties and allowing for user-friendly post-processing of data. In this study, a web-based application for calculation of slag properties both in solid and liquid state was developed in Python. The web-application predicts density, heat capacity, surface tension and other properties from temperature and slag composition provided by the user and subsequently the user has the possibility to interact with and visualize data, and compare results from various models. The architecture of the web-application was designed to address interoperability and data security concepts. In addition, the modularity of the web-application was based on standardized web architectural styles to facilitate the addition of new models or functions in the future. The current work is aimed at demonstrating the key functionality of the application and initiating discussion and further collaboration for its development.

## INTRODUCTION

Metallurgical processes are complex, therefore their modelling is important for advanced process control and optimization. There are many models which describe slag properties and processes, but these models are not gathered in one place, and thus it is of great importance to have a framework that integrates all available models to obtain and manipulate data in a more convenient and accessible way. Many properties can be extracted from commercial codes as for example FactSage (Bale et al. 2016) or HSC Chemistry (HSC Chemistry. 2021), but often it is required to have access to tools that are more user-friendly. A web-based application for calculating electrolyte properties (Electrolyte Properties. 2021), ElProp, has shown that it is completely possible to use advanced frameworks to create easily accessible interactive dashboards. To the best of our knowledge, there is no such tool for pyrometallurgical processes, especially for slags, and that is what we would like to address with this study.

The main goal of the present study was to develop a web-based application for calculation and search of slag properties. The publicly available version will be based on models and data published in previous studies on multi-component slag systems. In addition, the architecture of the application was designed taking into consideration interoperability and data security. The stored data and results generated by the models share a common representation that enables data exchange, comparison, and visualization. Moreover, access to data sets and models must be restricted by user authorization to be relevant for the process industry. To further increase the modularity, the web-based application will rely on micro-services called

Electronic copy available at: https://ssrn.com/abstract=3926702

via standardized REST API. It will facilitate the addition of new models or dashboard presentation in the future.

The application for calculating slag properties was developed in Python (Python.org. 2021) using four main tools: 1) Django framework for the front-end, 2) FastAPI for the micro-services, 3) Plotly for the interactive plots, 4) Azure Active Directory (AZD) for user authentication (via msal and fastapi_auth_aad libraries). The deployment and storage of the database were done on Microsoft Azure, with App Services and Cosmos Azure DB, respectively. The goal of this paper is to demonstrate the key functionality of the framework and initiate discussion and further collaboration for its development. Please note that the framework under development has no intrinsic restrictions on properties, slag system or model type (empirical, physical, neural network, etc.).

## OVERVIEW OF MODELS

A schematic describing physical properties of slags for solid and liquid state calculated in the application is shown in Figure 1. All applied models are described in detail in previous studies:

- density, heat capacity, surface tension - (Mills et al. 2016).
- viscosity – (Riboud et al. 1981; Urbain 1987; Iida et al. 2000).
- thermal conductivity – (Mills et al. 2011).
- electrical conductivity - (Zhang and Chou 2010; Zhang et al. 2011).

Density, heat capacity and enthalpy are calculated both for the solid and the liquid state, depending on slag composition and temperature range provided by the user, while surface tension, viscosity, thermal and electrical conductivity are calculated only for the liquid state.

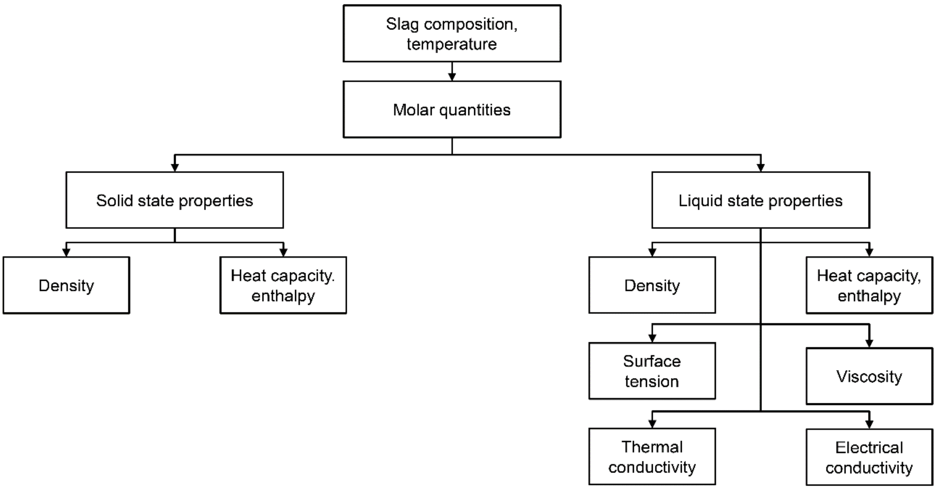

**Figure 1:** Schematic of slag properties in the solid and the liquid state calculated in SlagCalculator.

### Molar quantities

The molar quantities are calculated based on slag composition, which is provided initially by the user. The following molar quantities are used in various models in SlagCalculator:

- mass fraction ($w_i$):

$$w_i = \frac{m_i}{m_{tot}} \qquad \sum_{i=1}^{n} w_i = 1, \qquad [1]$$

Electronic copy available at: https://ssrn.com/abstract=3926702

where $m_i$ is the mass of i-component in the slag, $m_{tot}$ is the total weight of the slag.

- mass percentage (in wt pct):

$$w_i \cdot 100. \tag{2}$$

- number of moles ($n_i$):

$$n_i = \frac{m_i}{M_i} \quad n_{tot} = \sum_{i=1}^{n} n_i, \tag{3}$$

where $M_i$ is the molar mass of i-component in the slag, $n_{tot}$ is the total number of moles of all components.

- molar fraction ($x_i$):

$$x_i = \frac{n_i}{n_{tot}} \quad \sum_{i=1}^{n} x_i = 1. \tag{4}$$

- molar percentage (in mol pct):

$$x_i \cdot 100. \tag{5}$$

**Density**

The density (in kg/m$^3$) is expressed from partial molar volumes of each component in the slag:

- solid state:

$$V_{298} = \sum_{i=1}^{N} x_i V_{298,i}, \tag{6}$$

$$V_{T,sol} = V_{298}(1 + \alpha T_{sol})^3, \tag{7}$$

$$V_{T,sol} = \frac{M}{\rho_{T,sol}} \Rightarrow \rho_{T,sol} = \frac{M}{V_{T,sol}}, \tag{8}$$

where $V_{298}$ is partial molar volume of the slag at 298 K, $V_{298,i}$ is partial molar volume of i-component at 298 K (Mills et al. 2016), $\alpha$ is the average linear thermal expansion coefficient ($9 \cdot 10^{-6}$ K$^{-1}$), $T_{sol}$ is the temperature for the solid state calculations specified by the user, $V_{T,sol}$ is partial molar volume of the slag at the specified temperature for the solid state, $M$ is molecular weight of the slag, $\rho_{T,sol}$ is density of the slag in the solid state.

- liquid state:

$$V_{1773} = \sum_{i=1}^{N} x_i V_{1773,i}, \tag{9}$$

$$V_{T,liq} = V_{1773} + 0.01(T_{liq} - 1773), \tag{10}$$

$$V_{T,liq} = \frac{M}{\rho_{T,liq}} \Rightarrow \rho_{T,liq} = \frac{M}{V_{T,liq}}, \tag{11}$$

where $V_{1773}$ is partial molar volume of the slag at 1773 K, $V_{1773,i}$ is partial molar volume of the slag at 1773 K (Mills et al. 2016), $T_{liq}$ is the temperature for the liquid state calculations specified by the user, $V_{T,liq}$ is partial molar volume of the slag at the specified temperature for the liquid state, $\rho_{T,liq}$ is the density of the slag in the liquid state.

**Heat capacity and enthalpy**

The calculation for the heat capacity (in J/(mol·K) or J/(kg·K)) and the enthalpy (in J/mol or J/kg) is based on relationship between the heat capacity and temperature:

- solid state:

$$C_{m,sol} = a^* + b^* T_{sol} - \frac{c^*}{T_{sol}^2} = \sum_{i=1}^{N} x_i a_i + \sum_{i=1}^{N} x_i b_i T_{sol} - \sum_{i=1}^{N} \frac{x_i c_i}{T_{sol}^2}, \tag{12}$$

Electronic copy available at: https://ssrn.com/abstract=3926702

$$C_{p,sol} = \frac{C_{m,sol} \cdot 1000}{M}, \qquad [13]$$

$$\Delta H_{m,sol} = H_{T,sol} - H_{298} = \int_{298}^{T_{sol}} C_{m,sol} dT = a^{*}(T_{sol} - 298) + 0.5b^{*}(T_{sol}^{2} - 298^{2}) + \frac{c^{*}}{T_{sol}} - \frac{c^{*}}{298}, \qquad [14]$$

$$\Delta H_{p,sol} = \frac{\Delta H_{m,sol} \cdot 1000}{M}, \qquad [15]$$

where $C_{m,sol}$ is molar heat capacity in the solid state, $a^{*}$, $b^{*}$ and $c^{*}$ are constants treated as partial molar quantities, $a_i$, $b_i$ and $c_i$ are constants for i-component in the slag (Mills et al. 2016), $C_{p,sol}$ is specific heat capacity, $\Delta H_{m,sol}$ is molar enthalpy in the solid state, $H_{T,sol}$ is the enthalpy at the specified temperature for the solid state, $H_{298}$ is the enthalpy at 298 K, $\Delta H_{p,sol}$ is specific enthalpy in the solid state.

- liquid state:

$$C_{m,liq} = \sum_{i=1}^{N} x_i C_{m,i}, \qquad [16]$$

$$C_{p,liq} = \frac{C_{m,liq} \cdot 1000}{M}, \qquad [17]$$

$$\Delta S^{fus} = \sum_{i=1}^{N} x_i \Delta S_i^{fus}, \qquad [18]$$

$$\Delta H^{fus} = T_{liq} \Delta S^{fus}, \qquad [19]$$

$$\Delta H_{p,liq} = H_{T,liq} - H_{298} = (\Delta H_{m,sol})_{T_m} + \Delta H^{fus} + C_{p,liq}(T_{liq} - T_m), \qquad [20]$$

where $C_{m,liq}$ is molar heat capacity in the liquid state, $C_{m,i}$ is molar heat capacity of i-component in the slag (Mills et al. 2016), $C_{p,liq}$ is specific heat capacity in the liquid state, $\Delta S^{fus}$ is entropy of fusion, $\Delta S_i^{fus}$ is entropy of fusion of i-component in the slag, $\Delta H^{fus}$ is enthalpy of fusion, $H_{T,liq}$ is the enthalpy at the specified temperature for the liquid state, $(\Delta H_{m,sol})_{T_m}$ is the enthalpy at the liquidus temperature ($T_m$) for the solid state, $\Delta H_{p,liq}$ is specific enthalpy in the liquid state.

**Surface tension**

The surface tension (in mN/m) of the slag in the liquid state is calculated considering the individual contribution of surfactants and bulk components to the surface tension, as well as the temperature dependence of the surface tension:

$$\frac{d\gamma}{dT} = \sum_{i=1}^{N} x_i \frac{d\gamma_i}{dT}, \qquad [21]$$

$$\gamma_{1773} = \gamma_{bulk,1773} + \gamma_{surf,1773} = (\sum_{i=1}^{N} x_i \gamma_i)_{bulk} + (\sum_{i=1}^{N} x_i \gamma_i)_{surf}, \qquad [22]$$

$$\gamma_{T,liq} = \gamma_{1773} + \frac{d\gamma}{dT}(T_{liq} - 1773), \qquad [23]$$

where $\frac{d\gamma}{dT}$ is the temperature dependence of the surface tension, $\frac{d\gamma_i}{dT}$ is the temperature dependence for i-component in the slag, $\gamma_{1773}$ is the surface tension at 1773 K, $\gamma_{bulk,1773}$ is the surface tension of bulk components at 1773 K, $\gamma_{surf,1773}$ is the surface tension of surfactants

Electronic copy available at: https://ssrn.com/abstract=3926702

($B_2O_3$, $K_2O$, $Na_2O$, $CaF_2$) at 1773 K (Mills et al. 2016), $\gamma_{T,liq}$ is the surface tension at the specified temperature for the liquid state.

**Viscosity**

The viscosity of the slag in the liquid state is calculated from Riboud, Urbain and Iida models:

- Riboud model:

$$\eta = A \cdot T_{liq} \cdot \exp(\frac{B}{T_{liq}}), \tag{24}$$

$$A = \exp(-19.81 + 1.73 \cdot x_{basic} + 5.82 \cdot x_{CaF_2} + 7.02 \cdot x_{alkali} - 35.76 \cdot x_{amphoteric}), \tag{25}$$

$$B = 31140 - 23896 \cdot x_{basic} - 46356 \cdot x_{CaF_2} - 39159 \cdot x_{alkali} + 68833 \cdot x_{amphoteric}, \tag{26}$$

$$x_{basic} = x_{CaO} + x_{MgO} + x_{FeO} + x_{Fe_2O_3} + x_{MnO} + x_{NiO} + x_{CrO} + x_{ZnO} + x_{Cr_2O_3}, \tag{27}$$

$$x_{alkali} = x_{Na_2O} + x_{K_2O} + x_{Li_2O}, \tag{28}$$

$$x_{amphoteric} = x_{Al_2O_3} + x_{B_2O_3}, \tag{29}$$

where $\eta$ is the viscosity, A and B are experimental parameters. Note that the viscosity in Riboud model is expressed via the Weymann-Frenkel relation (Eq. [24]) and given in poise or dPa·s, therefore, the viscosity has to be divided by ten to convert it to Pa·s.

- Urbain model:

$$\eta = A \cdot T_{liq} \cdot \exp(\frac{10^3 \cdot B}{T_{liq}}), \tag{30}$$

$$A = \exp(0.29B + 11.57), \tag{31}$$

$$B = B_0 + B_1 x_G + B_2 x_G^2 + B_3 x_G^3, \tag{32}$$

$$B_0 = 13.8 + 39.9355\alpha - 44.049\alpha^2, \tag{33}$$

$$B_1 = 30.481 - 117.1505\alpha + 139.9978\alpha^2, \tag{34}$$

$$B_2 = -40.9429 + 234.0486\alpha - 300.04\alpha^2, \tag{35}$$

$$B_3 = 60.7619 - 153.9276\alpha + 211.1616\alpha^2, \tag{36}$$

$$\alpha = \frac{x_M}{x_M + x_A}, \tag{37}$$

$$x_G = x_{SiO_2}, \tag{38}$$

$$x_M = x_{CaO} + x_{MgO} + x_{FeO} + x_{MnO} + x_{NiO} + x_{CrO} + x_{ZnO} + x_{Na_2O} + x_{K_2O} + x_{Li_2O} + x_{CaF_2}, \tag{39}$$

$$x_A = x_{Al_2O_3} + x_{B_2O_3} + x_{Cr_2O_3} + x_{Fe_2O_3}, \tag{40}$$

where $\alpha$ is a constant describing the fraction of network modifiers and amphoterics, $x_G$, $x_M$ and $x_A$ is the molar fraction of glass formers, network modifiers and amphoteric oxides in the slag, respectively. Note that the viscosity in Urbain model is expressed via the Weymann-Frenkel relation written in a modified form (Eq. [30]) and given in poise or dPa·s, therefore, the viscosity has to be divided by ten to convert it to Pa·s.

- Iida model:

$$\eta = A \cdot \eta_0 \cdot \exp(\frac{E}{B_i}), \tag{41}$$

$$A = 1.029 + 2.078 \cdot 10^{-3} T_{liq} + 1.050 \cdot 10^{-6} T_{liq}^2, \tag{42}$$

$$E = 28.46 - 2.884 \cdot 10^{-2} T_{liq} + 4 \cdot 10^{-6} T_{liq}^2, \tag{43}$$

$$\eta_0 = \sum \eta_{0i} x_i, \tag{44}$$

Electronic copy available at: https://ssrn.com/abstract=3926702

$$B_i = \frac{\sum(\alpha_i w_i)_{basic}}{\sum(\alpha_i w_i)_{acidic}}, \qquad [45]$$

where $A$ is the pre-exponential term, $B_i$ is the basicity index, $E$ is the activation energy, $\eta_0$ is the sum of hypothetical viscosity ($\eta_{0i}$) for each i-component in the slag, $\alpha_i$ is the specific coefficient for i-component in the slag (Iida et al., 2000). Here, CaO, MgO, FeO, MnO, CrO, BaO, $Na_2O$, $K_2O$, $Li_2O$,$CaF_2$ are treated as basic oxides; $SiO_2$, $ZrO_2$, $TiO_2$ are acidic oxides; $Al_2O_3$, $B_2O_3$, $Fe_2O_3$, $Cr_2O_3$ are amphoteric oxides. For a more extensive description of Iida model, refer to (Iida et al. 2000) and (Kekkonen et al. 2012).

**Thermal conductivity**

The thermal conductivity (in W/(m·K)) can be calculation from three methods, where it can be expressed from the viscosity and/or structural parameters of the slag:

- relation with viscosity:

$$k = \exp(-2.178 + 0.282 \cdot \ln(\eta)), \qquad [46]$$

where $k$ is the thermal conductivity of the slag, $\eta$ is the viscosity calculated from Riboud, Urbain or Iida models.

- relation to structure and viscosity:

$$k = \exp(-1.8755 - 0.0893\ln(\eta) + 0.0352\ln(\eta)^2), \qquad [47]$$

$$\eta = 0.165\exp(\frac{Q}{0.817}), \qquad [48]$$

$$Q = 4 - NBO/T, \qquad [49]$$

where $Q$ and $NBO$ /T are measures of slag polymerization and depolymerization (Mills et al. 2016), respectively.

- relation to structure:

$$k = \exp(-1.914 + 0.00037 \cdot \exp(\frac{Q}{0.402})). \qquad [50]$$

**Electrical conductivity**

The electrical conductivity (in $\Omega^{-1}\cdot m^{-1}$) is calculated from the viscosity or the structure-viscosity relation if the slag contains alkali metal oxides.

- relation with viscosity:

$$\kappa = \exp(\frac{-0.08 - \ln(\eta)}{1.18}), \qquad [51]$$

where $\kappa$ is the electrical conductivity of the slag, $\eta$ is the viscosity calculated from Riboud, Urbain or Iida models.

- relation with structure and viscosity for alkali-containing slags:

$$\kappa = \exp(0.15 + 3.87 \cdot r - \frac{\ln(\eta)}{1.1 + 1.77 \cdot r}), \qquad [52]$$

$$r = \frac{2\sum x_{M^+}}{\sum(2x_{M^+} + x_{M^{2+}} + 0.667x_{M^{3+}} + 0.5x_{M^{4+}})}, \qquad [53]$$

where $r$ is the ratio between $M^+$ ions and $M^{2+}$, $M^{3+}$, $M^{4+}$ ions in the slag.

## OVERVIEW OF DIGITAL SOLUTIONS

**Platform security**

The web-based application needs to be secured both on the front-end and back-end, as the aim is to enable the use of public model and data but also in-house or confidential data

Electronic copy available at: https://ssrn.com/abstract=3926702

corresponding to industrial processes. The solution adopted is based on AZD: Microsoft's cloud-based identity and access management service. The platform uses AZD as a standards-based approach for adding single sign-on (SSO) to the app, allowing it to work with a user's pre-existing credentials. The allowed users are registered on the Azure portal for that application and are associated to roles. The role will grant different privileges. For example, a guess will have access only to public models and data, while a contributor will be able to add new experimental data to the database. The token received after the authentication by AZD while also be added to the request send to the different services. In the app, two types of services are implemented: query to the material database, and calculation of slag properties. The data is not access directly but through dedicated APIs (Application Programming Interface) following the REST standard and requiring authentication. This approach allows a more agile development and avoid availability of confidential information in the frontend part.

### Slag properties calculation

The model presented in the previous section are implemented as separated Python codes that are executed by sending a request to a service provider. As an example, the calculation of the density (Table I) will require the application to send the temperature and slag composition, to receive density values. The parameters and even the content of the model is not accessible to the users. The input and output are standardised in order to interchange models. It also allows for any other program to access the models and get results. The FastAPI library automatically generates an interactive documentation of the entry points.

**Table I: Input, output and parameters stored in the code in calculation of density.**

| Input (send in request) | Parameters (stored in code) | Output (send back to client) |
|---|---|---|
| Slag composition<br>Temperature<br>Model<br>Authentication token | $V_{T,sol}$<br>$V_{T,liq}$ | $\rho_{T,sol}$<br>$\rho_{T,liq}$ |

### Slag properties search and comparison

The central idea behind a unified platform is data integration from various sources to form a data lake. The data sets are represented in a shared database with a common data model. Similarly numerical models accept similar inputs (outside specific model parameters) and the output data could be stored next to experimental models. The web application will also allow for searching the database of experimental (or later model) results and visualize the results. Availability of large amount of formatted experimental data also enables the application of machine learning techniques such as Artificial Neural Network. Tang et al. 2021 have successfully applied this approach to the prediction of slag viscosity.

### User interface of the web application

Figure 2 shows a sketch of the graphical user interface for the slag properties calculation. The user interface is under development and different scenarios are studied. Two main scenarios are: 1) calculation of the properties for a specific slag composition, 2) exploration in a composition range. In the first case, after the definition of the reference composition, the interface will provide the closest data set available in the database before suggesting the properties available and the models valid for that composition. Then the user can select the models and a temperature interface to compute the properties. In the second scenario, a range of composition is defined, the available experimental data are found and then the selected models are run for the identified experimental compositions.

Electronic copy available at: https://ssrn.com/abstract=3926702

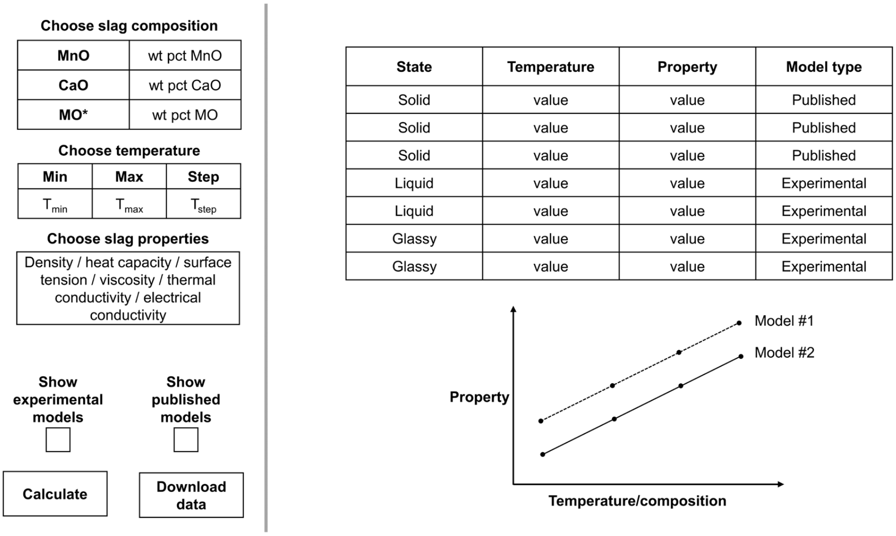

Choose slag composition

| | |
|---|---|
| **MnO** | wt pct MnO |
| **CaO** | wt pct CaO |
| **MO*** | wt pct MO |

Choose temperature

| Min | Max | Step |
|---|---|---|
| $T_{min}$ | $T_{max}$ | $T_{step}$ |

Choose slag properties

Density / heat capacity / surface tension / viscosity / thermal conductivity / electrical conductivity

| State | Temperature | Property | Model type |
|---|---|---|---|
| Solid | value | value | Published |
| Solid | value | value | Published |
| Solid | value | value | Published |
| Liquid | value | value | Experimental |
| Liquid | value | value | Experimental |
| Glassy | value | value | Experimental |
| Glassy | value | value | Experimental |

**Figure 2:** Sketch of the graphical user interface of SlagCalculator. MO* are other oxides in the slag. Please note that the web application is under development and its interface is evolving.

### Deployment of the web application

The application is deployed on Azure Services and relies on three services: App Service for the web front-end acting as the user interface, Cosmos DB for the storage of data in a NoSQL database, and Azure Functions for the models. Azure Functions is a serverless solution to execute simple models that allows for easy scalability. The current demonstrator is available at https://slagcalulator-v1.azurewebsites.net.

## FUTURE WORK

The future of the platform will depend on the improvement of two critical points: useability and accuracy. Therefore, the future work will focus on both model development and enrichment to provide accurate and relevant data, and on user experience and integration of this tool in the engineer workflow.

For further development of the application, it can be proposed to:

- include models for automatic calculation of liquidus and solidus temperature for slags.
- consider properties change in the glassy state.
- expand the available models for a more accurate calculation of physical properties of ferroalloy slags.
- provide access to public and restricted access to material databases.
- integration of neural network model development.

## CONCLUSIONS

In the current work, we have presented a framework for easy, secure, and consistent access to slag data and properties. The present version of the framework includes only data based on the literature, but we aim to extend the database in the future in close collaboration with industry, research institutes and other stakeholders.

Electronic copy available at: https://ssrn.com/abstract=3926702

## ACKNOWLEDGEMENTS

This work has been funded by several sources. Authors from NTNU would like to acknowledge support from SFI Metal Production (Centre for Research-based Innovation, 237738). The work performed by SINTEF has been financed by an internal project "Secured Material Properties APP".

## REFERENCES

Bale, C.W. et al. 2016. FactSage thermochemical software and databases, 2010–2016. *CALPHAD: Computer Coupling of Phase Diagrams and Thermochemistry* 54, pp. 35–53. doi:10.1016/j.calphad.2016.05.002.

Electrolyte Properties. 2021. https://peter-entner.com/E/ElProp-2/ElProp-2.htm

HSC Chemistry. 2021. https://www.hsc-chemistry.com/

Iida, T. et al. 2000. An Equation for Accurate Prediction of the Viscosities of Blast Furnace Type Slags from Chemical Composition. *ISIJ International* 40(Suppl), pp. S110–S114. doi: 10.2355/isijinternational.40.Suppl_S110.

Kekkonen, M. et al. 2012. Viscosity models for molten slags. https://research.aalto.fi/en/publications/viscosity-models-for-molten-slags

Mills, K.C. et al. 2011. Estimating the physical properties of slags. 111, p. 10.

Mills, K.C. et al. 2016. Calculation of Physical Properties for Use in Models of Continuous Casting Process-Part 1: Mould Slags. *ISIJ International* 56(2), pp. 264–273. doi: 10.2355/isijinternational.ISIJINT-2015-364.

Python.org. 2021. https://www.python.org/

Riboud, P.V. et al. 1981. Improvement of Continuous Casting Powders. *Fachber Huttenprax Metallweiterverarb* 19(10), pp. 859–869.

Tang, K. et al. 2021. Rheological Properties of Ternary SiO2-CaO-Al2O3 Silicate System. *11th international conference on Molten slags, Fluxes and Salts*, Virtual Venue, Korea, 21-25 February 2021.

Urbain, G. 1987. Viscosity estimation of slags. *Steel Research* 58(3), pp. 111–116. doi: 10.1002/srin.198701513.

Zhang, G.-H. et al. 2011. Relation Between Viscosity and Electrical Conductivity of Silicate Melts. *Metallurgical and Materials Transactions B* 42(2), pp. 261–264. doi: 10.1007/s11663-011-9484-7.

Zhang, G.-H. and Chou, K.-C. 2010. Simple Method for Estimating the Electrical Conductivity of Oxide Melts with Optical Basicity. *Metallurgical and Materials Transactions B* 41(1), pp. 131–136. doi: 10.1007/s11663-009-9298-z.

---

**Sergey Bublik**

*PhD Candidate, NTNU*

Sergey has a master's degree in Non-Ferrous Metallurgy from Norilsk Industrial Institute, Russia. He also has industrial experience in production of nickel, copper and platinum metals. Currently, Sergey is working with slag and metal separation in ferroalloy production, where he investigates interfacial phenomena and multiphase flow of molten slag and metal.

---

Electronic copy available at: https://ssrn.com/abstract=3926702

# Appendix A

# Computational resources

The multiphase simulations in OpenFOAM were performed on resources provided by the NTNU IDUN/EPIC computing cluster [93]. The cluster has more than 70 nodes and 90 GPGPUs. Each node contains two Intel Xeon cores, at least 128 GB of main memory, and is connected to an Infiniband network. Half of the nodes are equipped with two or more Nvidia Tesla P100 or V100 GPGPUs. Storage is provided by two storage arrays and a Lustre parallel distributed file system.

ISBN 978-82-326-5233-4 (printed ver.)
ISBN 978-82-326-6006-3 (electronic ver.)
ISSN 1503-8181 (printed ver.)
ISSN 2703-8084 (online ver.)

NTNU
Norwegian University of
Science and Technology